CRANFIELD UNIVERSITY
School of Aerospace, Transport and Manufacturing
Propulsion Engineering Centre

Computational Aerodynamics for Open Rotor Tip Vortex Interaction Noise Prediction

Tom Elson
Ph.D. Full Time

Supervisor: Dr. David G MacManus

November 29, 2015

Executive Summary

Open rotor engines can provide fuel savings of up to twenty seven percent compared to a modern high bypass turbofan engine. They were subject to intense research in the 1980s in response to the 1973 oil crisis. They have come back into consideration to combat the strict environmental regulations currently imposed on the aviation industry and to meet the ACARE 2020 requirements. Recent large scale European projects such as DREAM and Clean Sky have included significant research on the open rotor since their comeback.

Their major drawback is the noise levels generated when the wake and tip vortices of the front rotor interact with the aft rotor. The noise generated from these interactions is highly tonal which makes the open rotor prohibitively noisy.

The Unducted Fan (UDF) demonstrator engine was built in the 1980s by General Electric in collaboration with NASA. During the design phase of this project a computer code named CRPFAN was developed to predict the noise of open rotors. CRPFAN is used as a representative preliminary design noise prediction tool and was the only representative tool available to the author at the time of the project.

Included in CRPFAN is a vortex model which relies heavily on outdated empirical relations. There is currently a better knowledge of tip vortex properties relative to when the code was created. However, there has been no significant study on how the specific parameters of a tip vortex relate to the noise of an open rotor or how to more accurately predict the tip vortex parameters, which is what this project aims to do.

The first part of the project developed methods to quantify how the tip vortex parameters relate to the noise generated by its interaction with the aft blade row. The next step was to further develop the state of the art of tip vortex models. This is done using basic analytical models integrated into CRPFAN and the use of Computational Fluid Dynamics (CFD) to model the tip vortices.

CFD was used to develop bespoke tip vortex correlations which relate the tip vortex parameters to the open rotor performance parameters such as the lift, thrust and power coefficients. Correlations for the tip vortex axial velocity, trajectory, circulation and core size have been developed and integrated into CRPFAN with a detailed analysis of their performance relative to the current state of the art included.

This thesis includes recommendations to improve the tip vortex models such as taking into account the spatial orientation of the vortex, inclusion of a vortex axial velocity component and how strip theory codes can under predict the noise.

Acknowledgements

Firstly I would like to thank my supervisor David for his continued support and technical assistance throughout the project and for pushing me to achieve what I was capable of. I'd also like to thank Tory Parry of Rolls Royce for his assistance at the beginning of the project, particularly in the area of open rotor noise.

Whilst at Cranfield I made many good friends and had many good times. Especially with everyone on the Cranfield Rugby team and my house-mates at both West Road and Partridge Piece. Special mention needs to be made to my PhD compatriots Rob, Kish and Grant who made the experience that much easier.

Finally I would like to thank my family for their support in getting me to a PhD stage and during it also to Jessica for helping me get through the difficult period of writing up.

Contents

List of Figures

List of Tables

Nomenclature

Roman Symbols

$\bar{r}$	Non-dimensional tip vortex radius	
A_n	Fourier series coefficient	
B_D	chord to diameter ratio	
c	Chord	m
c_0	Ambient speed of sound	m/s
C_{Di}	Induced drag coefficient	
C_{Dk}	kth harmonic drag coefficient	
C_D	Drag coefficient	
C_{Lk}	kth harmonic lift coefficient	
C_L	Lift coefficient	
C_l	Sectional Lift coefficient	
C_P	Power coefficient	
C_T	Thrust coefficient	
D	Blade diameter	m
E	Vortex filament kinetic energy per unit length	N
g	Grid level	
J	Advance ratio	
J_n	Bessel function	
k	Order of load harmonic	
$k_{x,y}$	Non-dimensional wave number	

L	Lift	N
M	Mach number	
m	Sound harmonic	
M_r	Relative Mach number	
M_T	Tip Mach number	
M_x	Flight Mach number	
N	Rotational speed	$rads/s$
n	Vatistas shape factor	
P_0	Total pressure	Pa
Pi	Rotor induced power	Nm/s
Q	Torque	Nm
Q_F	Torque force	N
r	Radius	m
r_c	Vortex core size radius	m
R_e	Reynolds number	
S	Helical distance	m
s	Semi - span	m
S_W	Planform Area	m^2
T	Thrust	N
t	time	s
T_0	Total temperature	K
U_W	Relative velocity	m/s
V_0	Freestream velocity	m/s
V_θ	Tangential velocity	m/s
z	Observer radius/tip radius	

Abbreviations

ACARE	Aviation Research and innovation in Europe

AR	Asymptotic range	
BEMT	Blade Element Momentum Theory	
BPF	Blade Passing Frequency	
CAA	Computation Aeroacoustics	
CFD	Computational Fluid Dynamics	
CI	Circulation Index	
CROR	Counter Rotating Open Rotor	
DES	Detached Eddy Simulation	
EVM	Eddy viscosity model	
FA	Face Alignment	
GCI	Grid convergence index	
LDV	Laser Doppler Velocimetry	
LES	Large Eddy Simulation	
MCA	Mid chord alignment	
OASPL	Overall Sound Pressure Level	
OASPL	Overall sound pressure level	dB
PIV	Particle Image Velocimetry	
PSD	Power Spectral Density	
RANS	Reynolds Averaged Navier Stokes	
RPM	Revolutions per minute	
RSM	Reynolds Stress Model	
SHP	Shaft horsepower	
SPL	Sound pressure level	dB
SST	Shear Stress transport	
TVTI	Tip Vortex Trajectory Index	
UDF	Unducted Fan	

Greek Symbols

α	Relative angle of attack	radians
α_0	Zero lift angle of attack	radians
β	Blade pitch angle	radians
η	Efficiency	
Γ	Circulation	m^2/s
γ	Adiabatic index	
Ω	Rotational velocity	rad/s
ω	Vorticity	1/s
ϕ_o	Phase angle due to offset	radians
ϕ_s	Phase angle due to sweep	radians
Ψ_k	Transformation of chordwise distribution	
ψ_k	Fourier transform of generalized source function	
ρ	Density	kg/m^3
θ	Angle as defined	radians

Subscripts

$\frac{3}{4}$	Three quarter span
global	With reference to global coordinate system
i	Unit vector in x-direction
j	Unit vector in y-direction
k	Unit vector in z-direction
local	With reference to local coordinate system
max	Maximum
X	x- coordinate
Y	y- coordinate
Z	z- coordinate
A	Aft rotor
F	Front rotor
Root	Root portion of blade
Tip	Tip portion of blade

Chapter 1

Introduction

The open rotor is currently being re-considered as an alternative to the high by-pass turbofan engine for medium sized aircraft in an attempt to meet the Advisory Council for Aviation Research and innovation in Europe (ACARE) 2020 requirements. The key requirements related to engine performance and emissions include a reduction of 15 to 20% in specific fuel consumption, reduce NO_2 by 60 to 80 % and to reduce noise by 10 dB per operation[1].

One of the initiatives to achieve the ACARE 2020 goals is the formation of the Clean Sky Joint Technology Initiative (JTI) - a €1.6 billion European research programme. A specific part of Clean Sky is the Sustainable and Green Engines (SAGE) Integrated Technology Demonstrator (ITD) which has on objective for the open rotor to fly by 2019[2].

The open rotor was first considered seriously in the late 1970s and early 1980s after the 1973 Oil Crisis led the cost of fuel to rise considerably[3]. Open rotors achieve higher propulsive efficiencies than a standard advanced propeller by using a second row of blades downstream which rotates in the opposite direction.

The advantage of this second blade row is that it recovers the axial velocity lost due to the swirl in the flow. The disadvantage of this system is the occurrence of aerodynamic interactions between the front and rear blade rows which generates tonal noise. A major source of these interactions is the front rotor tip vortex interacting with the rear blade row. The presence of the front rotor tip vortex results in the aft blade operating in an unsteady distorted flowfield which causes interaction noise. The interaction mechanism of the front rotor tip vortex with the rear rotor is depicted in Figure 1.1.

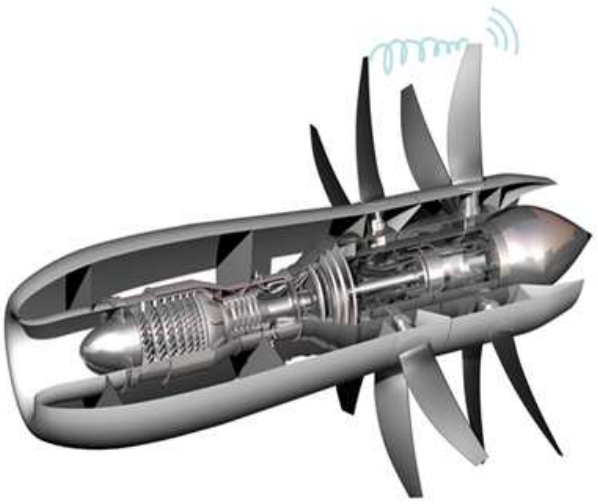

FIGURE 1.1: Tip vortex interaction mechanism adapted from [4]

An analytical method for predicting the noise due to tip vortex interaction exists [5] and is included in the open rotor noise prediction code CRPFAN. The analytical method requires a description of the tip vortex size, strength and location. CRPFAN acquires this information from empirical data derived from standard fixed wing cascade experiments [6].

The validity of this cascade data to predict the tip vortex of an open rotor is questionable. In Figure 1.2 CRPFAN is compared against anechoic wind tunnel data for the Unducted Fan (UDF) blading at a take off condition. The sound pressure level (SPL) directivity is presented for a two-one interaction tone. The directivity is based on the observer angle defined in Figure 1.3 and a two-one interaction tone means the frequency is twice the front rotor blade passing frequency (BPF) plus once times the rear rotor blade passing frequency. The measured anechoic wind tunnel data is compared to CRPFAN predictions, where CRPFAN is used in two modes. The first mode is CRPFAN in its default operation with the tip vortex model included and the second mode excludes the tip vortex model in the interaction noise calculation. The CRPFAN tip vortex model under predicts the noise produced by the tip vortex - especially at the higher observer angles.

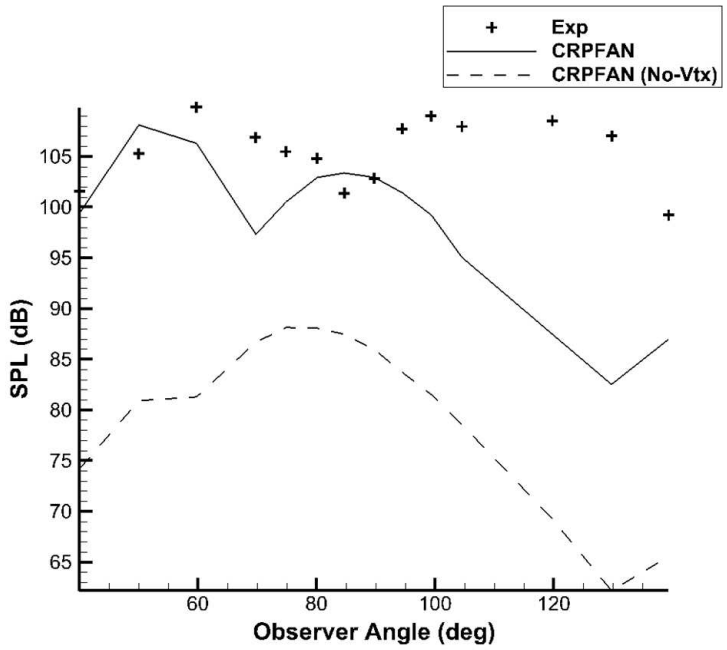

FIGURE 1.2: SPL directivity for 2-1 interaction of the UDF at take off[5]

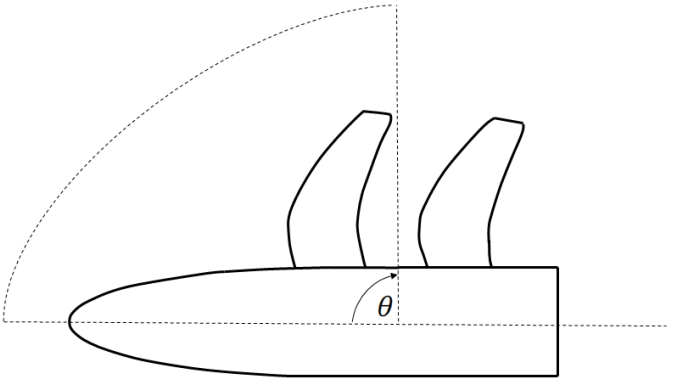

FIGURE 1.3: Definition of observer angle

The reason for the discrepancy between the experimental data and the CRPFAN calculation can be attributed to in-accuracies in the tip vortex model which is based on fixed wing cascade measurements from a limited set of data. But how essential is it to improve the current state of the art of open rotor tip vortex modelling for the application to preliminary design noise prediction codes?

The open rotor research and development came to a halt in the 1990s. Since the open rotor has been reconsidered the interaction noise issue has been further investigated. Modern computer power has led to the use of computational aeroacoustics (CAA) to calculate open rotor noise. CAA was used by[7] to examine the importance of the individual noise sources and showed the importance of the tip vortex interaction noise

relative to rotor alone and wake interaction sources. CAA is a powerful tool to predict open rotor noise, but its current turnaround time inhibits its applicability as a basic preliminary design tool.

This means that the development of noise prediction codes is still important, CRPFAN is used in[8] to evaluate the acoustic benefits of novel combinations of propeller re-pitch and rotational speeds. The capability of a noise prediction method to calculate tip vortex interaction noise is dependent on the sophistication of the vortex model used. Recent attempts to address this issue include[9] who compared the acoustic effect of using the standard CRPFAN vortex modelled developed in[10] and a helical line vortex developed in[11].

The vortex model selected will require a method to predict its parameters such as the vortex size and strength. This thesis presents suggestions for the most suitable tip vortex model and the development of semi-empirical correlations using validated 3-D CFD on open source advance propeller geometries. The tip vortex model and accompanying correlations can then be integrated into a preliminary design noise prediction code such as CRPFAN without the need to use a crude vortex model and correlations developed using cascade tests.

1.1 Thesis Structure

The thesis begins by introducing the topic in Chapter 1 which is followed by Chapter 2 which defines the aims, objectives, novelty and shows the project structure via the project road map. Chapter 3 is the literature review which presents the current state of the art with regard to open rotor tip vortex modelling and includes some key definitions, methodologies and concepts which are used in subsequent chapters.

Chapter 4 is a description of the CRPFAN methodology and its verification and validation in order to justify its inclusion as a suitable aeroacoustic tool within the project. CRPFAN is then used as a tool in Chapter 5 to quantify the effect that different tip vortex modelling approaches has on the interaction noise and highlights the tip vortex as a key noise source.

The methodology used to create a CFD model and how it will be used to develop a set of bespoke tip vortex correlations is then explained in Chapter 6. This methodology is then utilised in the Analysis and Synthesis of Chapter 7 which forms the key component of thesis and includes the development of the tip vortex correlations and their integration into CPRFAN. Also included in Chapter 7 are recommended approaches to model an open rotor tip vortex for predicting interaction noise, and a quantitative analysis of the importance of the input aerodynamic methodology when predicting open rotor noise.

The key findings and conclusions are summarised in Chapter 8 followed by Chapter 9 which suggests future work which can be used to address the deficiencies present in this research project.

Chapter 2

Project Scope and Rationale

Chapter 2 outlines the key aim, objectives and research questions to be answered in the project. Also included is a statement of the novelty of the work and a road map to show how the different packages of research knit together to achieve the key aim of the project.

2.1 Aim

The aim of the research is to improve the current state of the art of open rotor tip vortex modelling for the application to interaction noise prediction methods.

2.2 Objectives

In order to meet the key aim of the research a set of defined objectives need to be achieved. These objectives are listed below:

- Justify requirement for improved vortex modelling
- Set of correlations which can be used to predict Γ, r_c, V_θ and n for a range of geometries and operating conditions
- Quantify difference between bespoke correlations and the original CRPFAN correlations for the tip vortex parameters for a given geometry and conditions
- Provide recommended approaches to model the tip vortex most appropriately

2.3 Research questions

- Does the propeller shape affect the tip vortex parameters?
- Can a Vatistas vortex model be used to describe the tip vortex of an open rotor?
- How does the geometry and loading conditions of the propeller affect the tip vortex parameters?
- Does the spatial orientation of the tip vortex relative to the aft rotor have an effect on the interaction noise?
- What is the nature of vortex axial velocity component is it 'wake-like' or 'jet-like'?
- How important is the source aerodynamic methodology for aeroacoustic open rotor noise prediction tools?

2.4 Novelty

The novel aspect of this project is the examination of the effects of tip vortex parameters on open rotor interaction noise and the development of bespoke correlations to predict the tip vortex parameters and improved modelling techniques suggestions.

2.5 Roadmap

The outline of the project is summarised in the project road map in Figure 2.1. The research is categorised into three different modules which all combine to form a final improved version of CRPFAN. The first module is the vortex modelling importance which involves quantifying different tip vortex modelling factors on the interaction noise. The second module is the use of CFD to to generate tip vortex flowfield data in order to develop the tip vortex correlations. The third module involves coupling CRPFAN with a strip theory aerodynamics code to make CRPFAN easier to use and more accessible.

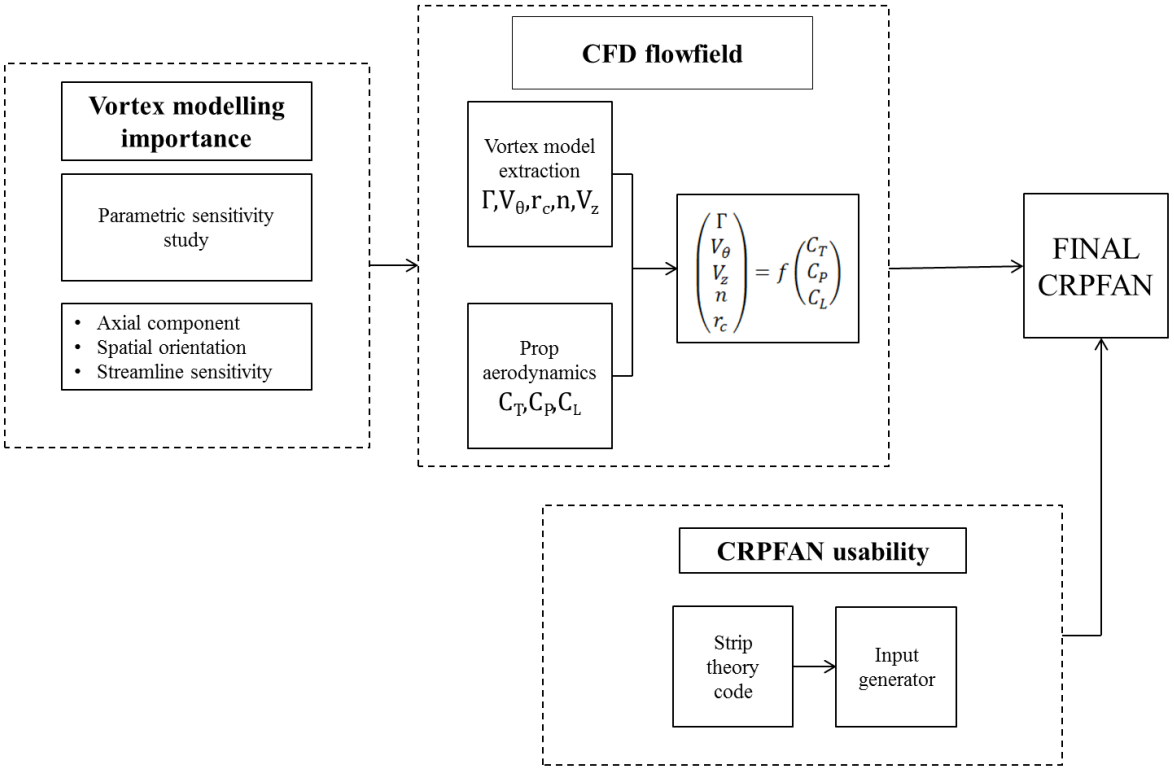

FIGURE 2.1: Project Road map

2.6 Key Milestones

Below is a list of the four key milestones in the project:

- Validation and verification of CRPFAN so it can be used as an appropriate tool
- Use of CRPFAN to be able to quantify the effect of tip vortex modelling on open rotor interaction noise
- Development and validation of a CFD model to extract the key flowfield features and tip vortex parameters
- The development of bespoke tip vortex correlations and their integration into CRP-FAN to quantify their impact on interaction noise relative to the current state of the art

Chapter 3

Literature Review

Chapter 3 is a review of the current state of the art of open rotor tip vortex interaction noise prediction methods. Included in this chapter is why the open rotor is an important concept for greener aviation, the contribution of tip vortex interaction to open rotor noise and what methods and models currently exist to predict these interactions.

3.1 Why the open rotor?

The open rotor is currently being re-considered as an alternative to the high by-pass turbofan engine for medium sized aircraft in an attempt to meet the Advisory Council for Aviation Research and innovation in Europe (ACARE) 2020 requirements.

The propulsive efficiency can be improved through the use of propellers instead of turbofans, they are more efficient because they accelerate a large volume of air by a small amount relative to the turbofan which accelerates a smaller volume of air by a greater amount. From Equation 3.1 where, V_J, is the velocity of the jet being accelerated and, $V_{aircraft}$, is the flight velocity of the aircraft, the propulsive efficiency, $\eta_{propulsive}$, is inversely proportional to the jet velocity at given flight speed[12].

$$\eta_{propulsive} = \frac{2}{1 + \frac{V_J}{V_{aircraft}}} \tag{3.1}$$

One solution would be to improve the by-pass ratio of a turbofan engine to achieve an improved specific fuel consumption, however, as the bypass ratio increases, so does the mass and drag of the nacelle which effectively limits the maximum fuel saving of an increased by-pass ratio.

Therefore, for a step change in efficiency an unducted propeller is advantageous, but the propulsive efficiency of a propeller drops rapidly after aircraft Mach numbers beyond

0.6 due to compressibility effects at the tip[12]. This effect can be reduced by using advanced propellers which have high blade numbers, thin airfoil sections - especially at the tip and are swept relative to a conventional propeller[13]. An improved propulsive efficiency is achieved with the use of a second row of blades downstream which rotate in the opposite direction. The advantage of this second blade row is that it recovers the thrust contributing axial velocity lost due to the swirl in the flow. This configuration was termed the propfan. The evolution of propeller planform shapes designed for standard low speed flight, to advanced propellers to the propfan is shown in Figure 3.1.

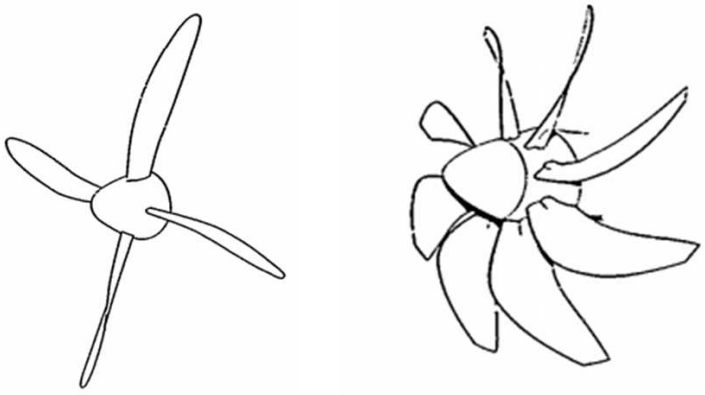

(a) Low speed propeller

(b) High speed propeller

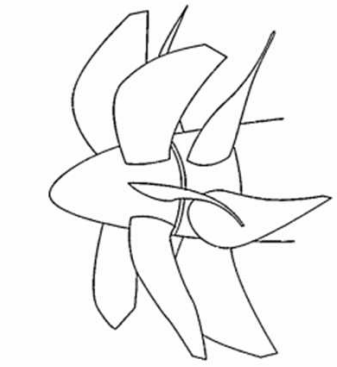

(c) Propfan

FIGURE 3.1: Propeller design evolution for high speed flows[14]

The term propfan, counter-rotating propeller, open rotor are all interchangeable, but the term open rotor will be used throughout to avoid confusion. The open rotor was first considered seriously in the late 1970s and early 1980s after the 1973 Oil Crisis led the cost of fuel to rise considerably[3].

Two technology demonstration engines were built and tested in the 1980s. Firstly, The direct drive General Electric 36 Unducted Fan Engine (GE-36 UDF) a NASA funded

project developed from 1983 to 1989 which completed a combined total of 500 hours of test flight on a modified McDonnell Douglas MD-80 shown in Figure 3.2 and a Boeing 727[5] shown in Figure 3.3.

FIGURE 3.2: GE-36 UDF technology demonstration mounted on a modified MD-80[15]

FIGURE 3.3: UDF engine on a Boeing 727[15]

The second demonstration engine was the geared Pratt & Whitney 578 DX developed with Allison Engine Company and Hamilton Standard from 1985 to 1989 shown in Figure 3.4. It completed 20 hours of flight on a modified MD-80 aircraft[15].

FIGURE 3.4: Pratt & Whitney 578 DX developed with Allison Engine Company and Hamilton Standard[15]

Both the UDF and 578 DX projects were terminated by the end of the 1980's, key factors attributed to this include the stabilised price of oil and the noise levels of the open rotor. The significance of the flight testing is that it proved the open rotor is a viable and implementable alternative propulsion method. The current industry target set by Clean Sky SAGE 1 is for an open rotor powered aircraft to fly by 2019.

3.2 Open rotor noise fundamentals

Section 3.2 gives an overview to the noise generated by a propeller in general and more specifically an open rotor.

3.2.1 Fundamental Acoustics

Firstly an overview of fundamental acoustics so the reader is familiar with the relevant terms and concepts when presented later in the thesis.

Monopoles, Dipoles and Quadrupoles
In acoustics a source for example a propeller creates a disturbance which is propagated through a medium such as air which reaches a receiver e.g. the human ear. The source term can be classified as a function of its directivity. The directivity of sound pressure refers to the manner in which the measured or predicted sound pressure, at a fixed distance from a source varies with angular position[16]. The nature of the directivity pattern determines whether the source is a monopole, dipole or quadrupole which are important in propeller noise and will be defined here.

Monopole
A monopole radiates equally in all directions. Any sound source whose dimensions are much smaller than the wavelength of the sound being radiated will act as a monopole[16]. An example of a simple monopole is a pulsating sphere.

Dipole
A dipole consists of two monopoles of equal source strength, but opposite phase and separated by a small distance. There is no net introduction of fluid by a dipole. As one source exhales, the other sources inhales and the fluid surrounding the dipole sloshes back and forth between the sources. A physical analogy for a dipole is two balloons a short distance apart, as one deflates exhausting its mass flux the other inhales the flux. The net force on the fluid causes energy to be radiated in the form of sound waves. A dipole consists of two monopoles but does not radiate pressure equally in all directions. Instead, it has the characteristic of maxima along the 0 and 180 degree directions and no sound radiated along the 90 and 270 degree directions. The directivity patterns are illustrated in Figure 3.5.

Quadrupole

A quadrupole source is two identical dipoles with opposite phase and separated by a small distance. They are often referred to as being non-linear.

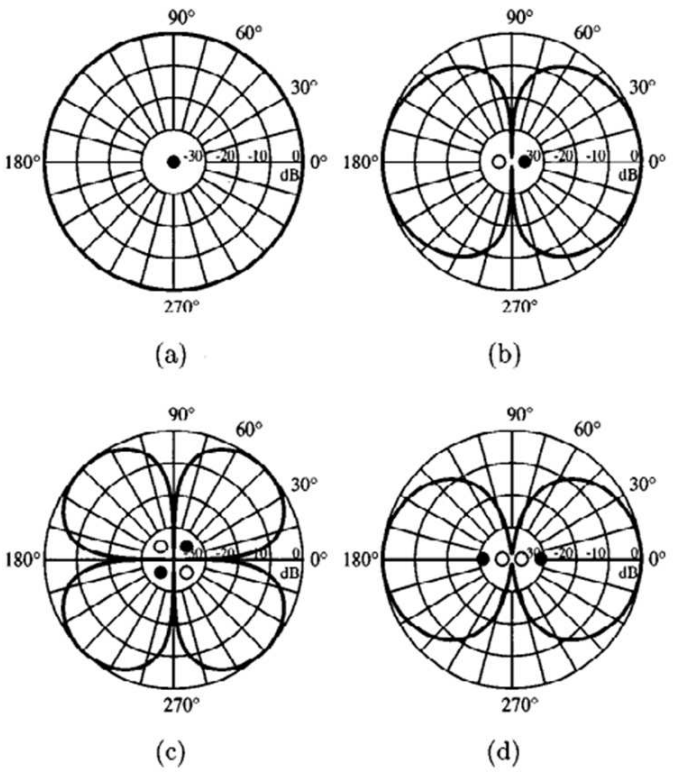

FIGURE 3.5: Directivity patterns for (a) monopole (b) dipole (c) lateral quadrupole and (d) longitudinal quadrupole[16]

3.2.2 Propeller noise

Propeller noise is often laden into three categories harmonic, broadband and narrow-band noise. The most important in this area of study is harmonic and hence will be the focus of most attention. By definition the noise generation from acoustic pressure propagation is an unsteady phenomenon, however Gutin[17] recognised that a moving body such as a propeller can be in a steady flowfield and induce noise. Propellers can produce noise from steady sources, they appear constant in time to an observer on the rotating blade and the noise is periodic due to the rotation of the blade. This noise is harmonic with the fundamental tone occurring at blade passing frequency (BPF). Steady propeller noise characteristics are shown in Figure 3.6 in both the time and frequency domain.

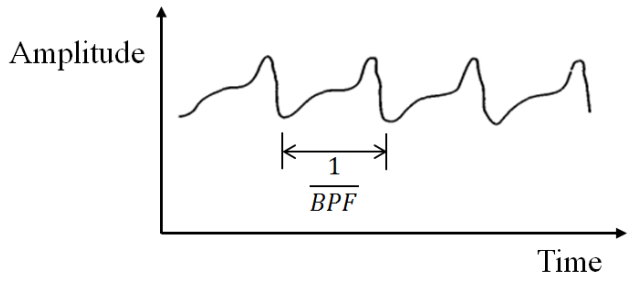

(a) Time domain

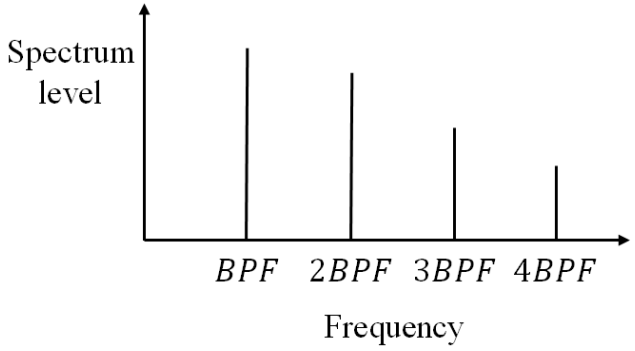

(b) Frequency domain

FIGURE 3.6: Propeller rotational noise characteristics in the time and frequency domain adapted from[14]

The two key sources of steady propeller noise, which occurs at multiples of BPF are thickness noise and loading noise.

Thickness Noise

Thickness noise is generated from the transverse periodic displacement of the air by the volume of a passing blade element[14]. The amplitude of a thickness noise source is proportional to the volume of the blade and the frequency characteristics a function of the aerofoil design and rotational speed. Thickness noise is a monopole source and its effect becomes important at high speed for example at cruise. This noise source can be abated by using thin blade sections and a planform sweep[14].

Loading Noise

Loading noise is generated by the lift and drag (and thrust and torque) force components derived from the propeller pressure field and propeller motion. The pressure disturbance

is then propagated as a noise source. Loading noise is a dipole source and becomes important at low to moderate speeds[14].

Figure 3.7 illustrates a typical directivity pattern for thickness noise (solid line) and loading noise (dashed line). The observer angle, is the angle of the observer relative to the flight axis, where 90 degrees is in the plane of the propeller.

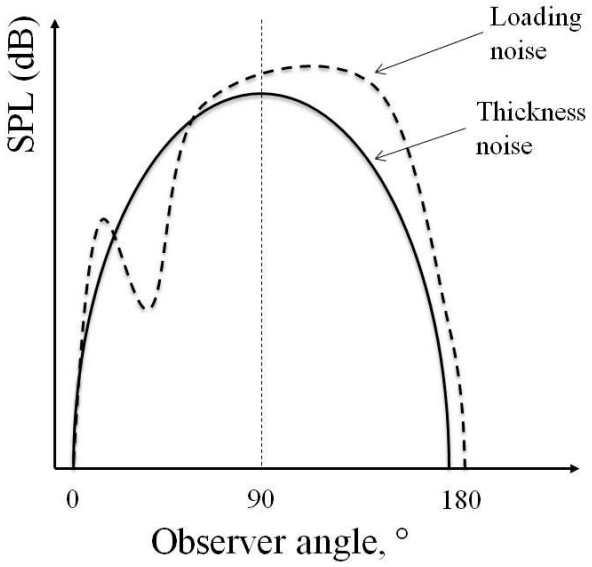

FIGURE 3.7: Thickness (solid line) and loading noise (dashed) directivity[18]

The thickness distribution represents a monopole directivity and peaks in the plane of the propeller, the loading noise demonstrates a dipole interference in the frontal lobe due to thrust and torque interaction, loading noise peaks rearward of the propeller plane[18]. Both sources are locked to the blade and are cut off at the low and high directivity angles as result.

3.2.3 Open rotor noise

The addition of an aft blade row rotating in a direction opposite to the front row has positive aerodynamic benefits. However, it gives rise to additional, unsteady noise sources, which contribute heavily to the open rotor having an undesirable acoustic signature. Figure 3.8 shows the additional noise generated by a counter-rotating system relative to a standard single rotation propeller.

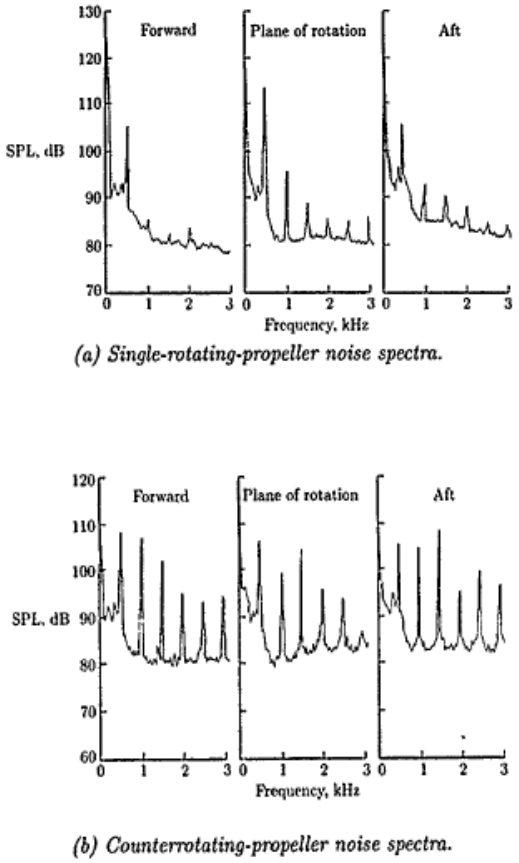

FIGURE 3.8: Noise spectrum for a single advanced propeller (a) and a counter-rotating advanced propellers such as in the open rotor (b)[14]

Unsteady noise sources are time dependent in the rotating-blade reference frame and include periodic and random variation of loading on the blades[14]. Periodic unsteady-loading noise occurs at harmonics of blade passing frequency. They are particularly important at low speeds such as at take off.

Sources of unsteady noise

These sources include interaction of the front rotor wake and tip vortex with the rear rotor and potential field interaction between the two blade rows.

A diagram of the key noise generating mechanisms is shown in Figure 3.9:

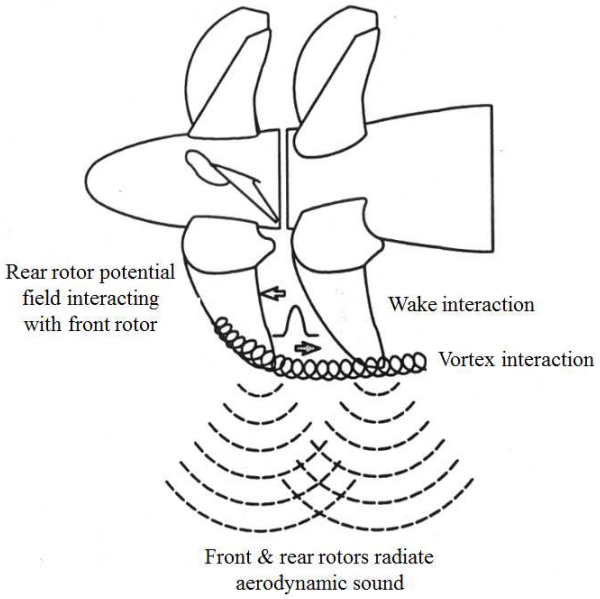

FIGURE 3.9: Open rotor noise sources adapted from[19]

Wake and Tip Vortex Effects

Tip vortices and wakes induced by the front rotor convect downstream and impact on the rear blade rows. The resulting flowfield can be highly complex consisting of downwash onto the blades and velocity defects due to the drag of the blade. This decreased magnitude in the velocity can change the angle of incidence onto the aft blade.

Potential Field Effects

The front and aft blade rows are both lift generating airfoils. Therefore a differential pressure distribution is present around each blade volume. The static pressure distribution is referred to as the potential field. It is often modelled that the presence of the aft blade row has no effect on the front blade static pressure field- such as in CRPFAN. This is not strictly true and the static pressure field from the front row will affect the aft and vice versa.

These unsteady effects occur at integer multiples of the fundamental harmonic of the front and aft blade passing frequency and are known as interaction tones. Figure 3.10 shows a typical acoustic spectrum of an open rotor, with the interaction tones occurring at harmonics of the blade passing frequency.

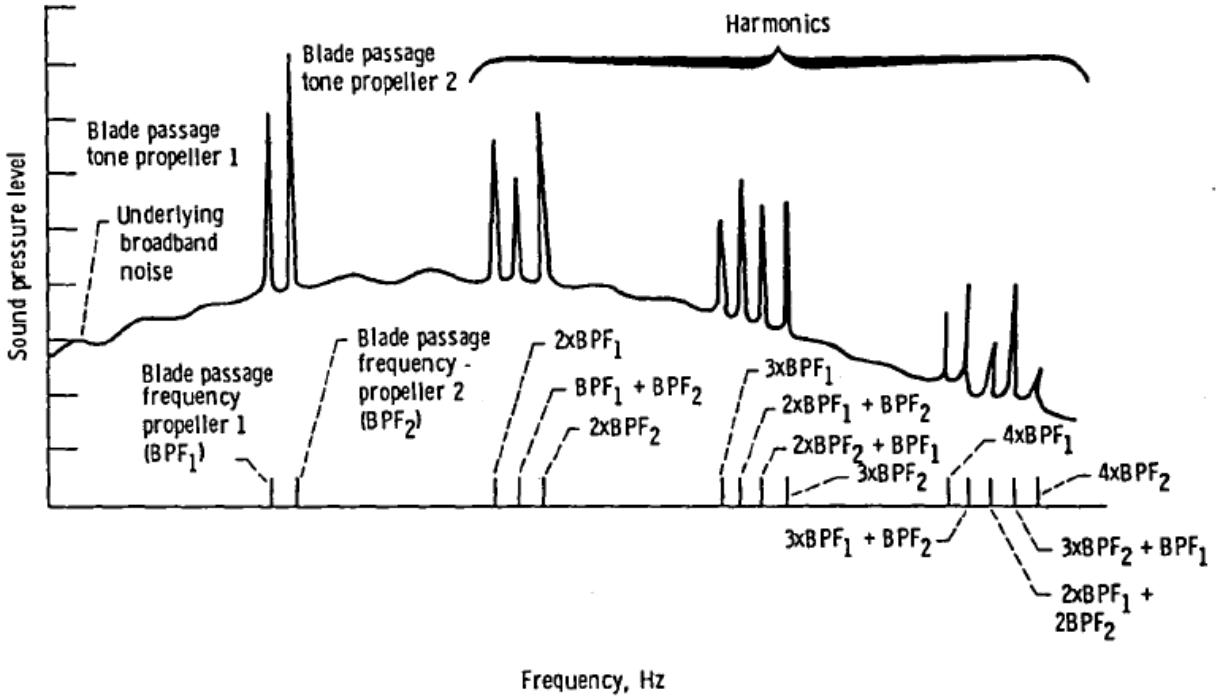

FIGURE 3.10: General acoustic spectrum of an openr rotor[20]

3.3 Aeroacoustic analysis of Open rotor tip vortex interaction noise

Section 3.3 presents the different methodologies which can be used to predict the noise generated by an open rotor, with particular focus on tip vortex interaction noise. The different methods include analytical tools such as CRPFAN, unsteady CFD coupled to Computational Aeroacoustics (CAA), full Computational Aeroacoustics, anechoic wind tunnel testing and full scale flight testing. Table 3.1 compares the relative fidelity and cost of each method.

Method	Cost	Fidelity
Analytical tools	low	Low
Coupled CFD/CAA	Medium	Medium
CAA	Medium	Medium
Anechoic tunnel testing	High	High
Flight testing	Very High	Very High

TABLE 3.1: Cost and fidelity of aeroacoustic prediction methods

Analytical methods take the least time to implement and require the lowest overhead, however this convenience is compromised by lower fidelity in terms of acoustic accuracy.

The study by Majjigi[10] combined anechoic wind tunnel testing with the analytical tool CRPFAN to investigate tip vortex interaction noise. Low speed tests at a take off Mach number of 0.2 were conducted in the GE Cell 41 tunnel on the F7-A7 geometry with 9 front and 8 aft blades. The effects of vortex radial and tangential location, strength (circulation) and clipping of the aft rotor were investigated.

The purpose of clipping the aft rotor is to try minimise or avoid any interaction of the tip vortex with aft blade - hence removing it as a noise source. The disadvantage is that less thrust is provided by the open rotor through two mechanisms, firstly, clipping the aft rotor will mean the aft rotor will provide less thrust providing there is no increase in chord , setting angle or rotational velocity and secondly there is less of the aft blade to convert the residual swirl from the front rotor wake into a thrust generating velocity component.

With reference to Figure 3.11, with the aft rotor clipped by 25 % span the measured data in Cell 41 shows a reduction of 10 dB in the aft lobe and roughly 5 dB in the plane of the propeller on the interaction tone sum. For the case with no aft clipping the CRPFAN calculation is within 2-3 dBs of the measured data at most directivity angles. However, when the aft rotor is clipped by 25 % CRPFAN under predicts the measured data by 8-10 dBs over most observer angles. This could be due to an inaccurate trajectory model under predicting the streamtube radial contraction and hence less vortex interaction with the aft blade. The effect of including the vortex model option within CRPFAN is also shown, the exclusion of the tip vortex and purely relying on the wake results in a difference of over 20 dBs with the nominal aft rotor and 10 dB with the 25 % cropped aft rotor.

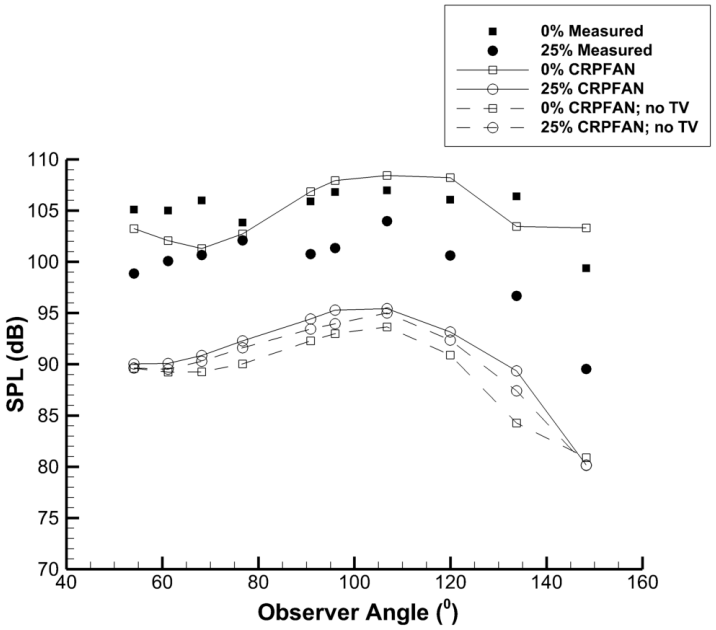

FIGURE 3.11: Effect of clipping aft blade on interaction tone sum[10]

The strength of the tip vortex was investigated by increasing a scalable parameter, Ci, defined in Equation 3.39 , values of Ci equal to one, two and three were used to control the strength of the tip vortex. The strength of the tip vortex contributed up to 13 dB to the interaction tone sum - the effect of the parameter is omnidirectional with regards to the directivity pattern and not confined to a specific lobe.

The tangential location of the vortex which defines the location of the vortex centre relative to the two adjacent blades has no appreciable effect on the interaction tone sum. The radial location of the tip vortex had a small effect on the interaction noise under the standard configuration, but its effect becomes more significant when clipping the aft rotor.

The details of the tip vortex models and correlations used in CRPFAN within the study are examined in Section 3.5.3.

Peters and Spakovsky[7] investigated the relative weight of each interaction tone mechanism to the overall noise on a baseline open rotor and used the results to modify the geometry for reduced interaction noise. The method involved using unsteady 3-D RANS to determine the unsteady blade pressures which were Fourier Transformed into the frequency domain and used to obtain the interaction noise based on Hansons method[21]. The methodology used is summarised in Figure 3.12.

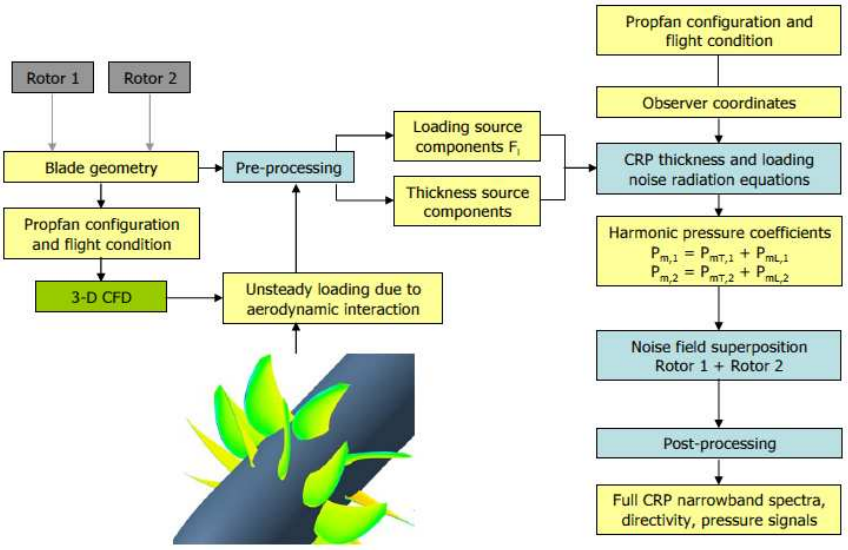

FIGURE 3.12: Open rotor noise prediction methodology used by [7]

The baseline design was based on assuming a NACA65A008 thickness distribution and circular arc camber lines. The interaction tones were dissected into four components, 1), the upstream influence of the aft rotor potential field on the front rotor, 2), the front rotor tip vortex interaction with aft blade, 3), front rotor wake with aft blade and, 4), the front rotor hub wake and boundary layer with the aft rotor. The mean SPL contributions for the six interaction tones at a take off Mach number of 0.25 with the baseline design are shown in Figure 3.13.

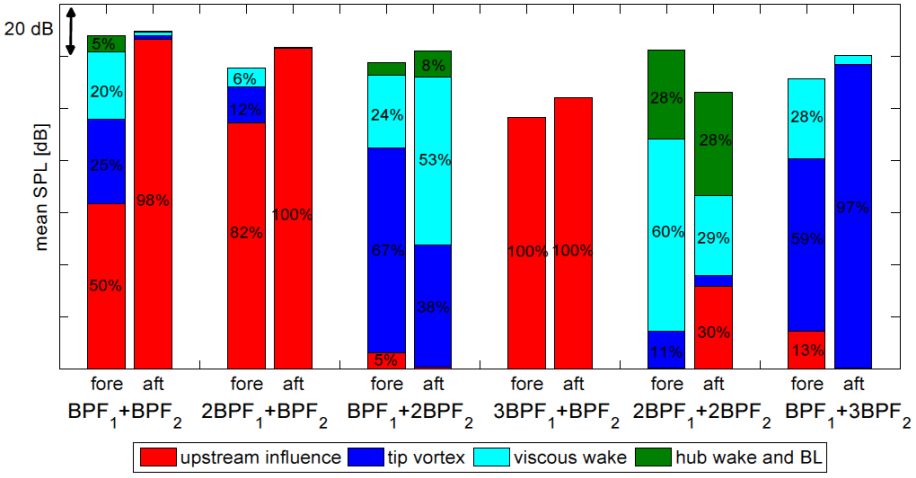

FIGURE 3.13: Contributing sources to aerodynamic interaction noise for baseline geometry used in [7]

It was observed that the tip vortex effects were most prominent at multiples of the rear rotor e.g. at BPF1+2BPF2 and BPF1 + 3BPF2 while upstream effects due to the aft rotor potential field are dominant at multiples of the front rotor at interaction tones of 2BPF1+BPF2 and 3BPF1+BPF2. The baseline geometry was re-designed to reduce the interaction noise . The new design included an increased axial blade row spacing of 0.35 from 0.224 (x/D1) where x is the axial ordinate and D1 is the front rotor diameter , rear rotor clipped by 25 %, and increased aft blade count from 8 to 11 with a reduced rear rotor rpm to maintain thrust settings of the baseline design. The effect of a clipped aft blade row is noticeable in Figure 3.14 which highlights two key things, firstly the apparent decay of the tip vortex and wake with axial distance and secondly the reduced interaction of the aft blade row with the tip vortex core.

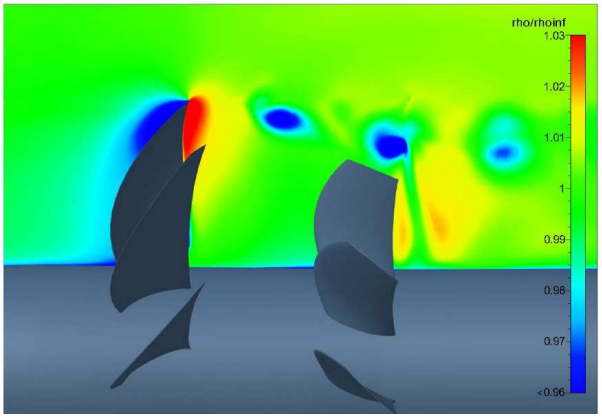

FIGURE 3.14: Contours of density for modified geometry with cropped aft rotor to minimise tip vortex interaction[7]

The relative contributions of each of the four key interaction mechanisms were assessed for the modified geometry as shown in Figure 3.15. The tip vortex was almost eliminated as a noise source. However potential field interactions were increased due to the higher aft blade count.

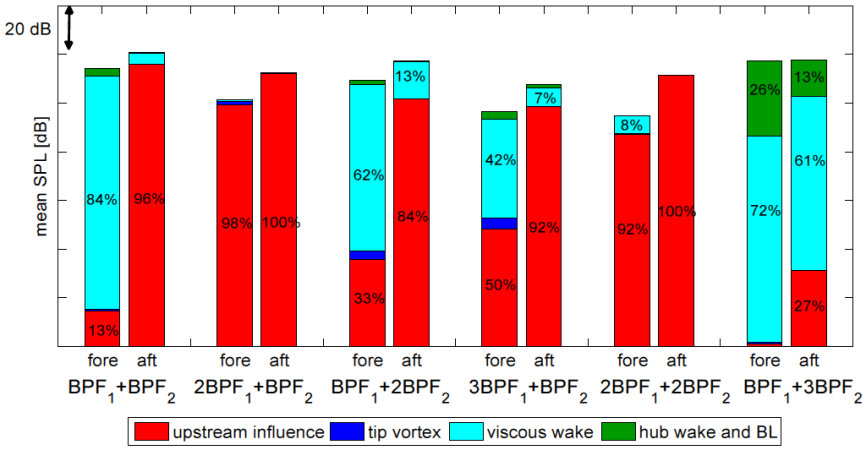

FIGURE 3.15: Contributing sources to aerodynamic interaction noise for modified geometry used in[7]

Overall the redesigned geometry resulted in an average reduction of over 7 dB in mean SPL over the measured directivity angles. Based on a FAR 36 flyover condition the new design achieved reductions of up to 9.2 EPNdB at the sideline location compared to the baseline configuration. The increased rotor spacing and cropping of the aft blade resulted in a sacrifice to the propulsive efficiency however.

Woodward and Gordon[22] measured the effect of cropping the aft rotor in the NASA Lewis 9 by 15 ft Anechoic Wind Tunnel at Takeoff/Approach representative conditions of Mach 0.2. Two geometries were used the F7/A7 and the F7/A3 in an 11 front by 9 aft rotor configuration. The propeller planform shape for both geometries are shown in Figure 3.16.

FIGURE 3.16: F7 -A7 and F7-A3 configuration profiles[22]

The A3 has a reduced diameter of 25% relative to the A7. The comparisons were made at two different blade spacings a minimum spacing of x/D of 0.14 and maximum of 0.24. At the maximum spacing of 0.24 the F7/A3 had relative to the F7/A7 a maximum

reduction of 20 dB for the $1F + 1A$ tone and 10 dB for $2F + 1A$ tone. For the minimum spacing of 0.14 the differences reduced to 8 dB for $1F + 1A$ tone and 6 dB for the $2F + 1A$ tone.

The success of cropping aft blade is greater for larger blade spacings because the tip vortex has more time to contract and has less interaction with the aft rotor. Woodward and Gordon[22] also investigated the effect of blade spacing for F7/A7 and F7/A3 independently. With reference to Figure 3.17 the F7/A3 interaction noise was more sensitive to changes in axial spacing with a 14 dB reduction for 1F+1A tone and 16 dB reduction for 2F+1A tone with increased spacing. The reduction with axial spacing for the F7/A7 was roughly 8 dB for both interactions tones.

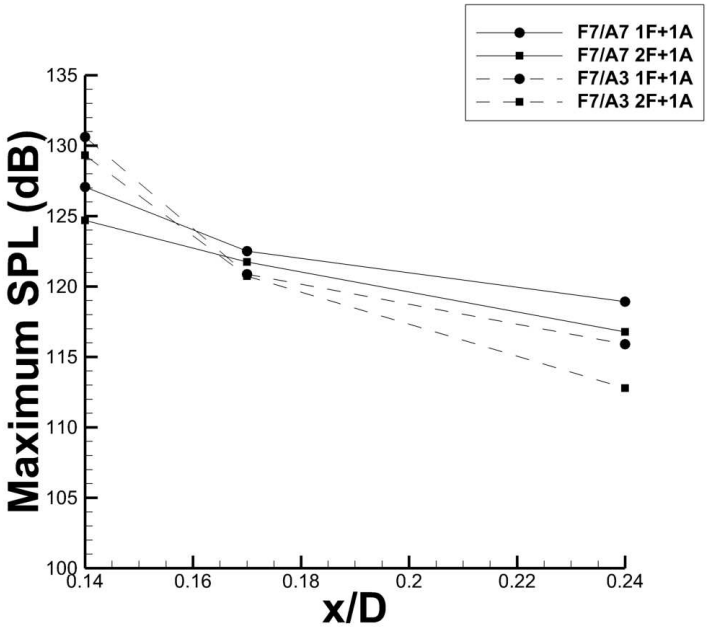

FIGURE 3.17: Effect of axial rotor spacing on F7/A7 and F7/A3 adapted from[22]

The F7/A3 was more sensitive to the axial spacing because the interaction noise is wake dominant with the clipped aft rotor, and the wake is considered to decay axially quicker than the tip vortex[22].

Dittmar[20] conducted a similar study but in the NASA Lewis 8 by 6 ft tunnel on the F7-A7 geometry at Cruise representative Mach numbers of 0.72, 0.76 and 0.8 for three spacing between pitch axis of 0.14, 0.17 and 0.24 x/D. At a Mach number of 0.8 there was a maximum of 8 dB noise reduction between the close condition at 0.14 and far condition at 0.24 x/D. For the lower Mach numbers of 0.76 and 0.7, increasing the axial spacing increased the interaction noise.

The mechanism is depicted in Figure 3.18, at a constant rpm and blade setting angle, a reduction in axial Mach number will generate more thrust which induces more streamtube contraction due to continuity. The A7 blade is set slightly lower than the F7, at

a Mach number of 0.8 the tip vortex contraction is not enough to interact with the aft blade, therefore the reduction in interaction noise is due to reduced wake strength.

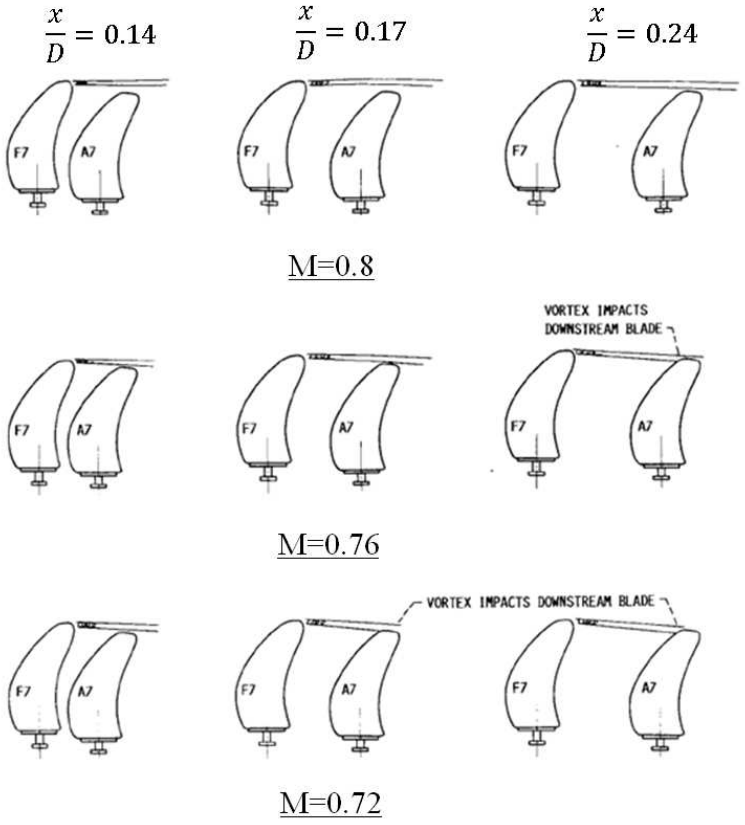

FIGURE 3.18: Effect of Mach number on tip vortex location at Cruise speeds[20]

At Mach 0.76 and 0.72, the thrust was greater which generated more streamtube contraction, therefore increasing the blade spacing meant more of the vortex was interacting with the aft blade row - which had the net effect of an increase in interaction noise.

Optimising propeller relative air angle

Zachariadis et al[8] investigated the concept of 'Re-Pitch' where the incidence (relative air angle) onto the blade is reduced by decreasing blade setting angle and increasing rpm to maintain the same power and thrust. The study used a combination of anechoic rig data, steady state CFD and CRPFAN. The geometry used was the straight bladed Rolls Royce Rig-140 at Mach numbers of 0.75 and 0.25.

To asses the validity of using CRPFAN to quantify the effect of Re-Pitch on the interaction noise, CRPFAN results were compared against the measured rig data for Rig 140 at take off conditions. The results for this are shown in Figure 3.19.

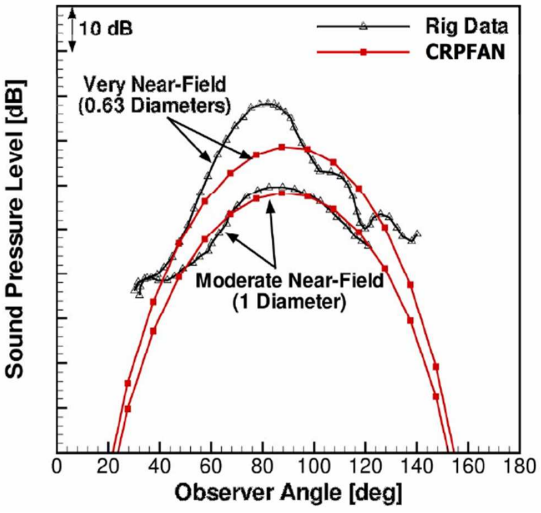

(a) Rotor alone tones

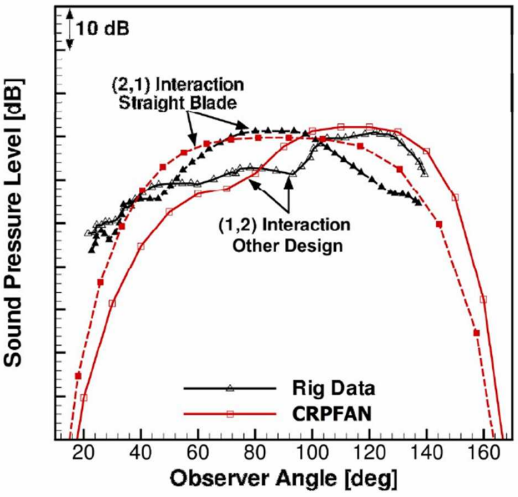

(b) Interaction tones

FIGURE 3.19: Comparison between CRPFAN and Rig measurements for the RIG 140 propeller blade[8]

CRPFAN under predicts the rotor alone tones in the very near field, but has good agreement in the moderate near field, the very near field discrepancy explained by a lack of detailed aerodynamic input to CRPFAN. The prediction for the interaction tones in the very near field is better because the near fields effects tend to decay with increasing frequency[8].

The motivation to reduce the incidence on the blade is highlighted in Figure 3.20 which shows contours of entropy and highlights the highly three-dimensional nature of the flowfield at a take off conditions where the incidence is greatest. The flow separates at around 55 % span and rolls up to form a leading edge vortex (LEV), the LEV and tip

vortex combine to form a large vortical structure which contributes to loss in efficiency of the rotor.

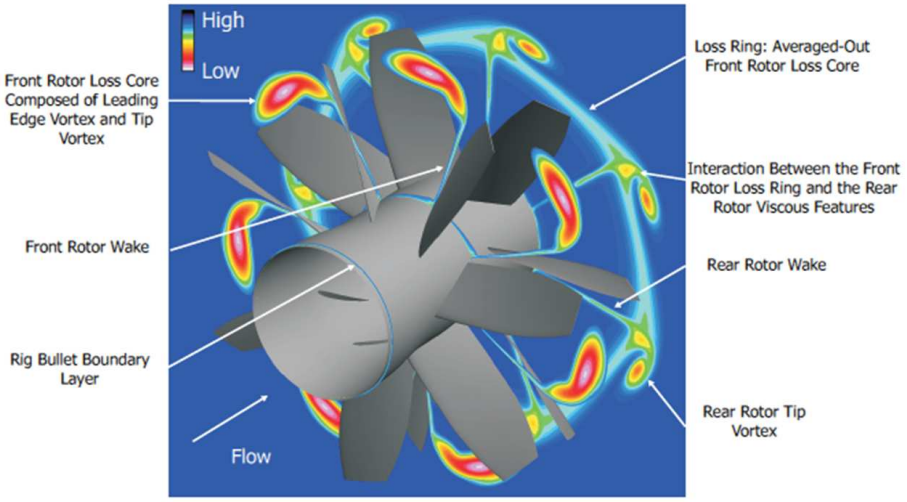

FIGURE 3.20: Aerodynamic interactions and 3D flowfield highlighted using contours of entropy[8]

Steady state RANS CFD simulations were conducted on the front rotor to optimise the use of 'Re-Pitch', with the aim of getting the lowest incidence on the blade but maintaining the same thrust. The aerodynamic effect of 'Re-Pitch' is shown in Figure 3.21 which shows a reduction in the tip leakage flow, due to a reduced LEV which is attributed to a reduced incidence onto the blade.

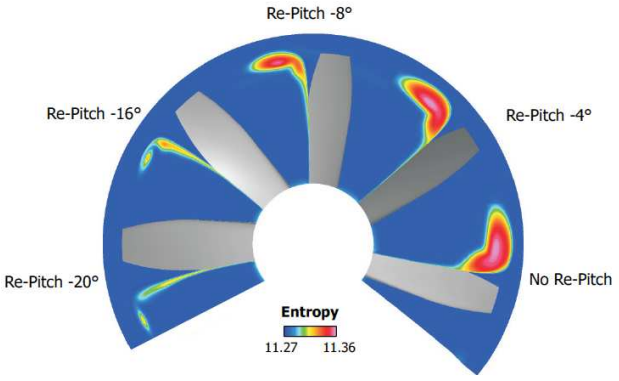

FIGURE 3.21: Plots of entropy for RIG 140 blade highlighting effect of 'Re-Pitch'[8]

The acoustic benefit of 'Re-Pitch' is shown in Figure 3.22, which is an output of a CRPFAN calculation where the input was the rotor radial lift and drag coefficients combined with tip vortex trajectory information extracted from the CFD.

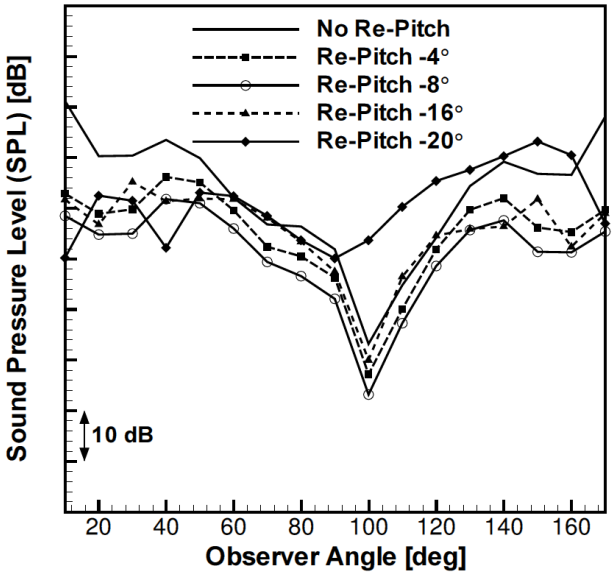

FIGURE 3.22: Aeroacoustic benefit of 'Re-Pitch' on 1F+1A interaction tone[8]

The optimum angle for reduced interaction noise is -8 °, this is because at higher 'Re-Pitch' angles, the adjusted rpm results in the formation of shock waves and increased rotor alone tones due to the higher relative Mach number. However, with a modest 'Re-Pitch' angle the noise reduction was up to 18 dBA.

3.4 Tip vortex modelling

Up till now there has been a focus on the significant role tip vortices have in CROR interaction noise but no exact description of what a vortex is and how they can be modelled. Section 3.4 presents the fundamental definitions and concepts used to describe a vortex, some of the key analytical tip vortex models used to describe a tip vortex including the one used in CRPFAN and finally some methods which are used to predict the tip vortex parameters.

3.4.1 Vorticity fundamentals

The exact definition of a tip vortex can be a contentious issue, for example Haller[23] proposes an objective definition of a vortex as "*a set of fluid trajectories along which the strain acceleration tensor is indefinite over directions of zero strain*". However the definition of a vortex by Anderson[24] is a flow which is highly tangential, this can be disputed because you can have a highly tangential flow which has no vorticity but still described as a vortex!

Therefore, for the sake of simplicity lets start with an objective definition of vorticity. Vorticity is defined mathematically as the the curl of the velocity vector, $\vec{\boldsymbol{V}}$, as shown in Equation 3.2. Physically vorticity is proportional to the rate of rotation of a fluid element about its own axes and is twice the angular velocity for a vortex which acts like a body of solid rotation[25].

$$\omega = \nabla \times \vec{\boldsymbol{V}} \tag{3.2}$$

The curl of a three dimensional velocity vector, $\vec{\boldsymbol{V}}$, in a Cartesian coordinate system is expressed in Equation 3.3 and by definition the vorticity is independent of its coordinate system and is thus said to be a Galilean invariant.

$$\omega = \nabla \times \vec{\boldsymbol{V}} = i\left(\frac{dw}{dy} - \frac{dv}{dz}\right) + j\left(\frac{du}{dz} - \frac{dw}{dx}\right) + k\left(\frac{dv}{dx} - \frac{du}{dy}\right) \tag{3.3}$$

The vorticity, ω, in the streamwise direction, z,is defined in Cartesian coordinates in Equation 3.4 and in polar in Equation 3.5. Where u and v are the horizontal and vertical components of velocity in Cartesian. V_θ and V_r are the tangential and radial velocity components respectively in a polar coordinate system where r is the radial distance from the tip vortex centre in a vortex local coordinate frame.

$$\omega_z = \left(\frac{dv}{dx} - \frac{du}{dy}\right) \tag{3.4}$$

$$\omega_z = \frac{1}{r}\left(\frac{\partial(rV_\theta)}{\partial r} - \frac{\partial V_r}{\partial \theta}\right) \tag{3.5}$$

An important mathematical concept related to vorticity is the fluid circulation, Γ. With reference to Figure 3.23, for a closed curve, C, the circulation is the line integral of the velocity, $\vec{\boldsymbol{V}}$, around it as shown in Equation 3.6[26].

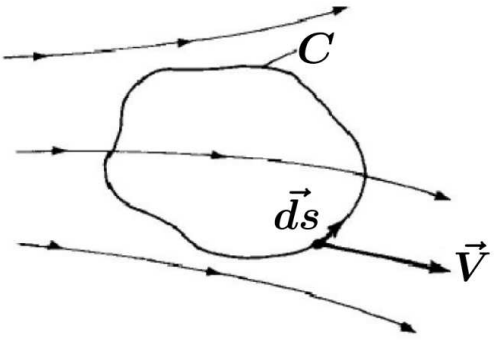

FIGURE 3.23: Closed curve 'C' to illustrate definition of Circulation adapted from[24]

$$\Gamma = \oint \vec{\boldsymbol{V}} d\vec{s} \tag{3.6}$$

Importantly, the circulation can be calculated from the area integral of vorticity. For example consider the streamwise vorticity, ω_z, and combining Equations 3.4 and 3.6 the circulation can be easily calculated from the scalar integration of the streamwise vorticity. This is the calculation used in post processing the CFD results and is described in Section 6.7 of Chapter 6 the CFD Methodology.

$$\Gamma = \oint \vec{\boldsymbol{V}} d\vec{s} = \int\int \nabla \times \vec{\boldsymbol{V}} dA = \int\int \omega_z dA = \int\int \left(\frac{dv}{dx} - \frac{du}{dy} \right) dxdy \tag{3.7}$$

The strength of a vortex is often defined by its circulation which is one of the reasons circulation is such an important parameter when dealing with vortices. Additional importance arises because of Kelvins's circulation theorem and the Helmholtz vortex laws which are crucial in the description and behaviour of tip vortices[24]. First define a vortex line as a line that is tangent to the local vorticity vector. This is the same definition as a streamline but interchanging vorticity and velocity. A vortex tube is then a collection of vortex lines connected in space analogous to a streamtube using the streamline analogy. An illustration of a vortex line and vortex tube is shown in Figure 3.24. With reference to Figure 3.24 Kelvin's Circulation theorem states that the circulation between S1 and S2 will be constant and independent of time for a barotropic and inviscid flow. An important consequence of Kelvin's theorem is that circulation is not present for flows which originally have no vorticity.

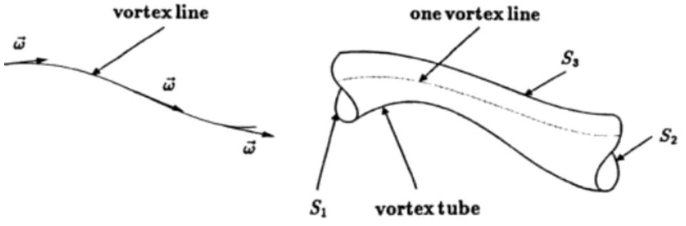

FIGURE 3.24: Illustration of a vortex line and vortex tubes[25]

The Helmholtz's vortex laws are defined by Shapiro[26] as:

1. "*Vortex lines never end in the fluid. They either form closed loops or end at a fluid boundary, and the circulation is the same for every contour enclosing the vortex line*"

2. "*A fluid which at any instant of time coincides with a vortex line will coincide with a vortex line forever*"

3. "*If the vortex line is stretched, the vorticity increases*".

The third law is akin to the conservation of angular momentum and is illustrated in Figure 3.25 where the axial stretching of a solid body increases its angular velocity, this is analogous to the vorticity increasing if a vortex line is axially stretched.

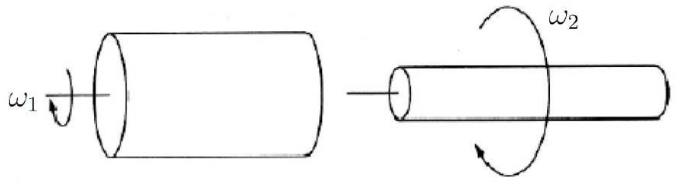

FIGURE 3.25: Vortex stretching through conservation of angular momentum [27]

3.4.2 Vortex models

Section 3.4.2 evaluates the different tip vortex models used to describe a tip vortex. In this context the tip vortex model means the mathematical description of the tangential velocity, V_θ, as a function of radial distance from the vortex centre. This does extend to the radial velocity, V_r, and axial velocity, V_x, components too. However, the simplest tip vortex model such as the Rankine only describes the tangential velocity component of the vortex [28]. More sophisticated models such as a Vatistas type also have descriptions for the V_r and V_z.

Rankine model

A simple tip vortex model is the Rankine type, where the vortex is separated into two distinct regions inside and outside the vortex core. Where the vortex core size, r_c, is the radial distance from the centre of the vortex to the location of maximum tangential velocity, V_θ. Inside the vortex core the tangential velocity is linear and acts like a body of rotation and outside the vortex core the flow is irrotational and the tangential velocity decreases hyperbolically with r^{-1}. A schematic of a Rankine vortex is shown in Figure 3.26 and the Equations set 3.8 which describe the radial tangential velocity distribution.

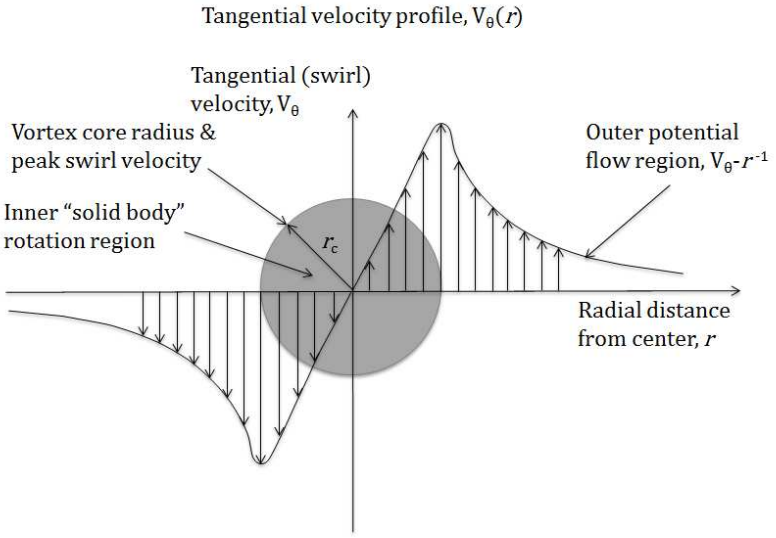

FIGURE 3.26: Typical tangential velocity distribution for a tip vortex adapted from [29]

$$V_\theta(\bar{r}) = \begin{cases} (\frac{\Gamma_V}{2\pi r_c})\bar{r} & \text{if} \quad 0 \leq \bar{r} \leq 1 \\ (\frac{\Gamma_V}{2\pi r_c})\bar{r}^{-1} & \text{if} \quad \bar{r} > 1 \end{cases} \tag{3.8}$$

$$\bar{r} = \frac{r}{r_c} \tag{3.9}$$

At the interface between the two regions there exists a discontinuity which is where most other vortex models differ from a Rankine type.

Lamb-Oseen Model

One model without this discontinuity is the Lamb-Oseen model described in its non-dimensional form by Equation 3.10 which is an analytical solution to the laminar Navier-Stokes equation in one dimension simplified for an axisymmetric tangential velocity and based on the assumption that the radial and axial velocities are zero [28].

$$V_\theta(\bar{r}) = \frac{\Gamma}{2\pi r_c}\left(\frac{1 - e^{-\alpha\bar{r}^2}}{\bar{r}}\right) \tag{3.10}$$

The term α is the Oseen parameter and is equal to 1.25643.

Vatistas model

A Vatistas type vortex is derived from a series expansion of the Lamb-Oseen tip vortex model. The tangential velocity, V_θ distribution is described by Equation 3.11, it is a

function of the vortex strength Γ, the core size r_c and shape factor n. Its useful property is that these different parameters can be used to fit the distribution of a range of tip vortices and the case where n is equal to two closely resembles the Lamb-Oseen vortex. For the case where n is equal to one, the Scully vortex is formed and is often used in helicopter aerodynamics[28].

$$V_\theta(\bar{r}) = \frac{\Gamma}{2\pi r_c}\left\{\frac{\bar{r}}{(1+\bar{r}^{2n})^{\frac{1}{n}}}\right\} \tag{3.11}$$

Figure 3.27 presents the tangential velocity distributions for the Rankine, Lamb-Oseen and Vatistas type vortex for three shape factors. As the shape factor increases the radial distribution of tangential velocity tends to a more inviscid solution. A shape factor equal to infinity represents the Rankine vortex with its noticeable discontinuity at the edge of the vortex core.

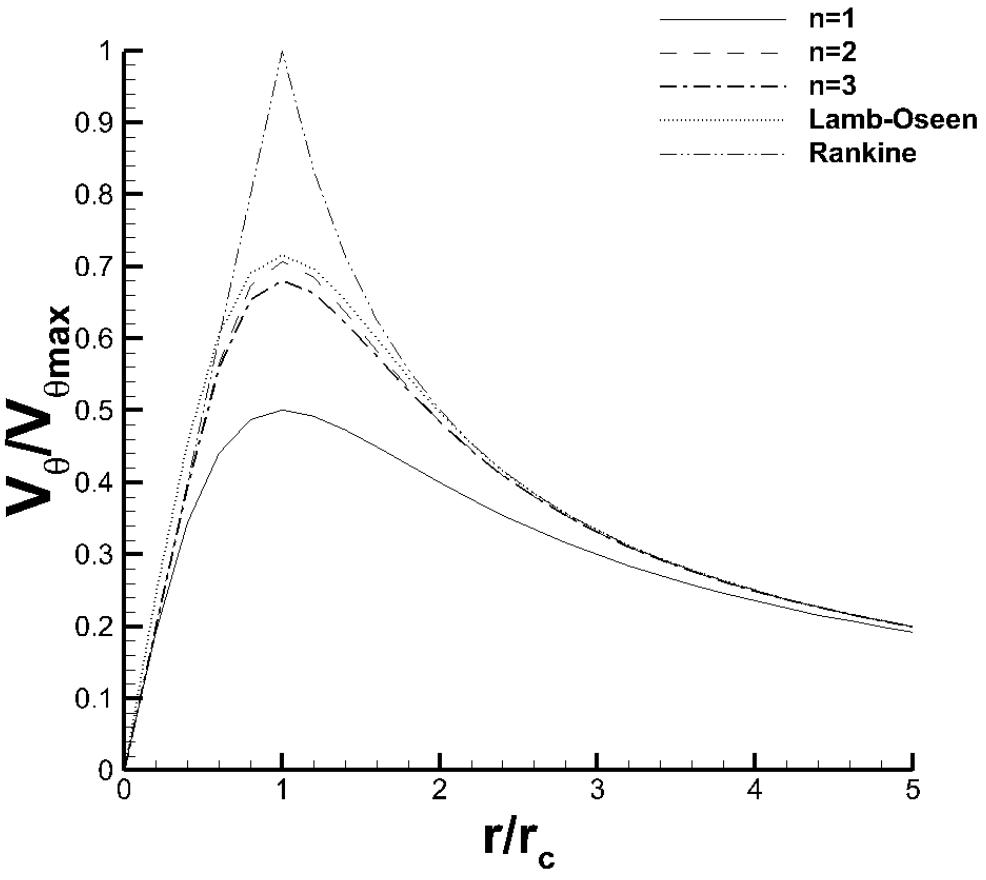

FIGURE 3.27: Tangential Velocity distributions for different vortex models[28]

CRPFAN vortex model

The CRPFAN vortex model uses an unwrapped annulus model as presented in [30], this theoretical model contains all the vorticity inside the vortex core region - outside of this region the flow is irrotational. With reference to Figure 3.28 which shows the unwrapped annulus coordinate system. The defining equations for the tip vortex velocity components are different for inside and outside of the tip vortex core

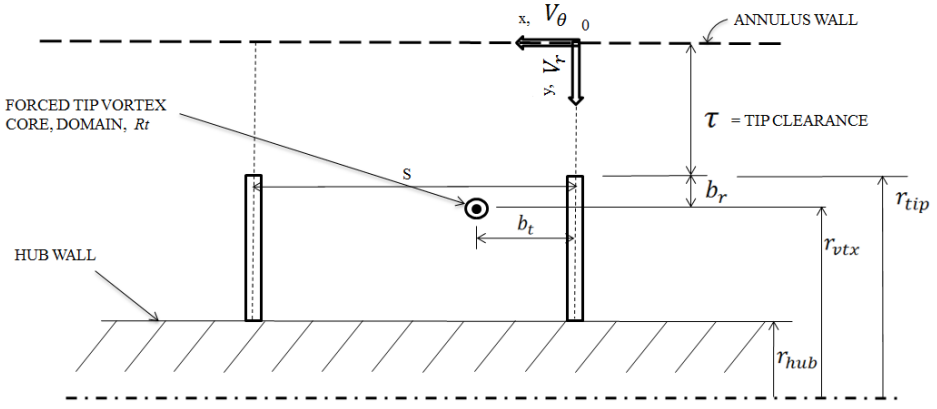

FIGURE 3.28: Unwrapped annulus coordinate system adapted from [10]

Inside the tip vortex core:

$$\omega = \frac{\Gamma_{vtx}}{2\pi r_c^2} \tag{3.12}$$

$$V_r = -\omega r \sin\alpha \tag{3.13}$$

$$V_\theta = \omega r \cos\alpha \tag{3.14}$$

$$r = \left\{(x - b_t)^2 + (y - b_r - t)^2\right\}^{0.5} \tag{3.15}$$

$$\alpha = \tan^{-1}\left[\frac{y - b_r - \tau}{x - b_t}\right] \tag{3.16}$$

Outside of vortex core:

$$V_\theta = -\frac{\Gamma_{vtx}}{2S}\left[\frac{\sinh M}{\cosh M - \cos P} - \frac{\sinh N}{\cosh N - \cos P}\right] \tag{3.17}$$

$$V_r = -\frac{\Gamma_{vtx}}{2S}\left[\frac{\sin p}{\cosh M - \cos P} - \frac{\sin p}{\cosh N - \cos P}\right] \tag{3.18}$$

$$M = \frac{2\pi}{S}(y - b_r - \tau) \tag{3.19}$$

$$N = \frac{2\pi}{S}(y + b_r - \tau) \tag{3.20}$$

$$P = \frac{2\pi}{S}(x - b_t) \tag{3.21}$$

Kingan and Self[9] investigated the acoustic effect of using two different types of vortex models using analytical methods - similar to CRPFAN. The first type of vortex model is a two-dimensional piecewise linear model similar to that of Majjigi et al[10] in that it uses an unwrapped annulus model based on the work of Lamb[30] and has a solid bold of rotation model inside the vortex core and irrotational model outside. The coordinate system used is illustrated in Figure 3.29.

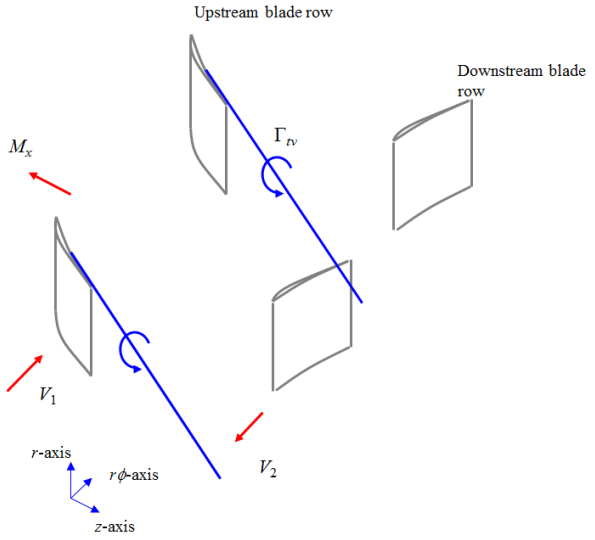

FIGURE 3.29: 2D vortex model system used by Kingan and Self[9]

The velocity component acting normal to the aft blade row, w_n, inside the vortex core is defined in Equation 3.22, outside of the core defined in Equation 3.23. Where α_1 and α_2 are the front and rear blade row stagger angles resepctivley.

$$w_n = -cos(\alpha_1 + \alpha_2)\frac{\Gamma_{vtx}}{2\pi r_c^2}(r - a) \tag{3.22}$$

$$w_n = -cos(\alpha_1 + \alpha_2)\frac{\Gamma_{vtx}B_1}{4\pi r\cos(\alpha_1)}\frac{\sinh(B_1(r-a)/r\cos\alpha_1)}{\cosh(B_1(r-a)/r\cos\alpha_1) - \cos(B_1\phi_1)} \tag{3.23}$$

Where the distance to a point a in the vortex, r_v, is defined in Equation 3.24 and, a, is the vortex radius:

$$r_v = \left[(r-a)^2 + (r\phi_1\cos\alpha_1)^2\right]^{0.5} \tag{3.24}$$

The second model approximates the tip vortex using a left hand helical vortex tube of infinite extent of the type[11] as represented in Figure 3.30.

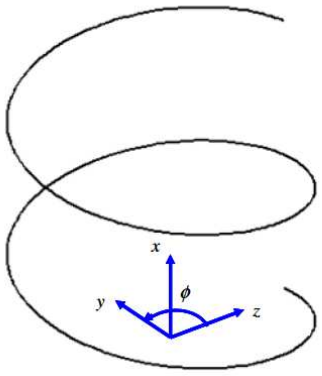

FIGURE 3.30: Rigid core helix vortex model of type[11] used by Kingan and Self[9]

The aeroacoustic effect of using the helical vortex model instead of the simple 2D model is a nearly 10 dB increase in the sound pressure level for 1F+1A interaction. The effect of the tip vortex has a significance effect on the noise relative to the wake, most noticeably at observer angles furthers away from the propeller plane of rotation.

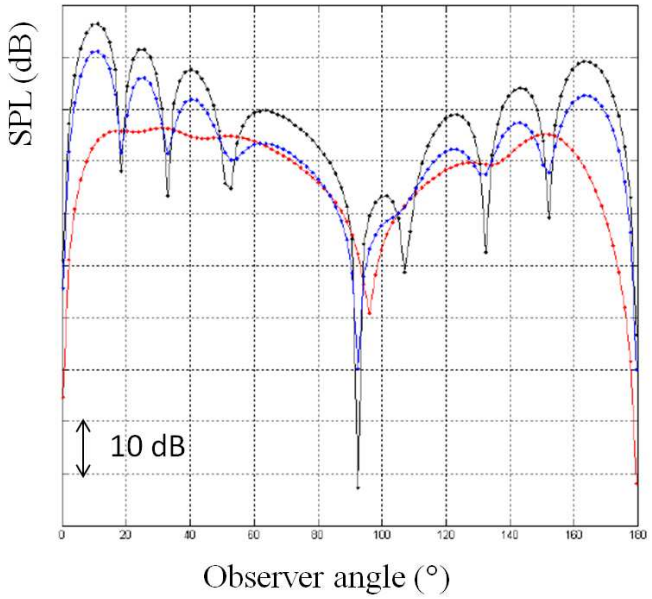

FIGURE 3.31: Directivity for 1F+1A interaction tone for helical vortex model(black), 2-D model (blue) and viscous wake (red)[9]

3.5 Tip vortex prediction methods

Section 3.5 presents some of the methods which can be used to predict the tip vortex parameters.

3.5.1 Lifting line theory to predict tip vortex strength

Lifting line theory is used as a tool for calculating the basic aerodynamic characteristics of a finite fixed wing. It is built from the basis that lift is generated by a bound vortex. However, due to the Helmholtzs laws of vorticity the bound vortex needs to be accompanied by two trailing vortices extending to infinity known as a horseshoe vortex system. This principle is shown in Figure 3.32.

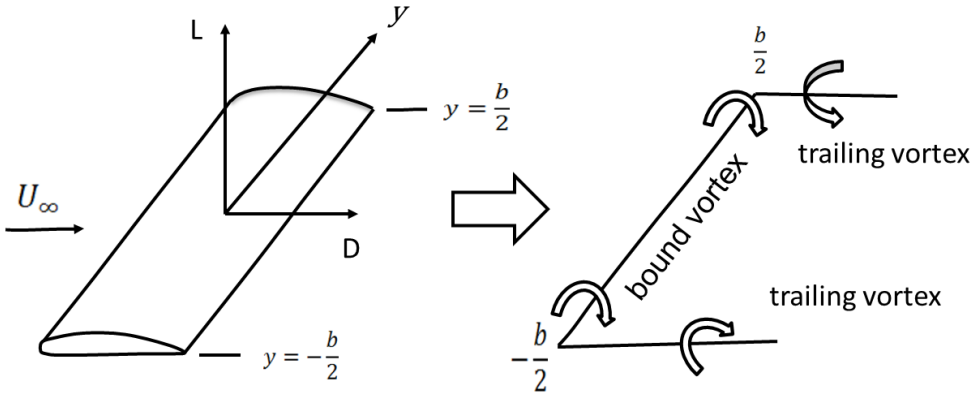

FIGURE 3.32: Horse shoe vortex system adapted from[24]

This idea can be developed further to include the superposition of a finite number of horseshoe vortices Figure 3.33. In Figure 3.33 three horseshoe vortices have been superimposed where the root circulation is equal to the sum of the three contributing circulation values. The strength of a trailing vortex is equal to the change in bound circulation.

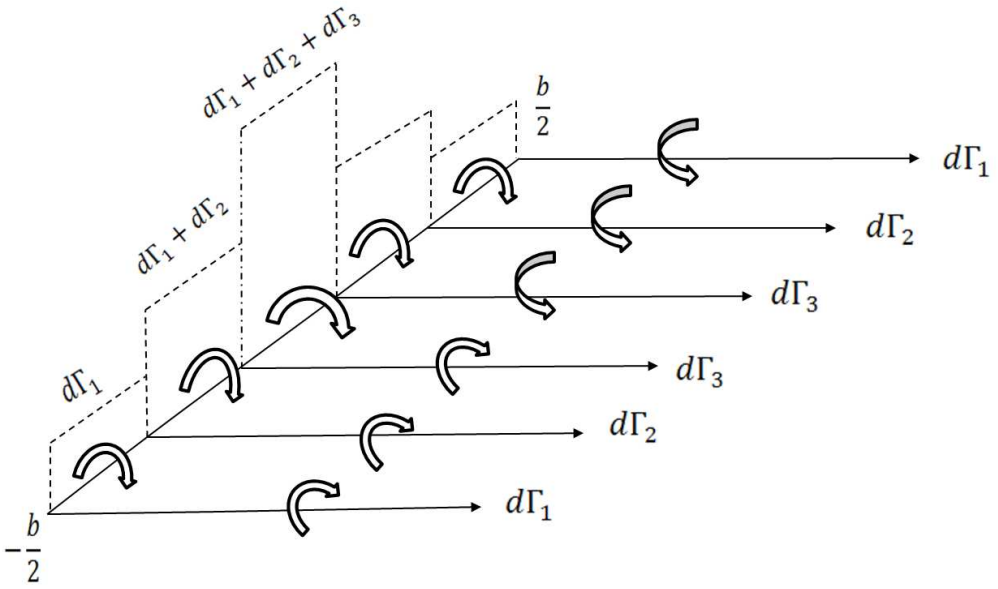

FIGURE 3.33: Superimposition of trailed vortices[24]

In order to calculate the lift distribution as a function of free stream conditions and bound circulation the Kutta-Joukowski theorem is used where the lift per unit span is defined as:

$$dl \approx \rho U_\infty \Gamma \tag{3.25}$$

Figure 3.34 represents the blade lift force (per unit span) discretised into finite sections along the blade span. Each section contributes a sectional lift force dl (acting normal to the page).

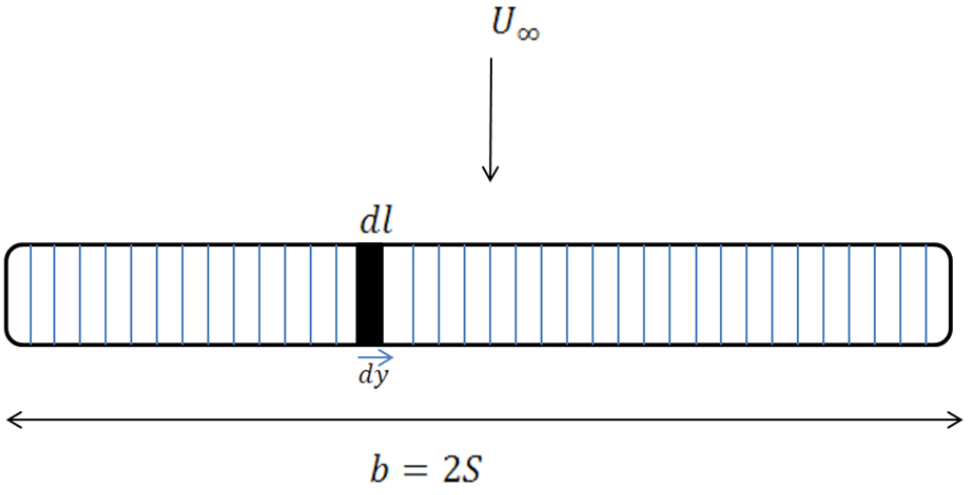

FIGURE 3.34: Blade lift force discritsed into differential segments

The total lift force is the integral of the finite lift forces. Equation 3.26 expressed as a function of bound circulation:

$$dl \approx \rho U_\infty \int_{-s}^{s} \Gamma dy \tag{3.26}$$

If the free stream conditions are known the only unknown in order to calculate the lift distribution is the circulation. The method to determine the bound circulation is to assume an elliptic distribution and represent it as a Fourier series[24]:

$$\Gamma = 4U_\infty s \sum_{n=1}^{\infty} A_n sin(n\theta) \tag{3.27}$$

The solution to the Fourier series is known as the monoplane equation:

$$\frac{\pi c}{4s}(\alpha - \alpha_0) sin\theta = \sum_{n=1}^{\infty} A_n sin(n\theta)[\frac{\pi cn}{4s} + sin\theta] \tag{3.28}$$

Now all the variables are known the lift distribution can be calculated and represented in the form of a lift coefficient by:

$$C_L = \frac{2}{U_\infty s} \int_{-s}^{s} \Gamma dy \tag{3.29}$$

Where:

$$y = scos(\theta) \tag{3.30}$$

This expression can be simplified to only a function of the aspect ratio and value of the first Fourier coefficient, A_1:

$$C_L = AR\pi A_1 \tag{3.31}$$

The validity of representing the lift via a superposition of horseshoe vortices and the subsequent derivation of the monoplane equation means the following assumptions need to be acknowledged and adhered to:

- 3-D steady potential flow
- Incompressible

- High aspect ratio
- Low sweep

3.5.2 Comparison of Lifting line theory to measured data for fixed wing tip vortex strength

The strength of a trailing tip vortex is calculated using lifting line theory and compared to wind tunnel measurements by Mason and Marchman[31].

Mason and Marchman[31] investigated the use of mass injection at the wingtip to hasten the vortex decay and used static and yaw-head pressure probes to measure the vortex properties at various location far downstream (up to 30 chords).

The test case conditions and airfoil geometry are presented in Table 3.2 for the semi-span, s, blade chord, c, angle of attack, α, total lift coefficient, C_L, freestream velocity, U_∞, and the Reynolds number for both velocities.

Property	Value
Airfoil	NACA 0012
s	1.2 m
c	0.2 m
α	7.5 °
C_L	0.674
U_∞	22 & 31 m/s
Re	2.5 & $3.5 * 10^5$

TABLE 3.2: Parameters for experiment by Mason and Marchman[31]

The strength of a trailing vortex is equal to the change in bound circulation, it is assumed that all the bound circulation is conserved into the trailing vortex.

The strength of the tip vortex is equal the change in bound circulation along the semi-span which is equal to the circulation at the root minus the circulation at the tip as shown in Equation 3.32. For an elliptic lift distribution this will be analogous to the maximum minus the minimum value for circulation.

$$\Gamma_{TipVortex} = \Gamma_{root} - \Gamma_{tip} \tag{3.32}$$

Table 3.3 compares the peak circulation measured by the experiments of Mason and Marchman[31] to the strength of a trailing vortex using Equation 3.32. The percentage difference is defined with the measured data as the reference value.

Case	Lifting line	Measured	Percentage difference (%)
22 (m/s)	1.32	1.1620	-13.35
31 (m/s)	1.88	1.78	-5.3

TABLE 3.3: Comparison between lifting line and experiment for tip vortex circulation

The lifting line results over predict the vortex circulation this can be attributed to the assumption that all the blade bound circulation is wrapped into the tip vortex and the theory negating effects such as turbulent diffusion. The discrepancy is also greater for the 22 m/s case where the vortex circulation was measured further upstream than the 31 m/s case, this could suggest that the vortex sheet had less roll up at the axial location of the 22 m/s measurement plane.

Prediction methods for vortex core size

Young[32] used a kinetic energy conservation approach to model the vortex core size in the near wake of helicopter rotors in hover and axial flow flight. Young assumed that the total power induced by the rotor, Pi, is equal to the kinetic energy, E, in the trailed vortex filaments. For, N, number of vortices at a rotor tip speed of, V_T, the induced power, Pi, is expressed in Equation 3.33.

$$P_i = NEV_T \tag{3.33}$$

The kinetic energy per unit length of vortex ring, E, with a given tangential velocity, V_θ, is defined in Equation 3.34[32].

$$E = \frac{\rho\Gamma^2}{4\pi}\left\{\ln\left(\frac{8R}{r_c}\right) - 2 + \left(\frac{2\pi}{\Gamma}\right)\int_0^{2r_c} V_\theta^2 r dr\right\} \tag{3.34}$$

A Vatistas vortex model was prescribed by Young[32] and substituted into Equation 3.34 to form Equation 3.35 which is configurable for any integer value of the shape factor, n.

$$E = \frac{\rho\Gamma^2}{4\pi}\left\{\ln\left(\frac{8R}{r_c}\right) - 2 + \int_0^{r_c} \frac{r^3}{(r_c^{2n} + r^{2n})^{2/n}} dr\right\} \tag{3.35}$$

Combining Equations 3.35 with Equation 3.33 and momentum theory defined in[32], for an, $n = 2$, Vatistas vortex model, the vortex core size can be expressed as a function of the rotor thrust coefficient, C_T, rotor inflow ratio, λ, and rotor axial-flow advance ratio, μ, as defined in Equation 3.36.

$$\ln(\frac{r_c}{R}) = \ln 8 - \frac{1}{4}\left\{8 - \ln 2 + \frac{C_T}{\lambda^2(\mu_z + \lambda)}\right\} \tag{3.36}$$

The model is compared to existing helicopter vortex data in Figure 3.35 for a Scully vortex, which is a Vatistas model with a shape factor of one and a Rankine type vortex model for induced power constants, k, of 1.1 and 1.25.

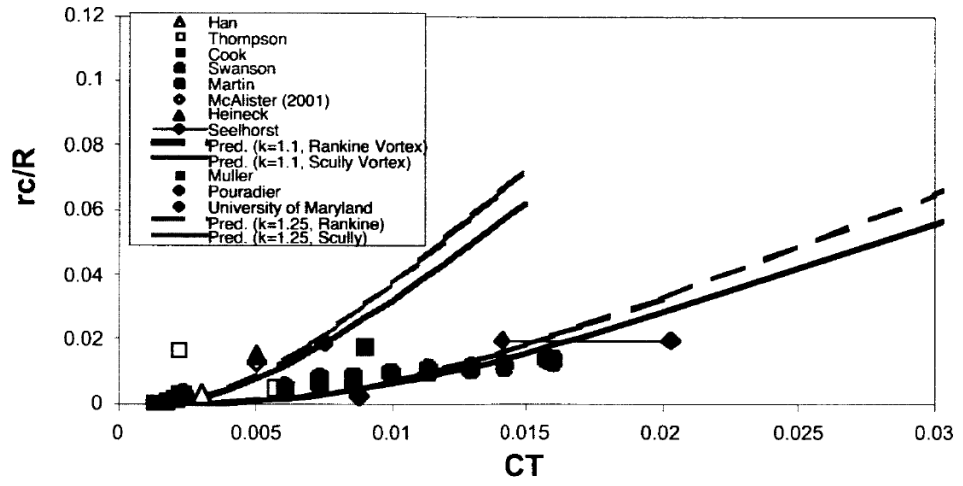

FIGURE 3.35: Young[32] model for vortex core size as a function of thrust compared to existing helicopter near wake studies

Figure 3.36 compares the non-dimensional vortex core size, r_c/R , effect of thrust coefficient, C_T for different Vatistas shape factors.

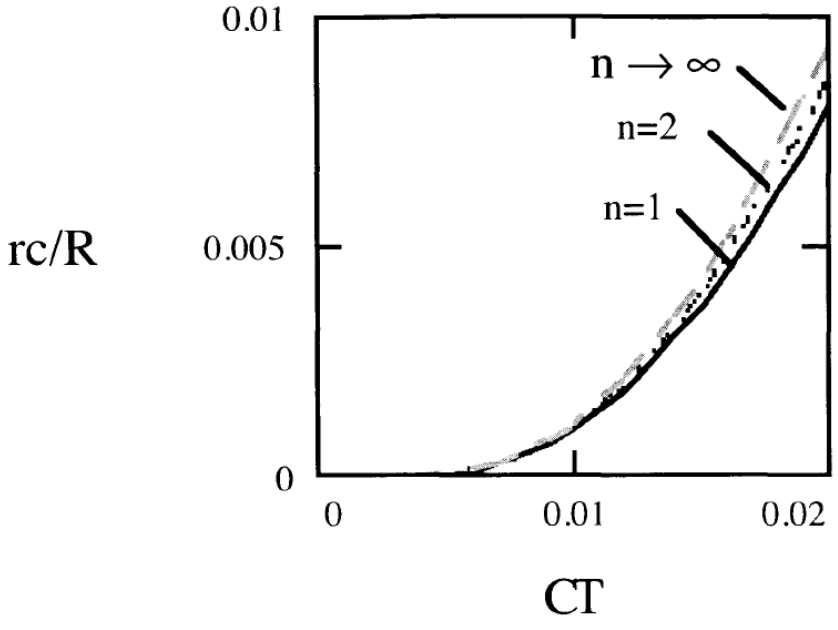

FIGURE 3.36: Effect of vortex profile shape factor on core size as a function of thrust[32]

It suggests that as a tip vortex tends towards a Rankine type vortex its core size will increase more with increasing thrust. However, that could be a by-product of the kinetic energy conservation method applied in the analysis neglecting effects diffusion of the vortex. Young[32] did note that the shape factor effect is small compared to other factors such as the rotor induced power and efficiency.

3.5.3 Tip vortex parameter correlations used in CRPFAN

The tip vortex parameters in CRPFAN and also used by[9],[8] are calculated using the correlations developed by Majjigi et al[10]. The correlations are used to calculate the tip vortex core size, r_c, maximum tangential velocity, $V_{\theta_{max}}$, and circulation, Γ_{vtx}. Measured vortex core size and peak tangential velocity from the cascade experiments on a NACA 0012 wing by[33] and[31] were combined to form linear rational functions which relate the propeller operating conditions to the tip vortex parameters.

The correlation developed to calculate the vortex core size, r_c, in Equation 3.37 is formed from the non dimensional core radius, $\frac{r_c}{\bar{c}\sqrt{\bar{C}_l}}$, measured at planes up to the 30 normalised streamwise distances, $\frac{S}{\bar{c}}$ downstream shown in Figure 3.37. The overbars represent properties averaged at the outer 30 % of the blade span.

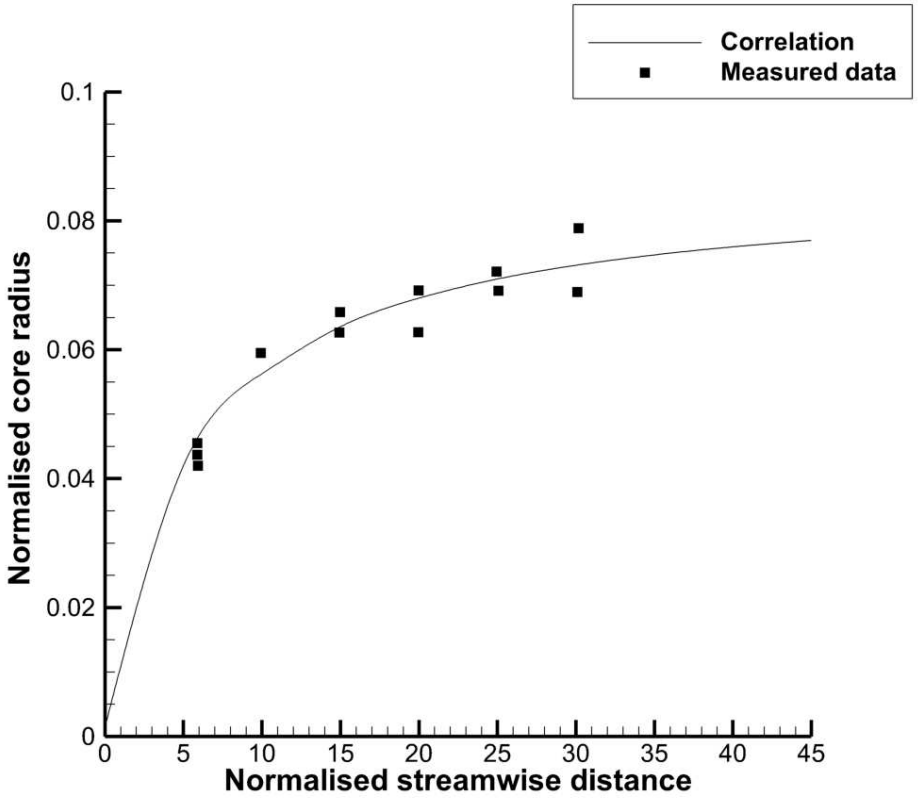

FIGURE 3.37: Core size source data adapted from[10]

The correlation is a linear rational function to form Equation 3.37 which is used in CRPFAN.

$$\frac{r_c}{\bar{c}\sqrt{\bar{C}_l}} = \frac{0.01584(S/\bar{c}) + 0.0014}{0.184(S/\bar{c}) + 1} \tag{3.37}$$

The maximum tangential velocity, $V_{\theta_{max}}$, is normalised to, $V_{\theta_{max}}/V_0\sqrt{\bar{C}_l}$, and plotted as a function of normalised streamwise distance, $S/\bar{c}$, shown in Figure 3.38 to form Equation 3.38 which is used in CRPFAN.

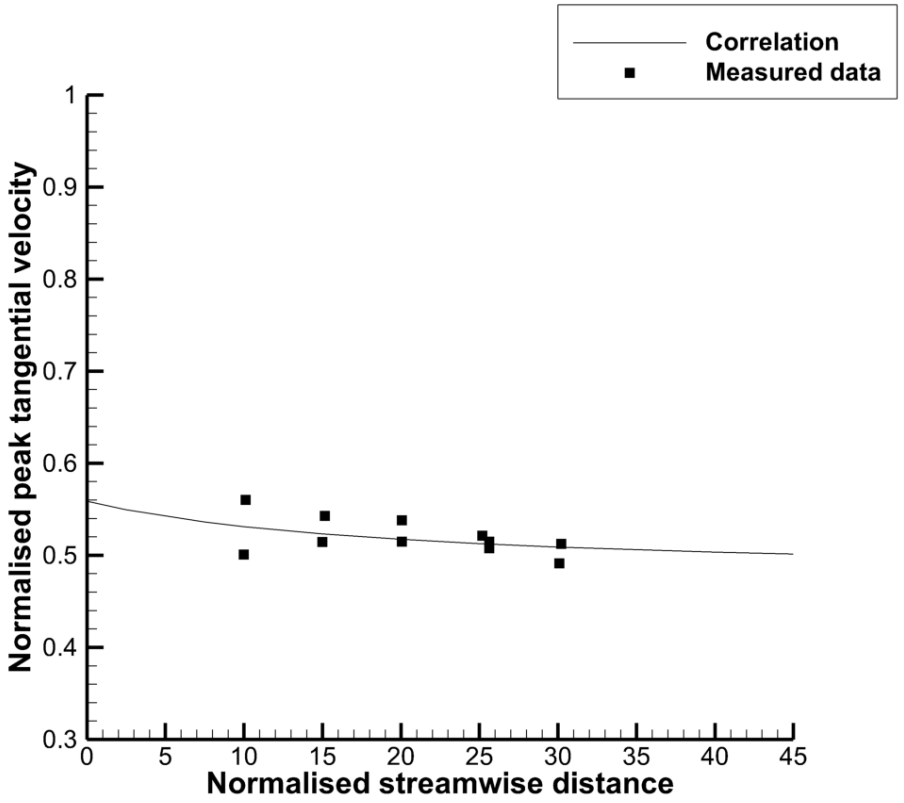

FIGURE 3.38: Correlation for maximum tangential velocity used in CRPFAN

$$\frac{V_{\theta_{max}}}{V_0\sqrt{\bar{C}_l}} = \frac{0.024(S/\bar{c}) + 0.5586}{0.0504(S/\bar{c}) + 1} \tag{3.38}$$

The tip vortex model assumes all the vorticity is confined to inside the vortex core, the additional assumption of no vortex radial velocity component means the circulation can be calculated through the radial integration of the peak tangential velocity within the vortex the core as shown in Equation 3.39.

$$\Gamma_{vtx} = Ci2\pi V_{\theta_{max}} r_c \tag{3.39}$$

To account for the correlations being derived from measured vortex characteristics downstream of a stationary NACA 0012 as opposed to a rotating propeller, a circulation parameter, Ci, is used which linearly scales the circulation, Γ_{vtx}. A decay function ζ is also included in an attempt to model the tip vortex circulation decay as it convects downstream. The final equation for the circulation is shown in Equation 3.40

$$\Gamma_{VTX} = \frac{Ci\Gamma_{VTX}}{(1 + S/\bar{c})^{\zeta}} \tag{3.40}$$

The same study in[10] also included a correlation for the tip vortex radial location as a function of axial distance which is integrated into CRPFAN. Schlieren visualisation of vortices of a helicopter in hover mode combined to form the measured data in Figure 3.39.

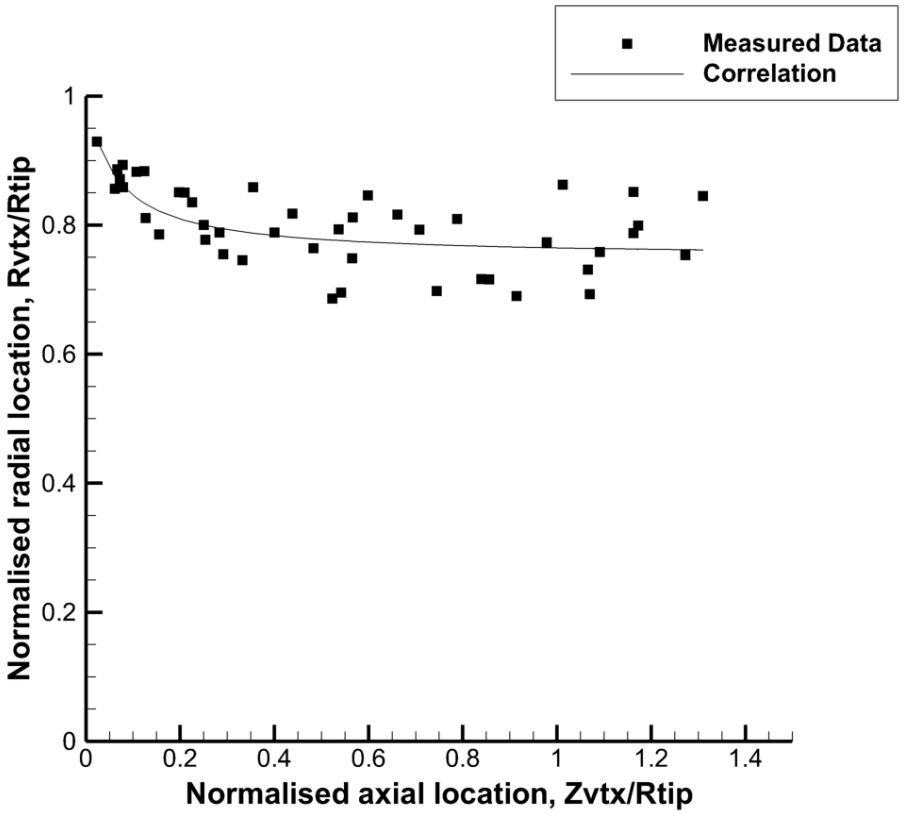

FIGURE 3.39: Source data for tip vortex trajectory model used in CRPFAN

Where, R_{vtx}, is the tip vortex centre, R_{tip}, is the radial location of the blade tip and Z_{vtx} is an axial distance downstream of the the rotor plane of rotation. A linear ration function of the same type used for the core size and peak tangential velocity is used as shown in Equation 3.41.

$$\frac{R_{vtx}}{Z_{vtx}} = \frac{12(Z_{vtx}/R_{tip}) + 1}{16(Z_{vtx}/R_{tip}) + 1} \tag{3.41}$$

With reference to Figure 3.28 the vortex radial location, b_r, defined in Equation 3.42:

$$b_r = R_{tip} - R_{vtx} \tag{3.42}$$

This definition can be substituted into Equation3.41 to form Equation 3.43:

$$\frac{b_r}{R_{tip}} = 1 - \frac{R_{vtx}}{Z_{vtx}} = \frac{4(Z_{vtx}/R_{tip})}{16(Z_{vtx}/R_{tip}) + 1} \tag{3.43}$$

An additional, scalable parameter, $TVTI$, is used to scale the radial location of the tip vortex centre, this is introduced to account for the streamtube contraction as it changes with thrust. Equation 3.44 is the radial trajectory model used within CRPFAN.

$$\frac{b_r}{R_{tip}} = \frac{TVTI(Z_{vtx}/R_{tip})}{16(Z_{vtx}/R_{tip}) + 1} \tag{3.44}$$

3.6 Open rotor tip vortex investigation

Section 3.6 provides a summary of the key findings from investigations of the wake and tip vortices downstream of a CROR and advanced turboprops that are of relevance to this project. Table 3.4 is a summary of the literature reviewed, the geometry the investigations are conducted on, the freestream Mach number of the experiments/computations and finally the method of their flowfield attainment.

Author	Geometry	Freestream Mach No	Method
Hanson and Patrick[34]	SR3	0.32	Hot wire anemometry
Serafini et al	SR3	0.8	LDV
Tillman et al[35]	CRP-X1	0.25	Hot wire anemometry
Podboy and Krupar[36]	F4/A5	0.72	LDV
Simonich et al[37]	F4/A5	0.72	LDV
Lavrich et al[38]	CR-9	0.165	Hot wire anemometry
Tsai et al[39]	SR3	0.3	Parabolised Navier Stokes

TABLE 3.4: Summary of key advanced propeller tip vortex investigations

Flow surface visualisation techniques including the use of oil and mini-tufts on a swept advanced propeller blade revealed a flow pattern similar to a delta wing where the flow separates at the leading edge which rolls into a leading edge vortex on the suction side of the blade. These flow features are evident in Figure 3.40.

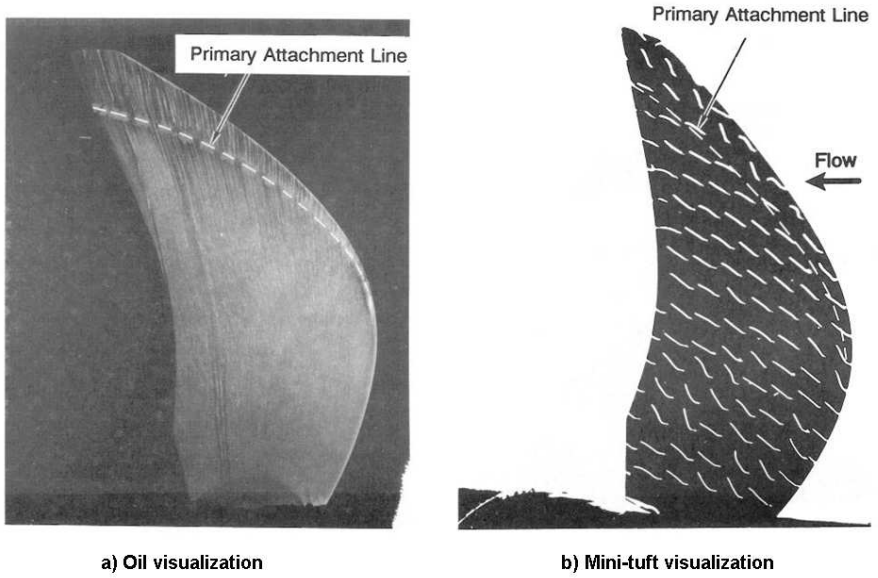

FIGURE 3.40: Flow visualisation on swept advanced propeller blade Vaczy[40]

The propeller vortex sheet wake, tip vortex and leading edge vortex start as separate structures but as the flow evolves downstream these features roll up to form one vortical structure. The roll up of the propeller vortex sheet and tip vortex is demonstrated in Figure 3.41. Which shows phase averaged laser velocimetry measurements at two planes downstream of the F4 propeller blade. The first plane is 85 % of the tip chord downstream of the F4's trailing edge while the second plane is 241%.

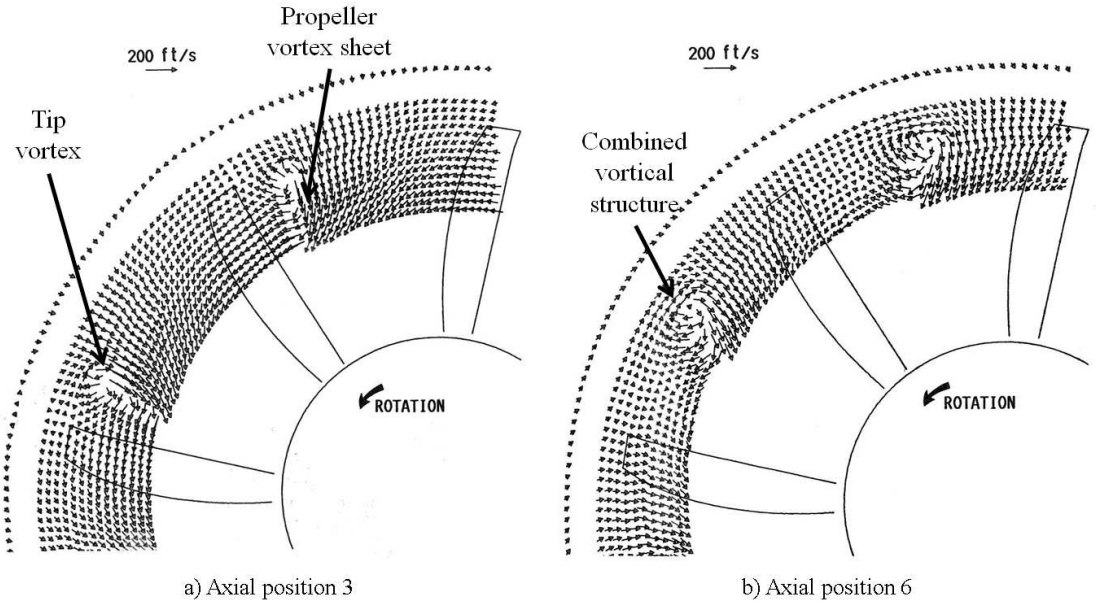

FIGURE 3.41: Phase averaged velocities from Laser Velocimetry measurements downstream of F4 propeller[36]

The phenomena of vortex core bursting was also detected at high loading conditions inside the leading edge vortex which has the effect introducing large levels of turbulence which increases the tip vortex core size and decreases the maximum tangential velocity. The vortex core size increases for take off relative to cruise because of the higher sectional lift coefficients. Hot wire anemometry by Lavrich et al[38] discovered a wake like velocity deficit core 70 % of the freestream velocity.

3.7 Literature Review Summary

The open rotor is a viable, greener future alternative to the turbofan engine. However, the additional noise generated due to the interaction of the front rotor tip vortices and viscous wakes with the rear rotor is a problem for the open rotor's advancement.

Chapter 3 presented published approaches to reduce the interaction noise such as decreasing the diameter of the rear blade and increasing the spacing of the blade rows. The methods used included anechoic wind tunnel experiments, computational aeroacoustics, CFD and lower order analytical tools such as CRPFAN. The methodologies to be used in this project will include CFD to generate the open rotor flowfield with focus on the tip vortices and the use of CRPFAN to quantify the acoustic impact of the tip vortex parameters.

Also included in Chapter 3 was a review of tip vortex theory and the current state of the art for predicting the tip vortex parameters such as the ones included in CRPFAN. The bespoke tip vortex correlations developed using CFD will be compared against the current state of the art as well as assessing the applicability of lifting line theory to predict the strength of an open rotor tip vortex.

Chapter 4

Aeroacoustic Methodology

Section 3.3 highlighted different methods of predicting open rotor tip vortex interaction noise. At one end of the scale there is anechoic wind tunnel testing such as [41] which is high fidelity, high cost and high lead times. The opposite end of the scale includes analytical tools which are lower in fidelity but the cost and lead time are also relatively low, this makes noise prediction codes such as CRPFAN efficient tools during the preliminary design stage.

This project is concerned with the development of any preliminary design tools for CROR interaction noise. The available example of such a tool to the author is CRPFAN and it will be used as an example of a generic preliminary design aeroacoustic tool for CROR interaction noise.

4.1 CRPFAN Overview

Section 4.1 gives an overview of CRPFAN as an aeroacoustic tool. It has the capability to calculate the rotor alone tones due to thickness and loading noise and interaction noise due to wake and tip vortex interactions, treating the propeller as an isolated system. Additionally, it has the capability to calculate installation effects due to the aircraft angle of attack and from the presence of aerodynamic bodies such as the pylon and fuselage. The isolated noise is calculated first and the additional noise due to installation is added as a 'delta' dB. This process is summarised in Figure 4.1.

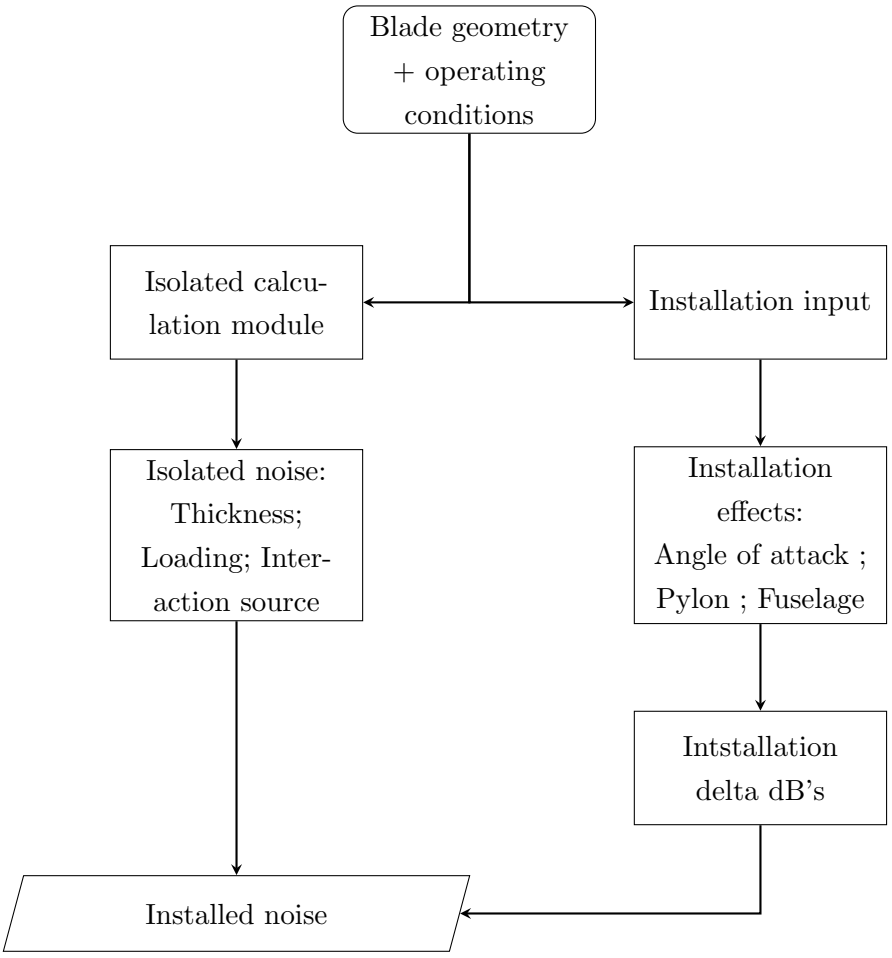

FIGURE 4.1: CRPFAN general use flow chart

However it must be noted that CRPFAN does not account for known open rotor noise sources such as broadband noise, potential field interactions between the rotors and source terms which are classified as a quadrupole. The open rotor noise capability is summarised in Table 4.1.

Open rotor noise source	Included in CRPFAN?
Propeller thickness noise	**Yes**
Propeller loading noise	**Yes**
Wake and tip vortex interaction noise	**Yes**
Installation effects (wing, fuselage, pylon and aircraft attitude)	**Yes**
Broadband noise	No
Potential field interaction between rotors	No
Quadrupole noise	No

TABLE 4.1: CRPFAN open rotor noise prediction capability summary

This project will focus on the isolated noise sources, particularly the interaction noise due to tip vortex interactions between the front and aft rotors.

4.2 Aeroacoustic Method

Section 4.2 presents the key equations used in CRPFAN to calculate the rotor alone tones and interaction noise.

4.2.1 Rotor alone noise

CRPFAN uses the analysis of Hanson[21] and Fourier transforms the Ffowcs-Williams and Hawkings equation to convert from the time into the frequency domain and uses an acoustically non-compact distributed source based on a helicoidal coordinate system[5].

The volume noise P_Vm is an acoustic monopole term and is due to the air displaced by the finite thickness of the rotor blades.

$$P_{Vm} = \frac{\rho_o c_o^2 B sin\theta e^{\left\{imB(\frac{\Omega_D r}{C_o} - \frac{\pi}{2})\right\}}}{8\pi(\frac{\gamma}{D})(1 - M_x cos\theta)} \int_0^1 M_r^2 e^{i(\phi_o + \phi_s)} * J_{mB}(\frac{mBzM_T \sin\theta}{1 - M_x \cos\theta}) * -k_x^2 t_b \psi_v(k_x) dz \tag{4.1}$$

The phase shift due to sweep ϕ_s and offset ϕ_0:

$$\phi_s = \frac{2mBM_T}{M_T(1 - M_x \cos\theta)} \frac{MCA}{D} \tag{4.2}$$

$$\phi_o = \frac{2mB}{zM_r} \frac{M_r^2 \cos\theta - M_r}{1 - M_x \cos\theta} \frac{FA}{D} \tag{4.3}$$

MCA is the mid-chord alignment, FA, the face alignment - both defined in Figure 4.2. Ω_D is the ratio of the rotational frequency, Ω, and the Doppler factor $1 - M_x cos\theta$ as shown:

$$\Omega_D = \frac{\Omega}{(1 - M_x cos\theta)} \tag{4.4}$$

The non-dimensional wave numbers k_x and k_y:

$$k_x = \frac{2mBB_D M_T}{M_T(1 - cos\theta)} \tag{4.5}$$

$$k_y = \frac{2mBB_D}{zM_T}(\frac{M_T^2 cos\theta - M_x}{1 - M_x cos\theta}) \tag{4.6}$$

Where B_D is the chord to diameter ratio. The thickness distribution, $H(X)$, is defined in the frequency domain as $\psi_V(k_x)$ by:

$$\psi_V(k_x) = \int_{-1/2}^{+1/2} H(X) e^{ik_x X} dX \tag{4.7}$$

The equation for the loading noise, P_{Lm} is very similar to the thickness noise $P_V m$ but $\psi_V(k_x)$ is replaced by the Fourier transformed chordwise loading term,$\psi_L(k_x)$, :

$$\psi_L(k_x) = \int_{-1/2}^{+1/2} f_L(X) e^{ik_x X} dX \tag{4.8}$$

Where:

$$f_L(X) = \frac{\triangle p(x)}{1/2\rho_o V_r^2 C_L} \tag{4.9}$$

To form:

$$P_{Lm} = \frac{\rho_o c_o^2 B sin\theta e^{\left\{imB(\frac{\Omega_D r}{C_o} - \frac{\pi}{2})\right\}}}{8\pi(\frac{\gamma}{D})(1 - M_x cos\theta)} \int_0^1 M_r^2 e^{i(\phi_o + \phi_s)} * J_{mB}(\frac{mBzM_T \sin\theta}{1 - M_x \cos\theta}) ik_y(\frac{C_L}{2}) \psi_L(k_x) dz \tag{4.10}$$

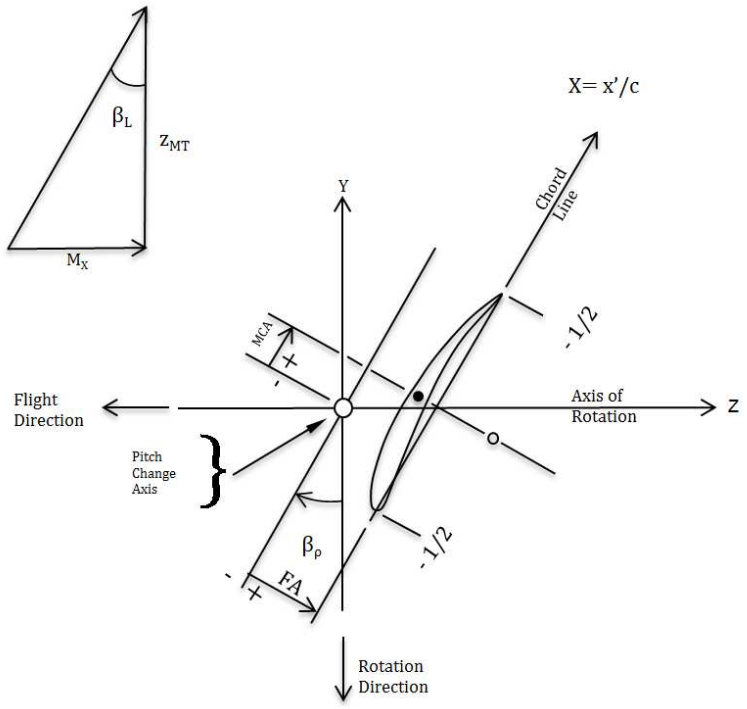

FIGURE 4.2: Acoustic coordinate system adapted from [21]

4.2.2 Interaction noise

The interaction noise occurs because the rear rotor loading becomes unsteady as a result of operating in the non-uniform flowfield shed by front rotor wake and tip vortex. For the interaction noise the lift and drag coefficients become harmonic coefficients in the form of C_{Lk} and C_{Dk} respectively, where k is the order of the load harmonic.

$$p = \frac{-i\rho_0 c_0^2 B_2 \sin\theta}{8\pi(r_1/D)(1 - M_x cos\theta)}$$

$$\sum_{m=-\infty}^{\infty}\sum_{k=-\infty}^{\infty} exp\left\{i\left[(mB_2 - kB_1)(\phi - \phi^{(2)} - \tfrac{\pi}{2}) + (mB_2\Omega_2 + kB_1\Omega_1(\tfrac{r}{c_0} - t)\right]\right\}$$

$$\mathrm{X}\int_{root}^{tip} M_r^2 e^{i(\phi_0+\phi_s)} J_{mB_2-kB_1}\left[\tfrac{(mB_2+kB_1\Omega_{12})z_0 M_T sin\theta}{1-M_x cos\theta}\right]\left[k_x\tfrac{C_{Dk}}{2}\Psi_{Dk}(k_x) + k_y\tfrac{C_{Lk}}{2}\Psi_{Lk}(k_x)\right] dz_0 \quad (4.11)$$

The wave numbers k_x and k_y are for the unsteady interaction noise are defined as:

$$k_x = \frac{2M_T}{M_r}\left[\frac{mB_2 + kB_1\Omega_{12}}{1 - M_x cos\theta} - kB_1(1 + \Omega_{12})\right] B_D \quad (4.12)$$

$$k_y = -\frac{2}{M_r}\left[\frac{(mB_2 + kB_1\Omega_{12})M_T^2 z_0 cos\theta}{1 - M_x cos\theta} - \frac{(mB_2 - kB_1)M_x}{z_0}\right] B_D \quad (4.13)$$

The phase shift:

$$\phi_s = \frac{2M_T}{M_r}\left[\frac{mB_2 + kB_1\Omega_{12}}{1 - M_X cos\theta} - kB_1(1 + \Omega_{12})\right]\frac{MCA}{D} \tag{4.14}$$

The phase offset:

$$\phi_0 = \frac{2}{M_r}\left[\frac{(mB_2 + kB_1\Omega_{12})z_0 M_T^2 cos\theta}{1 - M_X cos\theta} - (mB_2 - kB_1)\frac{M_X}{z_0}\right]\frac{FA}{D} \tag{4.15}$$

Note for the calculation of interaction noise the chord wise non-compactness factor is not taken into account unlike the rotor alone noise. In order to calculate the unsteady interaction noise the harmonic coefficients of lift and drag C_{Lk} and C_{Dk} need to be determined. From the input operating conditions and geometry a radial lift distribution is calculated, the geometrical parameters and radial lift distributions are used to calculate the maximum tangential velocity, $V_{\theta_{max}}$, and core size of the vortex, r_c, using the empirical correlations defined in Section 3.5.3.

With $V_{\theta_{max}}$ and r_c defined, an azimuthal distribution of the vortices' tangential velocity, V_θ, can be calculated. This is vector summed with the wake flowfield and coordinate transformed into a frame relative to the aft rotor. From here the velocity acting normal to the aft rotor 1/4 quarter chord line, V_{PN}, is calculated. The azimuthal distribution of V_{PN} is Fourier transformed which forms the upwash gust harmonics onto the aft blade, which is input into a Sear's type blade response function corrected for compressibility by Amiet[5]. The outcome of the blade response function is the harmonic lift coefficient, C_{Lk}, at each calculated radial location. The default number of harmonic loads, k, calculated is 15. This basic process is summarised in the flow chart of Figure 4.3.

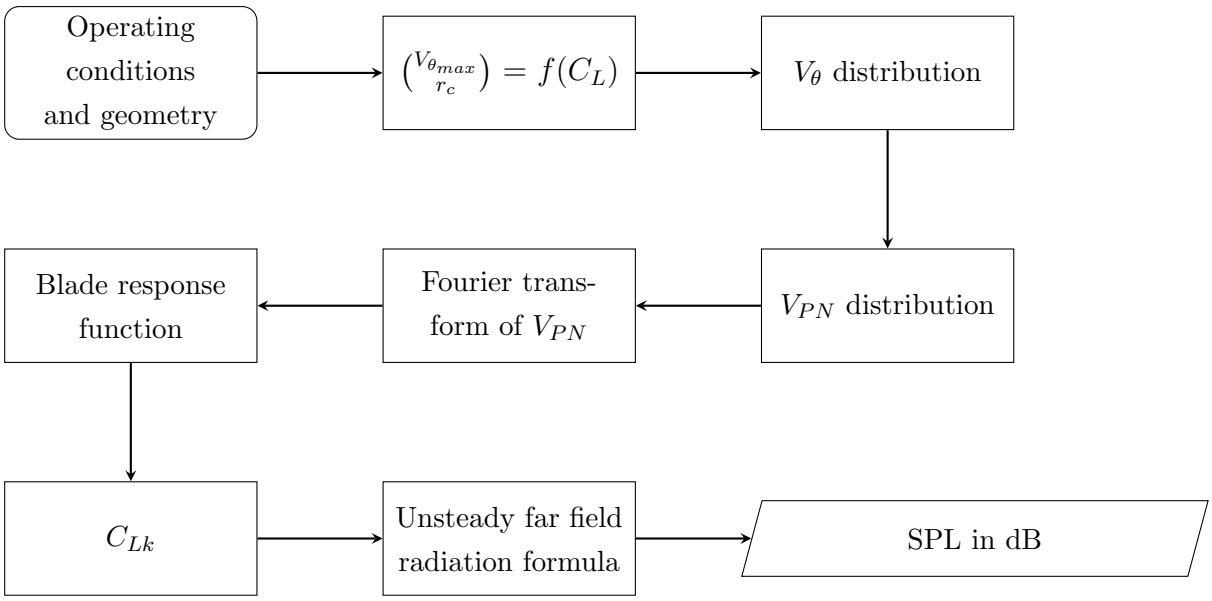

FIGURE 4.3: Basic summary of unsteady noise calculation

4.3 CRPFAN Verification and Validation

4.3.1 CRPFAN Verification

The purpose of the verification is to ensure the tool is being used in the intended manner and the calculations are implemented correctly. The test case for the verification uses the sample CRPFAN input and output file included in[10]. The verification test case geometry and operating conditions are summarised in 4.2:

Parameter	Value (Front, Aft)
Geometry	F7-A7
Blade numbers	11 , 9
rpm	7633, 7695
Mo	0.2
Cp	0.774, 0.909
$\beta_{3/4}$ (°)	36.4, 36.5

TABLE 4.2: CRPFAN verification case operating parameters

There is no difference between the original and verification noise for front rotor fundamental harmonic tone which occurs at the blade passing frequency of the front rotor, the rear rotor fundamental tone and the OASPL directivity which is a $1/3^{rd}$ octave sum of all the calculated tones. This is demonstrated in Figure 4.4.

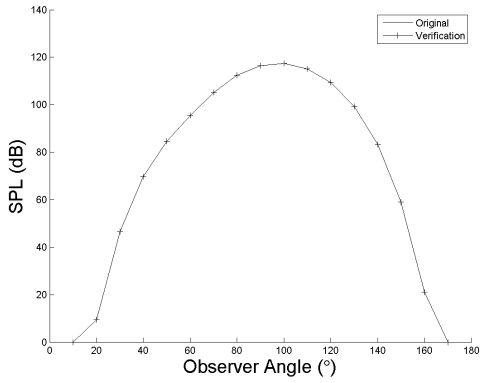

(a) Front rotor BPF

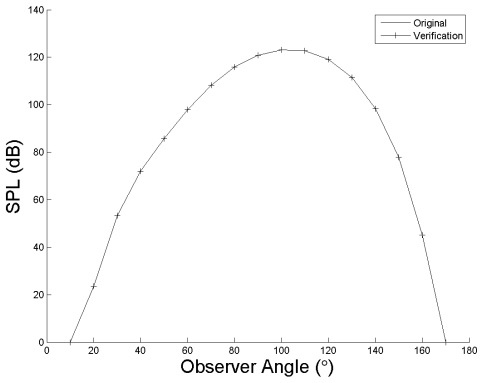

(b) Rear rotor BPF

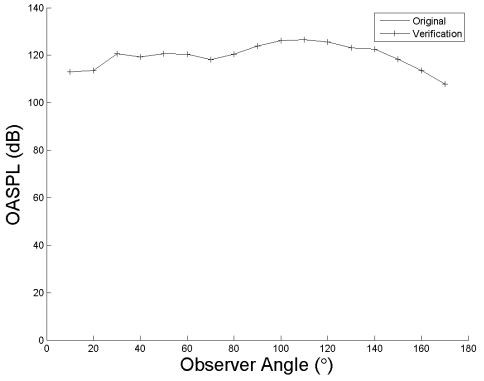

(c) OASPL

FIGURE 4.4: CRPFAN verification results

4.3.1.1 CRPFAN Verification summary

There is no difference between the data in [10] and that created using the in-house version of CRPFAN. This demonstrates that CRPFAN is being used in the correct manner. The next question is how well does CRPFAN predict open rotor tonal and interaction noise?

4.3.2 CRPFAN Validation

The validation study is used to assess the credibility of CRPFAN with reference to acoustic measurements. The measurements used to validate CRPFAN are for the F7-A7 geometry in the NASA Lewis 9 x 15 ft tunnel [5]. The conditions are summarised in Table 4.3.

Parameter	Value (Front, Aft)
Geometry	F7-A7
Blade numbers	11 x 9
rpm	6800
Mo	0.2
C_P	0.9856, 1.1639
$\beta_{3/4}$ (°)	36.4,36.5
Wind Tunnel	NASA Lewis 9 x 15 ft
Sideline distance	4.5 ft

TABLE 4.3: CRPFAN validation test case operating conditions

Rotor alone tones

The front rotor fundamental tone Figure 4.5 has good agreement between measured data and CRPFAN. However, there is a difference of 2-3 dB in the aft lobe.

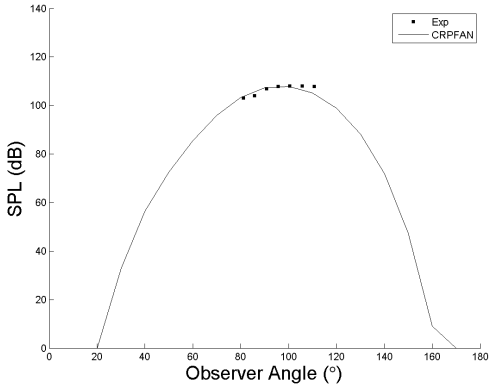

FIGURE 4.5: CRPFAN front rotor fundamental tone validation

The rear rotor fundamental tone shown in Figure 4.6 agreement is worse than agreement with front rotor fundamental with differences between CRPFAN and experiment in the order of 4-5 dB.

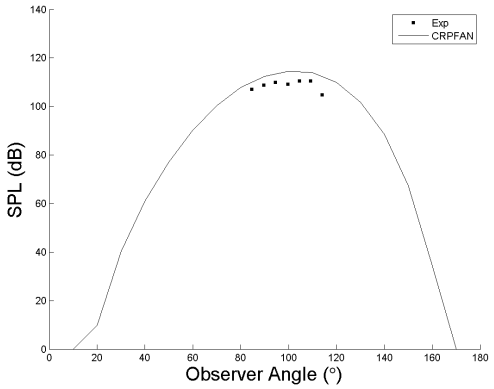

FIGURE 4.6: CRPFAN rear rotor fundamental tone validation

The authors[5] attribute the discrepancy partly to the fundamental tones being buried into the wind tunnel broadband noise.

Interaction tones

Presented here is a comparison between CRPFAN and measurement for the interaction tones due to the viscous wake and tip vortex interactions with the aft rotor. The sectional drag coefficient used is 0.02 at all radial stations. The nomenclature for each tone is $n_1F + n_2A$, the F and A stand for forward and aft rotors and n is the multiple of the BPF. For example the $1F+1A$ interaction tone is at a frequency equal to the front rotor BPF plus the rear rotor BPF. The subscripts $1, 2$ corresponding to front and rear rotor respectively.

There is acoustic measured data for the conditions stated in Table 4.3 for six interaction tones, $1F + 1A$, $1F + 2A$, $2F + 1A$, $1F + 3A$, $2F + 2A$ and $3F + 1A$. The comparison between CRPFAN calculations and the measured data are shown in Figures 4.7 to 4.12.

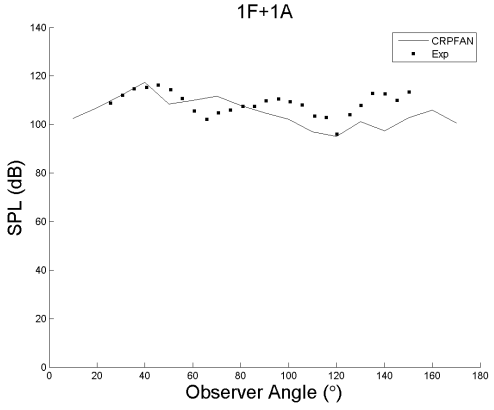

FIGURE 4.7: 1F + 1A rotor alone tone CRPFAN prediction against measurements

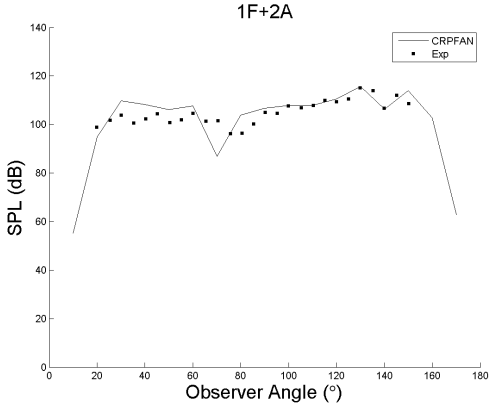

FIGURE 4.8: 1F + 2A rotor alone tone CRPFAN prediction against measurements

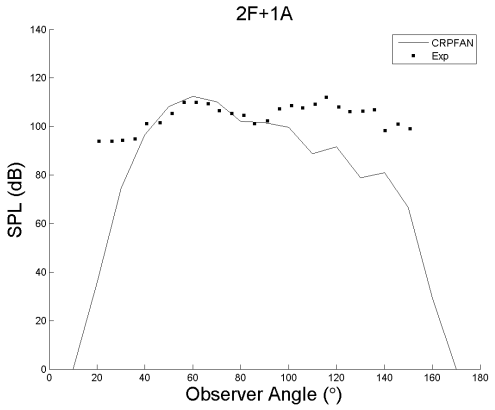

FIGURE 4.9: 2F + 1A tone CRPFAN prediction against measurements

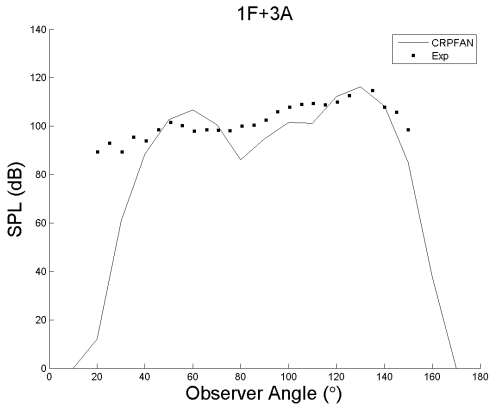

FIGURE 4.10: 1A+3A tone CRPFAN prediction against measurements

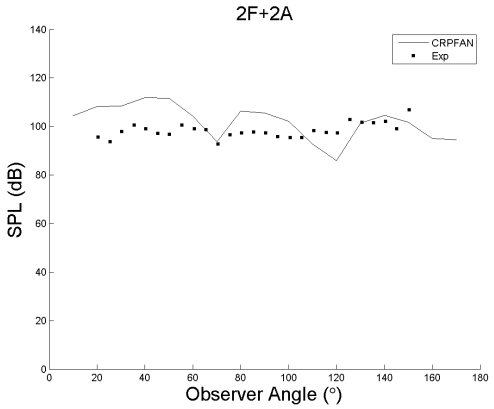

FIGURE 4.11: 2F+2A tone CRPFAN prediction against measurements

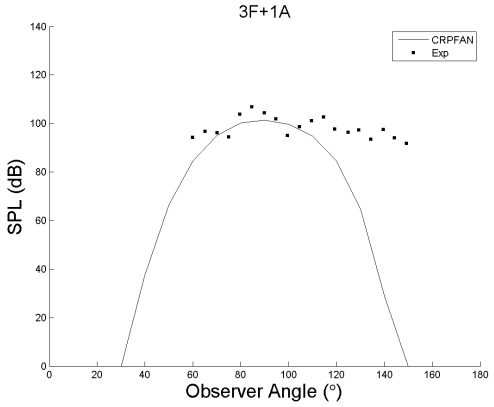

FIGURE 4.12: 3F+1A tone CRPFAN prediction against measurements

The agreement is best for the $1F + 2A$ tone, the $1F + 1A$, $1F + 3A$ and $2F + 2A$ tones show reasonable agreement. The $3F + 1A$ and $2F + 1A$ have very poor agreement particularly in the aft lobe of the directivity pattern. Theses differences could be due to a lack of credibility in the vortex and wake model however. Suggested improvements to the vortex model are presented in Chapter 7.

4.3.2.1 CRPFAN Validation summary

CRPFAN has been verified with reference to the example data supplied in[10]. A validation study has been conducted relative to measured data from the NASA Lewis 9 x 15 ft tunnel where the front rotor tone fundamental tone agreement is good, but the rear rotor fundamental tone agreement is under predicted by CRPFAN in the order of 4 - 5 dBs. For most interaction tones the agreement with measured data is good, with most tones being slightly under predicted by CRPFAN. The $2F + 1A$ and $3F + 1A$ tones noticeably vastly under predicted in the aft lobe.

4.4 CRPFAN Limitations

Section 4.4 highlights some observed limitations to the original version of CRPFAN. The Rankine type vortex model is not physically realistic so this can be replaced with the Vatistas vortex model used in helicopter aerodynamics [28]. In CRPFAN only the tangential velocity component of the vortex is considered - is there a case for considering the axial component as well?

The empirical input parameters such as the circulation index and tip vortex trajectory index needs to be calculated using bespoke correlations which consider the individual physics of each case. The correlations for $V_{\theta_{max}}$ and r_c are based on a limited set of fixed wing cascade data - is this appropriate for an open rotor configuration?

A key factor which is not considered in CRPFAN and treated in more depth in Chapter 7 is the spatial orientation of the vortex - due to the interaction of the vortex with the aft blade.

One area of improvement to CRPFAN is in its general usability for calculations of new geometries and configurations where no CFD or experimental data is available. To calculate the open rotor interaction noise a radial lift distribution is required, if interested in a novel geometry this information will not be immediately available. This can be remedied by coupling CRPFAN to a strip theory aerodynamics code whose output can be used as an input to CRPFAN for acoustic calculations.

A final consideration which will be addressed in the tip vortex trajectory study in Section 5.1.2, which relates to the number of streamlines in CRPFAN. It is an acoustic strip theory code, with a default value of 10 streamlines/strips. It was noted that the noise of the tip vortex interaction is sensitive to how close the vortex core is to the location of the nearest streamline. This can be corrected with the use of more streamlines in CRPFAN to ensure the vortex core is correctly captured.

CRPFAN limitations summary

Possible improvements to tip vortex specific issues:

- Type of tip vortex model used
- Inputs to the tip vortex model e.g. more suitable correlations
- How the spatial orientation of the vortex is modelled
- Inclusion of the vortex axial velocity component

General CRPFAN usability improvements:

- Method to automatically generate inputs for new cases
- Increase the spatial resolution from the default 10 streamlines

Chapter 5

Impact of tip vortex on Open rotor noise

Chapter 5 includes quantitative sensitivity studies, which relate the strength, location and the tangential velocity distribution of the tip vortex to the interaction noise - with CRPFAN used as an aeroacoustic tool to calculate the noise.

5.1 Effect of Input Vortex Parameters on Open Rotor Noise

In the original published version of CRPFAN[5] there are scalable inputs with reference to the tip vortex parameters which need to be known prior to its use. Two of these parameters are the circulation index (Ci) and tip vortex trajectory index (TVTI) which are defined in Section 3.5.3. Section 5.1 quantifies the sensitivity of the interaction noise to these parameters. The geometry and operating conditions are the same as the ones used in the validation study defined in Table 4.3.

5.1.1 Effect of circulation index value

The sensitivity study will use four values of the circulation index, 1) Ci=0 which corresponds to no tip vortex model and the noise in this mode is due to wake interaction effects, 2) Ci=1, this represents a physically realistic condition where the strength of the tip vortex for a propeller will be equal to that of a fixed wing for the same lift distribution, 3) Ci=2, which means the tip vortex will be twice the strength of the fixed wing strength and 4) Ci=3 which is three times stronger.

The results of this study are shown in Figures 5.1 to 5.6, for each of the six interactions tones there are two sub figures, a directivity with the four Ci values and the measured data for comparison and an additional stem plot showing the difference in SPL directivity

between Ci=3 and Ci=1, Ci=1 is used instead of Ci=0 to ensure differences are only due to the strength of the tip vortex.

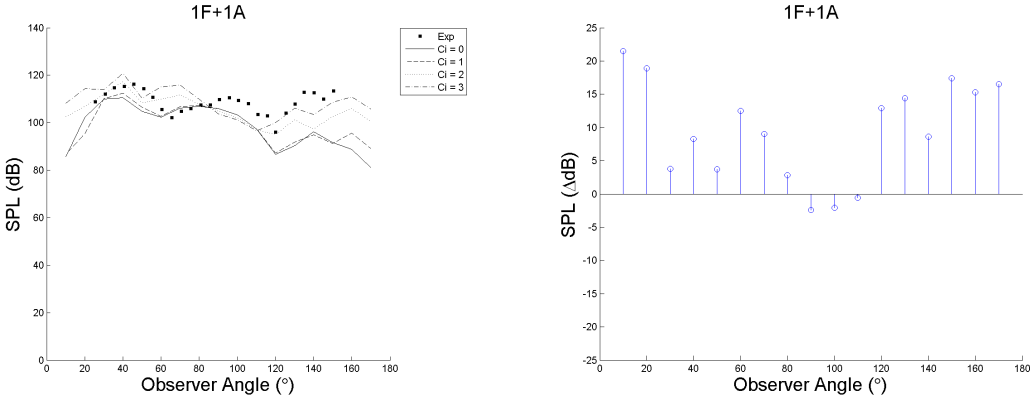

(a) Directivity (b) $Ci = 3$ - $Ci = 2$

FIGURE 5.1: Effect of Ci on 1F+1A interaction tone

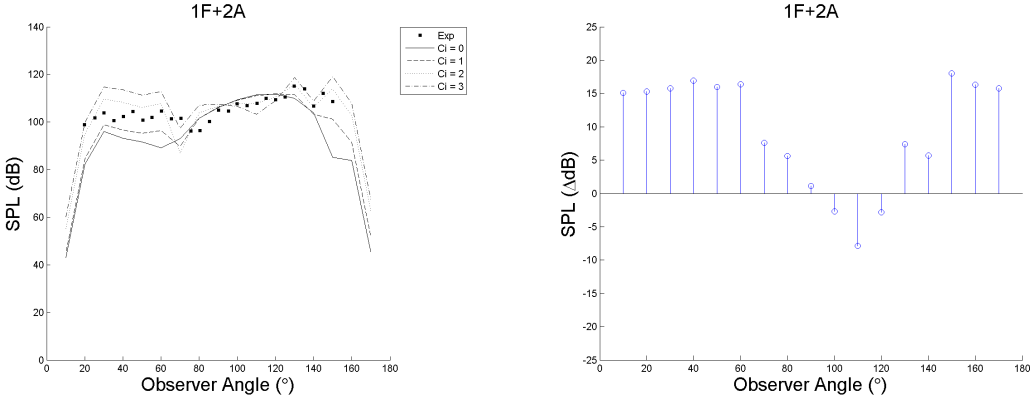

(a) Directivity (b) $Ci = 3$ - $Ci = 2$

FIGURE 5.2: Effect of Ci on 1F+2A interaction tone

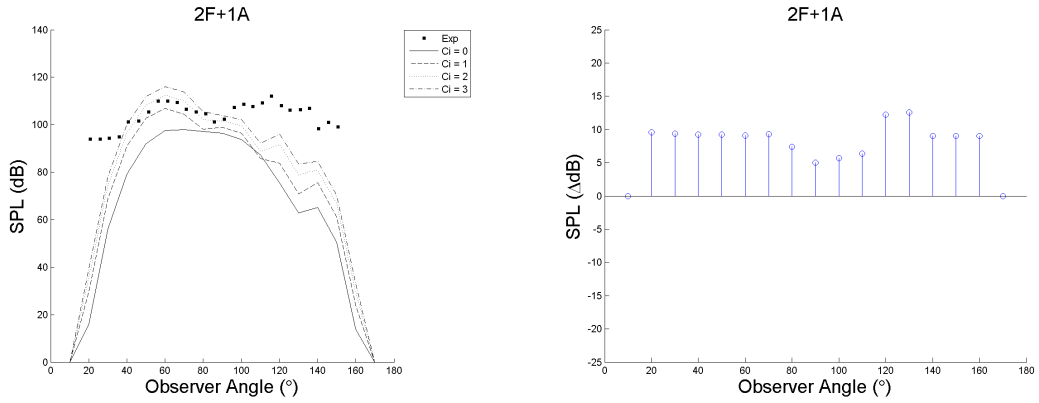

(a) Directivity (b) $Ci = 3$ - $Ci = 2$

FIGURE 5.3: Effect of Ci on 2F+1A interaction tone

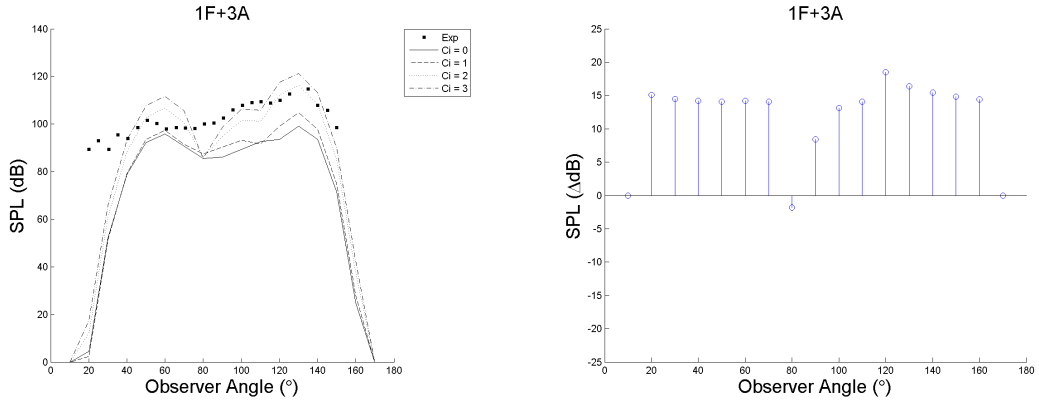

(a) Directivity (b) $Ci = 3$ - $Ci = 2$

FIGURE 5.4: Effect of Ci on 1F+3A interaction tone

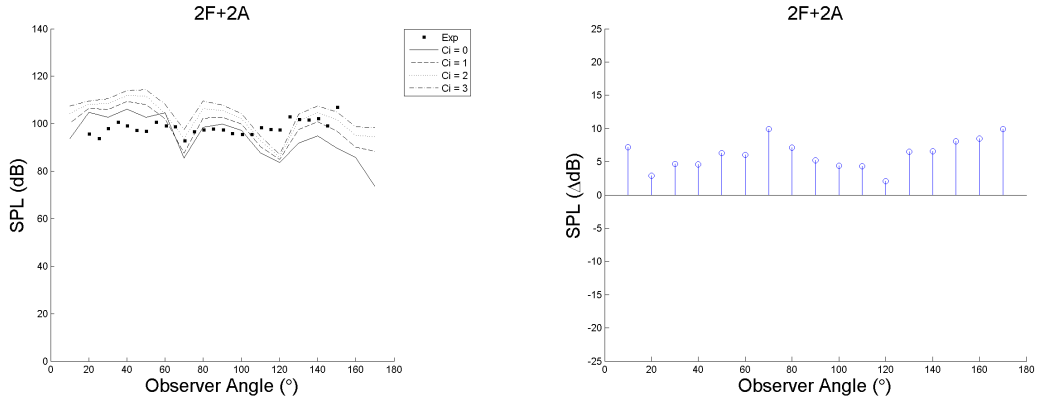

(a) Directivity (b) $Ci = 3$ - $Ci = 2$

FIGURE 5.5: Effect of Ci on 2F+2A interaction tone

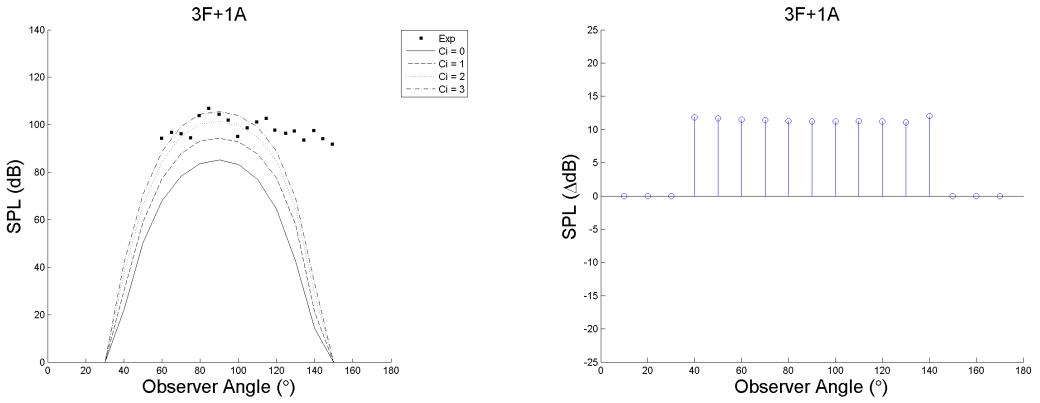

(a) Directivity

(b) $Ci = 3$ - $Ci = 2$

FIGURE 5.6: Effect of Ci on 3F+1A interaction tone

Excluding the $3F + 1A$ tone, observer angles in the range of 80 to 120 ° are the least effected by the changes in tip vortex circulation. The change in tip vortex circulation index value can contribute up to 22 dB in the extreme case, with differences in the order of 10 - 15 dB over a range of observer angles the norm within the study. This agrees well with the findings of[10]. The $2F + 1A$ interaction tone, the difference in agreement with measured experimental data improves with increasing circulation index - which suggests that a better vortex model could improve the overall CRPFAN aeroacoustic performance relative to experimental data.

5.1.2 Effect of tip vortex trajectory index value

The next input parameter to consider is the the tip vortex trajectory index, TVTI, again four values are used, the greater the value the greater the radial streamtube contraction and the lower the radial location of the tip vortex centre. Table 5.1 summarises the four values used and the non-dimensional radial location of tip vortex centre relative to the front rotor blade radius for each case.

TVTI	R_{Vortex}/R_{Blade}
2	0.89
1.5	0.92
1	0.95
0.5	0.97

TABLE 5.1: TVTI input sensitivity study parameters

The results for this study are shown in Figures 5.7 to 5.12 in the same format as for the circulation index sensitivity study. Here the residual stem plots show the difference

between the lowest vortex location with TVTI = 2 and the highest with TVTI = 0.5. The values of TVTI are in the range recommended in the CRPFAN user's manual[5].

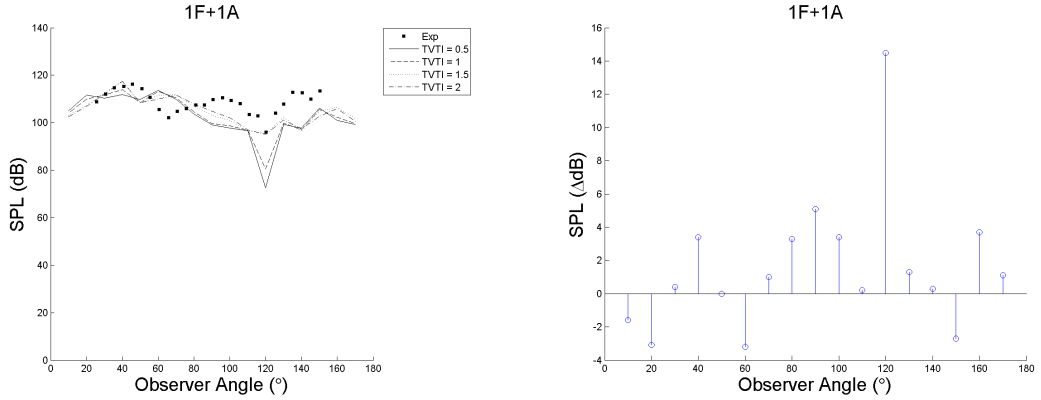

(a) Directivity (b) $TVTI = 2$ - $TVTI = 0.5$

FIGURE 5.7: Effect of TVTI on 1F+1A interaction tone

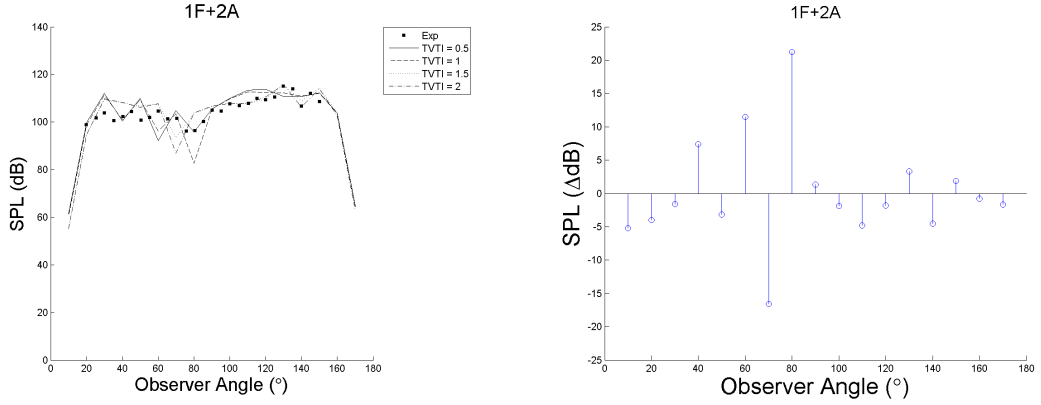

(a) Directivity (b) $TVTI = 2$ - $TVTI = 0.5$

FIGURE 5.8: Effect of TVTI on 1F+2A interaction tone

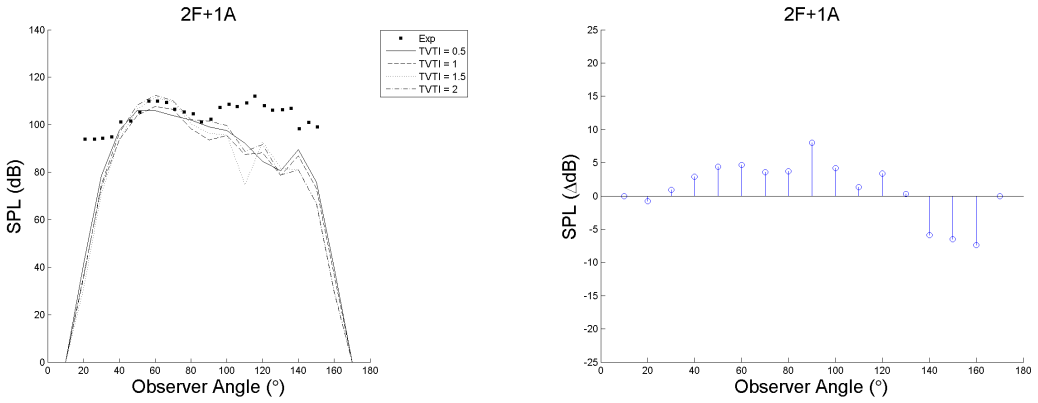

(a) Directivity (b) $TVTI = 2$ - $TVTI = 0.5$

FIGURE 5.9: Effect of TVTI on 2F+1A interaction tone

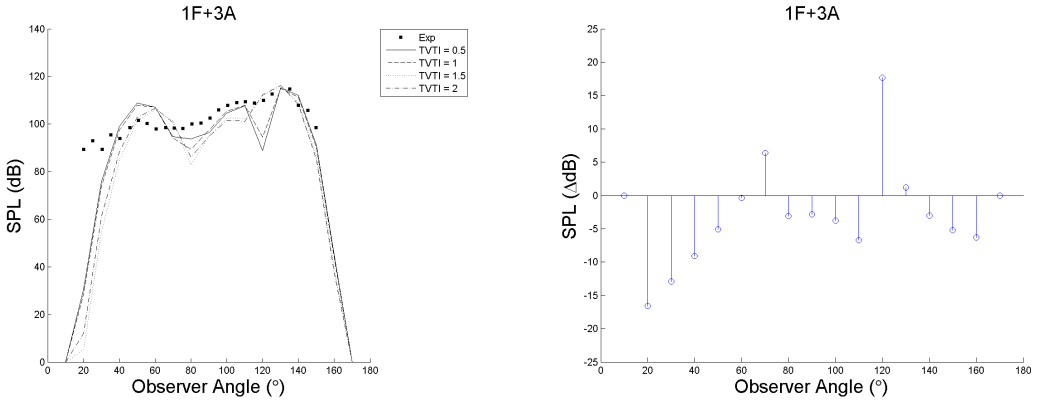

(a) Directivity (b) $TVTI = 2$ - $TVTI = 0.5$

FIGURE 5.10: Effect of TVTI on 1F+3A interaction tone

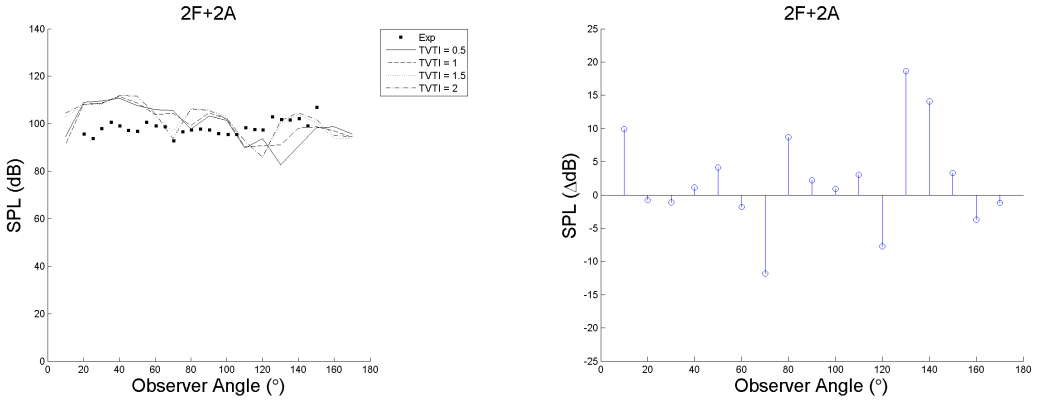

(a) Directivity (b) $TVTI = 2$ - $TVTI = 0.5$

FIGURE 5.11: Effect of TVTI on 2F+2A interaction tone

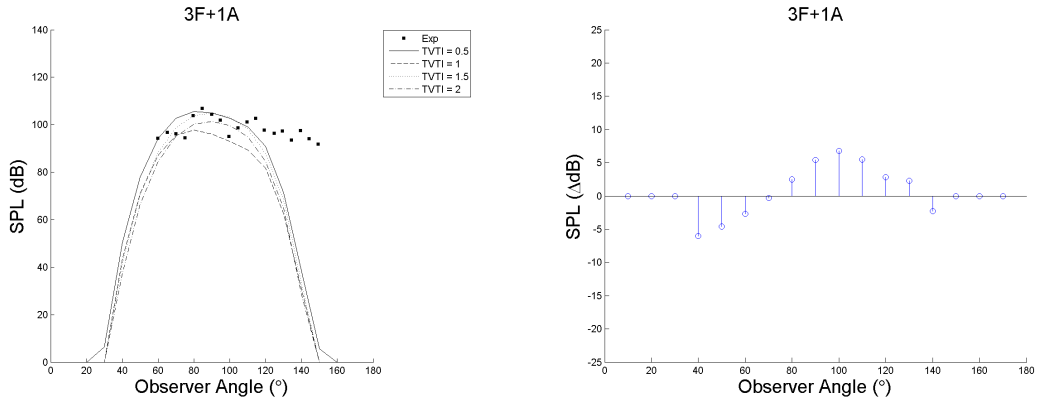

(a) Directivity

(b) $TVTI = 2$ - $TVTI = 0.5$

FIGURE 5.12: Effect of TVTI on 3F+1A interaction tone

The tip vortex trajectory location has an effect of up to 20 dBs, but mostly within the range of $\pm\, 0-10$ dB. The effect is a lot more omni-directional than changes in circulation index with no definitive trend present.

5.1.3 Effect of Input Vortex Parameters on Open Rotor Noise Conclusions

The results of the two sensitivity studies show that the interaction tones are highly sensitive to the value of the circulation parameter and tip vortex trajectory index - with 20 dB increases in interaction noise evident. If simulating a new case with no prior knowledge of which values to select, this can be expected to result in a large miscalculation of the interaction noise. The solution to this is to eliminate the need for either parameter and to calculate the tip vortex circulation and tip vortex radial location based on the the geometry and local physics. The development of this model and its aeroacoustic effect is presented in Chapter 7.

5.2 Effect of tip vortex parameters on interaction noise

Section 5.2 analyses what effect the individual tip vortex parameters such as the vortex core size, r_c, the maximum tangential velocity, $V_{\theta_{max}}$, and the vortex circulation, Γ_{vtx}, have on the interaction noise.

To individually analyse each parameter a Vatistas type tip vortex model is used instead of the Majjigi[10] tip vortex model. The form of the equation used to describe the tangential velocity distribution for the parametric studies is shown in Equation 6.14.

$$V_\theta = V_{\theta_{max}} 2^{1/n} \left\{ \frac{\bar{r}}{(1+\bar{r}^{2n})^{1/n}} \right\} \tag{5.1}$$

The tip vortex parameters are calculated using the standard CRPFAN correlations, only the description of the tangential velocity profile is changed.

5.2.1 Core size

The first parameter to consider is the vortex core size, to analyse this four core sizes are used 0.75, 1.55, 2.25 and 3 mm, where the datum core size calculated with the CRPFAN standard correlation is 1.55 mm for the conditions defined in Table 4.3. The source tangential velocity distribution in a vortex local coordinate system for these four cases are shown in Figure 5.13.

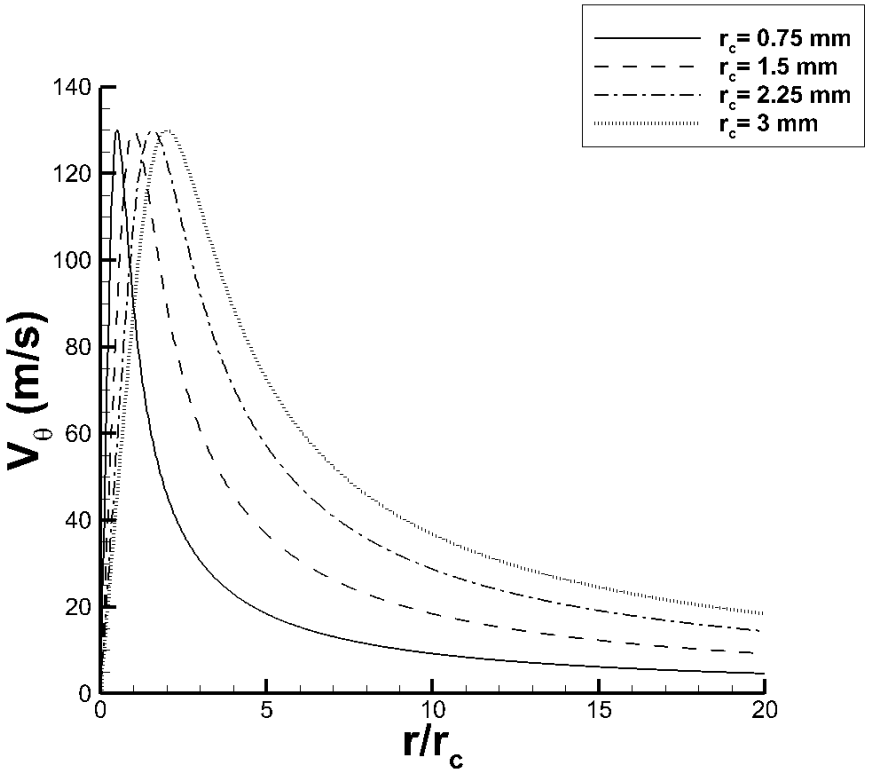

FIGURE 5.13: Tangential velocity profile input for core size sensitivity study in vortex local coordinate system

The maximum tangential velocity is the same for all cases, a shape factor, n, of 2 is used and the axial and radial tangential velocity are not included into the interaction noise calculation. An analytical tool used to asses how the input tangential velocity field acts as a disturbance field for the interaction noise is used here. The description of the method is included in the Section A.1 of the Appendix. Figure 5.14 shows the input disturbance field for the four vortex core sizes considered. Scaled engine order is the

number of periods the fundamental harmonic will occur in a full 360 ° sector divided by the number of front rotor blades. The y-axis is the radial location of the tip vortex and the contours are of Power Spectral Density (PSD) - which is derived from the FFT of the tangential velocity in a global coordinate system.

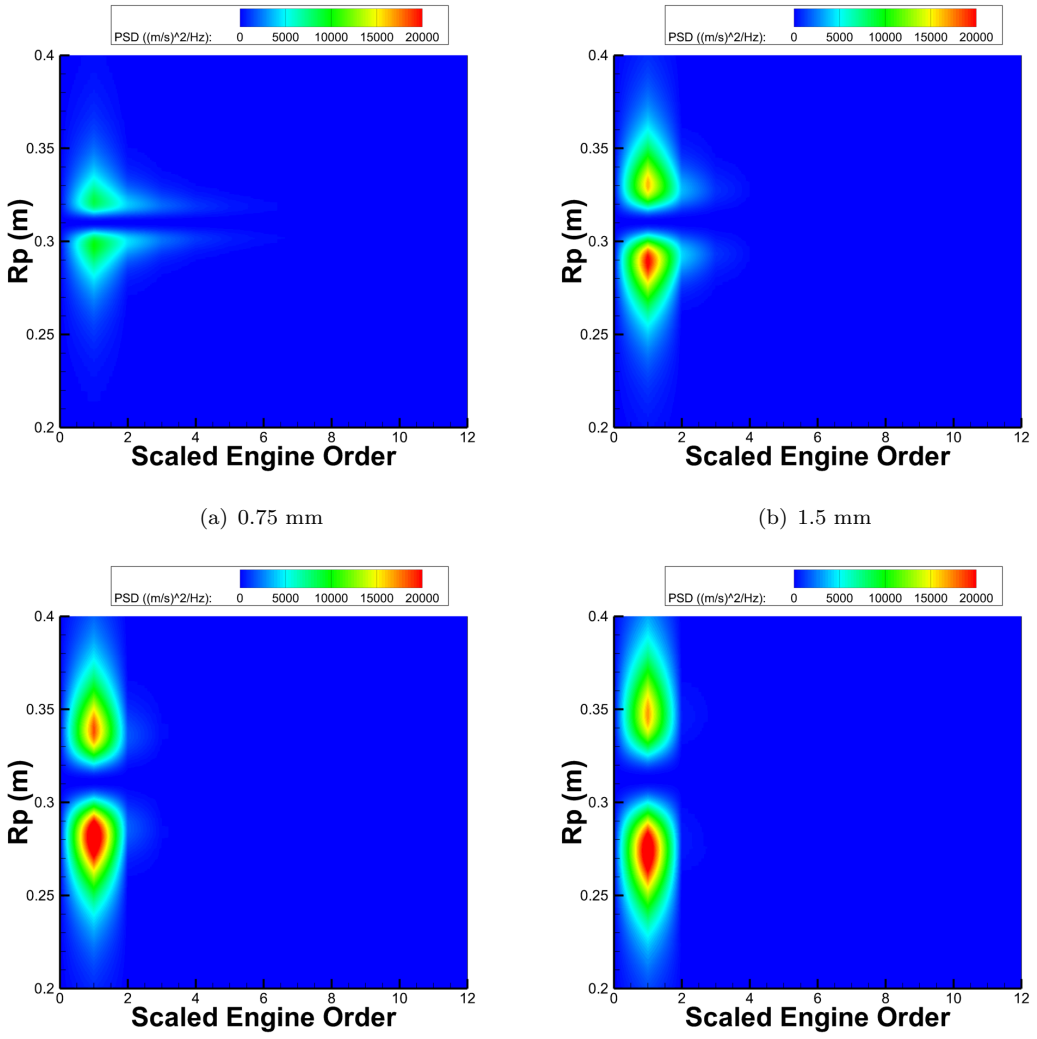

(a) 0.75 mm

(b) 1.5 mm

(c) 2.25 mm

(d) 3 mm

FIGURE 5.14: Effect of core size on input disturbance field

As the vortex core size increases so does the power spectral density at the lower harmonics (where lower harmonics correspond to a lower scaled engine order), but at the higher harmonics the disturbance field is reduced. This is because the broader input signal will have lower frequency content. Figure 5.15 is a map of the total noise spectrum for the four cases calculated in CRPFAN, where the tone number, M, is a non dimensional frequency referenced to the front rotor blade passing frequency. For n multiples of the front rotor BPF, and m of the rear rotor BPF.

$$M = (n+1)BPF_{front} + mBPF_{rear} \tag{5.2}$$

There are 170 tones, where 1-10 are the ten harmonics of the front rotor BPF and tones 11-20 are multiples of the rear rotor BPF. The first twenty tones should be independent of changes in the tip vortex parameters because they are dependant on the thickness and loading sources.

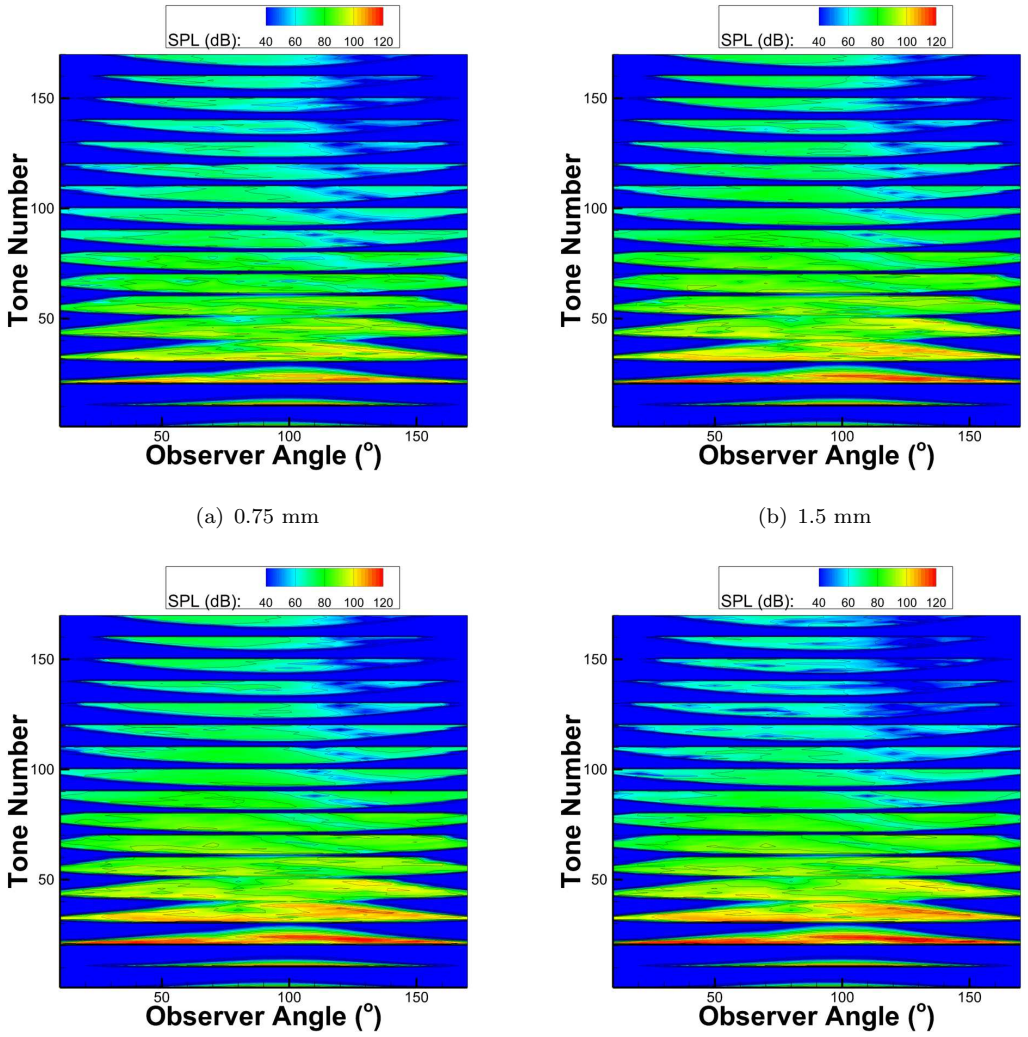

(a) 0.75 mm

(b) 1.5 mm

(c) 2.25 mm

(d) 3 mm

FIGURE 5.15: Effect of core size on interaction tones

The effect of increased core size is most notable at the lower frequency interaction tones, where the sound pressure level increases over most observer angles. It can also be noted that at the higher frequencies the noise actually decreases slightly, which is also indicated in Figure 5.14 as the result of a broadened FFT input.

The effect on the overall sound pressure level (OASPL) which is a 1/3rd octave metric of the sound pressure level is shown in Figure 5.16.

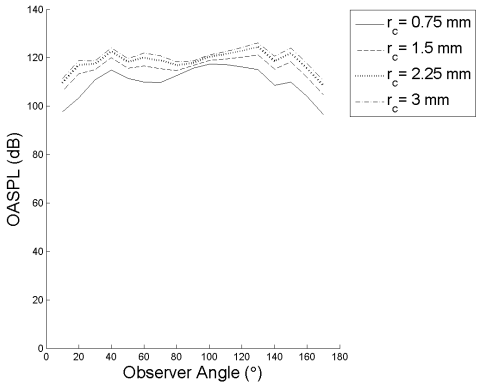

FIGURE 5.16: Effect of vortex core size on overall sound pressure level

As the core size increases as does the OASPL over all observer angles. The increase is non linear however, the biggest increase in OASPL is between the smallest core size of 0.75 mm to the datum case of 1.5 mm. The effect of the entire range of core sizes, i.e. from 0.75 to 3 mm is shown in Figure 5.17.

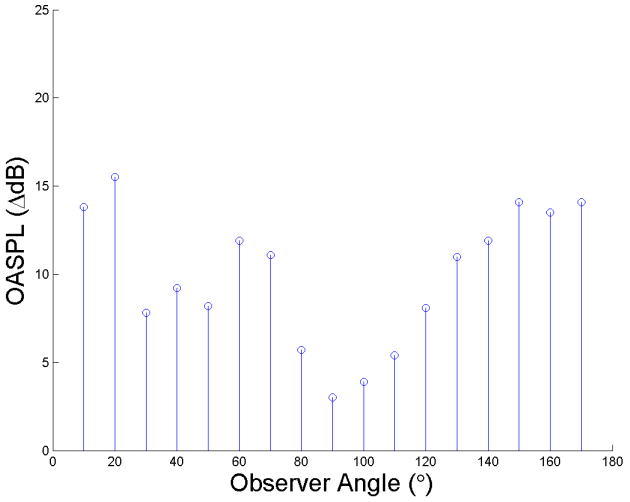

FIGURE 5.17: Effect of vortex core size on overall sound pressure residuals

The maximum effect of increasing the tip vortex core size from 0.75 to 3 mm is roughly 16 dB, and most noticeable at the extreme observer angles. The average increase in sound pressure level over all observer angles is 9 B.

5.2.2 Maximum tangential velocity

Here, the core size is kept constant but four peak tangential velocity profiles are considered, with magnitudes of 65, 130, 195 and 260 m/s. The input tangential velocity profiles are shown in Figure 5.18.

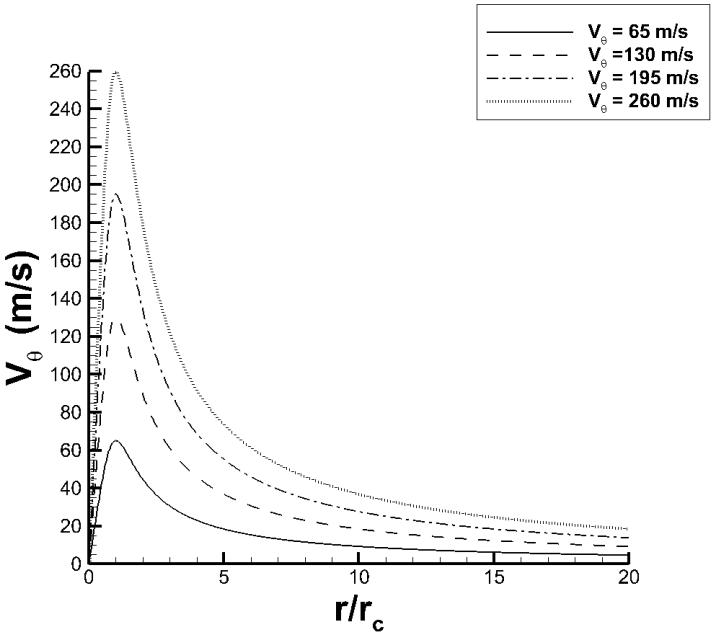

FIGURE 5.18: Input tangential velocity profiles for maximum tangential velocity effect

The input disturbance field for the four peak tangential velocities considered are shown in Figure 5.19.

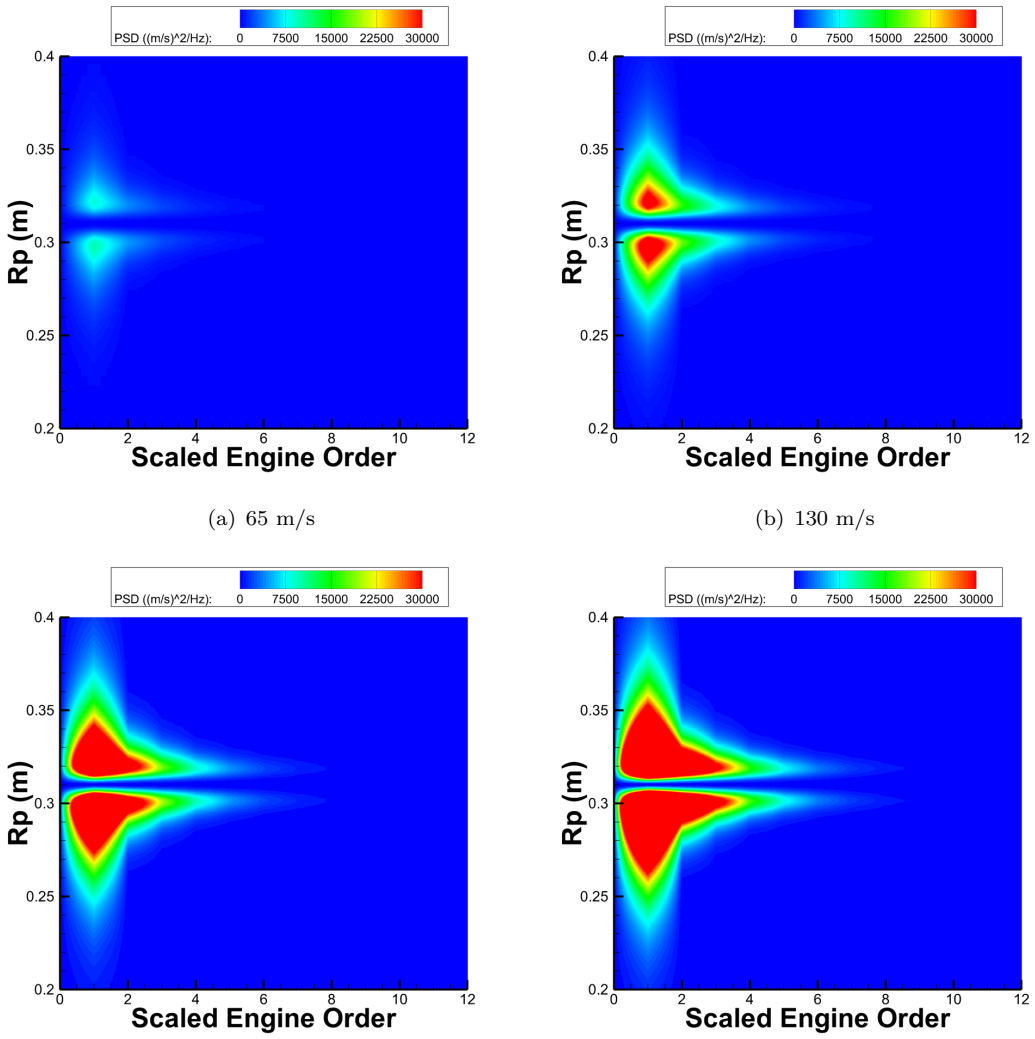

(a) 65 m/s

(b) 130 m/s

(c) 195 m/s

(d) 260 m/s

FIGURE 5.19: Input disturbance field for different maximum tangential velocities

The input disturbance field is sensitive to changes in the maximum tangential velocity across a range of frequencies. The sound pressure level map of Figure 5.20 shows the same trend where the interaction noise increases with increased maximum tangential velocity across the range of interaction tones.

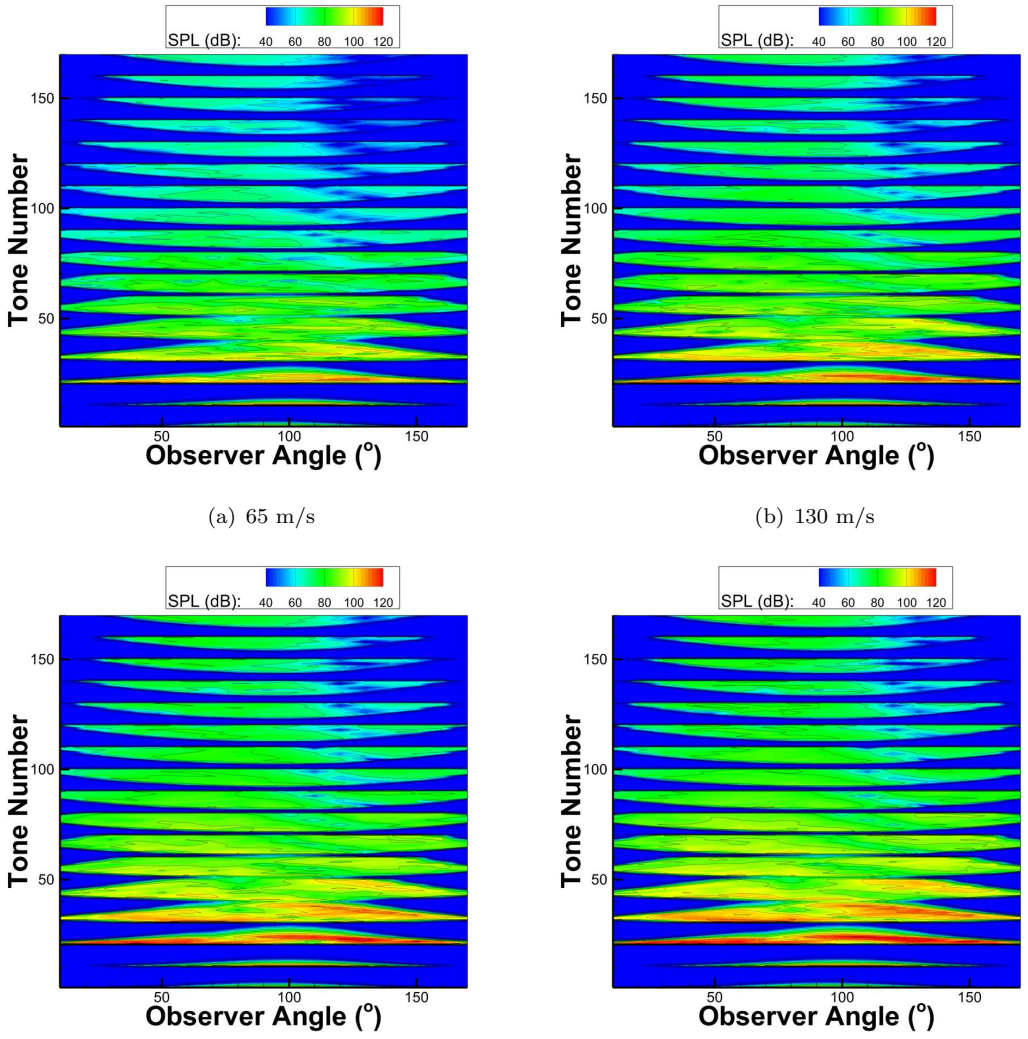

(a) 65 m/s

(b) 130 m/s

(c) 195 m/s

(d) 260 m/s

FIGURE 5.20: Sensitivity of interaction noise to maximum tangential velocity

The overall sound pressure level shows the same trends where the noise increases with tangential velocity over all observer angles as per Figure 5.21.

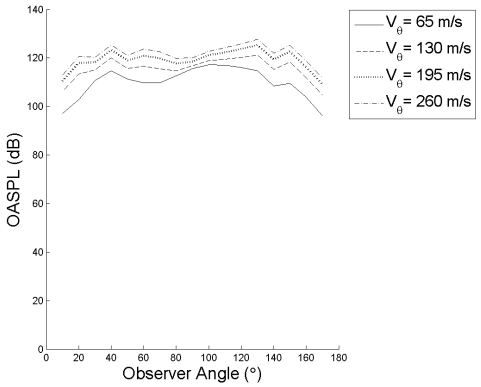

FIGURE 5.21: Effect of maximum tangential velocity magnitude on overall sound pressure level

Figure 5.22 shows the changes in OASPL between the lowest and highest tangential velocities' considered, which is from 65 to 260 m/s.

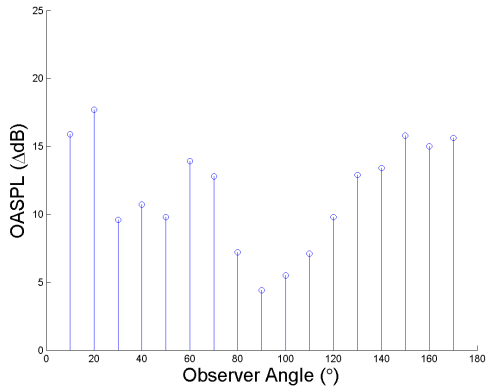

FIGURE 5.22: Overall sound pressure levels residuals for increased maximum tangential velocity

An increase in maximum tangential velocity from 65 to 260 m/s results in an increase of up to 18 dB, where the effect is also more noticeable at the more extreme observer angles.

5.2.3 Constant circulation different size and strength

The strength of a tip vortex is usually described by its circulation Γ_{vtx}, from Section 5.1.1, the noise is proportional to the circulation, however what happens if there are two vortices, with the same circulation but different velocity profiles?

The circulation for the two velocity profiles shown in Figure 5.23 are the same, case one has quarter the maximum tangential velocity but four times the core size of case two.

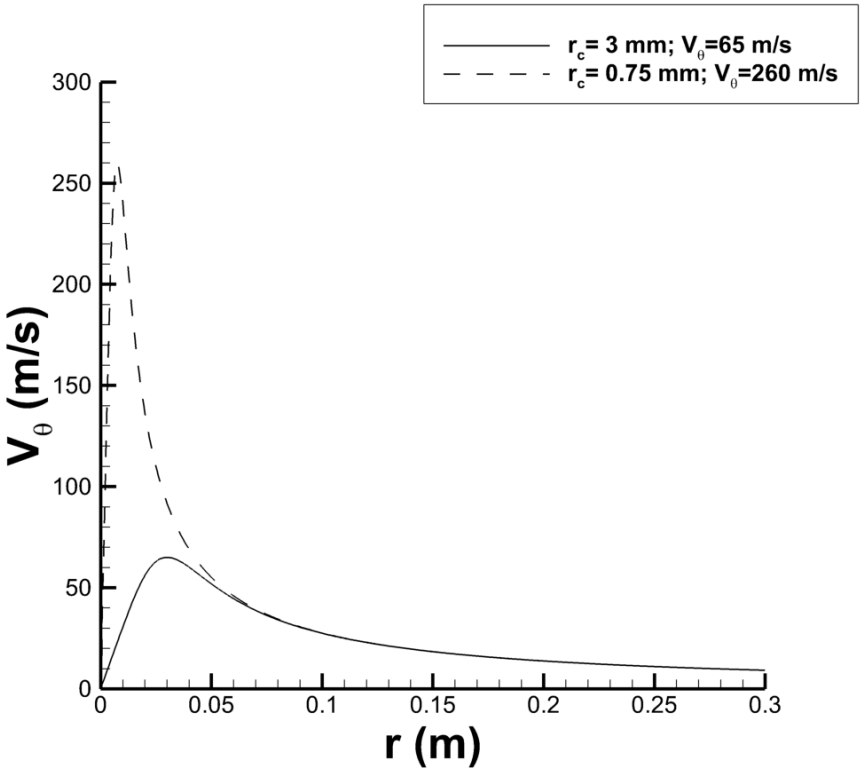

FIGURE 5.23: Input velocity profiles for constant circulation test case

Using the velocity profiles of Figure 5.23 as the input into the disturbance field model yields the following PSD maps:

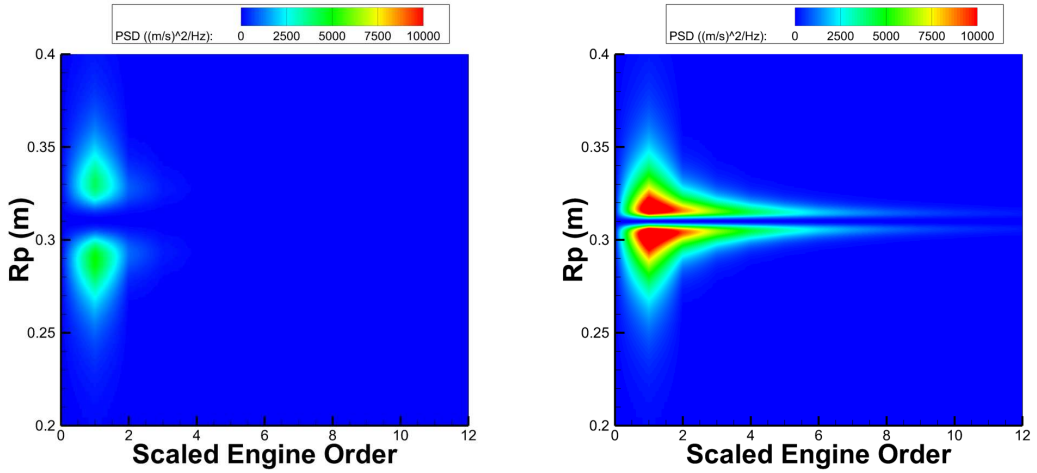

(a) Case 1 (b) Case 2

FIGURE 5.24: Input disturbance field map for two vortices with same circulation but different tangential velocity distribution

Case two produces a greater disturbance amplitude and over a wider spectrum, because the inlet tangential velocity profile is tending towards a Delta Dirac function which has

an infinite convolution of sine waves to compose the source input signal. The interaction noise also demonstrates this effect as shown in Figure 5.25 - especially at the higher frequency interaction tones.

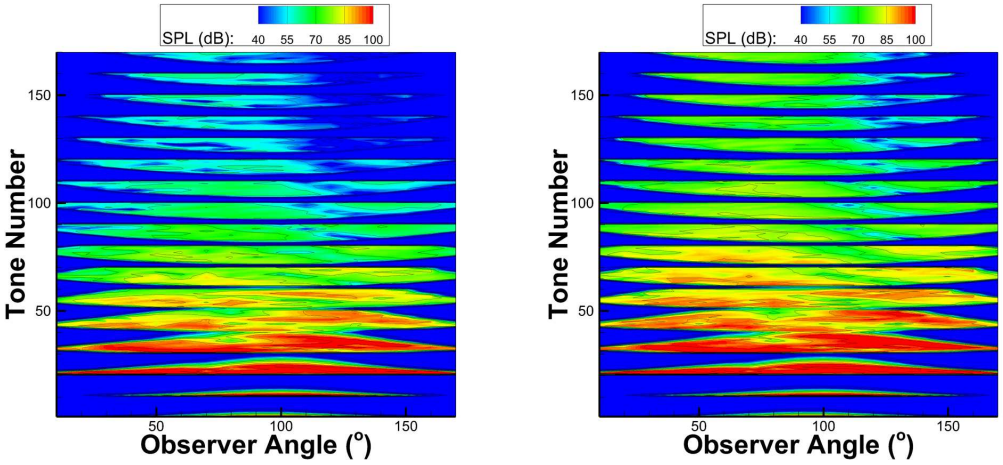

(a) Case 1 (b) Case 2

FIGURE 5.25: Interaction noise map for two vortices of same circulation but different tangential velocity profiles

The overall sound pressure level as a function of observer angle is shown in Figure 5.26 and the difference between the two cases in Figure 5.27.

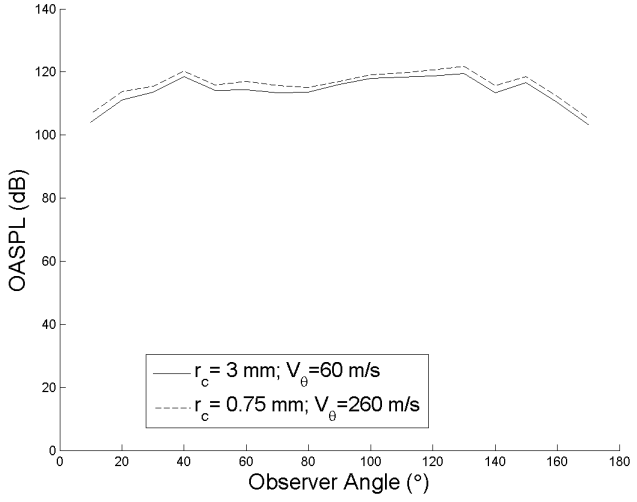

FIGURE 5.26: OASPL directivity for two vortices of same circulation but different tangential velocity profiles

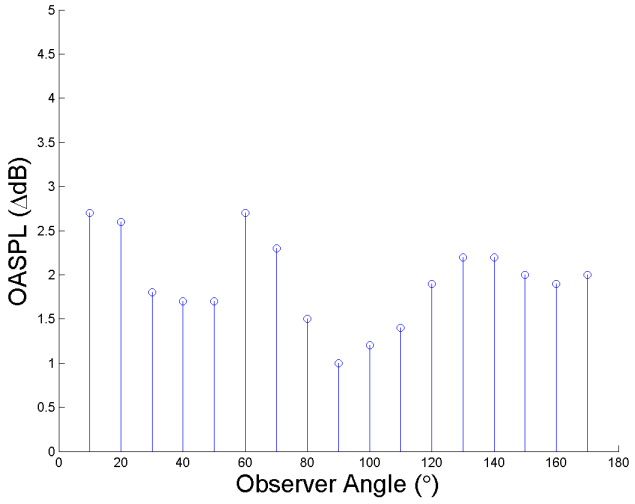

FIGURE 5.27: OASPL directivity residuals for two vortices of same circulation but different tangential velocity profiles

There is approximately a 3 dB difference in overall sound pressure level directivity for two vortices with same circulation but different swirl distribution. The vortex with the higher peak tangential velocity profile produces more interaction noise - with the effect most prominent at the higher frequency interaction tones.

5.2.4 Effect of tip vortex parameters on interaction noise conclusions

The tangential velocity distribution of the tip vortex has a big influence on the interaction noise, where, in general a vortex which has a greater core size or maximum tangential velocity will result in the generation of more interaction noise. The analysis also yields that purely defining a vortex by its circulation could be misleading - as the interaction noise spectrum can be different for two vortices with the same circulation. Therefore if looking to adjust the tip vortex to minimise tip vortex interaction noise a larger vortex with lower peak tangential velocity is desirable. However, the disadvantage to this method is that the increased radius of the tip vortex will mean more interaction of the vortex with the aft blade row depending on the level of aft blade cropping.

Chapter 6

CFD Methodology

Chapter 6 presents the approach and methodology of the CFD analysis within the project. Detailed within this Chapter include the method used to generate an appropriate grid, and the boundary conditions used to represent the physical model. This is followed by sensitivity studies to determine the correct level of spatial discretisation and domain extent. Also included is the validation of the model against measured experimental values for the thrust and power coefficients. The final part of Chapter 6 describes the methodology used to extract the relevant tip vortex properties used for further analyses.

Before starting any calculations a review of existing CFD work on open rotors was conducted. The work included[42],[7],[43],[44],[45],[46],[3],[47],[48] and[49]. As evident by the number of references reviewed, there is a lot of published CFD analysis on open rotors. However, none of these references specifically focussed on the development of correlations that can relate the key tip vortex parameters as a function of propeller geometry and operating conditions for integration into a preliminary design tool.

The application of CFD analysis in this project is focused on modelling the tip vortices generated by an open rotor over a range of flowfield conditions and the methodology used to obtain the flowfield information is described herein.

6.1 Geometry and key test cases

Section 6.1 outlines the key test cases and geometries used within the thesis to validate the models used.This is to inform the reader of which geometries and cases are used for the CFD analysis and why. There are four key geometries, the F7-A7, SR3, SR2 and a two bladed open rotor analogue.

6.1.1 F7-A7

The F7-A7 shown in Figure 6.1 is used for aeroacoustic verification and validation of CRPFAN, which was included in Chapter 4.

FIGURE 6.1: F7 A7 blade profiles

It is the blade combination used for the flight testing of the UDF and the acoustic measurements in the NASA Lewis 9 x 15 ft tunnel[5]. The test case parameters for which CRPFAN input data and acoustic measurements are known are summarised in Table 6.1.

Parameter	Value (Front, aft)
Geometry	F7-A7
Blade numbers	11 x 9
rpm	6800
Mo	0.2
C_P	0.9856, 1.1639
$\beta_{3/4}$ (°)	36.4,36.5
Wind Tunnel	NASA Lewis 9 x 15 ft
Sideline distance	4.5 ft

TABLE 6.1: CRPFAN validation test case operating conditions

This test case is used at two points within the project, firstly to aid the validation of CRPFAN as a credible aeroacoustic tool as presented in Chapter 4 and secondly as a comparison to quantify the relative effects of the different tip vortex modelling approaches and correlations suggested in the thesis. This would have also been a preferred choice to use within the CFD study, however, the exact geometry definition required for a 3D model is not open to the public domain.

6.1.2 SR3

The SR3 single rotation advanced propeller blade is used as an alternative to the F7. The SR3's characteristics relative to the F7, are shown in Table 6.2.

Characteristic	F7	SR3
Blade sweep angle (^{o})	33	45
Flight Mach No	0.72	0.8
Blade numbers	8	8
Advance ratio, J	2.8	3.1
Power Loading, SHP/D^2	55.5	37.5
Power Loading, SHP/A	85	50
Power Coefficient, C_P	2.66	1.695
Thrust Coefficient, C_T	0.81	0.45
Net Efficiency, η	0.849	0.812

TABLE 6.2: SR3 and F7 characteristics

A key difference between the two geometries is the blade tip sweep angle, the SR3 has 12 ^{o} more. Overall, the nominal design operating conditions between the two geometries are similar. An advantage of using the SR3 is the experimental data available[50]. The

measured data includes thrust and power measurements at take off representative Mach numbers. Take off is when the loading is greatest and the tip vortex interaction noise is most prominent[8].

The constituent 2-D airfoil sections which the SR3 is comprised are shown in Table 6.3, where the NACA airfoil definition as a function of non-dimensional radial location is presented. Towards the hub NACA 65 series are used and NACA 16 airfoils are used along the middle and upper span of the blade.

r/R	Airfoil Section	r/R	Airfoil Section
0.2375	NACA 65A–324	0.525	NACA 16-104
0.2625	NACA 65A–215	0.5625	NACA 16-103
0.2875	NACA 65A–111	0.6125	NACA 16-103
0.3125	NACA 65A–009	0.6625	NACA 16-202
0.3375	NACA 65A–007	0.7125	NACA 16-202
0.3625	NACA 65A–006	0.7625	NACA 16-202
0.3875	NACA 65A–006	0.8125	NACA 16-202
0.4125	NACA 65A–105	0.8625	NACA 16-202
0.4375	NACA 65A–105	0.9125	NACA 16-202
0.475	NACA 16-104	0.9625	NACA 16-202
0.5	NACA 16-104	1	NACA 16-202

TABLE 6.3: *SR3* sections

The 3D model of the highly swept SR3 propeller bladed used for CFD analysis is shown in Figure 6.2.

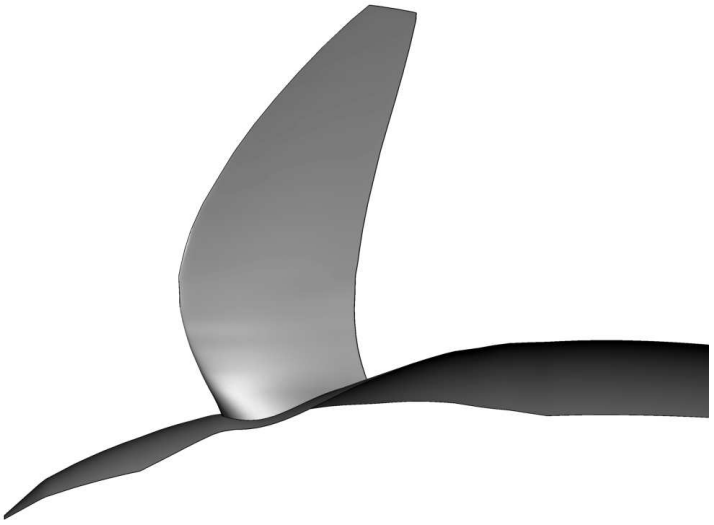

FIGURE 6.2: SR3 Propeller blade

6.1.3 SR3 test case

The SR3 was tested in the NASA Lewis 10 by 10 foot Supersonic Wind Tunnel by[50], this tunnel also has a facility to run subsonically from Mach 0.1 to 0.34, the key measurements taken were the thrust and torque using a rotating balance. Tip vortex interaction noise is dominant at low speed conditions[41] so the chosen test point as a validation case will be a Take off condition from the tests of[50] as summarised in Table 6.4.

Parameter	Value
Flight Mach No	0.2
Advance ratio, J	0.875
Power Coefficient, C_P	1
Thrust Coefficient, C_T	0.6274
Net Efficiency, η	0.54

TABLE 6.4: Validation case operating conditions

Where the advance ratio, J, is defined in Equation 6.1 which is a non-dimensional measure of how far the propeller advances in the direction of thrust per revolution.

$$J = \frac{V_0}{nD} \tag{6.1}$$

The power, C_P, and thrust, C_T, coefficients are defined in Equations 6.2 and 6.3 respectively.

$$C_P = \frac{P}{\rho n^3 D^5} \tag{6.2}$$

$$C_T = \frac{T}{\rho n^2 D^4} \tag{6.3}$$

The three parameters can all be combined to define the propeller efficiency, η, as shown in Equation 6.4.

$$\eta = J\frac{C_T}{C_P} \tag{6.4}$$

6.1.4 SR2 straight bladed propeller

To assess the effect of blade sweep on the open rotor aerodynamics and specifically the tip vortex formation and development, a second blade geometry was considered. The unswept SR2, which also uses NACA 65 and 16 airfoil sections, the constituent airfoils of the SR2 propeller blade as a function of radial location are shown in Table 6.5.

r/R	Airfoil Section	r/R	Airfoil Section
0.24	NACA 65A–120 1	0.64	NACA 16-103
0.28	NACA 65A–012 2	0.68	NACA 16-103
0.32	NACA 65A-009 3	0.72	NACA 16-103
0.36	NACA 65A-007 4	0.76	NACA 16-103
0.40	NACA 65A–106 5	0.80	NACA 16-102
0.44	NACA 65A–105 6	0.84	NACA 16-002
0.48	NACA-16-105 7	0.88	NACA 16-002
0.52	NACA-16-104 8	0.92	NACA 16-002
0.56	NACA-16-104 9	0.96	NACA 16-002
0.60	NACA 16-103 10	1.00	NACA 16-002

TABLE 6.5: *SR2* sections

The 3D model of the SR2 blade also used in the CFD study is shown in Figure 6.3.

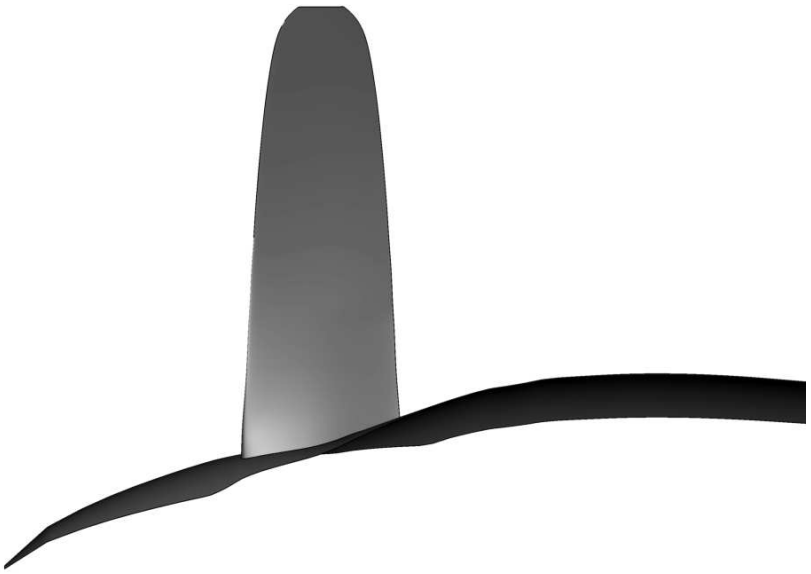

FIGURE 6.3: SR2 blade profile

The experiments of[50] used the SR2 alongside the SR3, which means both the SR3 and SR2 CFD can be validated against measurements for thrust and power and compared to each other at known operating points.

6.2 Two bladed open rotor analogue

The SR3 and SR2 CFD models can be validated for their key performance criteria using measured experimental data, however, appropriate and detailed measurements of the tip vortex characteristics shed from these blades are not openly available. To account for this a fourth geometry is introduced, which is a two bladed proper designed to be analogous to that of a modern open rotor concept. The blade profile for the two bladed analogue rotor is shown in Figure 6.4.

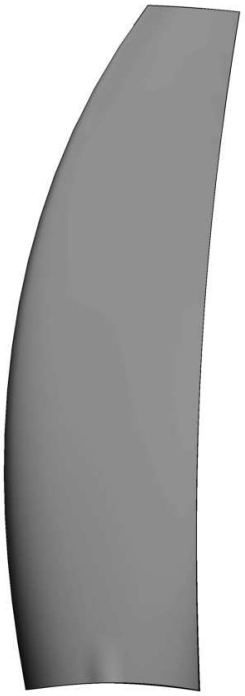

FIGURE 6.4: Two bladed open rotor analogue

Particle Image Velocimetry with focus on the tip vortex was conducted in-house using this geometry. Which is used to asses the CFD solver performance at calculating highly vortical flowfields.

6.2.1 Key test cases summary

- **F7-A7**: verification and validation of aeroacoustic method in CRPFAN and to quantitatively assess the effect of the different tip vortex modelling approaches
- **SR3 and SR2**:To generate CFD flowfield which tip vortex correlations are derived, validation date for thrust and power exists by [50]
- **Two bladed analagoue**: Tip vortex parameter comparison between CFD and in house PIV

6.3 Grid generation process

It is suggested that in order to capture the tip vortex with minimal dissipation that a fully structured mesh is used[51]. The vorticity contained in the tip vortex originates from the boundary layer, therefore to fully capture the vortex generation mechanism and wake roll up it is best to model the viscous sub layer instead of the use of wall functions. Based on these two factors a fully structured grid with a y^+ of one was sought due to the application of analysing tip vortex characteristics. This approach comes with a sacrifice in regards to the time required to obtain a good quality structured mesh relative to an unstructured one - especially for the twisted and typically swept geometry of an open rotor blade.

The initial approach was to solely use ICEM CFD to generate the grids. However, to obtain the satisfactory mesh quality a fairly complex blocking strategy was used in ICEM. It was felt that this approach was too in-efficient, especially if looking at different propeller geometries and setting angles.

With this in mind, a different more novel approach was considered. It involves using Turbogrid, a semi-automated mesh generator designed for turbomachinery applications. Turbogrid has the advantage of being able to generate good quality fully structured meshes with a quick turn around time, but a key disadvantage is that it is designed for ducted flows.

The maximum tip clearance allowable within Turbogrid is 50 % of the blade span, the domain size needs to be greater than this in the blade span-wise direction for a propeller. To account for this, ICEM is used to create an additional, non-conformal mesh that wraps around the one built in Turbogrid and extends out to the far-field conditions. This is illustrated in Figure 6.5 where the larger outer domain generated using ICEM remains stationary and the smaller inner domain containing the propeller rotates.

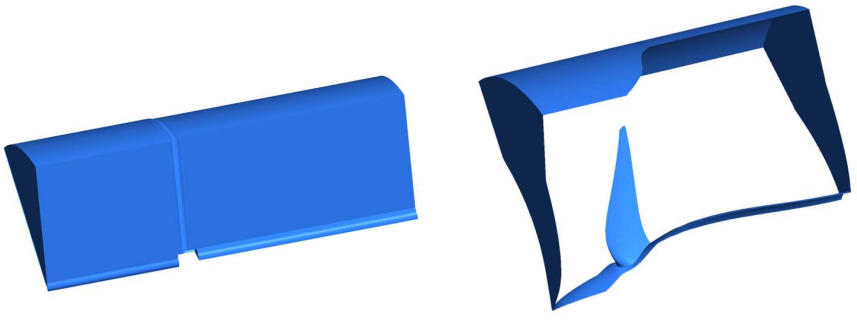

(a) Stationary domain (b) Rotational domain

FIGURE 6.5: Inner rotational and outer stationary domain which are combined

A 'H' type mesh topology is used around the blade as this gives good mesh quality at the trailing edge, a critical region for the tip vortices. The mesh used around the root of the blade at the hub region is shown in Figure 6.6 which illustrates the H type topology of the fully structured grid. In the radial direction roughly 150 nodes are used along the blade span (this varies for different mesh densities) with a close to uniform distribution. The mesh used for the swept SR3 blade, spinner and nacelle is shown in Figure 6.7. The same methodology was used for the SR2 propeller and images of its mesh are shown in Figures B.2 and B.3 of Appendix B accompanied by a close up view of the mesh on the SR3 as shown in Figure B.1.

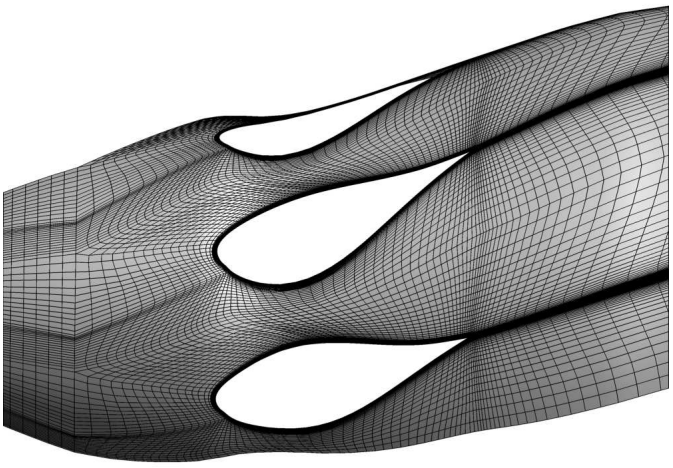

FIGURE 6.6: H type grid topology around blade

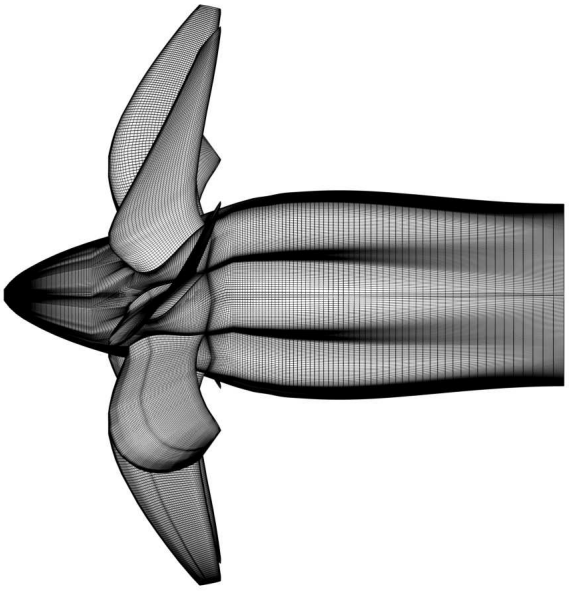

FIGURE 6.7: Structured mesh for SR3 blade

It was decided to include the spinner and nacelle as Zachariadis[42] found that it has an effect on the relative air angles on the lower portion of the blade due to its static pressure field. The current model clips the spinner at the front by 5 % of the maximum hub radius because Turbogrid cannot mesh a singularity. However, a sensitivity study to asses the effect of clipping the front part of the spinner on the thrust and power coefficients showed it had a negligible effect. The study extended the radial clipping to up to 20 %, therefore it is firmly felt that a 5 % clipping at the front of the spinner is an acceptable approach to use.

6.4 Boundary conditions

The mesh generated in Turbogrid which consists of the propeller, nacelle and spinner is set as a rotating domain while the outer domain generated in ICEM is stationary. The speed of rotation is equal to the revolutions per minute of the propeller for the operating point considered. The interface between rotating and stationary domains use a general grid interface (GGI) node interpolation scheme with a frozen rotor connection. The reason for a frozen rotor approach is because the calculations will all be steady steady state. A full data set of transient simulations was beyond the scope of the work.

The boundary conditions are shown in Figure 6.8 and described in accompanying Table 6.6. They consist a velocity inlet and pressure outlets with entrainment to allow for recirculating flow at the boundaries. The walls of the propeller hub and spinner have no slip conditions but the hub which extends towards and away from the rotational domain are set to free slip to avoid non-physical friction and boundary layer development. In the tangential direction, periodic interfaces are used with 1:1 node matching.

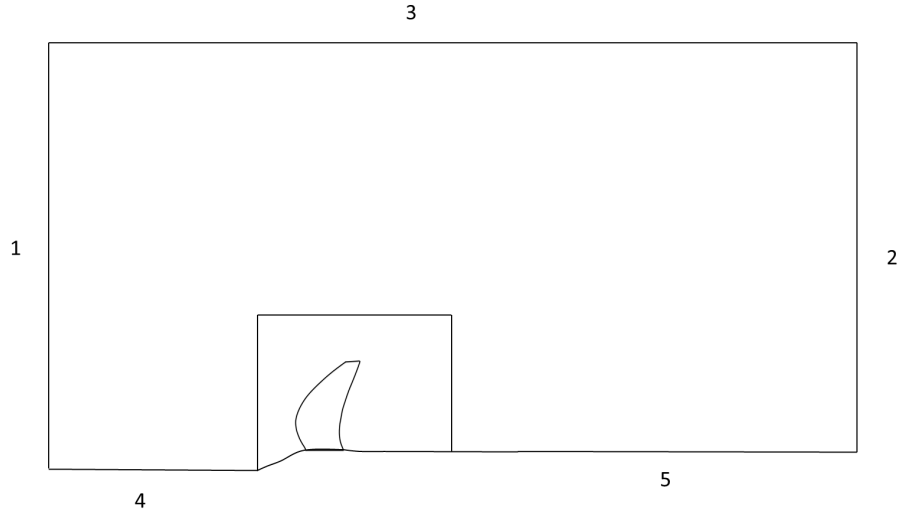

FIGURE 6.8: Boundary conditions schematic

Location	Boundary condition
Inlet (1)	Velocity inlet
Outlet (2)	Pressure outlet with entrainment
Radial outlet (3)	Pressure outlet with entrainment
Blade	No-slip wall
Spinner and nacelle	No-slip wall
Hub in and out (4) and (5)	Free slip (inviscid) wall

TABLE 6.6: Description of boundary conditions used in model

The static pressure is defined at the outlets, for a known Mach number at sea level conditions using the Isentropic relation of Equation 6.5. The energy equation is included in the calculations to account for thermal energy and viscous work terms, the static temperature defined as per Equation 6.6, the air is treated as an ideal gas.

$$\frac{P}{P_0} = (1 + \frac{\gamma - 1}{2} M^2)^{-\frac{\gamma}{\gamma - 1}} \tag{6.5}$$

$$\frac{T}{T_0} = (1 + \frac{\gamma - 1}{2} M^2)^{-1} \tag{6.6}$$

The model is solved using CFX version 12, using its higher order numerical advection scheme with a convergence target of $1e^{-4}$ for the residuals of mass continuity and the three Cartesian components of momentum. It uses a pressure based solver with an implicit numerical scheme, the calculations are steady state with automatic timestep setting.

6.5 Numerical implementation

6.5.1 Domain size sensitivity study

Selecting the correct domain size is important because too large of a domain will require more computational resources than necessary and too small of a domain will cause wave reflection problems, distorting the solution. The selected domain size used is shown in Figure 6.9. Smaller domain sizes were also tested and the difference in reported C_T and C_P were of order 1 %, therefore one of the smaller domain sizes could be used in future studies. The one shown in Figure 6.9 has been continued with as it gives time for the wake to dissipate and the mesh penalty is low where the flow gradients are small at the outer boundaries of the domain.

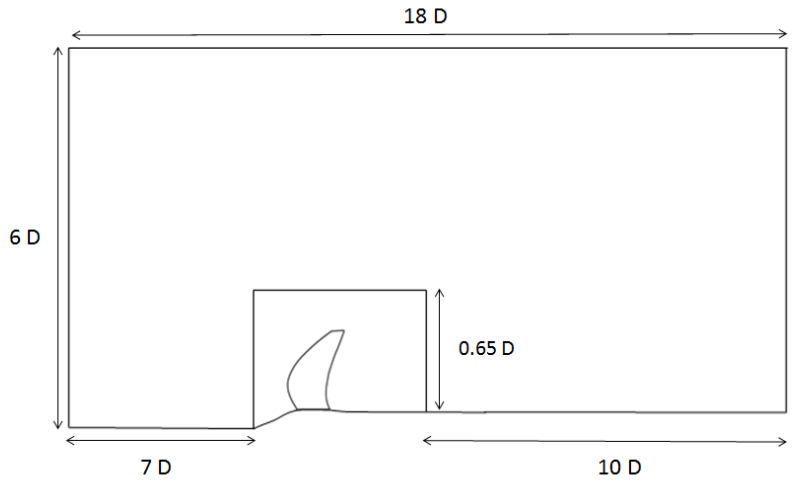

FIGURE 6.9: Domain size used for CFD models, where D is the blade diameter

6.5.2 Turbulence model sensitivity

With the domain size chosen, the next step was to chose an appropriate turbulence model. There were five models selected for the study, namely the Eddy Viscosity Transport Model (EVM), SST-$k-\omega$, SST-$k-\omega$ with the $\gamma-\theta$ transition model, SST-$k-\omega$ with a curvature correction term included and finally SST-$k-\omega$ with $\gamma-\theta$ and a curvature correction term. These were all compared to experimental data for C_T and C_P the results of which are shown in 6.7

Parameter	EVM	SST	SST-Trans	SST-CC	SST-Trans-CC	Exp
C_T	0.6141	0.6219	0.6147	0.6280	0.6216	0.627
C_P	1.0766	1.0858	1.066	1.0974	1.0791	1

TABLE 6.7: Turbulence model sensitivity study

The best overall turbulence model based on the comparison to measured C_T and C_P is the SST model with a transition model and curvature correction term. The use of a transition model has the additional advantage of capturing any laminar flow separation present and the curvature correction term helps prevent excessive numerical diffusion of the tip vortex due to the high strain components in the vortices. The SST model with transition and curvature correction is the model chosen for the mesh sensitivity study detailed next.

6.5.3 Mesh size sensitivity

This study assesses the mesh dependence of the calculations using a method based on Richardson's Extrapolation[52]. This method includes the use of three grid sizes, namely coarse, medium and fine where the medium grid has approximately half the spacing of the coarse mesh and the fine grid half the spacing of the medium mesh. The number of nodes used for each of three grids used are stated in Table 6.8, which gives a breakdown of the numbers in each of the two domains. Two, four and eight million nodes (rounded to the nearest million) were used in total for the coarse, medium and fine meshes resepctivley.

Grid	Coarse	Medium	Fine
ICEM	1070800	2024800	3986560
Turbogrid	1165652	2274822	4025843
Combined	2236452	4299622	8012403

TABLE 6.8: Mesh sensitivity study node numbers

Three CFD calculations were performed for each grid using the same conditions as defined in Table 6.4. For each grid size the thrust and power coefficients were calculated and their dependence on the grid size evaluated. Additional information of the methods used in the Richardson's Extrapolation are detailed in Section B.2 of Appendix B.

The defining metric from the study is that the asymptotic range (AR) should be close to one for the calculation to be sufficiently independent of grid size as to not compromise the credibility of the analysis. The key details from the Richardson's Extrapolation evaluated using C_P and C_T and the SR3 propeller grids are detailed in Table 6.9.

	Coarse (f_1)	Med (f_2)	Fine (f_3)	p	Zero (f_0)	ϵ_{12}	ϵ_{23}	GCI_{12}	GCI_{23}	AR
C_T	0.623	0.633	0.634	3.664	0.634	-0.016	-0.001	-0.004	-0.0003	1.016
C_P	1.081	1.097	1.099	3.511	1.099	-0.015	-0.001	-0.004	-0.0004	1.015

TABLE 6.9: Richardson Extrapolation

The reported values are within the asymptotic range, suggesting the grid size is acceptable. The reported values for C_P and C_T are shown plotted against the number of nodes in Figure 6.10. The graphs show two key things, firstly the monotonic variation of the coefficients as a function of grid size and secondly how the reported CFD values compare against the values measured in the NASA 10 by 10 ft supersonic wind tunnel. The difference with experimental data for C_T is of the order 1 % while C_P around 6 % for the case considered.

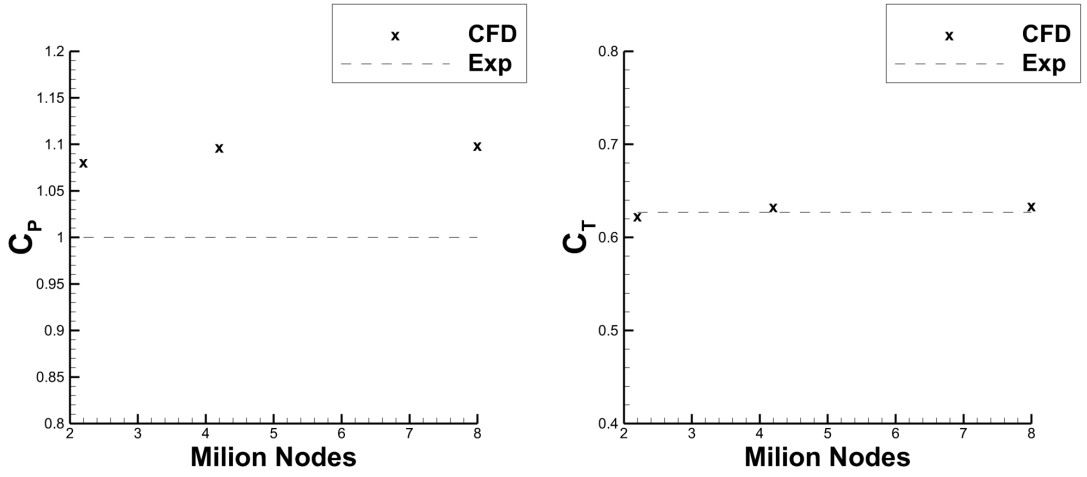

(a) C_P (b) C_T

FIGURE 6.10: Effect of spatial descritisation on C_P and C_T

Earlier in the Chapter two key requirements for the mesh were defined in order to best model the tip vortices, one was to use a fully structured grid which has been achieved and the second was to fully resolve the boundary layer on the blade. This is achieved for the SST turbulence model in CFX by having a y^+ of one and using the advanced wall treatment option. The y^+ distribution for the test case is shown in Figure 6.11, for both the pressure and suction side of the blade and the majority for both sides meet the requirement of a y^+ of one. However, above roughly 80 % blade span it is exceeded due to the higher relative velocity seen due to blade rotation, but the values are within the range of one to five - which is deemed acceptable for the advanced wall treatment method in CFX[53].

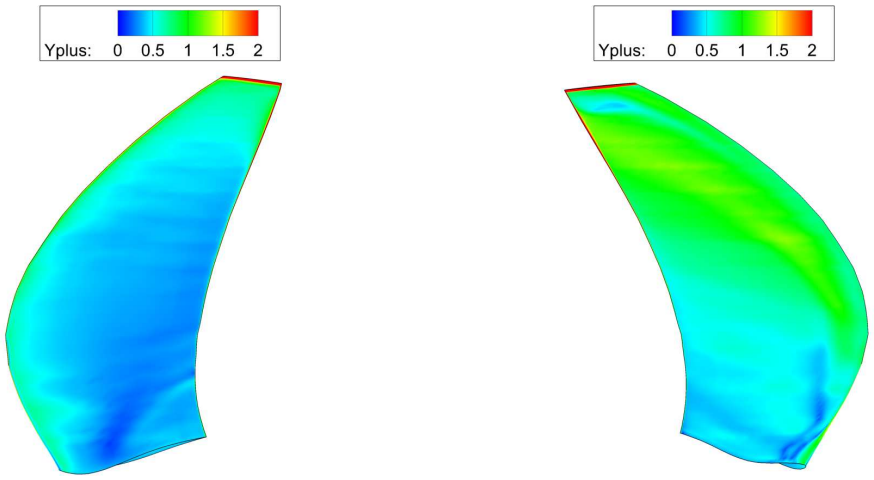

(a) Pressure Side (b) Suction Side

FIGURE 6.11: y^+ distribution along blade

6.6 Sensitivity study to operating parameters

This section describes a sensitivity study performed to analyse how the propeller aerodynamics change for different operating conditions. One of the reasons for this study is to verify that the CFD model makes physical sense when changing certain parameters and it also allows further comparisons to measured experimental data over a range of conditions. Additionally it is a good controlled way of obtaining a range of flowfield conditions which can be used later in the project when analysing and developing tip vortex correlations. Three key non-dimensional input parameters are used, namely, the advance ratio, J, blade reference pitch angle, β and freestream Mach number, M. The measured output parameters are C_P and C_T which are accompanied with measured data. The sensitivity of C_P to J, M and β is shown in Figure 6.12 and the sensitivity of C_T in Figure 6.13.

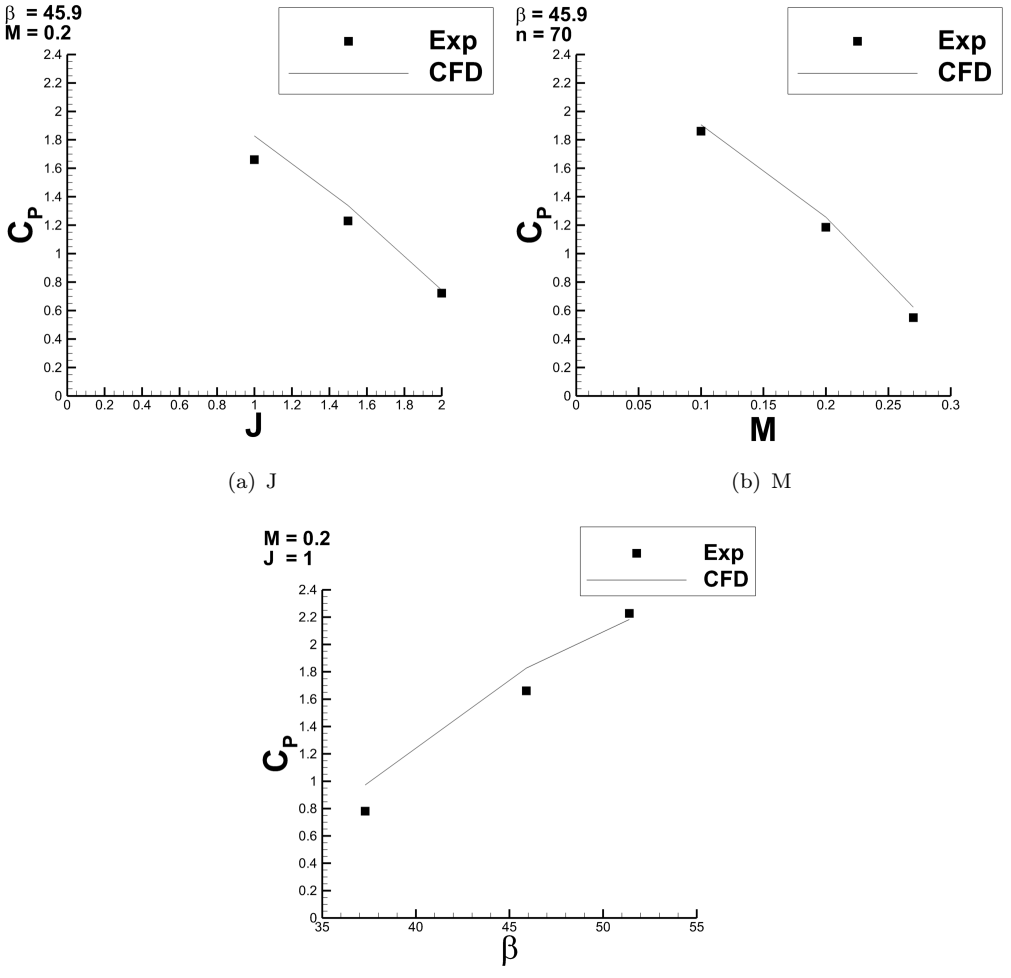

(a) J

(b) M

(c) β

FIGURE 6.12: Sensitivity of C_P to operating parameters

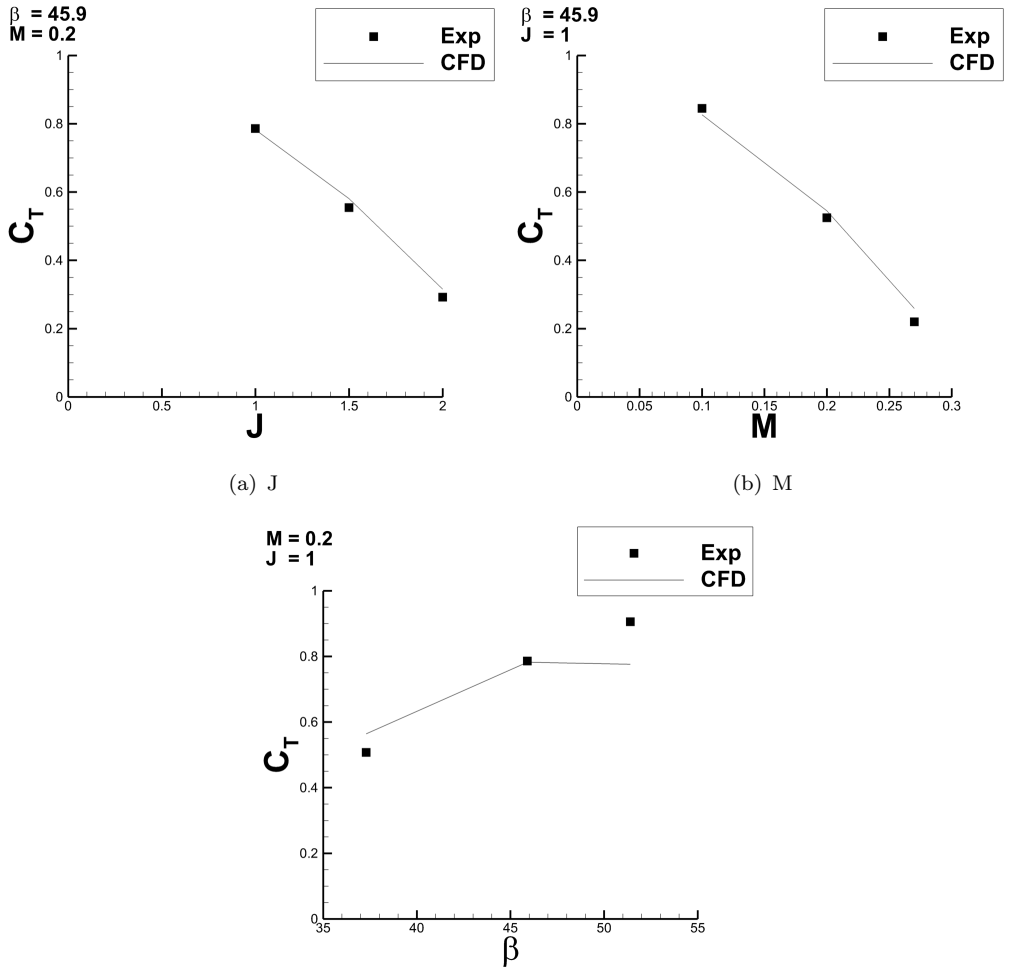

(a) J

(b) M

(c) β

FIGURE 6.13: Sensitivity of C_T to operating parameters

The trends observed in the sensitivity study make good physical sense and can be explained simply with velocity triangles which relate how the input parameters effect the incidence on to the propeller. Consider a blade element at an arbitrary radial location as illustrated in Figure 6.14.

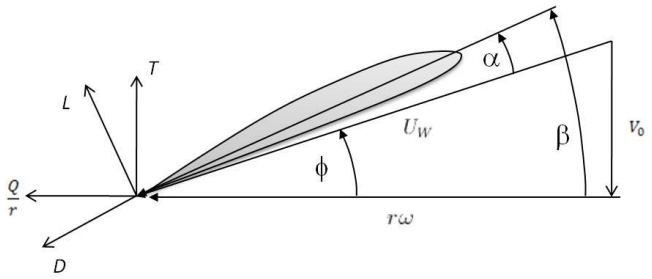

FIGURE 6.14: Blade forces acting on a blade element

The relative velocity, U_W i.e. the velocity the blade element will see is the vector sum of the freestream axial velocity, V_0 and the angular velocity at the radial location of interest as demonstrated in Equation 6.7. The relative air angle, α, calculated using Equation 6.8 and Equation 6.9.

$$U_W = (V_0^2 + r\omega^2)^{\frac{1}{2}} \tag{6.7}$$

$$\alpha = \beta - \phi \tag{6.8}$$

$$\phi = \tan^{-1}\left(\frac{V_0}{r\omega}\right) \tag{6.9}$$

The sectional lift dL and drag dD are defined by Equation 6.10 and Equation 6.11 with reference to Figure 6.14 and simple trigonometry.

$$dL = dT\cos(\phi) + dQ_F sin(\phi) \tag{6.10}$$

$$dD = dQ_F\cos(\phi) - dT sin(\phi) \tag{6.11}$$

These sectional values are integrated over the blade span to give the total lift and drag.

$$L = \int_{r=r_{hub}}^{r=r_{tip}} dL \tag{6.12}$$

$$D = \int_{r=r_{hub}}^{r=r_{tip}} dD \tag{6.13}$$

The lift and thrust is directly related to the relative air angle α, therefore an isolated increase in β, rpm, or freestream M at a constant speed of sound will result in an increase in α and hence lift, thrust and power. These were the trends observed from the CFD calculations which gives confidence in the method. The agreement with measured data is generally satisfactory too, the largest differences between CFD and experiment tend to occur where the incidence onto the blade is high and there is lots of flow separation.

6.6.1 SR2 model validation

As stated in Section 6.1 the straight bladed SR2 propeller is also used in this project. The SR3 was used as a test case to obtain the required CFD set-up. The same domain size, boundary conditions, turbulence model and grid strategy were used for the SR2 as the SR3. However, due to the possibility of different flowfield characteristics in the propeller near field a separate grid sensitivity study was conducted. The Richardson's Extrapolation method was used again and the results are shown in Table B.1 of Appendix B, an asymptotic range of one was achieved. To validate the SR2 model, measured data from NASA 10 by 10 ft supersonic wind tunnel were used again in the same experiment as for the SR3. The conditions for the test case are $M = 0.2$, $J = 1.1$ and $\beta = 45.8$ and the comparison between the CFD calculations and measured experimental data are shown in Table 6.10.

Parameter	CFD	Experiment	% Difference
C_T	0.632	0.642	1.63
C_P	1.457	1.428	-2.02

TABLE 6.10: Comparison between measured experimental data and CFD for integrated blade forces on SR2 propeller blade

The comparison to measured data is good with differences of 1.63 % and -2.02 % for C_T and C_P respectively - which is better than the SR3 validation case. With a model for the SR3 and SR2 successfully validated and grid independent the next step is to analyse the tip vortex characteristics.

6.7 Vortex Postprocessing Methodology

Section 6.7 describes the method used to extract the relevant tip vortex parameters from the CFD flowfield. The parameters of interest include the tip vortex circulation, Γ_{vtx}, core size, r_c, maximum tangential velocity, $V_{\theta_{max}}$ and the Vatistas shape factor, n. These are the parameters of interest because they allow a complete description of the tangential velocity as a function of radial distance from the vortex centre if using a Vatistas type vortex model. The ability to reconstruct the tangential velocity distribution from a set of key parameters lends well to the development of the desired tip vortex correlations. It should be noted that in the overall scope of the project the requirement extends to knowledge of the radial location of the tip vortex centre and out of plane velocity in the direction of the vortex path, the methodology of these two requirements are described separately in Sections 7.6 and 7.5 resepctivley.

The parameters are evaluated at eight separate axial locations downstream from the propeller pitch change axis, normalised at 1,1.25,1.5,1.75,2,2.25,2.5 and 3 chords downstream, where the chord is the reference chord at 75 % blade span. The first step is creating a slice at one of the designated eight axial locations normal to the engine axis and calculating the vorticity normal to this plane in the thrust acting direction. The first step is shown in Figure 6.15 which shows contours of stream wise vorticity in a plane taken normal to the engine axis.

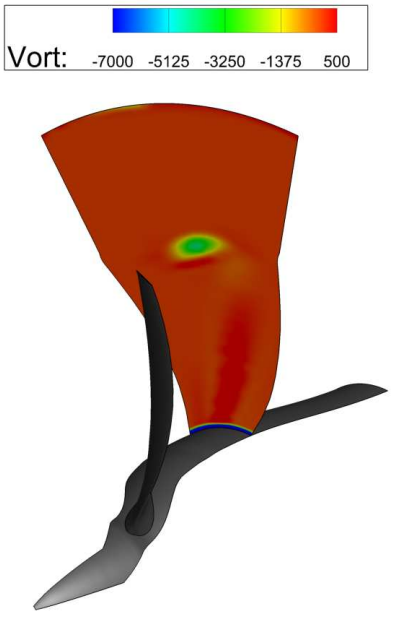

FIGURE 6.15: Contours of vorticity downstream of propeller in plane normal to engine axis

Inspection of Figure 6.15 reveals the elliptical distribution of the tip vortex, this is because the tip vortex will travel in a helicoidal path as it leaves the propeller trailing

edge and a slice normal to the engine axis will result in an oblique plane across the vortex which displays an elliptical spatial distribution of vorticity. This concept is analysed in more depth in Section 7.3. To obtain a circular and axisymmetric vortex, a slice normal to vortex path is required, this is done using Tecplot and details of the coordinate transformation including the coordinate system, assumptions and equations are included in Section B.3 of Appendix B. To get coordinates of the tip vortex centre, the magnitude of vorticity is used. The process is automated and the method of avoiding erroneous locations for the tip vortex centre is to isolate the region of the tip vortex by neglecting the radial locations close to the hub boundary layer for example.

Once in a plane normal to the vortex path with the tip vortex centre identified a new fully structured circular zone is created onto which the vorticity and velocity components are linearly interpolated onto. Figure 6.16 provides an isometric view of the structured circular zone normal to the tip vortex path and its orientation relative to the original planar slice normal to the engine axis. Also included in Figure 6.16 is a view of the vortex in the cross plane normal to the tip vortex with a more circular and symmetric vortex relative to Figure 6.15.

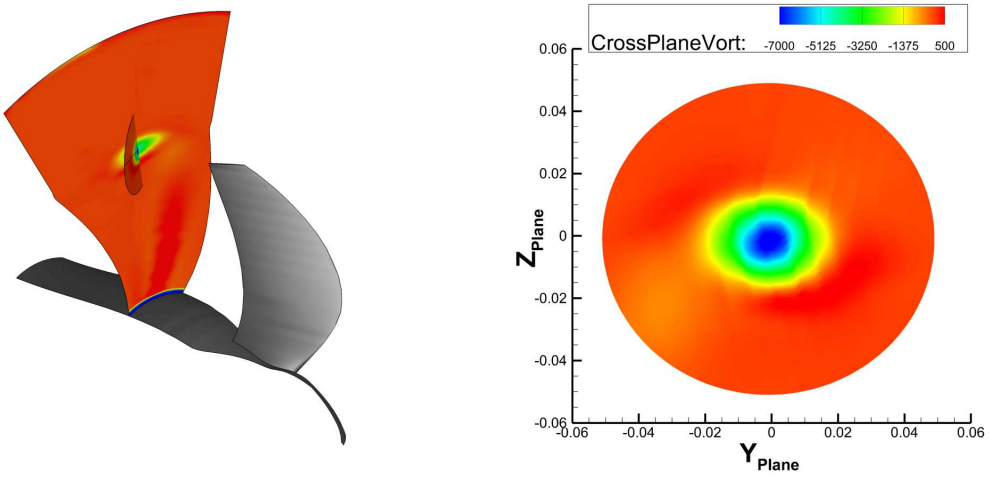

(a) Isometric (b) Normal

FIGURE 6.16: Orientation of vortex cross plane circular zone relative to engine normal plane and close up view of vortex in 2D cross-plane normal to tip vortex path

One of the advantages of using a fully structured zone of defined radii is to simplify the circumferential averaging of the tangential velocity. The circumferential averaging assumes the vortex is axisymmetric, however this may not be the case for high loading cases where the leading edge vortex (LEV) and tip vortex mix together. After the averaging process a radial distribution of tangential velocity is obtained, where the centre of the vortex corresponds to the centre of the structured zone at r=r(o) in a polar coordinate system.

To obtain a Vatistas vortex model a regression fit using Equation 6.14 is applied where the value of the shape factor, n, is iterated through from one to four. The shape factor which results in a regression with the lowest variance between the circumferentially averaged tangential velocity distribution from the CFD and the analytical description defined in Equation 6.14 is selected. Section 7.4 , evaluates the relative merit of using a integer or real number for the shape factor, n.

$$V_\theta = V_{\theta_{max}} 2^{1/n} \left\{ \frac{\bar{r}}{(1+\bar{r}^{2n})^{1/n}} \right\} \tag{6.14}$$

The tangential velocity distribution and chosen shape factor can be used to obtain the vortex core size and maximum tangential velocity, this leaves the tip vortex circulation as the remaining tip vortex parameter to determine. The circulation is calculated using a scalar integration of the vorticity normal to the cross plane in a Cartesian coordinate system in two dimensions. This method is then repeated for different downstream locations and flowfield operating points, for both the SR2 and SR3.

6.8 CFD Methodology summary

The CFD model consists two fully structured domains combined with a general grid interface with a steady-state frozen rotor frame. An SST turbulence model with transition and curvature correction term was selected along with an appropriate grid and domain size based on comparison to measured experimental data for both the SR2 and SR3 propeller blades. A method is also defined to extract the key tip vortex parameters to be used for further analyses.

Chapter 7

Analysis and Synthesis

Chapter 7 presents suggested approaches to model the tip vortex of an open rotor for interaction noise prediction tools. Table 7.1 summarises the tip vortex model sensitivity considered and the methodology tool required to investigate its effect. Cases one and two compare the vortex model which describes the tangential velocity distribution, the comparison is between the baseline model in CRPFAN and the proposed Vatistas type model. Case three analyses the effect of the number of streamlines used in an aeroacoustic tool such as CRPFAN. Case four examines the spatial orientation of the vortex as seen by the aft blade.

The first four cases do not require detailed CFD flowfield information and are presented first. The next step is to analyse the flowfield from the CFD calculations for both the SR2 and SR3 propellers to understand how the different loading conditions effect the tip vortex profile. Case five uses the CFD flowfield to model the axial component of the tip vortex and determine the aeroacoustic effect of its inclusion. Case six presents a revised model of the tip vortex trajectory model through the use of CFD and the aeroacoustic effect of using the revised model compared the baseline trajectory model in CRPFAN. Case seven then develops revised correlations for the key tip vortex parameters with an aeroacoustic comparison between the revised correlations and baseline correlations included. The final model analyses the aeroacoustic effect of including all the suggested vortex modelling approaches and which one aspect has the most significant aeroacoustic effect.

The final part of the analysis investigates the aeroacoustic effect of using different aerodynamic methodologies to generate the source lift distribution as an input to CRPFAN. The three methodologies include the use of a Blade Element Momentum Theory (BEMT) strip theory code, a Theodorson Method strip theory code and the third methodology is the use of CFD.

Case	Sensitivity	Methodology Tool Required
One	Baseline Model	CRPFAN
Two	Vatistas Model	CRPFAN
Three	Number of Streamlines	CRPFAN
Four	Spatial Orientation	CRPFAN
Five	Vortex Axial Velocity Component	CRPFAN & CFD
Six	Trajectory Model	CRPFAN & CFD
Seven	Core Size and Tangential Velocity Correlations	CRPFAN & CFD
Eight	State of the Art Model	CRPFAN & CFD

TABLE 7.1: Aeroacoustic Synthesis Matrix

7.1 Effect of Tip Vortex Model

Section 7.1 examines the aeroacoustic effect of replacing the baseline vortex model in CRPFAN developed by Majjigi et al[10] with a Vatistas type vortex model. The Majjigi model uses a linear body of solid rotation inside the vortex core and an irrotational model outside of the core. This is similar to a Rankine type vortex model and both include a discontinuity at the edge of the core where the model transitions from rotational to irrotational type flow. This discontinuity is a mathematical construct and not a physical mechanism which is expected in a tip vortex. The Vatistas type vortex model does not contain all its vorticity inside the vortex core and there is no such discontinuity in the radial tangential velocity distribution.

An additional version of CRPFAN was created which replaced the baseline Majjigi vortex model with the suggested Vatistas type vortex model. The CROR operating conditions used in the test case to determine the aeroacoustic effect of replacing the vortex model are described in Table 7.2 and are the same used for the CRPFAN validation study of Section 4.3 in Chapter 4.

Parameter	Value
Geometry	F7-A7
Blade numbers	11 x 9
rpm	6800
Mo	0.2
C_P	0.9856, 1.1639
$\beta_{3/4}$ (°)	36.4,36.5
Sideline distance	4.5 ft

TABLE 7.2: CRPFAN validation test case operating conditions

The only difference between the cases presented are the type of vortex model used, the inputs to CRPFAN for both cases are identical. The empirical correlations to predict the tip vortex parameters are therefore also the same. The tangential velocity distribution in a local coordinate system as a function of radial distance for a given maximum tangential velocity, $V_{\theta_{max}}$, and vortex core size, r_c, for both a Vatistas type vortex model with a shape factor, n, of two and the baseline CRPFAN vortex model developed by Majjigi et al are shown in Figure 7.1. Note the lack of discontinuity and smoother distribution of V_θ around the core of the vortex at r/r_c of one.

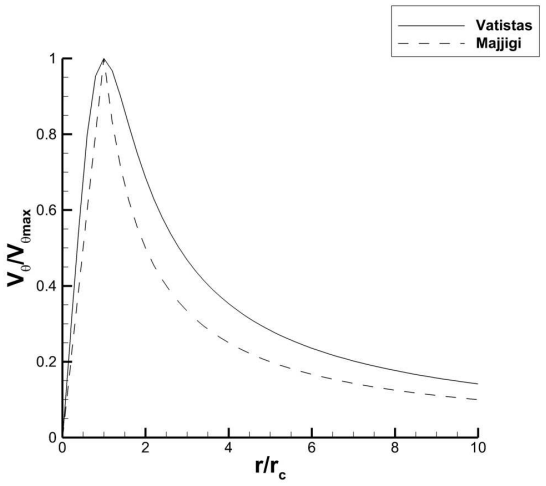

FIGURE 7.1: Majjigi and Vatistas vortex model comparison

The sound pressure level contour map for both cases are shown in Figure 7.2 accompanied with the difference in OAPL at each observer angle. The difference is calculated using Majjigi minus Vatistas. The inclusion of a Vatistas type vortex model generates more interaction noise overall with up to 4 dB 80 ° from the plane of rotation at 170 °. Additional directivity responses for six interaction tones are included in Section D.1.1 of Appendix D. The Vatistas vortex model generates more interaction noise overall because of its greater magnitude of V_θ, particularly outside of the vortex core, where V_θ does not decrease as rapidly as a function of radial distance compared to Majjigi model.

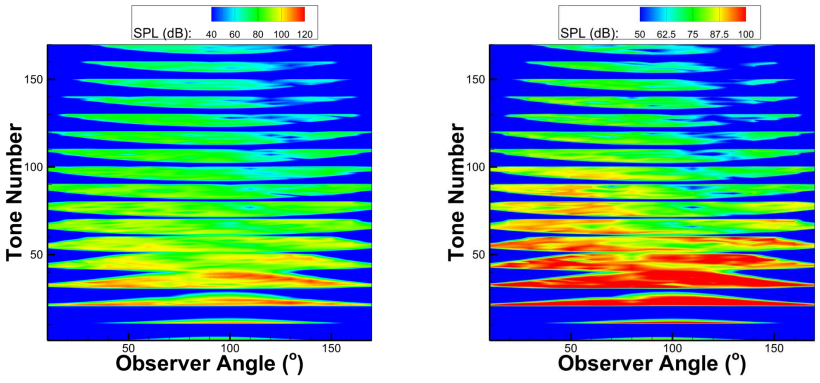

(a) Majjigi (b) Vatistas

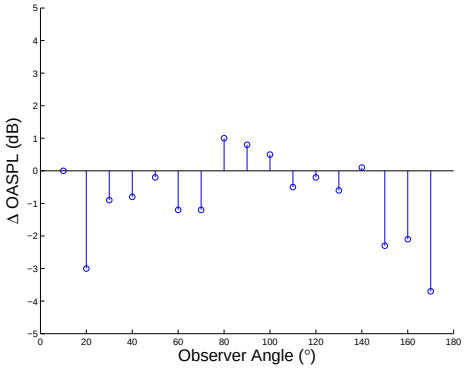

(c) OASPL Residuals

FIGURE 7.2: Effect of Majjigi and Vatistas vortex model on interaction noise

7.1.1 Effect of tip vortex model conclusions

It is suggested to use a Vatistas type tip vortex model instead of the baseline model used in CRPFAN. A Vatistas type vortex model was integrated into CRPFAN and the interaction noise compared to the amount generated when the baseline is used under the same operating and test conditions. It was found that the Vatistas type vortex model increased the interaction noise relative to the baseline model by up to 4 dB. The difference in interaction noise signifies the importance of the tip vortex model but the reason the Vatistas vortex model is recommended is because it more appropriately represents the tip vortex physics without the inclusion of discontinuities.

7.2 Effect of streamline discretisation

Section 7.2 is only pertinent to aeroacoustic codes which utilise a strip theory approach, such as CRPFAN. The default operation of CRPFAN uses ten streamlines from hub to tip of the blade. If only ten streamlines are used the vortex core could be radially located in-between two streamlines. This lack of fidelity could result in a miscalculation of the disturbance field generated by the tip vortex.

In order to test the significance of only using ten streamlines a simple sensitivity study was conducted. In the study the tip vortex radial location was adjusted by 0.6 % four times for two versions of CRPFAN. Version one uses CRPFAN in its default mode with ten streamlines. Version two uses a modified version of CRPFAN which uses a parabolic interpolation routine to increase the number of streamlines to 51. There are four vortex radial locations used in total which are described in Table 7.3. Location 1 was chosen so that the edge of the vortex core is placed at the same location as a streamline in the lower fidelity version. For the three subsequent locations the vortex is moving away from that streamline.

Case	R_V/R_T
Location 1	0.9090
Location 2	0.9035
Location 3	0.8981
Location 4	0.8926

TABLE 7.3: Vortex radial locations used to assess significance of strip theory code streamline descritisation

Apart from the adjustment of the tip vortex centre location, the operating conditions and inputs are the same as defined in Table 7.2, which are the same as the previous Case where the effect of the tip vortex profile was assessed.

With reference to Figure 7.3, sub figure (a) is the OASPL directivity for each location calculated with the datum version of CRPFAN with ten streamlines and sub figure (c) is the difference in OASPL levels between Location 1 and Location 4 for this case. As the tip vortex core moves away from the streamline some of the disturbance field information of the vortex is not resolved and the interaction noise decreases as a result. The maximum difference between Location 1 and 2 is up to 9 dB with the lower fidelity version of CRPFAN. Sub figures (d) and (d) are the equivalent but with a version of CRPFAN with 51 streamlines. The maximum difference between Location 1 and 2 is then reduced to 1 dB. The effect of the vortex location is heavily reduced because the disturbance field is less sensitive to the location of the vortex relative to a streamline because the required disturbance field information is captured for every vortex location

unlike the previous case with a lower fidelity version of CRPFAN. It is expected for there to be a difference in interaction noise between Location 1 and Location 4 due to the change in the blade to blade azimuthal angle as the vortex radial location moves inboard. However this effect should be small for the same operating conditions and tip vortex modelling approach.

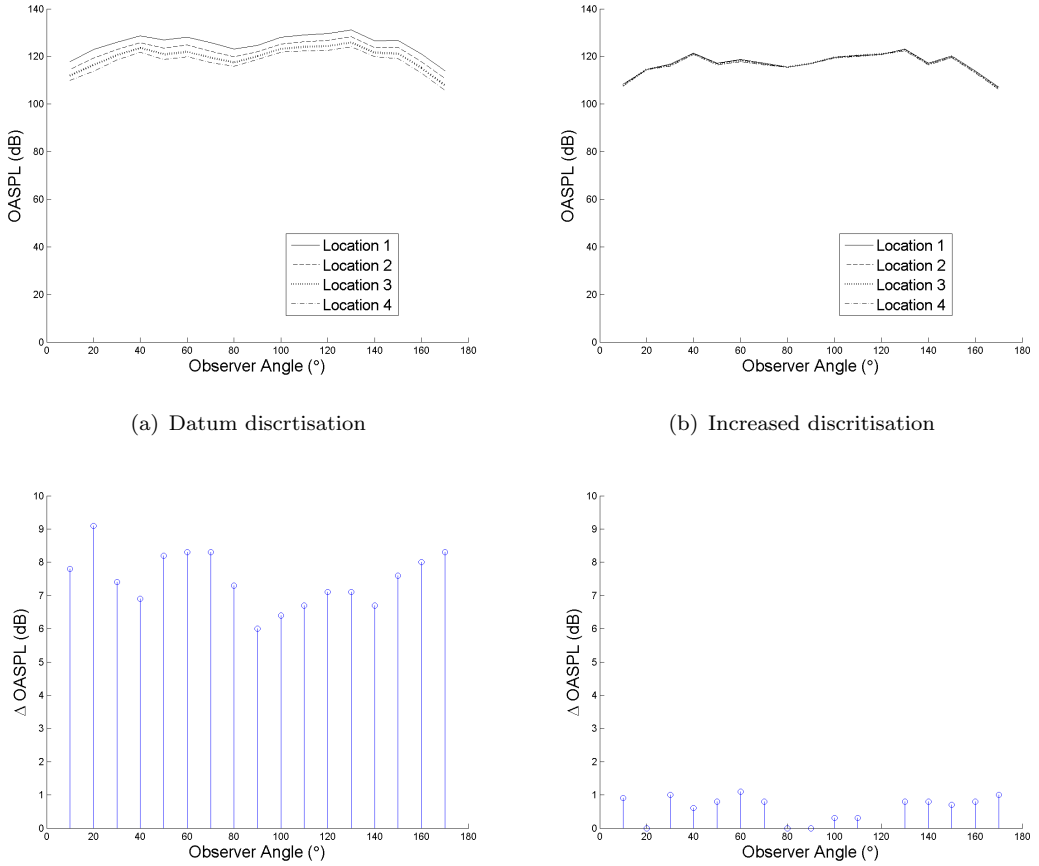

(a) Datum discrtisation

(b) Increased discritisation

(c) Datum discrtisation

(d) Increased discritisation

FIGURE 7.3: Effect of CRPFAN spatial discretisation on OASPL directivity

The results show that the interaction noise is sensitive to the location of the vortex relative to a strip theory streamline point. The closer the vortex core to a streamline point, the more noise produced, this is because the interaction noise will be calculated based on a disturbance of greater magnitude. The next step is to determine the aeroacoustic effect of using the increased version of CRPFAN using its datum vortex location calculated using the baseline CRPFAN trajectory model for the test case defined in Table 7.2. The CRPFAN baseline model calculates the tip vortex centre radial local, R_V at R_V/RT of 0.945. The aeroacoustic effect of this test case is shown in Figure 7.4 with the sound pressure level contour map for both the datum and increased descritisation version of CRPFAN. The overall sound pressure levels are the datum minus increased

descritisation and additional directivity responses for six interaction tones for Case 3 are included in Section D.1.2 of Appendix D.

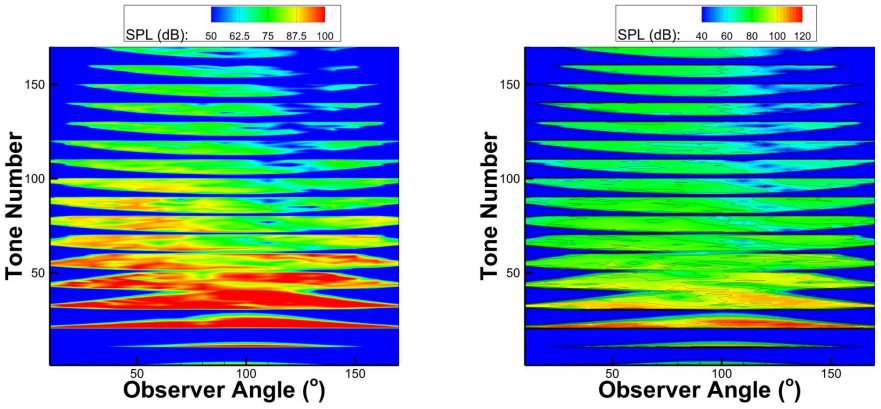

(a) Datum

(b) Increased

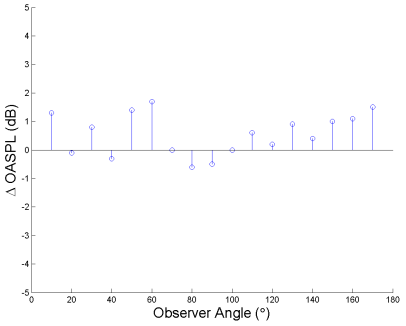

(c) OASPL Residuals

FIGURE 7.4: Comparison between datum and increased streamline discretisation within CRPFAN

The effect of aeroacoustic effect of using the version of CRPFAN with increased streamlines is very low with the differences mostly within 1 dB. However, this is for one test and this discrepancy changes for different vortex radial locations. It is suggested all aeroacoustic prediction codes pay attention to this number of streamlines if using a strip theory approach.

7.2.1 Effect of streamline discretisation conclusions

Ten streamlines is too few to fully capture the disturbance field generated by the vortex. An interpolation routine is used in CRPFAN to increase the number of streamlines. The increased number of streamlines reduces the uncertainty of how much of the vortex disturbance field is being captured.

7.3 Effect of vortex spatial orientation

Section 7.3 examines the aeroacoustic impact of the the spatial orientation of the tip vortex. Spatial orientation is the shape of the front rotor tip vortex as seen by the aft blade as they interact. With reference to Figure 7.5, the aft blade cuts through the vortex at an oblique angle, this means that it will see an elliptic shaped vortex and not a circular shaped vortex.

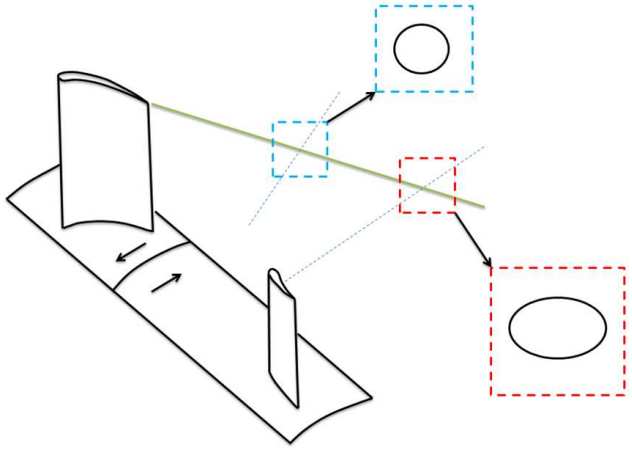

FIGURE 7.5: Illustration of normal and oblique interaction

In order to investigate the importance of the vortex spatial orientation (i.e. circular or elliptic) the flow field was constructed for both cases using the method described in Appendix A. The harmonic content of the vortex disturbance field was calculated and the two different scenarios integrated into CRPFAN to measure its aeroacoustic effect. A key assumption used to model the elliptical vortex is that the vortex itself is columnar in its axial direction. This means that only the spatial distribution of the velocity field will be changed and not the magnitude of the velocity vectors. Therefore the maximum tangential velocity will be the same but the distribution will be different for a circular and elliptical vortex.

The vortex flowfield was constructed to be representative of the one that will be seen by an aft rotor for the conditions in the aeroacoustic test case defined in Table 7.2. A sector with an angle of 40 ° was created to represent one of the sectors of the nine aft blades in the azimuthal direction. Figure 7.6 shows the flowfield for the two cases, with a circular vortex on the left and elliptical on the right. Where, $\Gamma = 1.2m^2/s$, $r_c = 1.5$ mm, $V_{\theta max}$ =130 m/s and $n = 2$ these parameters are the ones calculated using the correlations in CRPFAN with the same input as used for the validation test case. The shape factor is assumed to be 2. The spatial distribution for the oblique case is

representative of a front blade setting angle of 30 ° at the upper portion of the blade. This is fairly typical for take-off and high loading conditions. The relative width of the oblique vortex will be the inverse cosine of this angle, and therefore twice as wide as the circular vortex for this case.

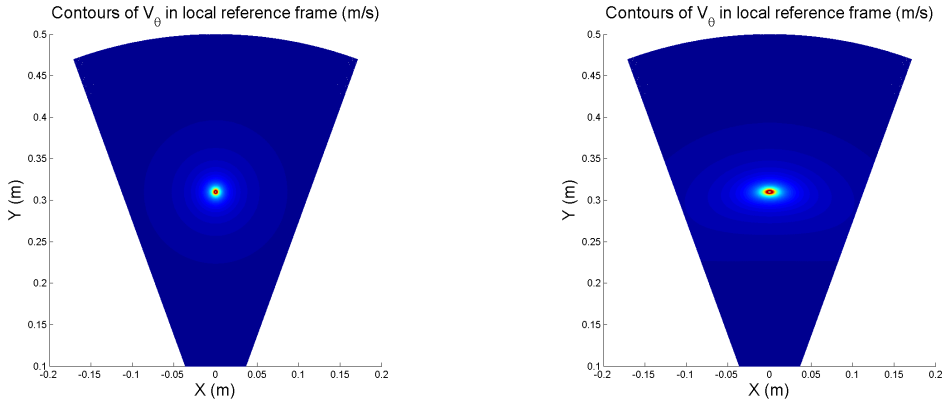

(a) Normal (b) Oblique

FIGURE 7.6: Incident flowfield for normal and oblique interaction of tip vortex with rear rotor

Figure 7.7 is a plot of $V_{\theta global}$ as a function of azimuthal distance taken at the edge of the vortex core for both the circular and elliptical shaped vortices. The global coordinate system is used as this is consistent with what the aft rotor will see as it cuts through the vortex. With the columnar vortex assumption the maximum tangential velocity is the same for both vortices. The velocity profile for the oblique case is broader due to its elliptic spatial distribution as expected.

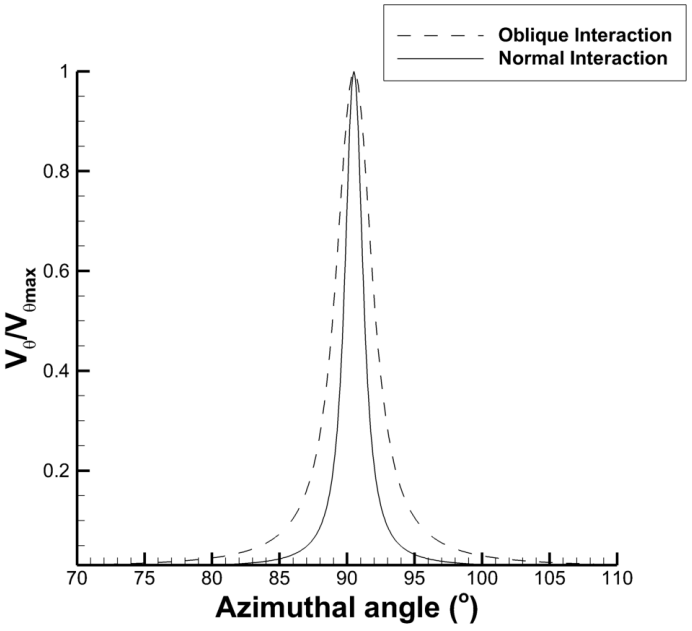

FIGURE 7.7: Azimuthal sections of $V_{\theta global}$ for the normal and oblique interactions

The next step in the analysis of the effect vortex orientation is to determine the harmonic content for the two cases. The harmonic content is calculated from the FFT of the $V_{\theta global}$ and shown in Figure 7.8. The case with an oblique interaction has a higher power spectrum at lower frequencies, while the normal interaction has a higher power spectrum at higher frequencies. This is because an FFT of a broader input signal will produce lower frequency sine wave relative to a a less broad signal which is closer to a Delta Dirac function which contains infinite high frequency sine waves.

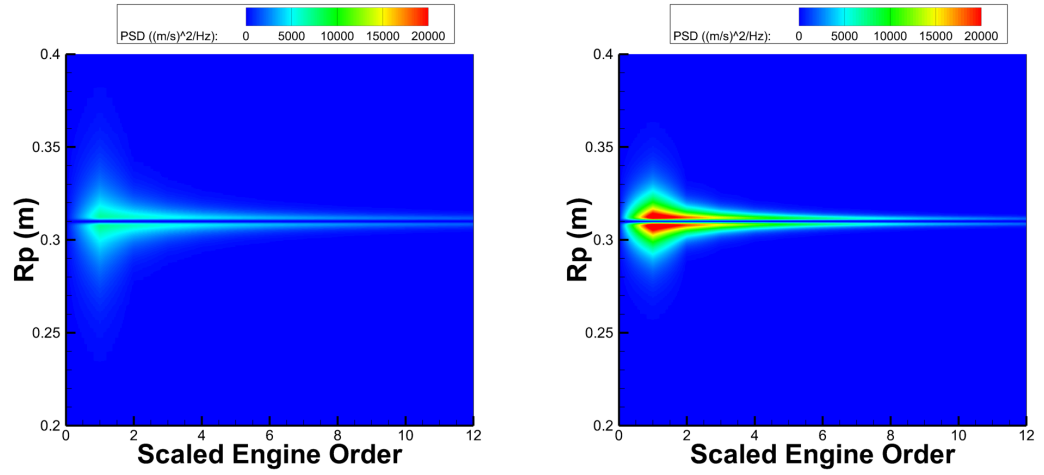

(a) Normal (b) Oblique

FIGURE 7.8: Power Spectral Density contour map on input disturbance field for normal and oblique interactions

The final step in the analysis of the spatial orientation of the vortex is to determine its aeroacoustic impact. This is done using CRPFAN at the validation test case defined in Table 7.2. The default mode of CRPFAN does not factor in the oblique interaction and therefore models a circular shaped vortex. The effect of the the oblique interaction was added into CRPFAN and compared to the datum case where it is modelled as circular. The only variable changed between the two cases is the spatial distribution of the vortex tangential velocity distribution with the maximum value the same for both because of the columnar vortex assumption.

The results of this are shown in Figure 7.9 with the sound pressure level contour map for both the normal and oblique interaction cases. Also shown are the overall sound pressure residuals over all directivity angles where the difference is oblique minus normal. The case with an oblique interaction generates more noise, with a peak difference of around 3.5 dB and the increase being present over most observer angles. Thus demonstrating that it is essential to take into account the vortex spatial orientation when calculating CROR interaction noise. The results are also in agreement with the power spectrum previously calculated, where there is more noise at lower frequencies for the oblique case, but at higher frequencies the normal case is greater.

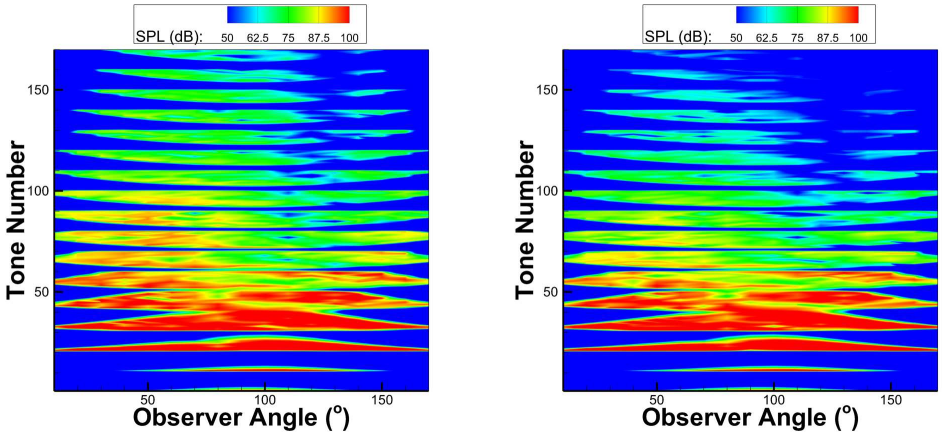

(a) Normal Orientation

(b) Oblique Orientation

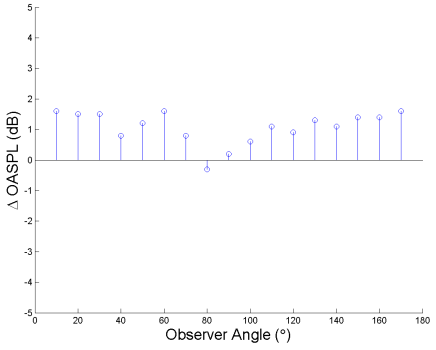

(c) OASPL residuals

FIGURE 7.9: Interaction noise effect of Vortex Spatial Orientation

7.3.1 Effect of vortex spatial orientation conclusions

The aft rotor will typically cut through the front rotor tip vortex at an oblique angle, this results in a tip vortex with a spatial orientation which is elliptical as seen by the aft rotor. It has shown using the input disturbance field methodology developed in this project and through modifications within CRPFAN that the oblique interaction is an important aspect to consider. For the CRPFAN validation test case the elliptical shaped vortex as a result of an oblique interaction generates more noise with up to 3.5 dB in the OASPL scale relative to the circular shaped vortex. Its effect is most dominant at the lower frequencies relative to the circular shaped vortex.

7.4 CFD Flowfield Analysis

Prior to developing correlations for the vortex axial velocity component, tip vortex trajectory and parameters for the vortex size and strength the flowfield for both the SR2 and SR3 will be analysed. Firstly to determine if there are any key flowfield differences between the SR2 and SR3 propeller and secondarily to determine the effect of the loading on the applicability of using a Vatistas vortex model.

With reference to Table 7.4 which lists the key non-dimensional parameters used for the test cases where the flowfield and tip vortex parameters are compared between the SR2 and SR3 propellers.

Parameter	SR2	SR3
β (°)	38	37.3
J	1.2	1.2
M	0.2	0.2
C_T	0.4	0.44
C_P	0.71	0.62

TABLE 7.4: Flowfield case comparison

The operating conditions are nearly identical apart from a 0.7 ° difference in setting angle but the SR3 has greater thrust and less power. This is attributed to its greater average chord length, which will result in more lift produced which has a dominant effect on the thrust but will also produce more drag which has a dominant effect on the power. The radial bound circulation, Γ_{bound}, distribution was calculated for both cases using Equation 7.1 and shown in Figure 7.10.

$$\Gamma_{bound} = \frac{dL}{\rho U_W dr} \tag{7.1}$$

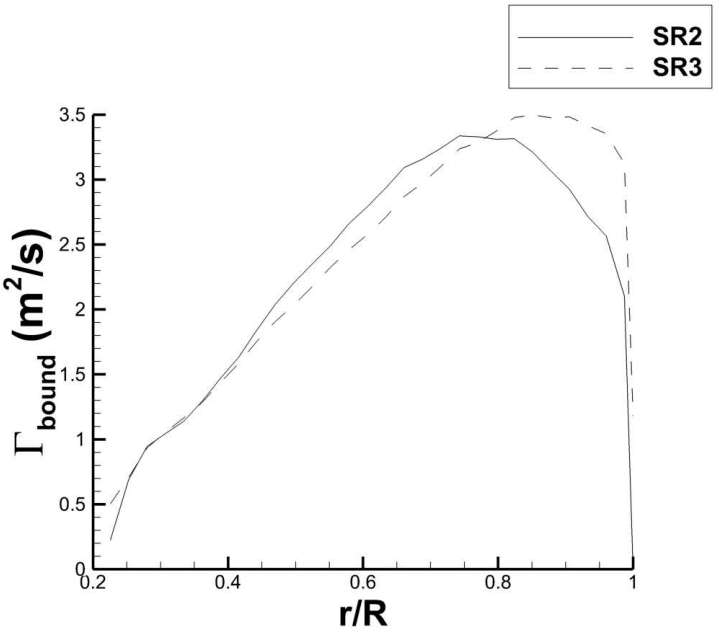

FIGURE 7.10: Radial distribution of bound circulation for both the SR2 and SR3 propeller geometries

The peak bound circulation is greater for the SR3 case than the SR2 and this should result in a tip vortex with greater strength as will be discussed in Section 7.7.1. To compare the flowfield and vorticity distributions for both case five slices normal to the engine axis at 1, 1.5, 2, 2.5 and references chords downstream of the propeller pitch change axis were created and the streamwise vorticity calculated in each of them. Figure 7.11 shows the slices for the SR2 and Figure 7.12 for the SR3. Also included in each figure are streamlines of wall shear stress on the blade suction side to inspect for levels of flow separation. Note that x/c is referred to as the axial location normalised by the chord, c, at 75 % radius. In some figures the CFD coordinate system is not always consistent with this nomenclature. But x/c will always mean the non dimensional axial distance unless stated otherwise despite any inconsistencies with the CFD coordinate system.

The general flow characteristics are similar for both the SR3 and SR2 with a primary tip vortex and the propeller wakes showing similar magnitudes and distribution. The propeller wake has a vorticity which is of opposite sign to the tip vortex this is because with reference to Figure 7.10 the gradient of $\frac{d\Gamma_{bound}}{d\frac{r}{R}}$ is positive up to an r/R of approximately 0.7. The vorticity is proportional to this gradient and the tip vortex has a negative gradient and hence negative vorticity. Inboard of the tip vortex is a region of 'residual' positive vorticity. This is present for both the SR2 and SR3 cases. The greater the level of flow separation emanating from a radial location where the $\frac{d\Gamma_{bound}}{d\frac{r}{R}}$ is greater than zero the more residual positive vorticity that will be entrained into the primary tip vortex.

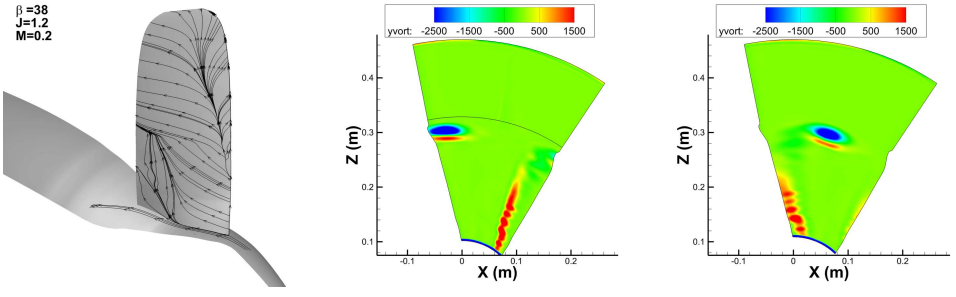

(a) Blade flow pattern (b) x/c=1 (c) x/c=1.5

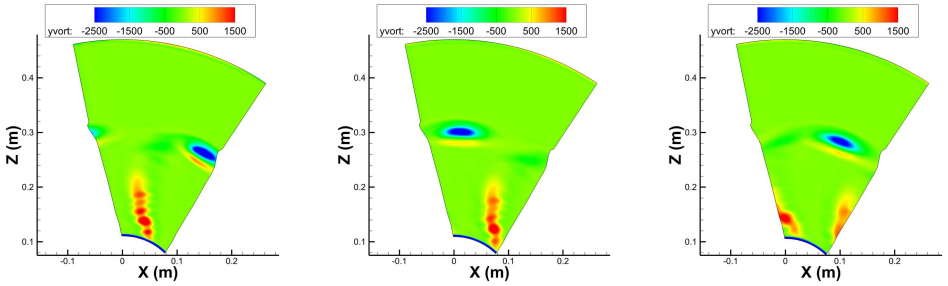

(d) x/c=2 (e) x/c=2.5 (f) x/c=3

FIGURE 7.11: SR2 streamwise vorticity at different axial locations

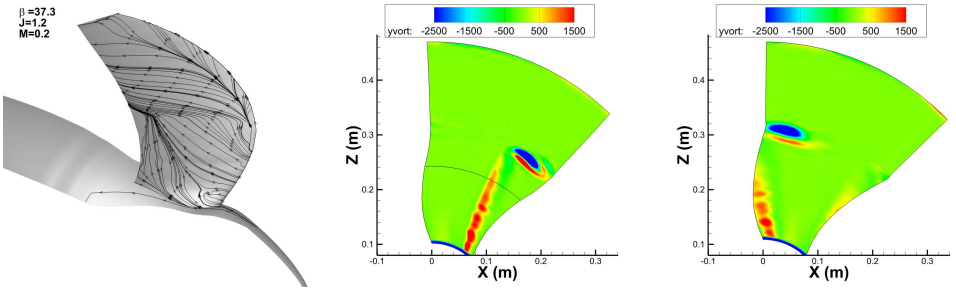

(a) Blade flow pattern (b) x/c=1 (c) x/c=1.5

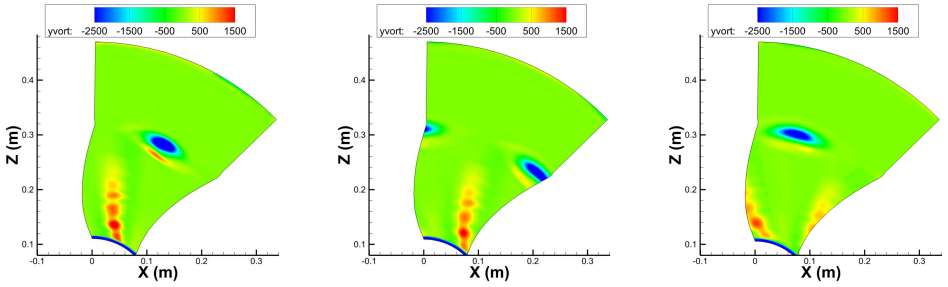

(d) x/c=2 (e) x/c=2.5 (f) x/c=3

FIGURE 7.12: SR3 streamwise vorticity at different axial locations

Of particular interest is the tip vortex tangential velocity profile for both cases. To obtain the tangential velocity profiles a coordinate transformation into the vortex cross plane was used and the vorticity in the plane was also calculated. The cross plane

vorticity for both cases are shown in Figure 7.13. As stated the greater peak bound circulation value of the SR3 should result in a stronger vortex with a greater circulation. This is demonstrated by Figure 7.14 and Table 7.5 where the vortex for the SR3 is indeed stronger. The tip vortex core size and maximum tangential velocity are both larger for the SR3 case. Also included in Table 7.5 is a comparison between the peak bound circulation, Γ_{bp} and the circulation calculated from the scalar integration of the cross plane vorticity, Γ_{CFD}.

Note the circular distribution of the cross plane vorticity relative to the vorticity distributions of Figure 7.11 and Figure 7.12 this is because of the angle of the plane relative to the tip vortex path confirming again the need to take into account the spatial orientation of the tip vortex as previously demonstrated,

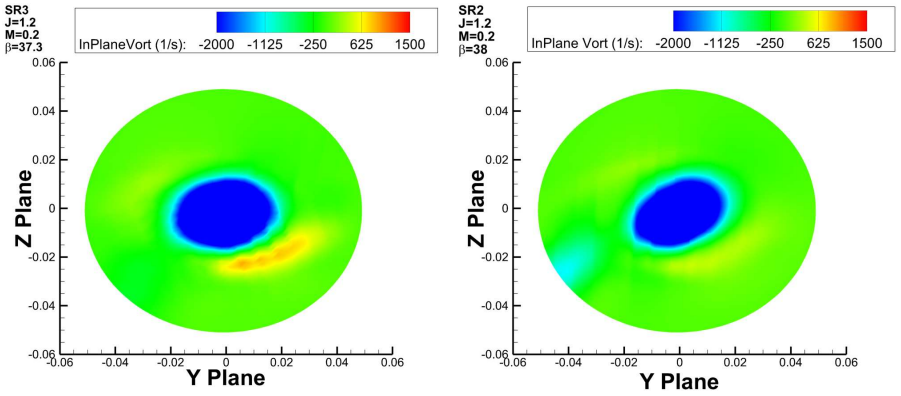

(a) SR3 (b) SR2

FIGURE 7.13: In plane vorticity in vortex normal plane for SR2 and SR3 under similar loading conditions

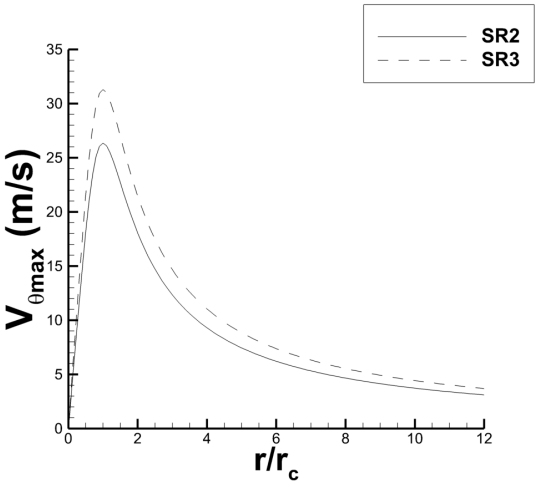

FIGURE 7.14: Tangential velocity profile for both SR2 and SR3 under similar loading conditions

Parameter	SR2	SR3
Γ_{bp} (m^2/s)	3.32	3.48
Γ_{CFD} (m^2/s)	2.98	3.35
r_c (m)	0.011	0.012
Maximum V_θ (m^2/s)	26.5	31.5
Shape factor	1.88	2.47

TABLE 7.5: SR2 and SR3 flowfield case comparison tip vortex parameters

The comparison was made at a roughly constant loading condition and both the SR2 and SR3 had similar flowfield characteristics. However, as the loading changes the flowfield will have different characteristics such as more separated flow for high loading conditions for example. To investigate the effect of loading on the flowfield of both the SR3 and SR2 iso-surfaces of static entropy are created for both propellers over a range of loading conditions. Defining the power loading , PL, as $\frac{C_P^3}{J}$, where J is the advance ratio and C_P the power coefficient. Iso-surfaces were calculated for six different cases covering a range of power loading values for both the SR2 and SR3.

At lower loading conditions, typically with a PL less than one, there is one distinct tip vortex and low levels of flow separation. As the power loading increases the incidence onto the blade is increased and the flow starts to separate similar to the mechanism of a delta wing and a leading edge vortex (LEV) is formed. As the loading increases two separate flow structures are formed and the LEV and tip vortex are separable. For the very high loading conditions most of the blade flow is separated and one large distorted flow structure is present.

The SR2 is more susceptible to high levels of flow separation than the more swept SR3 at a given loading condition. The flow follows the contour of the swept SR3 blade profile but for the straight bladed SR2 the flow starts to separate at mid span of the blade. Therefore, for a given medium to high loading condition for example a power loading greater than two there will be more flow separation for the SR2 compared to the SR3. The iso-surfaces of static entropy are shown for the SR2 and SR3 in Figure 7.15 and Figure 7.16 resepctivley.

Note that as the calculations were all steady state, these flowfield observations are at a snap shot in time. In reality the flowfield will be unsteady.

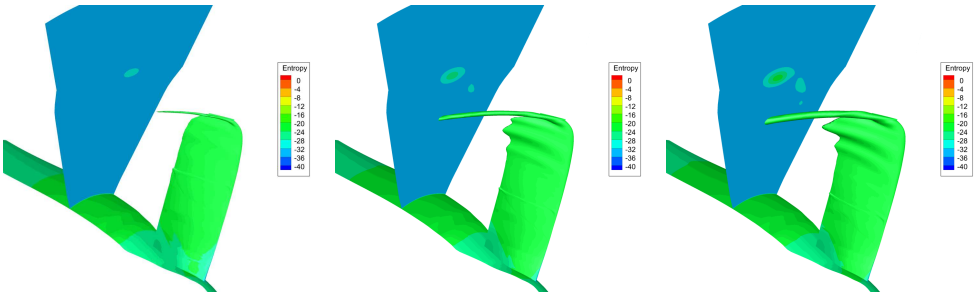

(a) PL=0.1 (b) PL=0.4 (c) PL=0.6

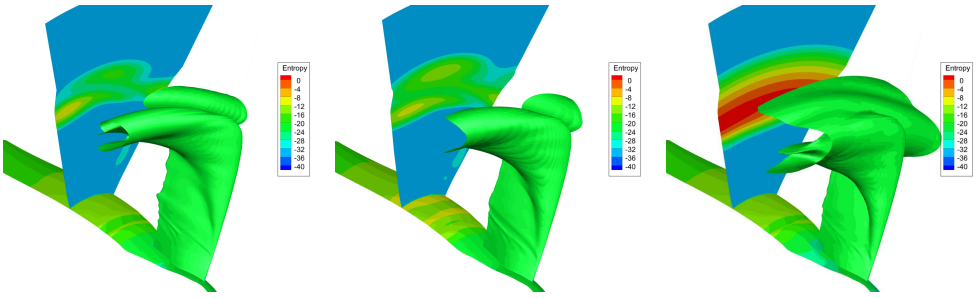

(d) PL=2.8 (e) PL=5 (f) PL=5.9

FIGURE 7.15: Iso-surfaces of static entropy for SR2 blade under range of power loading conditions

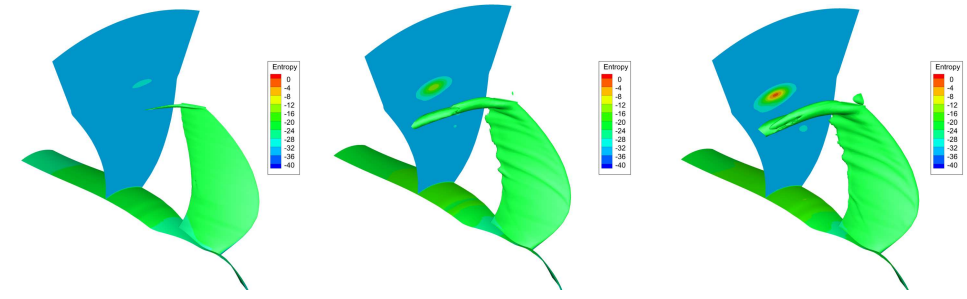

(a) PL=0.01 (b) PL=0.4 (c) PL=0.6

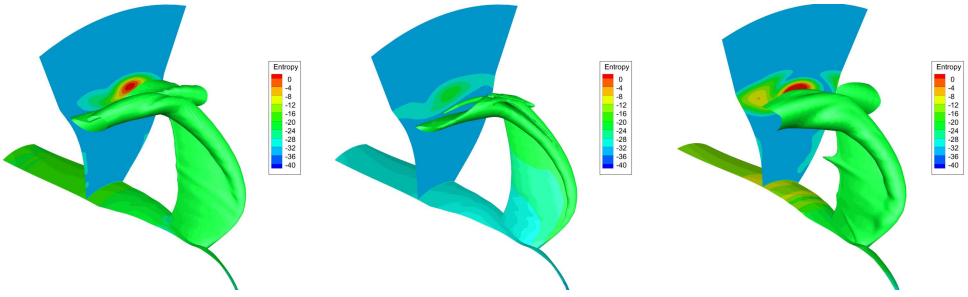

(d) PL=3.7 (e) PL=5.7 (f) PL=9.7

FIGURE 7.16: Iso-surfaces of static entropy for SR3 blade under range of power loading conditions

7.4.1 Vatistas vortex model regression analysis

Some of the key research questions in this project are related to how accurately a Vatistas vortex model describes the tip vortex of a CROR vortex, under different conditions, axial locations and for different propeller planform profiles. These questions will be considered here where the quality of the Vatistas analytical description is compared to the CFD description of the tangential velocity profile. With reference to Equation 8.2 which is used to calculate the variance of the least squares fit of the Vatistas analytical model used to describe the tangential velocity profile calculated by CFD.

$$S^2 = \frac{1}{n-1}\sum_{i=1}^{n}\left(\frac{V_{\theta CFD} - V_{\theta Vat}}{V_{\theta max}}\right)^2 \quad (7.2)$$

To allow for comparisons between different cases the tangential velocity is normalised by its maximum value. Figure 7.17 is the normalised tangential velocity as a function of normalised radius and the variance is the sum of the square of the difference between the CFD data and Vatistas model. The lower the standard deviation (square root of the variance) the better the fit and the more appropriate it is to use a Vatistas type vortex model.

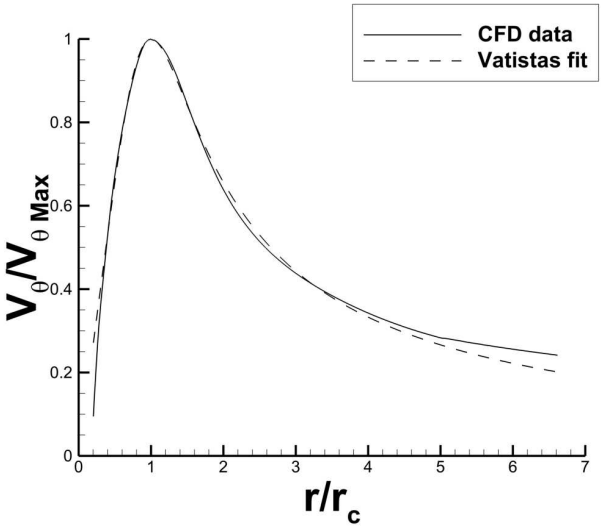

FIGURE 7.17: Regression between CFD data and Vatistas model

As evident from the flowfield investigation, that at one chord downstream the flow has multiple vortical structures from the wake, leading edge vortex and tip vortex therefore a Vatistas model is not appropriate due to the distortion of the vorticity field and the standard deviation is the highest for this plane. Plane two has the best quality of fit overall, providing the loading is not too great, at the time of reaching plane two the vortical structures have coalesced into one structure which is predominantly a tip vortex which can be modelled appropriately with a Vatistas vortex model. The quality of the

fit decreases relative to plane two at plane three this is possibly a result of the vortex dissipating as it evolves downstream.

The 'cut-off' point for the use of a Vatistas type vortex model is lower for the SR2 relative to the SR3 because of the increased levels of flow separation relative to the SR2. The 'cut-off' point for the SR2 at plane two is at a C_T of approximatively 0.65. This value increases to around 0.8 for the SR3 but it is not as distinct as it is for the SR2. The Vatistas vortex model quality of fit is better for the SR3 relative to the SR2 for cases at similar thrust coefficients. These findings are shown in Figure 7.18 which included the standard deviation for both the SR2 and SR3 at three different different planes downstream of the propeller pitch change axis.

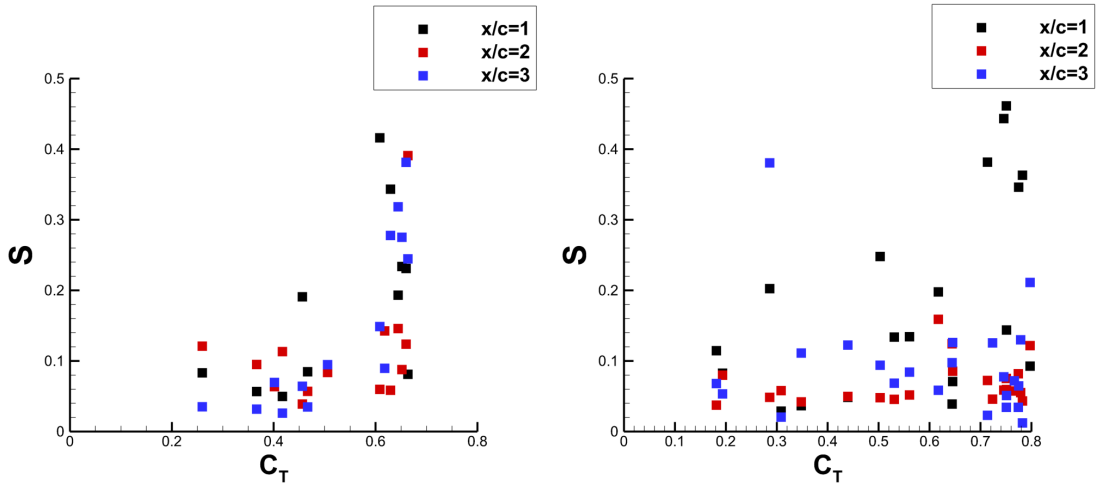

(a) SR2 (b) SR3

FIGURE 7.18: Standard deviation of Vatistas vortex description of CFD data for both the SR2 and SR3

The Vatistas shape factor, n, should mathematically be an integer number to satisfy the power series solution to the simplified Navier stokes equations. However, in practice it can be an integer or real number as its purpose is to model the tangential velocity distribution. The shape factor is iterated from one to four and the value which yields the best least square fit is selected. Two methods are used one where the iteration is only for integer numbers and a second method where any real number between one and four can be used. The standard deviation for each method is shown for plane two for both the SR2 and SR3 in Figure 7.19.

There is no considerable advantage to using either an integer or real shape factor in terms of the quality of the regression. Therefore, either can be used but an integer number will be used in the project for correctness.

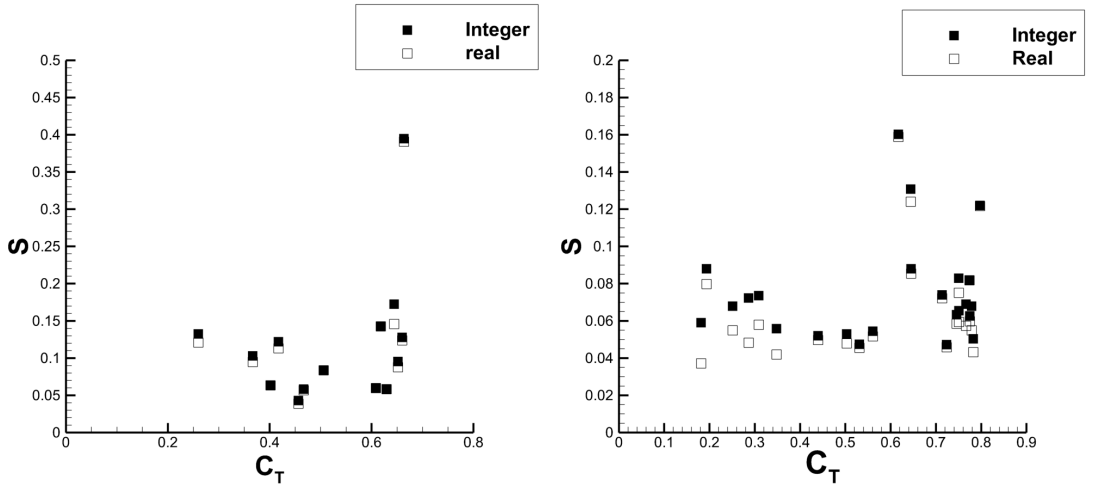

(a) SR2 (b) SR3

FIGURE 7.19: Sensitivity of standard deviation to using an integer or real number for Vatistas shape factor

7.5 Effect of vortex axial velocity component

The CRPFAN inbuilt vortex model does not explicitly model the axial velocity component of the tip vortex. Section 7.5 determines how significant this term is to open rotor noise tip vortex interaction noise. The model proposed to describe the vortex axial velocity term, V_x, is the Vatistas model shown in Equation 7.3 as presented in[28].

$$V_x = V_{Xmin}\left[1 - \frac{r^2}{(r_c^2 + r^{2n})^{\frac{1}{n}}}\right] \tag{7.3}$$

The vortex axial velocity component , V_x, is the velocity acting along the $X - Plane$ in Figure B.6 of Section B.3 in Appendix B. The ratio of V_{xmin} to V_x defines whether or not the vortex is wake like or jet like. If the axial velocity component is greater than the freestream velocity it is considered jet like and conversely if it less than the freestream it is considered wake like. The axial velocity induced by the trust of the propeller is area averaged and subtracted from the velocity in the axial direction in order order to obtain V_x in the relative reference frame.

The first question is whether or not Equation 7.3 is an appropriate choice to model the tip vortex axial component. This question is answered with reference to Figure 7.20 which shows the comparison between CFD data and the analytical fit using Equation 7.3 as a function of normalised radial distance from the tip vortex centre for different loading conditions for both the SR2 and SR3.

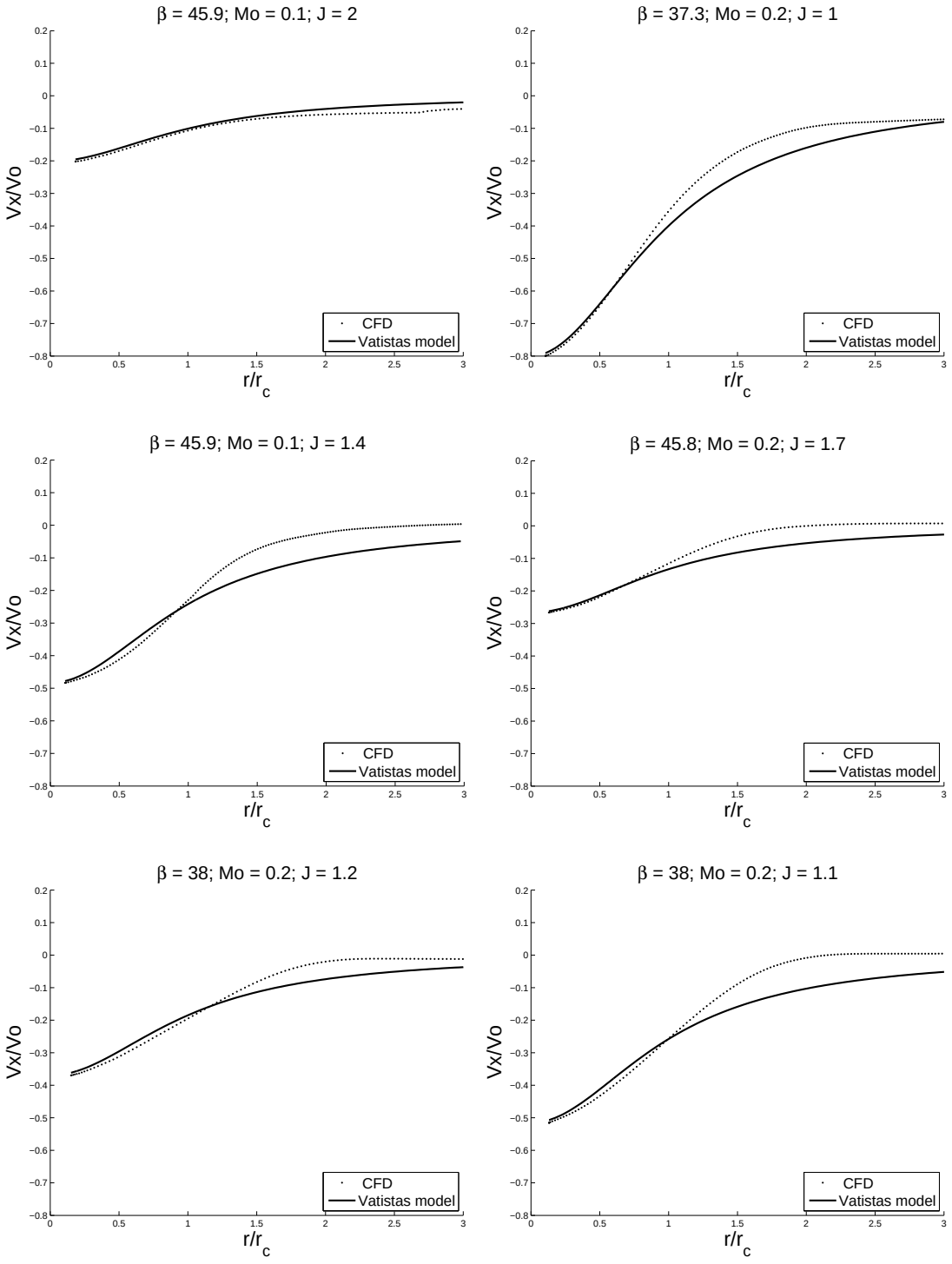

FIGURE 7.20: Comparison between Vatistas vortex model and CFD data as a function of radial distance for both the SR2 and SR3 under different loading conditions

The nature of the tip vortex axial component is wake like because V_{xmin} is less than V_0. The V_x term is negative as a result of the coordinate system used and not representative of reversed flow. In order to to use Equation 7.3 to model V_x a value for V_{xmin} is required. For this reason correlations are derived from the CFD values of the minimum

V_x as a function of propeller operating conditions. The term used will be the power loading, $\frac{C_P^3}{J}$, this is because it characterises the tip vortex path, loading and amount of drag for a given condition. Correlations which relate the power loading to the ratio of $\frac{V_{xmin}}{Vo}$ to the power loading are derived for both the SR2 and SR3. They are taken from the vortex cross plane which was transformed about a plane normal to the engine axis at two chords downstream of the propeller pitch change axis. The correlations are defined in Equation 7.4 for the SR2 and Equation 7.5 with the source distribution shown in Figure 7.21.

Up to values of one, as the power loading increases the vortex axial velocity component becomes less and wake like with V_{xmin} approaching the value of V_o. But as the power loading increases more flow separation occurs which contains flow separated from the boundary layer which causes the flow to be more wake like and the value of V_{xmin} tends away from the freestream velocity V_o. Because the flow separation is dependent on the level of blade sweep correlations are derived for swept and unswept blades for the SR3 and SR2 resepctivley. The correlations are also split according to the power loading with a value of two being the transition point for the value of V_{xmin} increasing or decreasing with an increase in power loading.

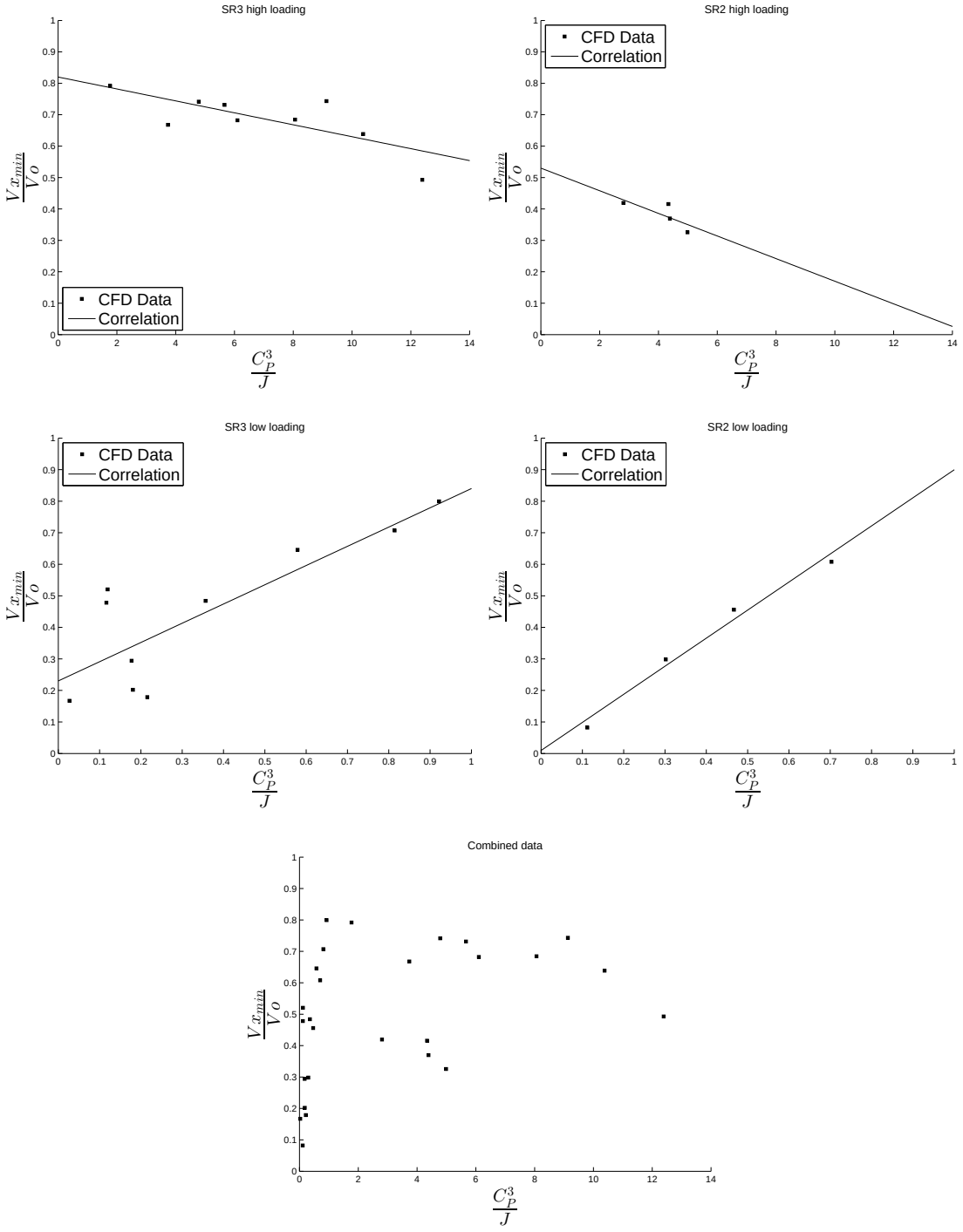

FIGURE 7.21: CFD data for V_{xmin} correlations broken down into loading level and source geometry with their matching correlation

$$\frac{V_{Xmin}}{V_0} = \begin{cases} 0.9\frac{C_P^3}{J} & \text{if} \quad \frac{C_P^3}{J} < 2 \\ -0.04\frac{C_P^3}{J} + 0.5 & \text{if} \quad \frac{C_P^3}{J} \geq 2 \end{cases} \tag{7.4}$$

$$\frac{V_{Xmin}}{V_0} = \begin{cases} 0.6\frac{C_P^3}{J} + 0.2 & \text{if} \quad \frac{C_P^3}{J} < 2 \\ -0.02\frac{C_P^3}{J} + 0.8 & \text{if} \quad \frac{C_P^3}{J} \geq 2 \end{cases} \tag{7.5}$$

The Vatistas type description for the axial velocity component with the derived CFD correlations where integrated into CRPFAN. To determine the aeroacoustic significance of the inclusion of the axial velocity term the interaction noise was compared to a baseline version of CRPFAN which does not include the vortex axial velocity term. The case to be compared to is Case 2, which uses a Vatistas type vortex model for tangential velocity and this case is identical to Case 5 which is the version with the integrated correlations and model for V_x. Therefore the only difference between Case 2 and Case 5 is the inclusion of the vortex axial velocity term. The operating conditions are defined in Table 7.2 and are the same as the CRPFAN validation case.

The effect of including the vortex axial velocity term is noticeable over a range of directive angles and frequencies. In general the inclusion of the terms acts as a source of noise addition with a peak difference in overall sound pressure level of up to 3 dB relative to the case without its inclusion. This confirms the importance of including the vortex axial velocity component when investigating tip vortex interaction noise. The sound presser level contour maps for Case2 and Case 5 are shown in Figure 7.22 alongside the overall sound pressure level residuals which is Case 5 minus Case 2. Additional directivity responses for six interaction tones for Case 5 are included in Section D.1.4 of Appendix D.

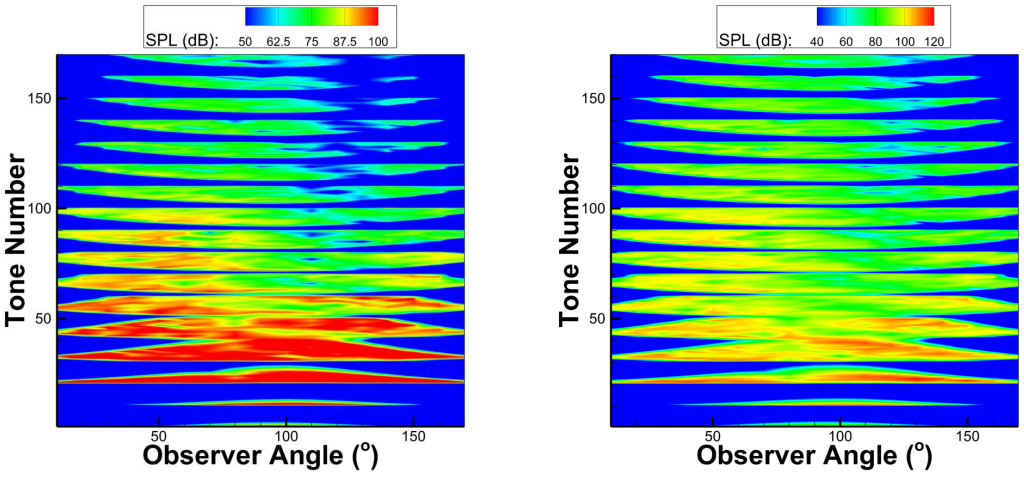

(a) Without Vx

(b) With Vx

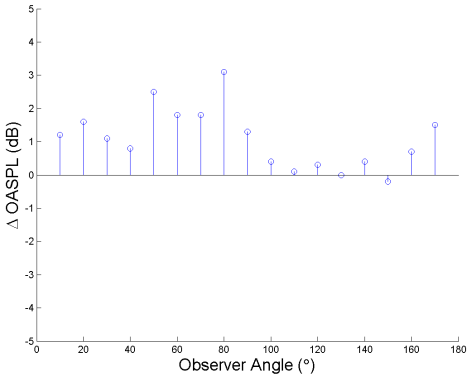

(c) Case 5 - Case 2

FIGURE 7.22: SPL Contour map effect of vortex axial velocity component

7.5.1 Vortex axial velocity component modelling conclusions

The vortex axial velocity component was modelled using CFD flowfield data and it was found it can be described by a Vatistas model. The nature of the axial velocity component is wake like and the level of how wake like V_{xmin} is relative to V_o is dependent on the power loading. As a result four correlations have been derived which relate $\frac{V_{xmin}}{Vo}$ for different power loading and propeller blade sweep. The inclusion of this term in CRPFAN acts as a noise source with up to 3 dB change in overall sound pressure level with its inclusion. It is highly recommend that this term is included in tip vortex interaction noise calculations.

7.6 Tip Vortex Trajectory Modelling

Section 7.6 presents a revised model to calculate the radial location of the tip vortex centre as a function of downstream axial distance from the front rotor. The revised model is derived from the CFD models for both the SR2 and SR3 propellers. The CRPFAN tip vortex trajectory model is based on a user defined and scalable parameter the tip vortex trajectory index (TVTI). It was demonstrated in Section 5.1.2 that the sensitivity of the interaction noise to the scalable input parameter, TVTI, is up to 20 dBs when using values in the range of 0.5 and 2. This presents large uncertainty with regards to the interaction noise if the correct value of TVTI is not known prior to a calculation. The revised model removes this particular uncertainty with the use of known integrated propeller parameters such as lift and thrust coefficients which govern the extent of tip vortex radial contraction.

The TVTI parameter simulates the effect of the streamtube contraction present due to the thrust on the fluid volume. Figure 7.23 presents a simplified model of a single streamtube up and downstream of the propeller plane of rotation.

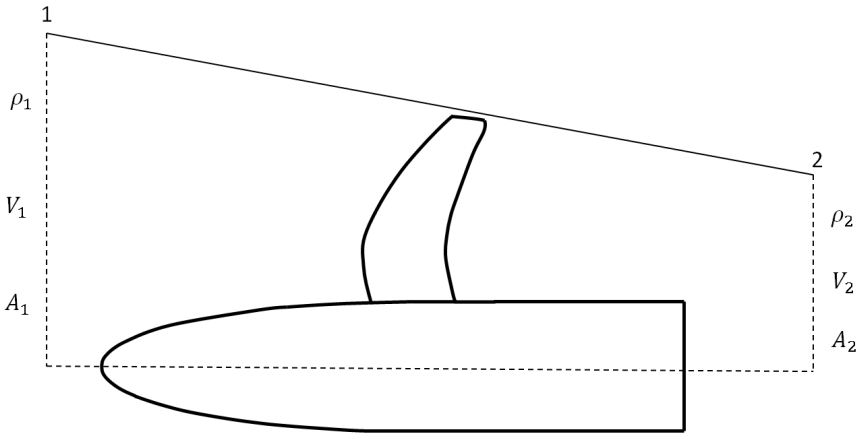

FIGURE 7.23: Streamtube contraction schematic

The continuity equation applied to Figure 7.23 can be used to define Equation 7.6.

$$\dot{m}_1 = \dot{m}_2 = \rho_1 V_1 A_1 = \rho_2 V_2 A_2 \tag{7.6}$$

With the assumption that the flow is incompressible along the streamtube, Equation 7.7 shows that for an increase in velocity which is required for thrust generation, the area of the streamtube must reduce. The level of reduction is proportional to the acceleration along the streamtube which is driven by the thrust of the propeller.

$$\frac{V_2}{V_1} = \frac{A_1}{A_2} \tag{7.7}$$

The revised model will express the radial contraction of the tip vortex in the axial direction as a function of the non-dimensional thrust coefficient. This is instead of using the scalable input parameter, TVTI.

7.6.1 Trajectory Modelling Method

The coordinate system used to define the revised tip vortex trajectory model is illustrated in Figure 7.24, where the radial location of the tip vortex centre is defined as, R_V, and the front rotor tip blade radius as, R_T, which is half the blade diameter, D. The radial location of the vortex decreases in the axial positive $X - direction$.

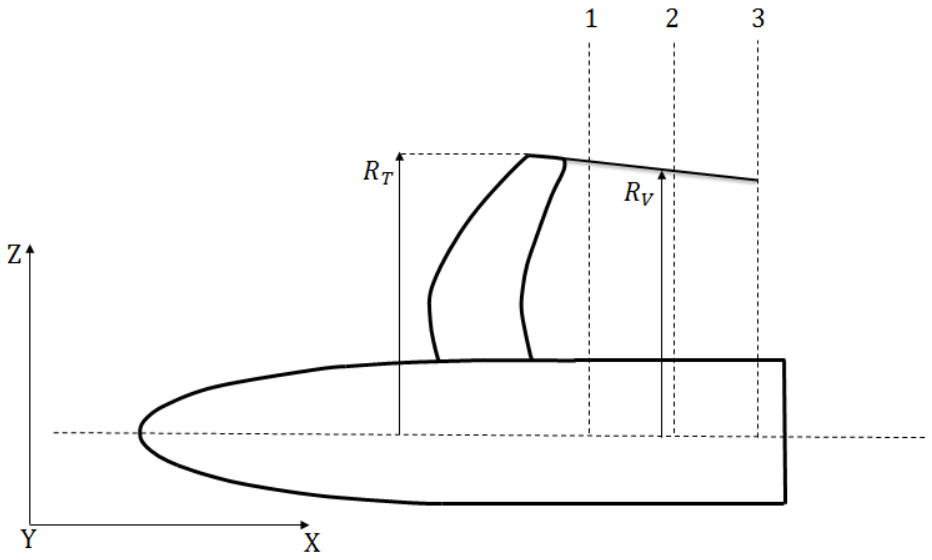

FIGURE 7.24: Tip vortex trajectory diagram

Three equidistant reference planes '1', '2', and '3' normal to the engine axis ($Z - Y - Plane$) are defined which correspond to one, two and three reference chords (at r/R of 75%) downstream of the propeller pitch change axis. At each of these planes the tip vortex centre is identified using a Tecplot subroutine, where the tip vortex centre is defined as the point of the maximum vorticity magnitude. This subroutine was run for all cases of the SR2 and SR3 CFD calculation so a database of the tip vortex centre radial location over a range of loading conditions was obtained to build a correlation.

Dimensional analysis using the method of Buckingham Pi was used to select the correct parameters to form the tip vortex radial location correlation from the CFD flowfield data. With reference to Figure 7.24 and knowledge of the streamtube contraction physics it is proposed that the tip vortex centre radial location, R_V, depends on the tip radius of the propeller blade, R_T, the freestream density of the fluid, ρ, the propeller thrust, T, the propeller rotations per second, n, and the axial distance downstream, X. This proposed function is shown in Equation 7.8.

$$R_V = f(R_T, \rho, T, n, X) \tag{7.8}$$

This function includes three dimensions and six variables which means there should be three Pi groups. The three Pi groups are shown in Equations 7.9, 7.10 and 7.11. The Buckingham Pi analysis results in three groups which are the non dimensional tip vortex radial location, $\frac{R_V}{R_T}$, non dimensional axial distance, $\frac{R_T}{X}$, and the thrust coefficient, C_T.

$$\pi_1 = \frac{R_V}{R_T} \tag{7.9}$$

$$\pi_3 = \frac{R_T}{X} \tag{7.10}$$

$$\pi_2 = \frac{T}{\rho n^2 R_T^4} = \frac{T}{\rho n^2 (\frac{D_T}{2})^4} = C_T \tag{7.11}$$

The three groups can be expressed as a function of each other as shown in Equation 7.12, with the form of the correlation to be developed shown in Equation 7.13. For the correlation a least squares fit linear regression is used with, R_V/R_T plotted against some product of the functions of R_T/X and C_T. The best regression is achieved with C_T raised to the power of two and the non-dimensional axial location to the negative square root. This model assumes an ax-symmetric wake contraction in the azimuthal direction. The source data for the linear regression is shown in Figure 7.25 and the resulting correlation in Equation 7.14.

$$\pi_1 = f(\pi_2, \pi_3) \tag{7.12}$$

$$\frac{R_V}{R_T} = f(C_T, \frac{R_T}{X}) \tag{7.13}$$

$$\frac{R_V}{R_T} = -0.16\sqrt{\frac{X}{R_T}}C_T^2 + 0.9925 \tag{7.14}$$

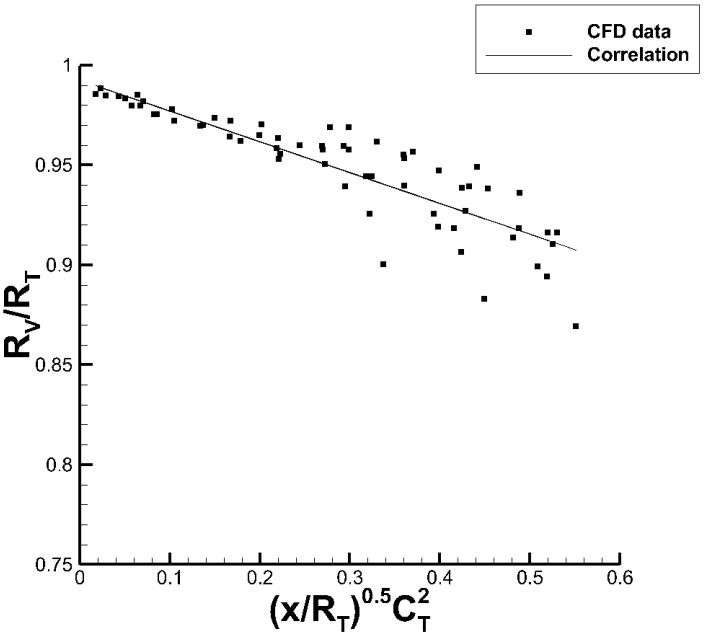

FIGURE 7.25: Correlation for tip vortex radial location

The radial contraction of the tip vortex centre is up to 10 % of the blade tip radius for the high loading conditions. The significance of Equation 7.14 relative to tip vortex interaction is that for an increase in C_T of 0.6 to 0.7 at an axial location of X/R_T of 0.48 the tip vortex radial location, $\frac{R_V}{R_T}$, will move from 0.953 inboard to 0.938. This coupled with the increase in tip vortex core size with thrust can be used to calculate the required clipping of the aft rotor in attempt to minimise the tip vortex interaction noise.

7.6.2 Aeroacoustic effect of tip vortex trajectory

The revised tip vortex trajectory model was integrated into CRPFAN to form Case 6, which is the same as Case 2 except for the inclusion of the revised tip vortex model instead of the baseline CRPFAN model. Case 6 is compared to Case 2 and the non-dimensional radial location of the tip vortex at the quarter chord of the aft blade for test case conditions of Table 7.2 are summarised in Table 7.6. Because the CRPFAN model is dependent on the user parameter, TVTI, two values are quoted of one and two which are within the recommended range of values in CPRFAN documentation. The revised model from CFD compares closest to the CRPFAN model when a TVTI of two is selected.

Model	R_V/R_T
CRPFAN 1 (TVTI=1)	0.945
CRPFAN 2 (TVTI =2)	0.89
Revised	0.885

TABLE 7.6: Vortex Radial location for CRPFAN datum model and revised trajectory model

The comparison between the CRPFAN and revised trajectory model is made for four versions of CRPFAN. Case 2a uses CRPFAN with a TVTI of 1 and has ten streamlines. Case 2b is the exact same except 51 streamlines are used in CRPFAN. Case 6a uses CRPFAN with the revised trajectory model with ten streamlines and Case 6b uses the revised trajectory model in CRPFAN with 51 streamlines.

The use of the revised trajectory model reduces the noise by up to 3 dB for the datum descritisation and 4 dB for the increased descritisation. This difference will reduce if a TVTI of 2 is used. Also of significance is the importance of using more streamlines for an aeroacoustic strip theory code because the acoustic response to the revised trajectory model is under predicted when using only ten streamlines. The sound pressure level contour map for all for Cases 2a, 2b, 6a, 6b and the overall sound pressure level residuals for Case 6a minus case 2a and Case 6b minus Case 2b are shown in Figure 7.26. Additional directivity responses for six interaction tones are shown in Section D.1.5 of Appendix D

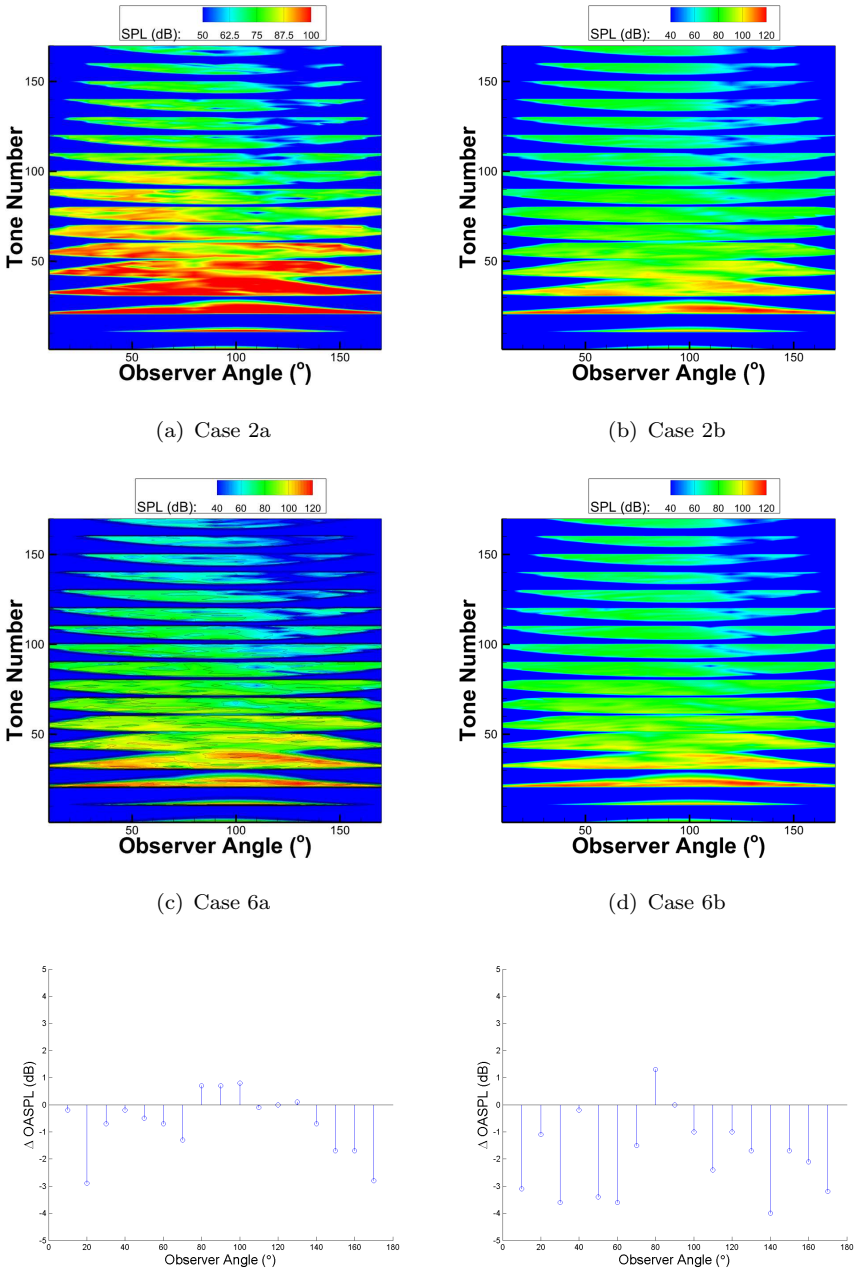

(a) Case 2a

(b) Case 2b

(c) Case 6a

(d) Case 6b

(e) Case 6a minus Case 2a

(f) Case 6b minus Case 2b

FIGURE 7.26: Interaction sound pressure level map and OASPL residuals for CRPFAN and revised trajectory model with datum and increased resolution versions of CRPFAN

7.6.3 Trajectory modelling conclusions

A revised model for the tip vortex trajectory has been derived using CFD flowfield data combined with dimensional analysis. This model reduces the required knowledge required to accurately predict the tip vortex trajectory because it eliminates the use of TVTI. The inclusion of this model in CRPFAN reduces up to 4 dB OASPL interaction noise when using CRPFAN with an increased number of streamlines.

7.7 Tip vortex correlations derived from CFD flowfield

Section 7.7 presents the development of correlations for the tip vortex size and strength using the flowfield from the CFD on the SR2 and SR3 advanced propeller blades. As previously stated the intended application of the correlations is for the use in a preliminary design tool such as CRPFAN. The proposed model to describe the tip vortex tangential velocity distribution is a Vatistas type. To fully describe the tangential velocity distribution of a Vatistas type tip vortex four out of the circulation, Γ, core size, r_c, maximum tangential velocity, $V_{\theta_{max}}$, and shape factor, n, is required. The first parameter to be considered will be the tip vortex circulation , Γ.

7.7.1 Correlations for tip vortex circulation

It was demonstrated in Section 5.1.1 of Chapter 5 that variations of the tip vortex circulation can contribute up to 20 dB to the interaction noise when iterating values of the circulation index, Ci, between values of 1 and 3. This effectively presents an uncertainty to an aeroacoustic calculation as the exact value of the Ci to the user may not be known at the time of the calculation. The use of a correlation based on known or easily calculated propeller aerodynamic coefficients to determine the tip vortex circulation reduces this uncertainty. To asses the credibility of the derived correlation a comparison to PIV is used. The CFD model uses a RANS turbulence model which assumes isotropic turbulence[54]. A concern could be that the isotropic turbulence assumption leads to a highly dissipative calculation for the vortex, which will result in an incorrect magnitude vorticity distribution and therefore incorrect tip vortex circulation.

The comparison to a limited set of in-house high resolution PIV measurements will help determine how dissipative the CFD model is. The comparison is made for the two blade analogue rotor between CFD and PIV for the integrated vorticity at different axial locations downstream of the propeller pitch change axis. Further details of the two blade analogue PIV methodology is described in Appendix C.

The rotor operating conditions for case one are a 75 % reference blade setting angle of 26.5° , rotational speed of 6875.5 revolutions per minute and a freestream Mach number of 0.1. The measurements planes for case one are at one and two chords downstream of the propeller pitch change axis, where the chord is referenced at the 75 % radius.

The measurements planes are normal to the engine axis, and with reference to Figure 7.27 which demonstrates the different sized circular zones used for the integration. Figure 7.27 is a contour plot of the stream wise vorticity in a plane normal to the engine axis at one reference chords downstream of the front rotor pitch change axis calculated with the CFD model. The three zones around the tip vortex region are 30, 40 and 50 mm in radius and are regions in which a scalar integration of the streamwise vorticity is

performed to yield the tip vortex circulation. This was done for both the CFD and PIV measurements and the comparison between the circulation values are summarised in Table 7.7.

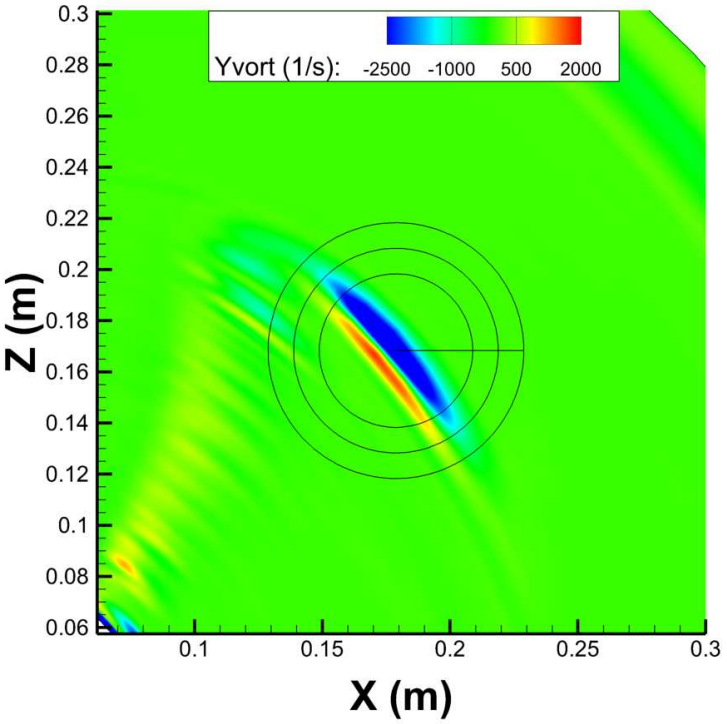

FIGURE 7.27: Tip vortex for PIV Case One at x/c=1 normal to engine axis

	Zone radius (mm)	CFX	PIV	% difference
Plane 1	30	1.35	1.394	3.2
	40	1.595	1.5382	-3.7
	50	1.7742	1.7659	-0.5
Plane 2	30	1.1	1.15	4.3
	40	0.86	1.265	32.0
	50	1.34	1.375	2.5
	70	1.6192	1.6162	-0.2

TABLE 7.7: Comparison of tip vortex circulation between CFD and PIV for β =22.8 , rpm=6875.5, M=0.1

The circulation values between CFD and PIV are in good agreement, with most of the comparisons within 5 % of each other. The comparison at x/c of 2 with a 40 mm radius is attributed to a large ratio of vorticity with an opposing sign originating from the wake to the bulk vorticity from the tip vortex. This process was repeated for a different case where the variable change is the freestream Mach number which increases from 0.1 to 0.144. The comparison between PIV and CFD for this case is shown in Table 7.8. The

comparison overall is not as good as for the previous case but the plane most appropriate for the end application is at x/c of two. This is because plane two is closest to the axial distance between pitch change axis used for the UDF for example. At plane two and with the nominal integration zone radius the agreement between PIV and CFD is good with the CFD calculating a value 2.7 % greater.

	Zone radius (mm)	CFX	PIV	% difference
Plane 1	30	1.68	1.48	-13.7
	50	1.82		
Plane 2	30	1.39	1.15	-20.4
	50	1.7	1.66	-2.7
	70	1.62		
Plane 3	30	0.98	1.33	26.09
	50	1.41		

TABLE 7.8: Comparison of tip vortex circulation between CFD and PIV for β =22.8 , rpm=6875.5, M=0.144

In summary the agreement between CFD and PIV for the tip vortex circulation is very good, especially when considering the end application of the correlation. This gives confidence in the CFD calculations to derive a bespoke tip vortex correlation for the tip vortex circulation.

Dimensional analysis for circulation parameter

The first step is to determine an appropriate non-dimensional parameter for the tip vortex circulation. The same approach will be taken as for the tip vortex trajectory model using the method of Buckingham Pi.

With the laws of Circulation by Kelvin and Helhmholtz under consideration it is proposed that the circulation will be a function of the density, ρ, the relative velocity onto the blade, U_W, the lift, L , and propeller tip diameter, D. This means there are five variables and three dimensions which results in two Buckingham Pi groups. Two resulting Buckingham Pi groups are shown in Equations 7.16 and 7.17.

$$\Gamma = f(\rho, U_W, L, D) \tag{7.15}$$

$$\pi_1 = \Gamma, U_w, L, D \tag{7.16}$$

$$\pi_2 = \rho, U_w, L, D \tag{7.17}$$

The first group, π_1, will be named the circulation parameter, Γ^*. The second group, π_2, is dimensionally equivalent to the propeller total lift coefficient defined in Equation 7.23.

Therefore the circulation parameter will be some function of the lift coefficient. From finite wing theory the relationship between induced drag, C_{Di}, and C_L is shown in Equation 7.22. Where for a given aspect ratio, AR, and efficiency factor, ϵ, the induced drag is a function of the lift coefficient to the power of two.

$$\pi_1 = \frac{\Gamma}{U_w D} = \Gamma^* \tag{7.18}$$

$$\pi_2 = \frac{\rho U_w^2 D^2}{L} \tag{7.19}$$

$$\frac{\Gamma}{U_w D} = f(\frac{\rho U_w^2 D^2}{L}) \tag{7.20}$$

$$\Gamma^* = f(C_L) \tag{7.21}$$

$$C_{Di} = \frac{C_L^2}{\pi \epsilon AR} \tag{7.22}$$

$$C_L = \frac{L}{\frac{1}{2}\rho U_{w_{ref}}^2 S_W} \tag{7.23}$$

A linear regression of the circulation parameter as a function of the lift coefficient to the power of two was determined and the resulting correlation is shown in Equation 7.24. The circulation parameter is determined from the integrated vorticity in the vortex cross plane with the incident velocity at the 75 % section on the blade. The cross plane is normal to an axial location of x/c equal to two, however the circulation by definition should be constant for each plane. The same process was applied to the thrust coefficient because of its significance in propeller aerodynamics and design. The correlation for the thrust coefficient is shown in Equation 7.25 and the source data for both the lift and thrust coefficient correlations is shown in Figure 7.28.

The agreement between correlation and CFD source data is not as good at the higher loading conditions such as a $\frac{C_T^2}{B}$ of 0.07 and greater because there is more flow separation at these conditions with multiple vortical structures merged into one.

$$\Gamma^* = 0.26 C_L^2 + 0.018 \tag{7.24}$$

$$\Gamma^* = 1.5 \frac{C_T^2}{B} + 0.007 \tag{7.25}$$

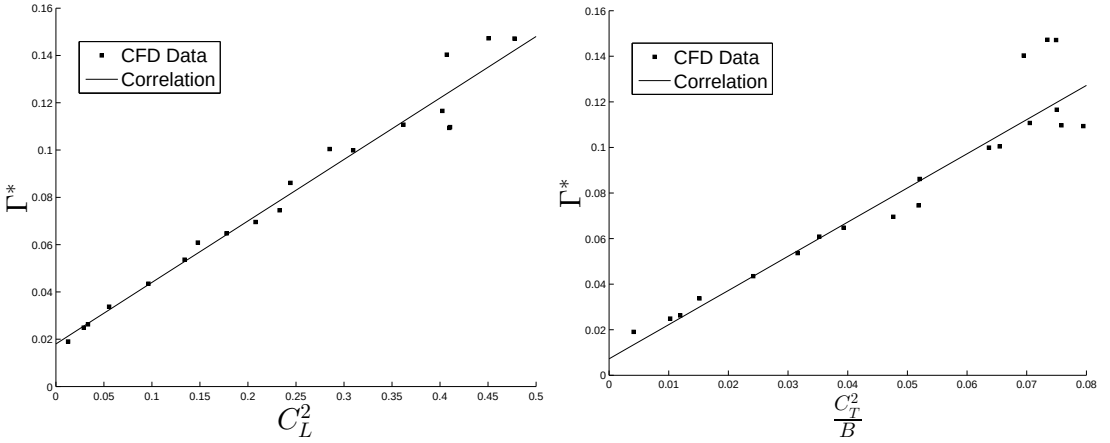

(a) Lift coefficient

(b) Thrust coefficient

FIGURE 7.28: Source data for correlations for tip vortex circulation parameter as a function of list and thrust coefficient

In Section 3.5.1 of Chapter 3 lifting line theory was used to predict the strength of the tip vortex. Where the peak bound circulation is approximated as equal to the strength of the tip vortex. The bound circulation can be calculated from the sectional lift distribution through Kutta-Joukowski theory[24] shown in Equation 7.26. In Chapter 3 the peak bound circulation was calculated analytically using lifting line theory and compared to measured experimental data.

$$\Gamma_{bound} = \frac{dL}{\rho U_W dr} \tag{7.26}$$

Here the source data for the comparison is both from the CFD. The bound circulation is calculated from the radial lift distribution and the tip vortex circulation from the integrated cross plane vorticity. Figure 7.29 shows how good of an approximation the peak bound circulation is to the tip vortex circulation. There are two vorticity integration methods included, one where all the vorticity in the zone is integrated regardless if it is a positive or negative in sign. The other integration method only includes vorticity that is negative. At low thrust conditions there is little difference between the peak bound circulation and both versions of the integrated vorticity. As the thrust increases the final integrated tip vortex will have more content from the separated flow of the leading edge vortex and the wake which will have a different sign of vorticity to the original tip vortex. This is why at the larger thrust coefficients the difference between the combined and only negative vorticity derived circulation increases. Note that the integration for the PIV comparisons included vorticity which is both positive and negative. The correlations of Equations 7.24 and 7.25 were derived using circulation calculated from only negative vorticity because this is the vorticity attributed to the tip vortex.

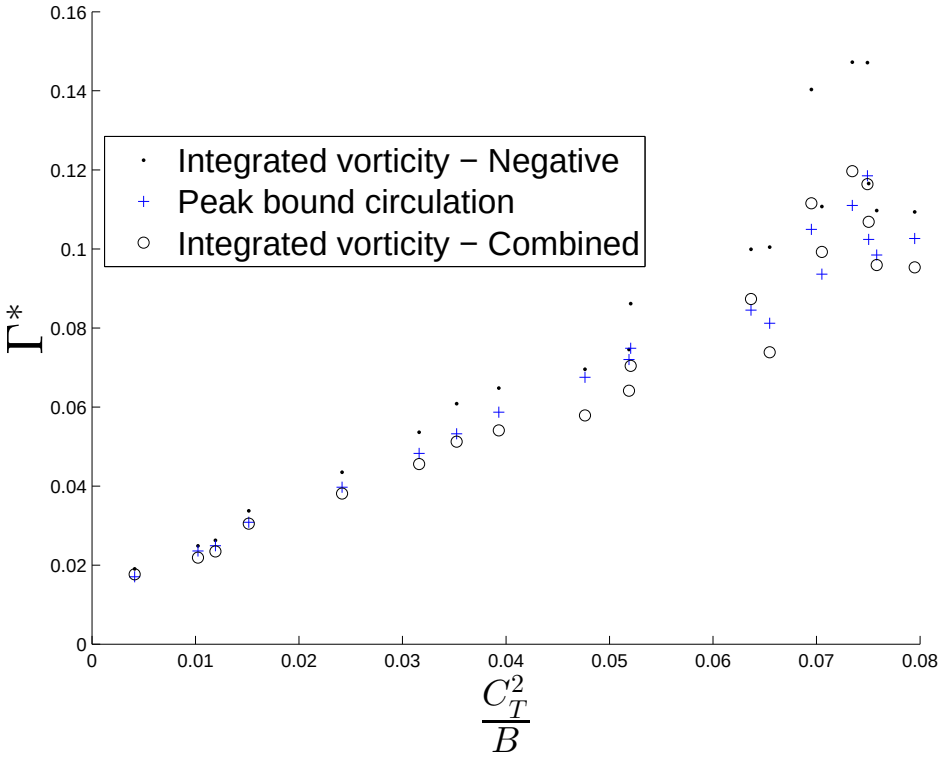

FIGURE 7.29: Comparison between peak bound and integrated vorticity

The correlations for Γ^* use the combined flowfield data from both the SR2 and SR3. The sensitivity of Γ^* to rotor operating conditions is very similar for both the SR2 and SR3 and separate correlations are not required. This is demonstrated in the multi-dimensional maps for both the SR2 and SR3 CFD in Figure 7.30 which shows the sensitivity of Γ^* to the power coefficient over a range of operating conditions.

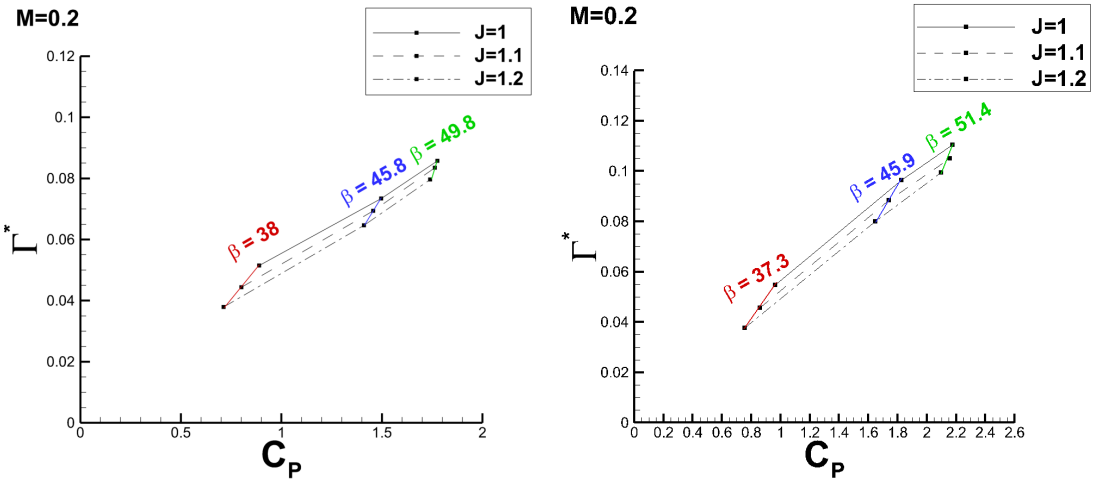

(a) SR2

(b) SR3

FIGURE 7.30: Multidimensional maps of Γ^* versus C_P for SR2 and SR3 where J is the advance ratio and β reference pitch angle

7.7.2 Tip vortex strength correlation conclusions

The method used to calculate the tip vortex strength using CFD has been validated against PIV with reasonable agreement. The peak bound circulation is a good approximation of the tip vortex strength over a range of thrust coefficients. It does however tend to break down at the higher thrust conditions. Correlations have been developed to predict the non-dimensional circulation parameter, Γ^*, as a function of both the lift and thrust coefficient with trends that represent the induced drag law of finite wing theory.

7.7.3 Vortex core size correlations

With correlations derived for the tip vortex strength, the next tip vortex parameter to consider is the vortex core size, r_c. Prior to the development of bespoke correlations using the CFD within this project the correlations used in CRPFAN will be analysed for their suitability.

7.7.3.1 Analysis of CRPFAN Cascade correlations

The correlations used in CRPFAN were developed by Majjigi[10] and are based on two cascade experiments by Mason and Marchman[31] and Grow[33]. With most of the data points in the final correlation for the tip vortex core size derived from the Mason and Marchman experiment. There are three key questions in the analysis of the correlations. Firstly, how do the measurements of the source experiments used compare to other similar experiments? Secondarily how well does the correlation model the core size from other cascade experiments? Thirdly, which is key to this project, how appropriate is it to use the fixed wing measurements for a CROR tip vortex generated from a rotating wing?

To address the first question measurements of the tip vortex core size from additional fixed wing cascade experiments were compiled. The measurements are from four sources and are summarised in Table 7.9. The four data sources include different wing sections such as NACA 0015 and NACA 0012, aspect ratios, incidence onto the blade and tip shape geometry at a variety of normalised measurements planes downstream of the wing trailing edge, x/c.

Author	Wing definition	AoA, α	Aspect Ratio	x/c	Tip geometry shape
Birch[55]	NACA 0015	0-18	1.49	1.5	Square
Lee[56]	NACA 0012	4-15	3.6	5	Square and circular
Zhou[57]	NACA 0012	8,16	1.6	0-5	Square
McAlister[58]	NACA 0015	12	9.6,8.1,6.6	0-6	Square

TABLE 7.9: Additional Cascade measurements summary

Figure 7.31 shows the relationship between the non-dimensional vortex core size, r_c/c, where c is the wing chord and the angle of attack (AoA) onto the blade, α. The core size is a strong function of the angle of attack, for example for the Birch[55] measurements for an increase in incidence from 2 to 18 degrees the non-dimensional tip vortex core size increases by 188 %.

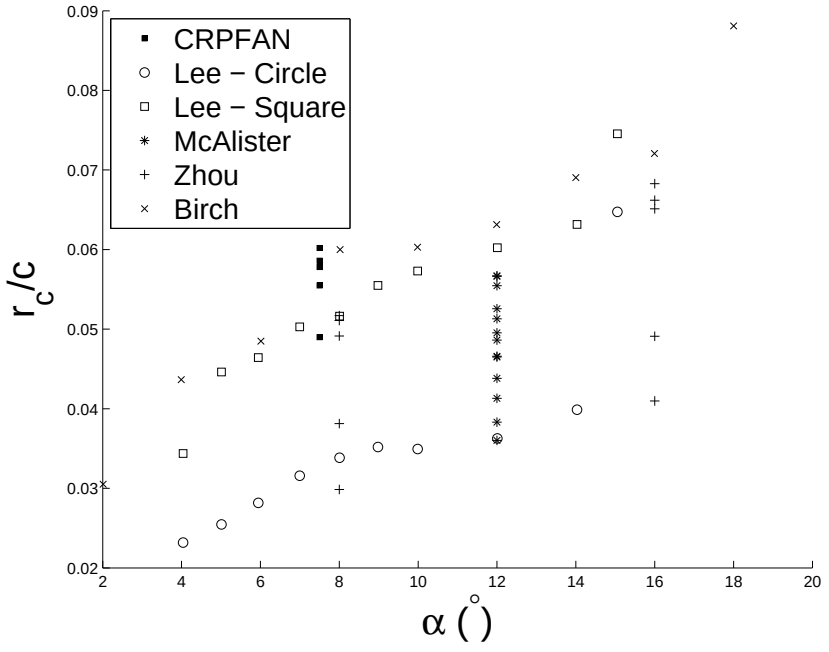

FIGURE 7.31: Comparison of cascade data as a function of angle of attack

The measurements used for the CRPFAN correlations fall in the range of other measurements with a tip vortex size ranging from approximately 5 to 6 % of the chord. This means the measurements which are used for the CRPFAN correlations are representative of similar studies. The next key question is how well does the correlation used in CRPFAN for the tip vortex core size predict the tip vortex core size over a range of measurements parameters. To answer this question the parameter $r^* = \frac{r_c}{\sqrt{C_L}c}$ was calculated for the available data and plotted against x/c with the CRPFAN empirical correlation defined in Equation 7.27 mapped on.

$$\frac{r_c}{c\sqrt{C_L}} = \frac{0.01584(x/c) + 0.0014}{0.184(x/c) + 1} \tag{7.27}$$

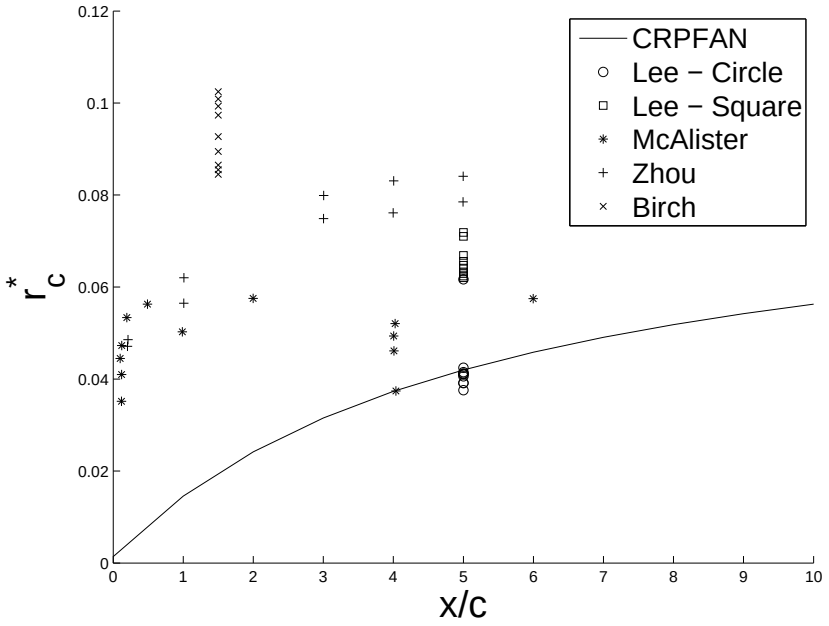

FIGURE 7.32: Comparison of CRPFAN correlation to additional cascade measurements

Although the correlation agrees well with one of the measurements of McAlister[58] and the circle tip measurements of Lee[56] in general there is a large range of scatter and the correlation simply does not capture the effect of aspect ratio, tip shape and incidence well enough. In general, over the range of values in Figure 7.32 the CRPFAN correlation under predicts the core size relative to the other measurements. Figure 7.33 shows an attempt by the author to reduce the scatter and to capture the effects of aspect ratio, incidence and tip shape better where $\bar{x}$ is x/c and $\bar{r_c}$ is $\frac{r_c}{c}$. The corresponding correlations from the regression of Figure 7.33 are shown in Equation 7.28 and Equation 7.29 for square and circular shaped wing tip geometries resepctivley.

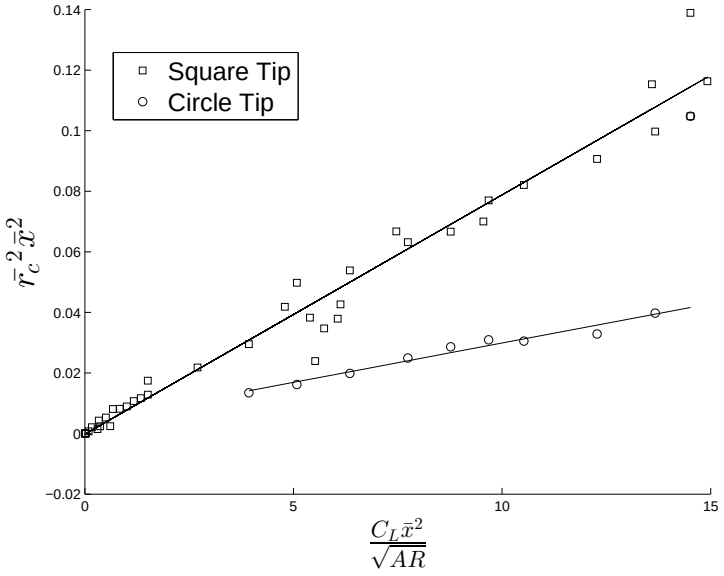

FIGURE 7.33: Correlation for combined cascade data

$$\bar{r_c}^2 = \frac{1}{\bar{x}^2}\left[0.0078\frac{C_L\bar{x}^2}{\sqrt{AR}} + 0.0008\right] \tag{7.28}$$

$$\bar{r_c}^2 = \frac{1}{\bar{x}^2}\left[0.0026\frac{C_L\bar{x}^2}{\sqrt{AR}} + 0.004\right] \tag{7.29}$$

To answer the third question and to determine how appropriate the CRPFAN tip vortex core size correlation is for a rotating wing such as a propeller the correlation was compared to the tip vortex core size calculated from the CFD flowfield for the SR2 and SR3. This comparison is shown in Figure 7.34. The first observation is the greater magnitude of the vortex core size calculated from the CFD relative to the CRPFAN correlations. This will be discussed in more depth in subsequent sections. The other noticeable observation is the large range of scatter in the data. This suggests that the correlation is not applicable to rotating wings. The conversion from fixed wing to rotating wing was very simplistic.

The regression constants in the linear rational function were kept constant when the lift coefficient, C_L, was changed to $\bar{C_l}$. Where $\bar{C_l}$ is the averaged outer 30 % of the propeller radial lift distribution. The same conversion was done for the wing chord, c, into $\bar{c}$. The reason for this outboard 30 % averaging was attributed to that being the pertinent region of the lift distribution for tip vortex generation. The axial distance downstream of the wing trialling edge, x/c, was also changed to $s/\bar{c}$ which is the total distance travelled by the vortex in its helical path.

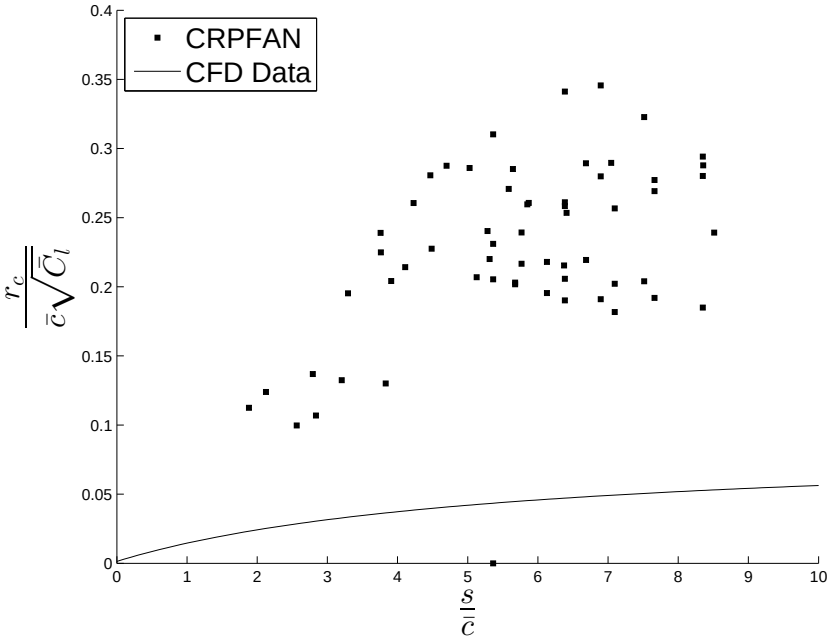

FIGURE 7.34: Comparison between CFD data and CRPFAN correlation for tip vortex core size

Analysis of the cascade tip vortex measurements confirms the need to develop a new correlation for the tip vortex core size for a propeller. The revised correlations are derived from CFD calculations for the SR2 and SR3 propeller. Figure 7.35 shows three correlations for the tip vortex core size of an advanced propeller sourced from CFD data. The cascade measurement analysis revealed a large dependency of the vortex core size on the incidence. For this reason the thrust coefficient , C_T, and peak sectional lift, $C_{l_{peak}}$, is raised to the power of two. Two versions of the C_T are used one which is based on the helical distance travelled by a vortex on its path, s/c, and the second is that axial distance from the pitch change axis x/c. The x/c version is more for reference than for use in an aeroacoustic calculation. Note that c is the reference chord at 75 %. The final correlations are shown in Equations 7.30, 7.31 and 7.32.

Only cases where the Vatistas model linear regression had a standard deviation (normalised by the maximum tangential velocity) of 5 % or less where used. This was used as a quality criteria to avoid the inclusion of erroneous data in the correlations. It should be noted that the applicability of the correlation is only for up to and below $\frac{C_T}{B}$ of 0.0875. Where B is the number of blades. Beyond this range there is lots of flow separation, a large leading edge vortex and possible vortex bursting. The correlation includes values from reference planes between x/c of 1.5 to 3 and within this region the vortex is fully rolled up and the effect of the distance travelled by the tip vortex will have a small effect on its core size.

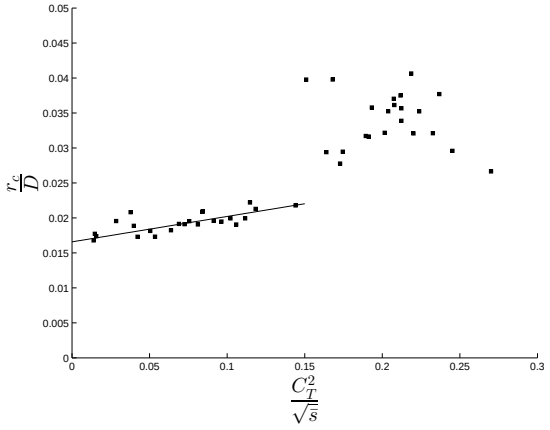

(a) C_T Helical

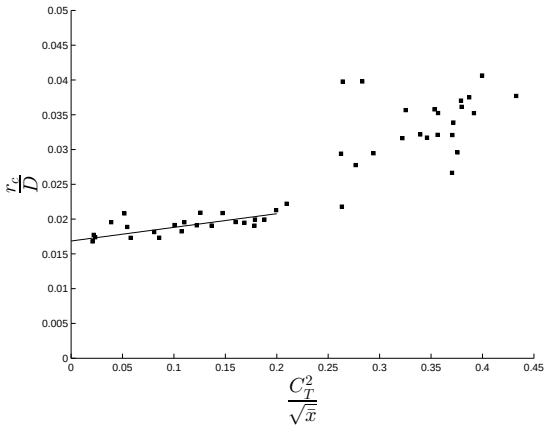

(b) C_T Axial

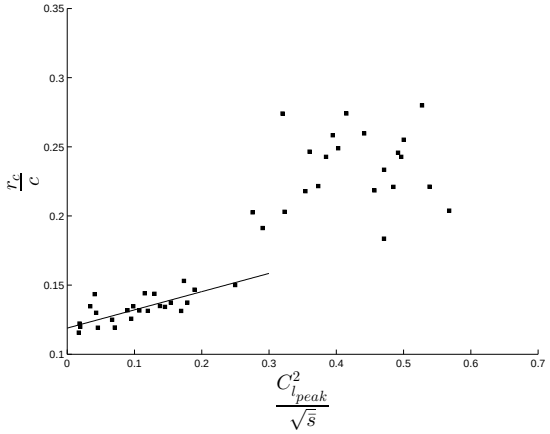

(c) C_l Helical

FIGURE 7.35: Vortex core size correlations for helical and axial evolution

$$\frac{r_c}{D} = 0.036\frac{C_T^2}{\sqrt{\bar{s}}} + 0.017 \tag{7.30}$$

$$\frac{r_c}{D} = 0.02\frac{C_T^2}{\sqrt{\bar{x}}} + 0.017 \tag{7.31}$$

$$\frac{r_c}{c} = 0.1318\frac{C_{l_{peak}}^2}{\sqrt{\bar{s}}} + 0.1189 \tag{7.32}$$

Figure 7.36 shows how at a location $s/\bar{c}$ of five downstream of the propeller pitch change axis and for a variation of the $\bar{C}_l$ from 0.1 to 1 comparison between the core size calculated using the CRPFAN correlations and revised CFD correlations. For a fair comparison a modified CFD correlation based on $\bar{C}_l$ was derived from the CFD data and is shown in Equation 7.33. The comparison highlights the greater magnitude of the tip vortex core size for the CFD and the greater influence of the source lift distribution which is not captured as much in the CRPFAN correlation.

$$\frac{r_c}{c} = 0.2535\frac{\bar{C}_l^{\,2}}{\sqrt{\bar{s}}} + 0.1157 \tag{7.33}$$

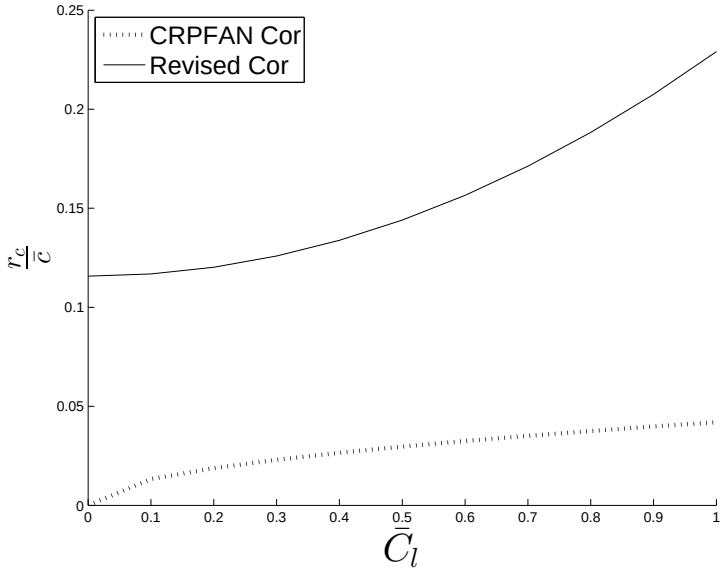

FIGURE 7.36: Comparison of revised correlation to CRPFAN for tip vortex core size

7.7.4 Aeroacoustic impact of bespoke tip vortex correlations

With revised correlations for the tip vortex core size, r_c, and circulation, Γ, and the assumption of a shape factor, n of 2 there is enough information to fully construct a Vatistas type vortex model. With the application of Equation 7.34 the maximum tangential velocity, $V_{\theta max}$, can be determined and used to calculate the tangential velocity distribution as a function of the vortex local radius.

$$V_\theta = V_{\theta_{max}} 2^{1/n} \left\{ \frac{\bar{r}}{(1+\bar{r}^{2n})^{1/n}} \right\} \tag{7.34}$$

Where:

$$V_{\theta_{max}} = \frac{\Gamma}{2\pi r_c} \tag{7.35}$$

The validation test case defined in Table 7.2 was used for the operating conditions to determine the aeroacoustic effect of using the revised tip vortex correlations derived using the CFD data. The correlations to calculate r_c and Γ and Equation 7.34 were integrated into CRPFAN and compared to a version of CRPFAN with the original correlations included. A Vatistas type vortex model is used for both to limit the degrees of freedom within the comparison. Therefore Case 2 is compared to Case 7, where Case 2 uses the CRPFAN correlations to calculate the tangential velocity distribution with a Vatistas type vortex model and Case 7 uses the revised tip vortex correlation from CFD

to calculate the distribution also a Vatistas type. Additional effects such as streamline descritisation, spatial orientation, trajectory and the vortex axial velocity component are not considered for this current comparison.

The results of this comparison are shown in Figure 7.37 with a sound pressure level contour map for Case 2 and Case 7 for comparison and OASPL residuals where it is Case 7 minus Case 2. The increase in tip vortex core size with the CFD correlations results in a significant increase in the interaction noise with a nearly uniform increase of approximately 16 dB over all observer angles. Additional directivity plots for six interaction tones are shown in Section D.1.6 of Appendix D where the noise increases beyond the experimental values.

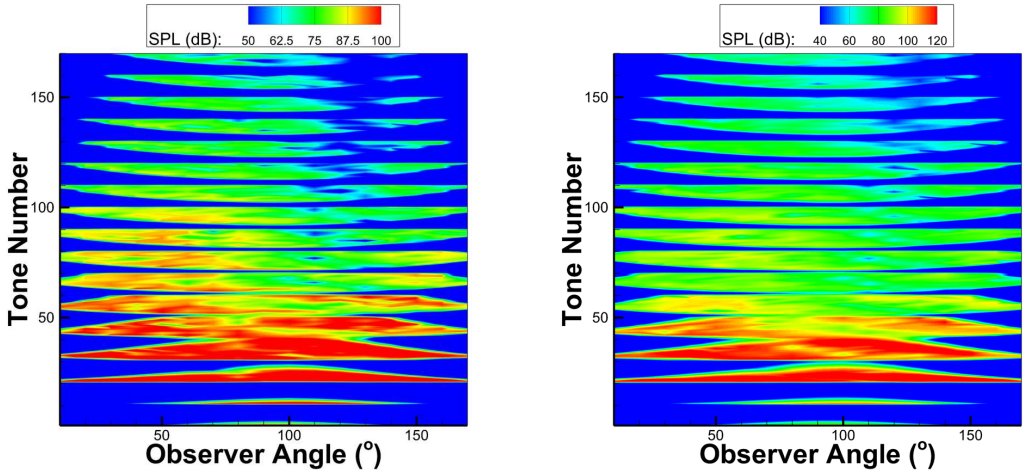

(a) Case 2

(b) Case 7

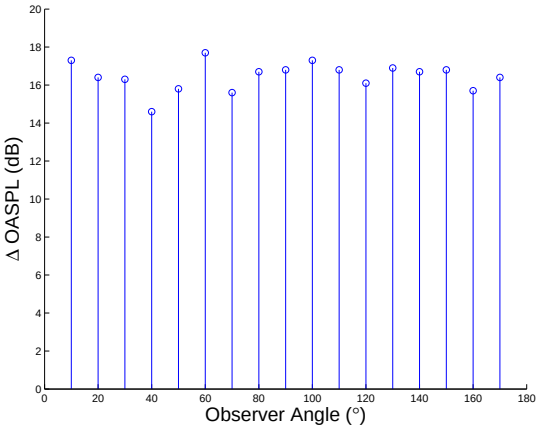

(c) Case 7 - Case 2 Residuals

FIGURE 7.37: Aeroacoustic effect of revised tip vortex correlations compared to CRP-FAN

Analysis of Tip Vortex Core Size

The tangential velocity profile calculated by CFD was compared to PIV for the open rotor analogue at $\beta = 26.4$, $M = 0.144$ with an RPM of 6875.5 at two chords downstream of the propeller pitch change axis. This comparison is shown in Figure 7.38, the tip vortex core size calculated with CFD is approximately three times that of the PIV.

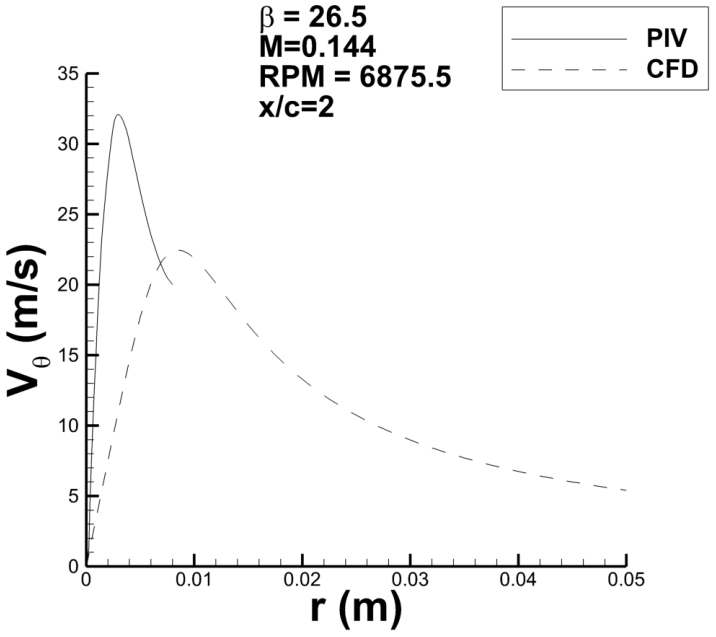

FIGURE 7.38: Comparison between CFD and PIV for radial V_θ distribution for two blade open rotor analogue

One of the reasons the tip vortex is larger is because the CFD model is very dissipative. The CFD model uses an eddy viscosity model approach which is based on the Boussinesq hypothesis and assumes isotropic turbulence[54]. Where flow is not isotropic such as in the vortex additional turbulent kinetic energy will be produced which effectively damps out the vortex which results in the larger core size and smaller tangential velocity which can result in obtaining the correct level of circulation, but for the wrong reason. This is one of the reasons for the curvature correction term used in conjunction with the SST turbulence model.

Attempts at a Reynold's Stress Model (RSM) were made using the quadratic pressure strain formulation. The advantage of an RSM model is that it does not have the isotropic turbulence assumption because the Reynold stresses are calculated individually. The disadvantage of an RSM model is the difficulty in achieving iterative convergence when using them. This was the case for models used in this study and convergence could not be achieved. The author made attempts at a tactical convergence strategy such as starting from an upwind solution and initialisation from a converged SST model for example. However, the attempts proved unsuccessful and iterative convergence was not achieved.

Another reason for the larger core size relative to the PIV is related to the spatial descritisation of the tip vortex. Grid sensitivity studies were completed for the SR2, SR3 and two blade analogue rotor meshes and the asymptotic range was achieved for each. However, the parameters used where the thrust and power coefficients which are integrated parameters which will be less sensitive to spatial descritisation than a tip vortex.

This is especially significant for the two bladed rotor when compared to the SR2 and SR3.The finest grids used for the two bladed rotor included 11.5 million nodes in the inner rotational domains. The two blade rotor domain has an azimuthal angle of 180 degrees. The SR2 and SR3 have eight blades and therefore an azimuthal angle of 45 degrees. With reference to Figure 7.39 the effect this large azimuthal angle on the spatial descritisation is evident. A vortex with a phase angle which locates the vortex closer to the centre of the domain will have more points per vortex core than a vortex which is located closer to the periodic boundaries with better quality lower aspect ratio cells. This is the disadvantage of using a fully structured grid and attempts were made to increase the mesh density but the 11.5 million nodes was at the limit of the memory of the meshing application at the time of use. The effect of increased spatial descritisation on the tip vortex tangential velocity profile at one plane downstream is shown in Figure 7.40. Where the coarse, medium and fine grids include 5.5, 7.5 and 11.5 million nodes in the inner rotational domain resepctivley.

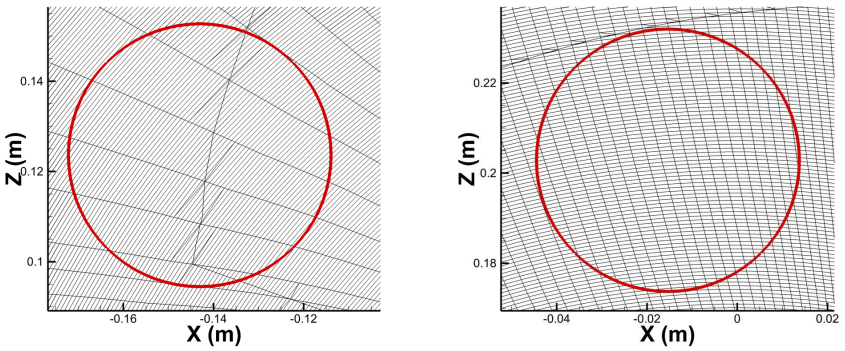

(a) Coarse Section

(b) Fine Section

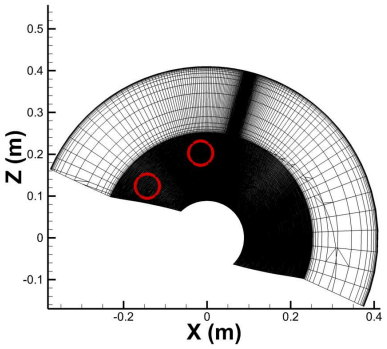

(c) Overview

FIGURE 7.39: Two blade analogue mesh density at different azimuthal locations

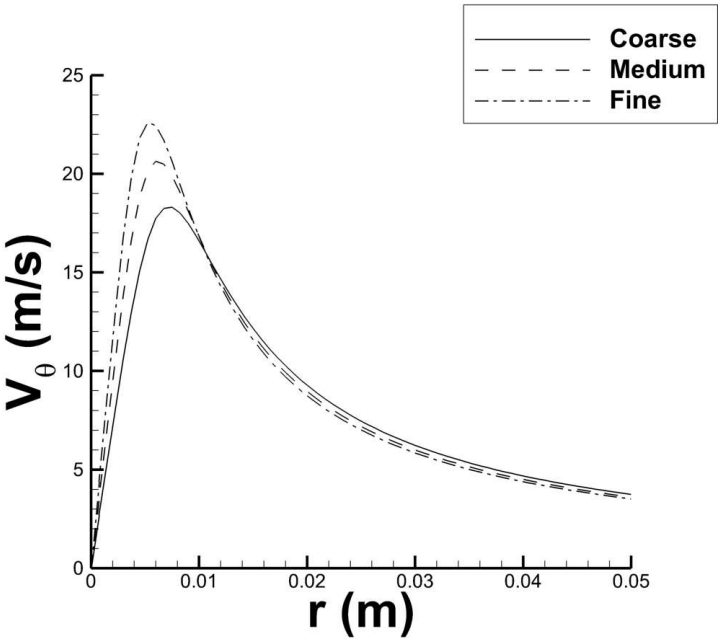

FIGURE 7.40: Effect of mesh density on V_θ distribution for two bladed rotor at β=22.8, M=0.144, rpm=6875.5 and x/c of 1

It is thought that the 'true' value of the tip vortex core size lies between the CFD and CRPFAN correlations. For example for the PIV and CFD comparison of two blade analogue rotor in Figure 7.38, using the lift distribution and helical path calculated by CFD the CRPFAN predicted tip vortex core size is 1.3 mm. This agrees well with the cascade measurement analysis where the CRPFAN correlations under predicted the tip vortex core size compared to other similar measurements. The correlations were derived from the SR2 and SR3 CFD models which will have a better spatial descritisation per vortex core for two reasons. Firstly, the two bladed analogue is operated at a lower loading conditions than the SR2 and SR3 for example the thrust coefficient per blade, C_T/B, range for the two bladed rotor was 0.01 to 0.05 but for the SR2 and SR3 it is 0.02 0.1 and the vortex core size will increase with C_T/B to the power of two. The second reason is highlighted in Figure 7.39 which is the difficulty in creating a grid with a uniform azimuthal spatial descritisation for the 180 degree domain.

However, as a conservative approach a correction factor will be applied to the tip vortex core size. The ratio of the $\frac{r_{cPIV}}{r_{cCFD}}$ is used to adjust the tip vortex core size to the levels of the PIV measurement and increase the maximum tangential velocity accordingly to keep the circulation constant, which compared favourably to the PIV in previous comparisons.

7.7.5 Vortex core size correlation conclusions

Revised correlations for the tip vortex core size have been developed using the CFD flowfield data for the SR2 and SR3. When these correlations where integrated into CRPFAN the interaction noise increased by 16 dB relative to the CRPFAN correlations. A single test case comparison between the two blade analogue CFD and PIV showed the CFD model to produce a larger core size and smaller maximum tangential velocity. Possible reasons for this include the spatial descritisation of the 180 ° domain at certain azimuthal angles combined with the assumptions implicit to an eddy viscosity model based CFD approach. It is recommended that the correlations are tested against high fidelity non-intrusive aerodynamics measurements over a wide range of flowfield conditions to fully assess their suitability.

7.8 Synthesis

The individual aspects of tip vortex modelling have been assessed independently. Here their combined aeroacoustic effect is assessed. It is done in three stages as outlined in Table 7.10. There are three versions of Case 8 to be considered. Case 8a which includes all the recommended vortex model approaches such as using a Vatistas type vortex model, increased spatial descritisation of CRPFAN, correct modelling of the vortex spatial orientation, the tip vortex axial velocity component, the revised tip vortex trajectory model and the correlations for the tip vortex parameters derived from CFD. Case 8b includes all the effects except the original CRPFAN tip vortex correlations are included instead of the revised ones derived for CFD. Case 8c used the correlations derived from CFD but with the correction factor of one third core size applied.

Vortex feature considered	Case 8a	Case 8b	Case 8c
Vatistas model	✓	✓	✓
Increased streamlines	✓	✓	✓
Elliptical vortex spatial orientation	✓	✓	✓
Vortex axial velocity component	✓	✓	✓
Revised tip vortex trajectory model	✓	✓	✓
Revised tip vortex parameter correlations	✓	x	x
Revised tip vortex parameter correlations adjusted for r_c	x	x	✓

TABLE 7.10: Synthesis Matrix

The most dominant contributing source are the revised tip vortex correlations for r_c, Γ and the calculated maximum V_θ. The inclusion of the correlations add an extra 10 dB in some cases on top of the other vortex modelling effects. The use of a correction for the core size reduces the interaction noise. But the levels are still very high, this is because as the core size is reduced, to maintain the circulation the maximum tangential velocity also increases. Therefore the net reduction in noise is mostly negligible. Relative to experimental data for interaction tones Cases 8a and 8b over predict the noise as shown in Section D.1.7 of Appendix D.

However, this is just for one test case due to the limited amount of acoustic data available in the open literature which have known propeller and geometry conditions. It is therefore suggested for further research that acoustic calculations using the revised correlations are compared to experiment such as flight testing or anechoic wind tunnel testing to really assess the suitability of the correlations. Alternatively, comparisons to high fidelity PIV or other non intrusive measurement techniques such laser Doppler velocimetry (LDV) or hot wire anemometry be used to obtain suitable correction factors for tip vortex core size and maximum tangential velocity over a range of operating conditions.

The sound pressure level contour maps Case 8a, 8b and 8c including their respective overall sound pressure level residuals relative to Case 2 are shown in Figure 7.41.

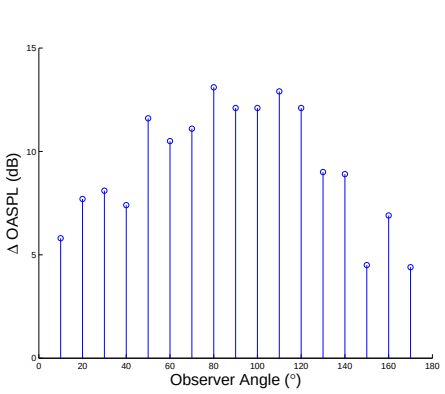

(a) Case 8a - Case 2

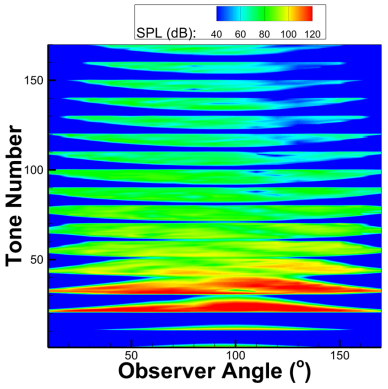

(b) Case 8a

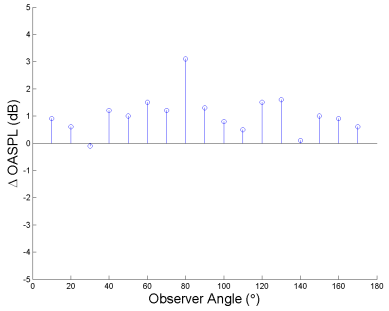

(c) Case 8b - Case 2

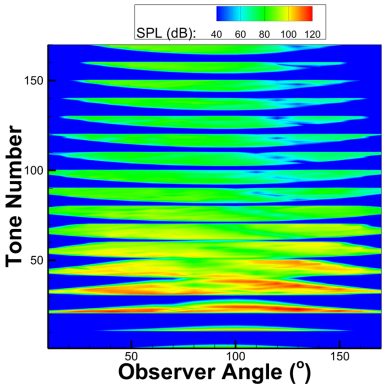

(d) Case 8b

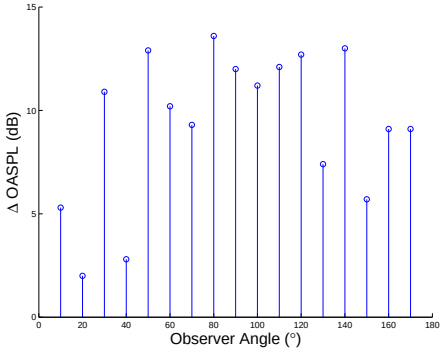

(e) Case 8c - Case 2

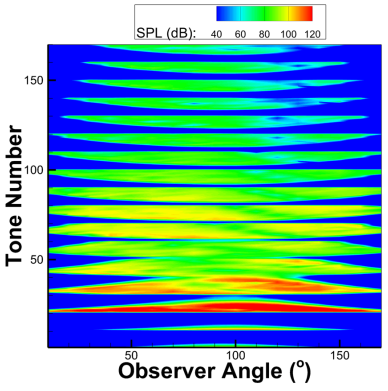

(f) Case 8c

FIGURE 7.41: Interaction noise for Cases 8a, 8b and 8c

The agreement between CRPFAN version 8b and experimental data is better than for Cases 8a and 8c and is shown in Figure 7.42. This is because they interaction noise is not offset by the large tip vortex parameters. To determine which vortex model aspect is the most significant Case 2, 3, 4, 5 and 6 overall sound pressure levels as a function

of observer angle are compared to each other as shown in Figure 7.43. The operating conditions are again the same as defined in Table 7.10. The degrees of freedom for each case are summarised in Table 7.11.

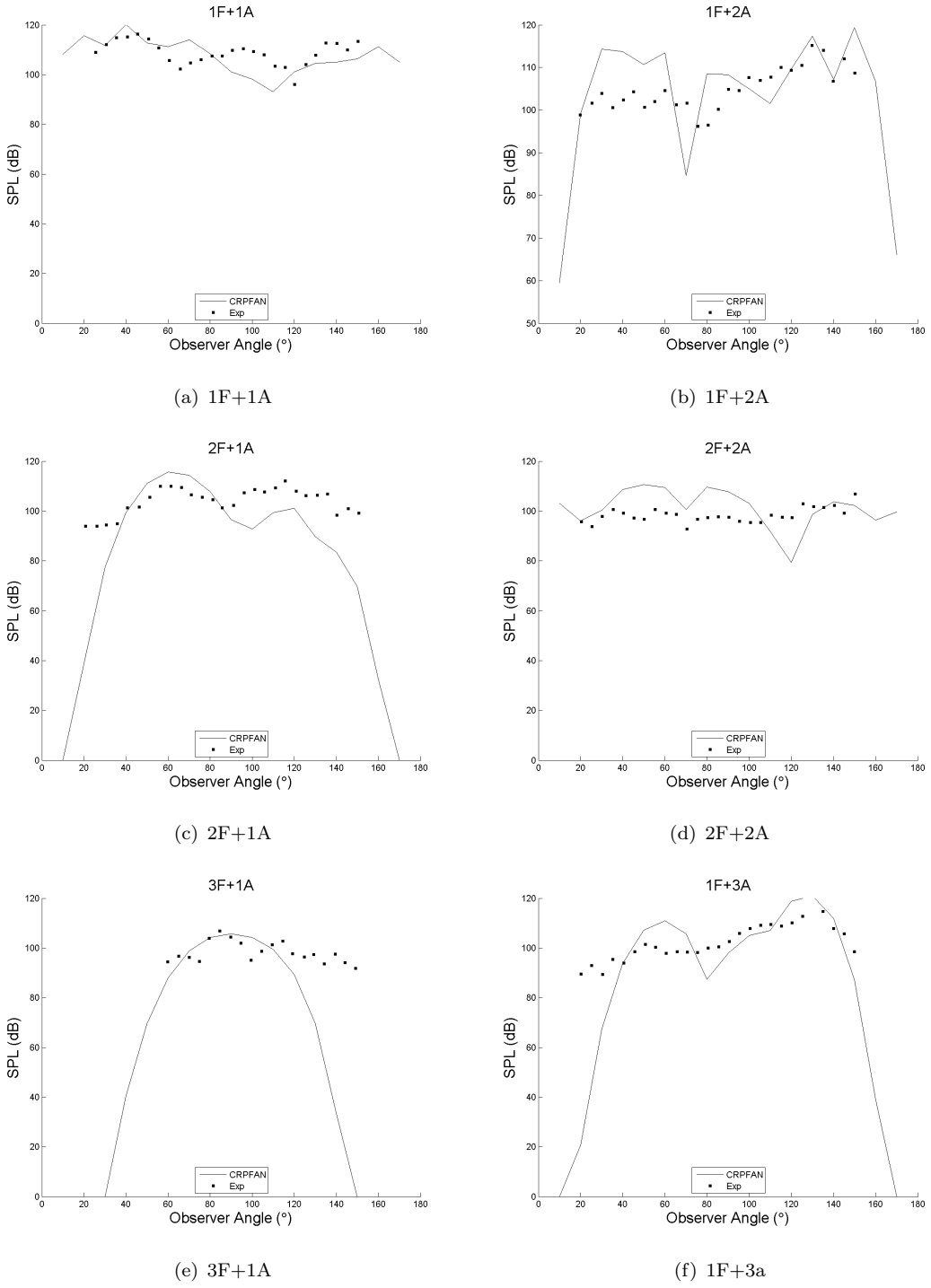

FIGURE 7.42: Difference between experiment and CRPFAN version 8b

Vortex feature considered	Case 2	Case 3	Case 4	Case 5	Case 6
Vatistas model	✓	x	x	x	x
Increased streamlines	x	✓	x	x	x
Elliptical vortex spatial orientation	x	x	✓	x	x
Vortex axial velocity component	x	x	x	✓	x
Revised tip vortex trajectory model	x	x	x	x	✓

TABLE 7.11: Synthesis Matrix

The most dominant source of noise addition is the vortex axial velocity component contributing up to 3 dB near the propeller plane of rotation. Conversely, the revised trajectory model tends to reduce the noise relative to the baseline model of Case 2 with overall sound pressure level reductions of up to 3 dB. The general impact of the vortex spatial orientation and increased streamline descritisation is to increase the noise in the range of 1 to 2 dB. Even though the different aspects of tip vortex modelling have different levels of effect on the interaction noise as demonstrated in Figure 7.44 it does not mean that the aspect which has the lowest effect should be ignored. Every aspect considered is suggested because they are perceived as an increase in the state of the art of tip vortex modelling and analysing each term individually eliminates possible synergistic effects between them.

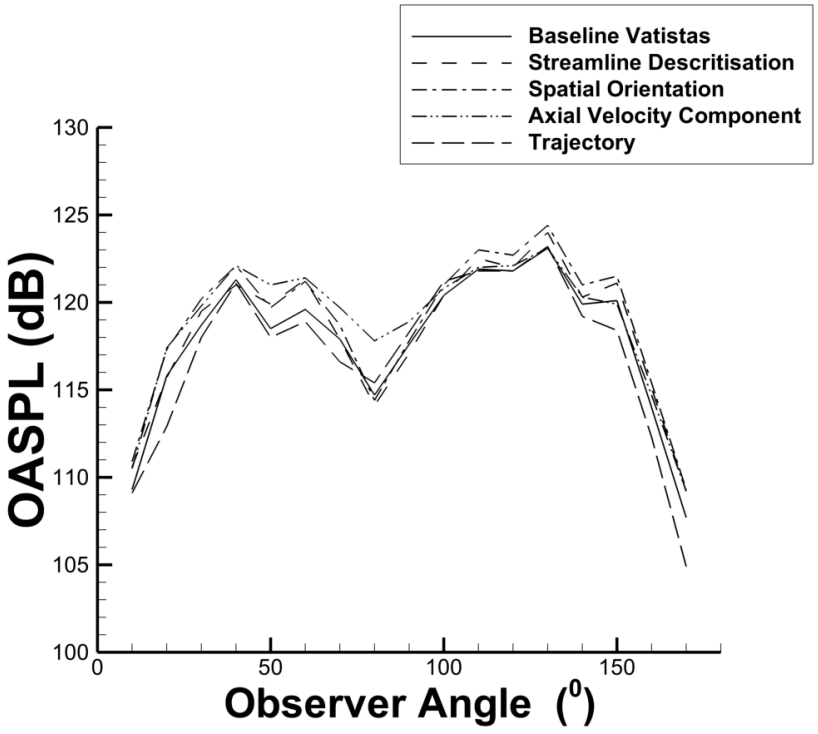

FIGURE 7.43: Breakdown of vortex modelling aspects for overall sound pressure level

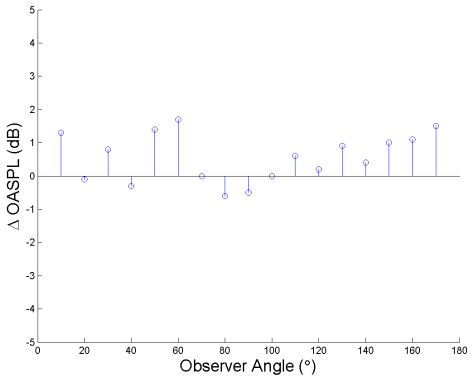

(a) Case 3 - Case 2

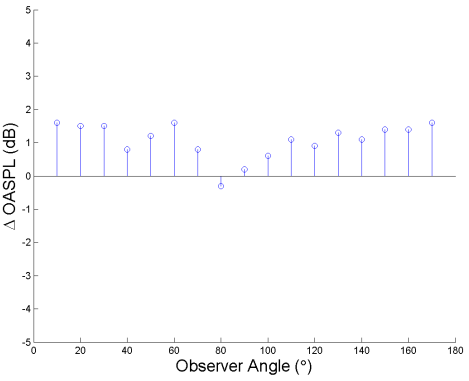

(b) Case 4 - Case 2

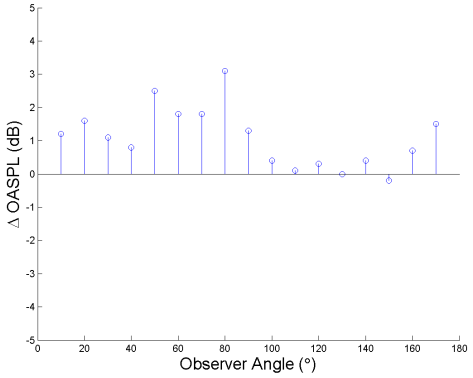

(c) Case 5 - Case 2

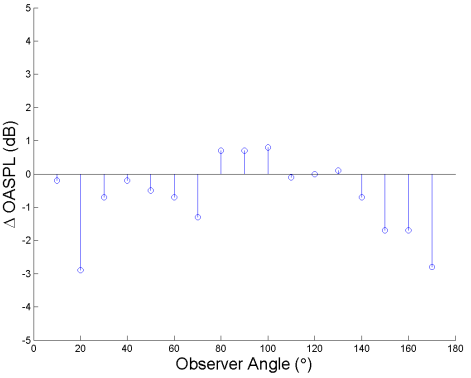

(d) Case 6 - Case 2

FIGURE 7.44: Overall sound pressure level breakdown for each case

7.9 Aeroacoustic sensitivity to source aerodynamics

7.9.1 Source aerodynamics

Section 7.9 investigates the significance of the source aerodynamics on the fidelity of the aeroacoustic calculation. The input files used for Cases 2 to 8 were obtained from[5] where an Euler code was used to obtain the radial lift distribution.

In the absence of detailed flowfield information either from CFD or experiment, in order to use CRPFAN a lift distribution is required to perform an aeroacoustic calculation. A method of obtaining this could be a strip theory code. Here two different strip theory codes are used to generate a radial lift distribution and compared to CFD. The three lift distributions are then input into CRPFAN to determine what the aeroacoustic significance of the source of the input aerodynamics is. The two strip theory codes are a Blade Element Momentum Theory (BEMT) code developed in conjunction with an MSc student[59] and a Theodorson Method described in Appendix E. The SR2 propeller blade will be used for the comparison under three different loading conditions defined in Table 7.12.

Parameter	Low	Medium	High
β (°)	38	45.8	49.8
J	1.2	1.2	1.2
M	0.2	0.2	0.2

TABLE 7.12: Non dimensional parameters for input aerodynamics sensitivity study

The order of fidelity for the aerodynamic methods used are BEMT, Theodorson Method and CFD with CFD considered the highest. The BEMT is the simplest and ignores compressibility effects, the radial component of flow velocity and is generally considered to over predict thrust and under predict power. With a typical over prediction of theoretical efficiency of 5 - 10%[60]. The Theodorson Method code is a vortex theory similar to a Goldstein Method code except wake contraction effects are considered unlike the Goldstein method which uses a Betz style rigid wake model[61]. The radial lift distribution for the low, medium and high loading conditions are shown in Figure 7.47. As the loading increases with increasing setting angle the flow becomes more separated and the BEMT code tends to over predict the lift distribution as expected. The Theodorson method is higher fidelity than the BEMT code and predicts the lift distribution relative to the CFD better than the BEMT code. However, both the BEMT and Theodorson method poorly resolve the list distribution in the outer span of the blade where there is the most separated flow.

To verify the flowfield features observed in the lift distributions, for each case wall shear streamlines with contours of static pressure are shown from the CFD in Figure 7.46.

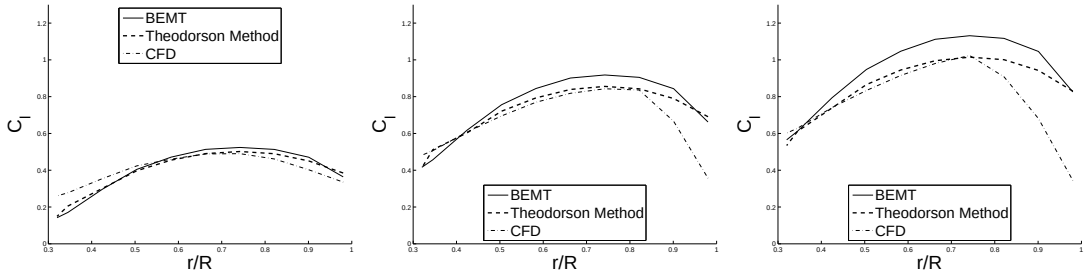

(a) Low Loading (b) Medium Loading (c) High Loading

FIGURE 7.45: Source lift distributions

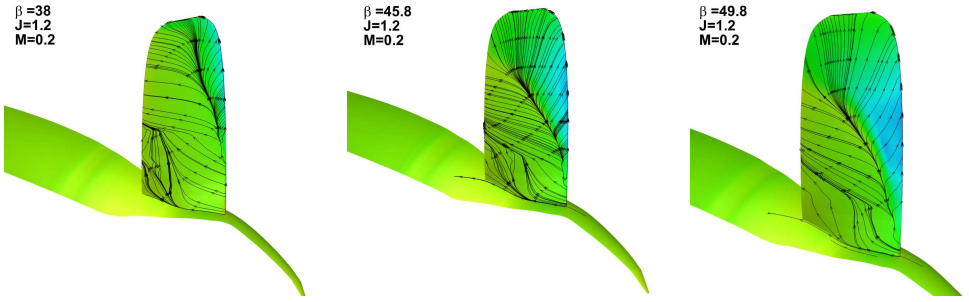

(a) Low Loading (b) Medium Loading (c) High Loading

FIGURE 7.46: Flowfield for each case

7.9.2 Aeroacoustic effect

For the low, medium and high loading cases the three source lift distributions were input into CRPFAN for both Case 2 and Case 8b. The configuration in CRPFAN uses two rows of eight counter rotating SR2 propeller blades separated by a distance of 0.24 tip diameters. The shaft power is kept constant and only the source lift distribution and blade setting is angle is changed for each case. The first aspect to consider is the steady noise due to thickness and loading of the propeller. The front rotor fundamental harmonic directivity for each case is shown in Figure 7.47. The effect of the source aerodynamics on the steady loading noise negligible. The thickness noise should be unaffected for a constant propeller geometry and loading noise is more dependent on the shaft power which is kept constant here to isolate the effect of the input radial lift distribution. Note the steady noise will be the same for Case 2 and Case 8b because the modifications are only pertinent to the unsteady interaction noise.

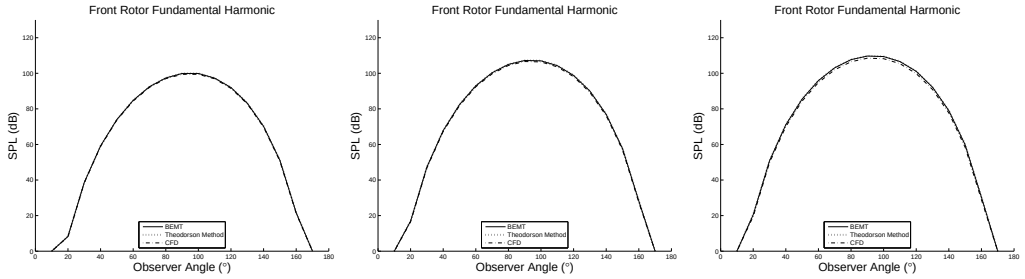

(a) Low Loading (b) Medium Loading (c) High Loading

FIGURE 7.47: Front rotor fundamental harmonic for different loading cases and source lift distributions

The effect of the source lift distribution is more significant for interaction noise sources. The CFD source lift distribution calculates the lowest level of interaction noise because the lift distribution on the outer span of the blade is lower, which will result in tip vortex with smaller core size and lower tangential velocity. For CRPFAN version Case 2a a difference of approximatively 2 dB is present between the CFD and BEMT source inputs for the high loading cases. This difference increases to approximately 3db for CRPFAN version 8b because of the additional vortex modelling aspects included in this version. The overall sound pressure level between the BEMT and Theodorsen Method are very similar because of the similarity of the source lift distributions. The values for tip vortex core size and maximum tangential velocity are shown in Figure 7.50 which demonstrates the larger properties for the BEMT and Theodorson Method relative to CFD.

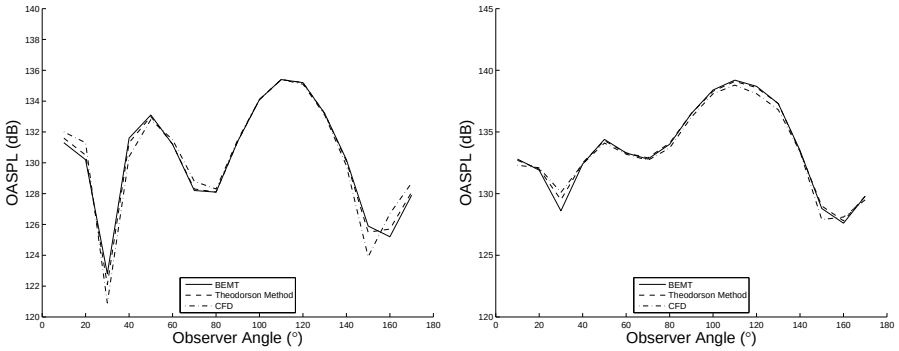

(a) Low Loading

(b) Medium Loading

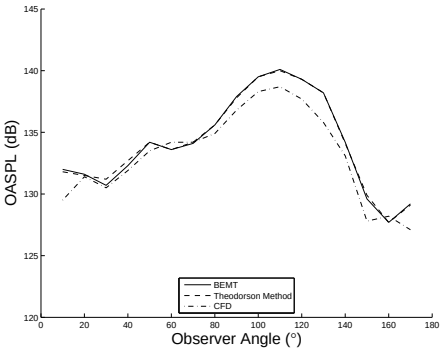

(c) High Loading

FIGURE 7.48: Overall sound pressure level for different loading conditions and source lift distribution for CRPFAN version 2

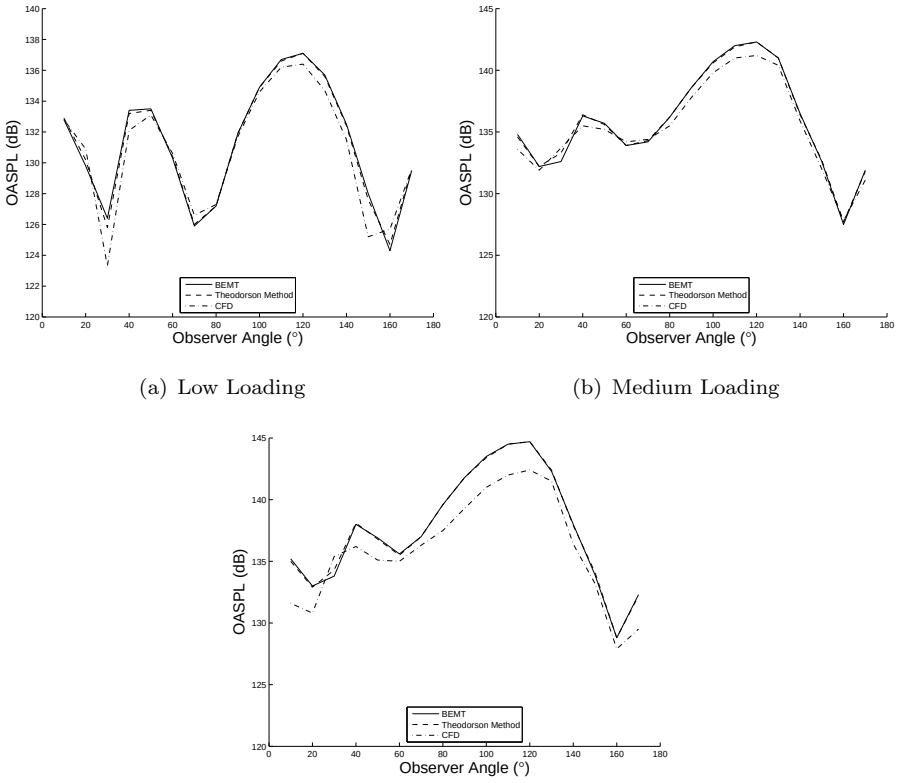

(a) Low Loading

(b) Medium Loading

(c) High Loading

FIGURE 7.49: Overall sound pressure level for different loading conditions and source lift distribution for CRPFAN version 8b

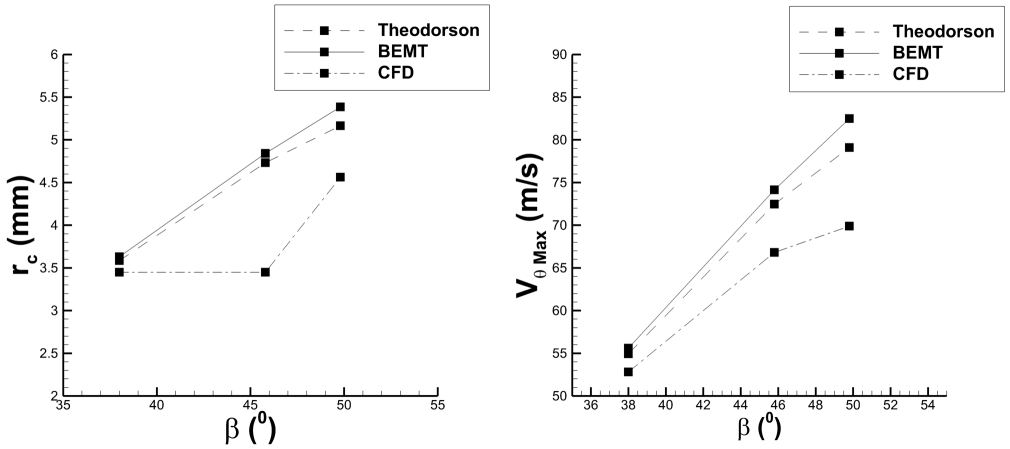

(a) Tip vortex core size

(b) Maximum tangential velocity

FIGURE 7.50: Sensitivity of tip vortex parameters to source aerodynamic method with increased blade loading

7.9.3 Effect of source aerodynamics conclusions

The method of obtaining the input aerodynamics has a negligible effect on the steady loading noise but does have an effect on the unsteady interaction noise. The most noticeable difference between the strip theory codes and CFD are at the tip region of the blade where there is flow migration and separation which increases with increasing loading. The use of a strip theory code can lead to predictions of the tip vortex parameters such as the core size and maximum tangential velocities higher than what would be calculated using a CFD source distribution. However, it has been demonstrated that for first order approximations using a preliminary design tool such as CRPFAN the acoustic code can be coupled with an aerodynamic strip theory code in the absence of detailed flowfield measurements.

Chapter 8

Conclusions

During the course of the project the following conclusions were found:

- The maximum value of the tip vortex tangential velocity has a bigger influence on interaction noise than the tip vortex core size.
- The datum number of streamlines used CRPFAN is too few and it is recommended to increase the spatial resolution of strip theory based noise prediction tools in order to fully capture the disturbance field of the vortex.
- The vortex spatial orientation as seen by the aft rotor influences the interaction noise. A vortex with an elliptical spatial orientation will generate more noise than a circular vortex with the effect most significant at lower frequencies.
- The vortex axial velocity component can be modelled using a Vatistas type distribution and it is 'wake-like' relative to the freestream velocity.
- The level of sweep and loading of the propeller effects how 'wake-like' the axial velocity is.
- A Vatistas type vortex model can be used to model the tip vortex of an advanced propeller blade. A tip vortex generated by the swept SR3 can be modelled by a Vatistas type vortex model over a wider range of operating conditions than the straight bladed SR2.
- The peak bound circulation is a good method of approximating the strength of the tip vortex.
- The CFD model using CFX has good agreement with PIV for the tip vortex strength. However, it tends to over predict the tip vortex core size and under predict the maximum tangential velocity.

- The aerodynamic method used to obtain the source lift distribution as an input to CRPFAN has a negligible effect on the steady noise but it influences the unsteady interaction noise.

Some of the key outcomes of the project include:

- Quantified analysis of the effect of tip vortex parameters on the interaction noise
- A disturbance field tool which can be used to determine the harmonic content of a vortex
- A detailed analysis of the suitability of CRPFAN vortex model and correlations
- Empirical correlations to predict the size of a tip vortex for a fixed wing
- Validated CFD model for both the SR2 and SR3 propeller blades using a method of generating structured grids with a quick turnaround time
- Correlations to model the tip vortex trajectory as a function of propeller non-dimensional operating parameters
- Correlations to model tip vortex axial velocity component as a function of propeller non-dimensional operating parameters
- Correlations to predict the tip vortex strength and core size as a function of propeller non-dimensional operating parameters
- A method to assess the effect of source aerodynamic methodology on noise prediction tools

Novelty

The novel aspect of this project is the examination of the effects of tip vortex parameters on open rotor interaction noise and the development of bespoke correlations to predict the tip vortex parameters and improved modelling techniques suggestions.

Chapter 9

Future Work

Chapter 9 offers a description of recommended work which can be used in conjunction with the findings from this thesis and also address some of its deficiencies.

Evaluation of tip vortex correlations

One of they key aspects of the project was the development of tip vortex correlations from CFD flowfield data. Partly due to the time and computational resources available a steady-state RANS model was used to generate the flowfield. It is recommended that unsteady CFD is performed on a similar configuration to identify how significant the transient effects are to the tip vortex parameters. Similarly, the eddy viscosity based RANS method should be compared to a Reynolds Stress Model (RSM) where possible, to determine how much dissipation occurs as a result of the isotropic turbulence assumption inherent to all eddy viscosity based turbulence models. Additionally, non RANS based turbulence models such as Large Eddy Simulation (LES) and Detached Eddy Simulation (DES) would also be useful studies.

Additional comparisons should be made to a detailed set of PIV (or any other high fidelity non-intrusive method) measurements over a range of operating conditions. The correlations were derived from the SR2 and SR3 propeller blades due to the availability of their geometries. Since the 1980s when these propellers were developed the open rotor blade designs have evolved and a comparison between the vortical flowfield generated by a modern design and the ones presented in the thesis for the SR2 and SR3 would be beneficial for future progress in open rotor design.

Additional aerodynamic input methodologies

Section 7.9 evaluated the significance of the aerodynamic methodology used to generate inputs lift distributions for a noise prediction code such as CRPFAN. The three methodologies were BEMT, Theodorson Method and CFD, it would be interesting to see how other aerodynamic methodologies compare for example a lifting line theory and

Goldstein method code. It is not expected that the aerodynamic input will influence the steady noise but it will have an impact on the the interaction noise.

Acoustic comparison

Only a limited set of acoustic measurements were available for comparison with CRP-FAN. A good evaluation of CRPFAN and the bespoke correlations would be to compare its results to a comprehensive set of interaction noise measurements derived from anechoic wind tunnel tests on an open rotor with a modern design.

Appendix A

Disturbance Field Model

Appendix A includes details of the coordinate systems and methodology of the disturbance field model used in the thesis. The disturbance field model is used for two key reasons, firstly, to visualise the tip vortex and its velocity distributions in a sector representative of the blade to blade spacing of a CROR stage and secondarily to determine the harmonic content of a tip vortex which helps determine the radial extent of the disturbance field from the tip vortex centre for example.

A.1 Disturbance Field Model - Process

The flowfield domain is shown as a schematic in Figure A.1 where a tip vortex is imposed onto the centre of the domain in the azimuthal direction and located at a radial location representative of the tip radius of a propeller blade. The tip vortex is originally defined in a coordinate system local to the tip vortex where the radius is defined as the distance from the tip vortex centre. However, the tip vortex interaction mechanism is between the front rotor tip vortex and the aft blade row and needs to be defined in a coordinate system relative to a global coordinate system.

The process begins with creating the domain shown in Figure A.1 and imposing a tip vortex described by a Vatistas model in a vortex local coordinate system. The tangential velocity distribution is then converted into a global coordinate system. The flow field for a vortex in both the local and global coordinate system are shown in Figure A.2. Section A.2 includes more details of the coordinate systems and defining equations. With reference to Figure A.3 which highlights the process of obtaining the PSD disturbance field from the source velocity field in a global coordinate system. The tangential velocity in a global coordinate system, V_{θ_g}, as a function of the azimuthal angle, θ_g, is Fast Fourier Transformed and the power spectral density (PSD) is calculated. Shown is the velocity at two section one and two tip vortex core radii away from the tip vortex centre. The contour map of PSD is generated from every radial section.

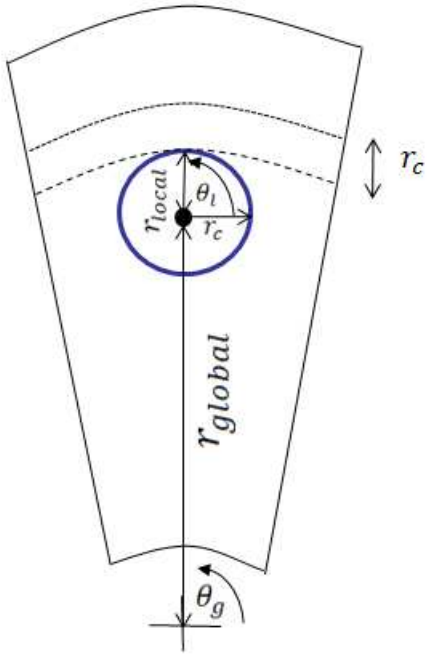

FIGURE A.1: Disturbance field schematic

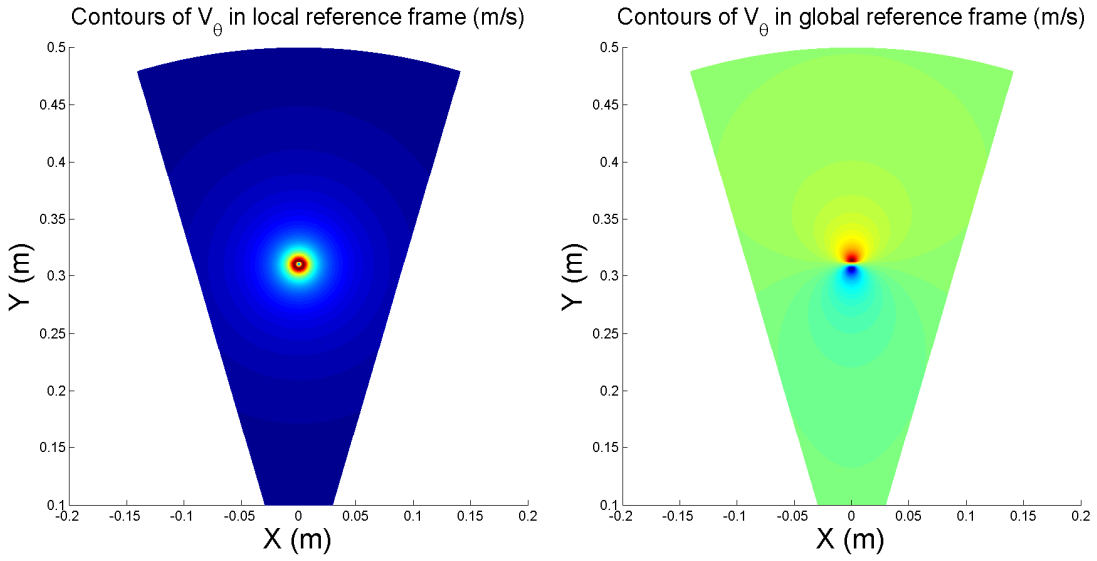

(a) Local (b) Global

FIGURE A.2: Contours of V_θ in a local and global coordinate system

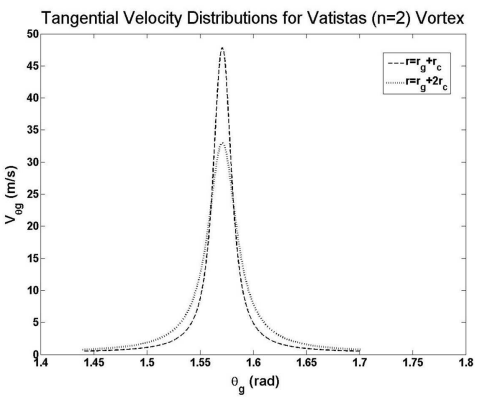

(a) V_θ Sections

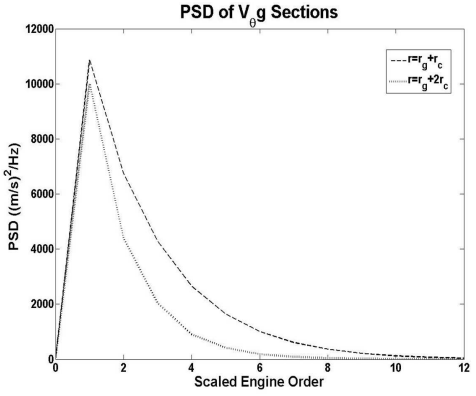

(b) PSD Sections

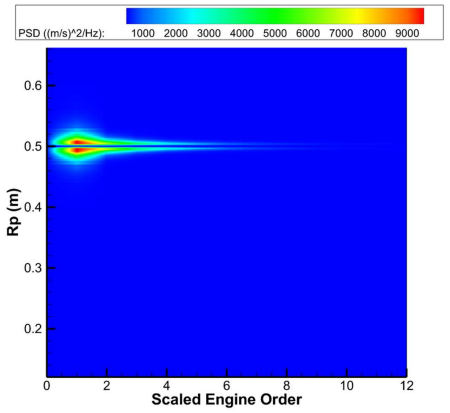

(c) PSD Contour Map

FIGURE A.3: Sequence of events to obtain PSD contours of vortex disturbance field

A.2 Disturbance Field Model - Coordinate systems

Figure A.4 is a simplified diagram of the coordinate system used to calculate $V_{\theta global}$ from $V_{\theta local}$. Figure A.5 is then a more detailed definition of the coordinate system from which the defining equations are derived.

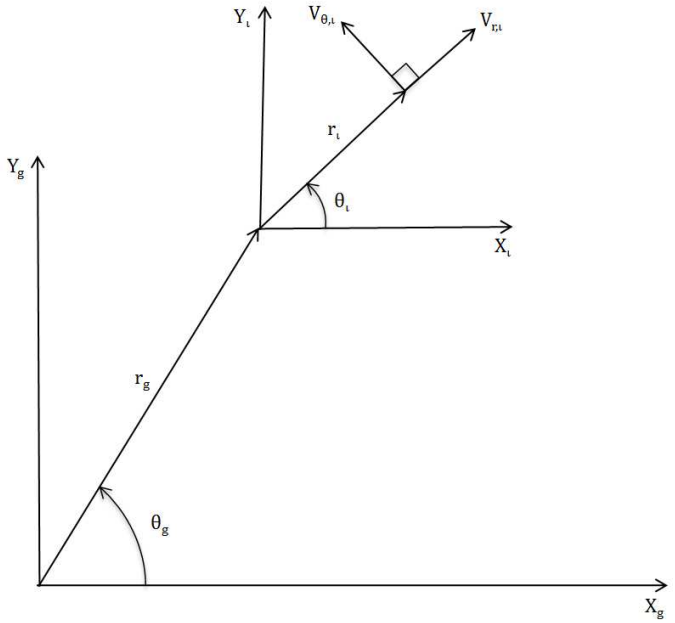

FIGURE A.4: Simplified coordinate system for disturbance field velocity field

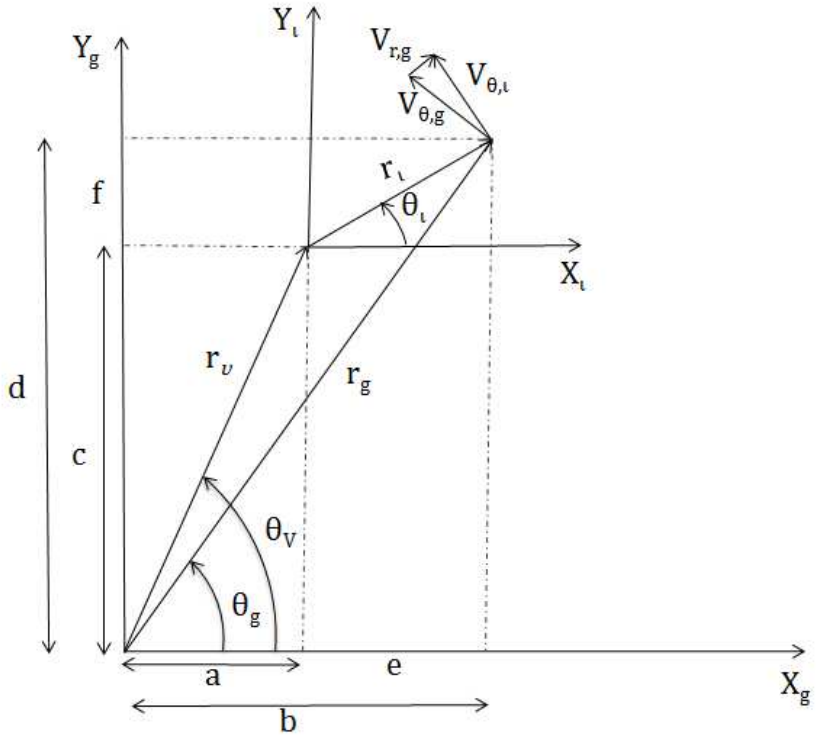

FIGURE A.5: Detailed coordinate system for disturbance field velocity field

From the coordinate system in Figure A.5

$$a = r_v \cos\theta_V \tag{A.1}$$

$$b = r_g \cos\theta_g \tag{A.2}$$

$$c = r_v \sin\theta_V \tag{A.3}$$

$$d = r_g \sin\theta_g \tag{A.4}$$

$$e = b - a = r_g \cos\theta_g - r_v \cos\theta_V \tag{A.5}$$

$$f = d - c = r_g \sin\theta_g - r_v \sin\theta_V \tag{A.6}$$

$$\theta_l = \tan^{-1}(\frac{f}{e}) \tag{A.7}$$

$$V_{\theta,g} = V_{\theta,l} cos(\theta_g - \theta_l) \tag{A.8}$$

$$V_{r,g} = V_{\theta,l} sin(\theta_g - \theta_l) \tag{A.9}$$

Use of the cosine rule to calculate the radius in the vortex local coordinate system, r_l:

$$r_l^2 = r_v^2 + r_g^2 - 2 r_g r_v cos(\theta_g - \theta_l) \tag{A.10}$$

The tangential and radial velocity components in a local and global coordinates are then related by:

$$V_{\theta,g} = V_{\theta,l} cos(\theta_g - \theta_l) \tag{A.11}$$

$$V_{r,g} = V_{\theta,l} sin(\theta_g - \theta_l) \tag{A.12}$$

The Cartesian velocity components in both local and global coordinate systems then defined as:

$$V_{x,g} = -V_{\theta,g} sin\theta_g + V_{r,g} cos\theta_g \tag{A.13}$$

$$V_{y,g} = V_{\theta,g} cos\theta_g + V_{r,g} sin\theta_g \tag{A.14}$$

$$V_{x,l} = -V_{\theta,l} sin\theta_l + V_{r,l} cos\theta_l \tag{A.15}$$

$$V_{y,l} = V_{\theta,l} cos\theta_l + V_{r,l} sin\theta_l \tag{A.16}$$

Where:

$$V_\theta(\bar{r}) = \frac{\Gamma}{2\pi r_c} \left\{ \frac{\bar{r}}{(1 + \bar{r}^{2n})^{\frac{1}{n}}} \right\} \tag{A.17}$$

$$V_{r,l} = \frac{\upsilon 2(n+1)\bar{r}^{2n}}{r_c(1 + \bar{r}^{2n})} \tag{A.18}$$

Appendix B

Additional CFD Content

Appendix B includes additional CFD content such as close up views of the mesh, grid refinement studies and the coordinate transformation in the vortex cross plane.

B.1 Additional mesh views

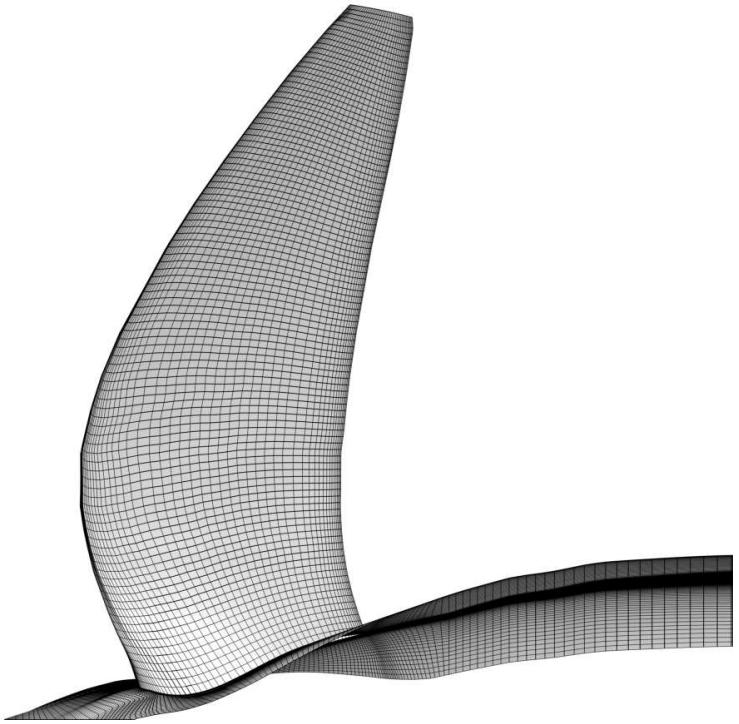

FIGURE B.1: Close up view of mesh on SR3 propeller blade

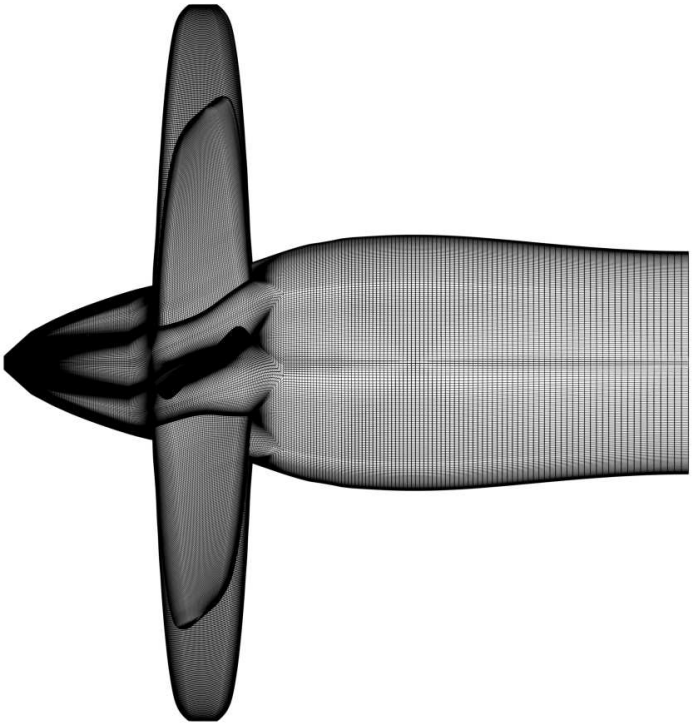

FIGURE B.2: Full circumference view of mesh on SR2 propeller blade

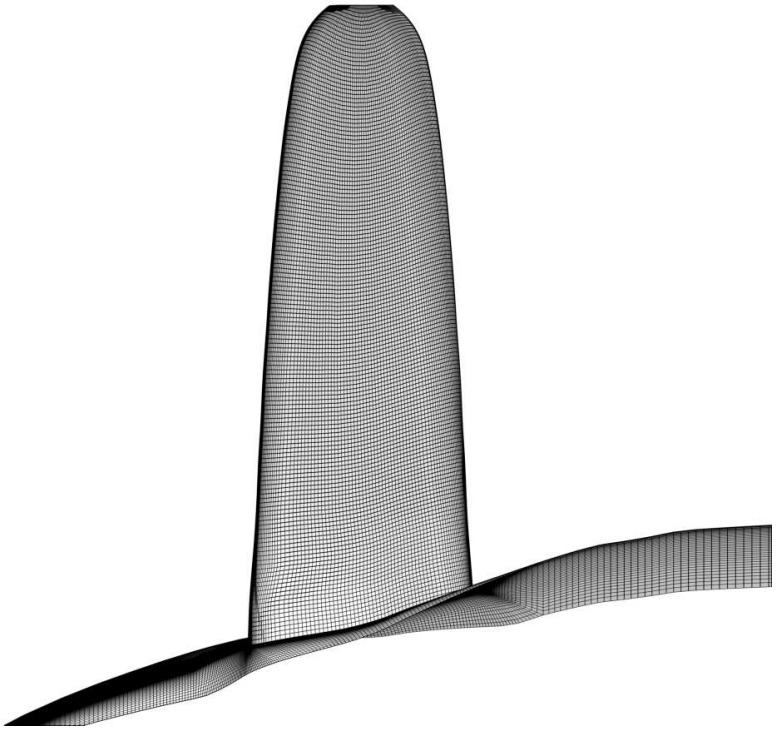

FIGURE B.3: Zoomed in view of mesh on SR2 propeller blade

B.2 Richardson Extrapolation

The method used to assess the level of spatial resolution of the CFD grids used in the project is a Richardson Extrapolation as described in Roache[52]. The order of convergence of the solution, p, is defined in Equation B.1 for three variables, f_1, f_2, f_2 which corresponds to the parameter of interest such as the thrust coefficient for a coarse, medium and fine grid resepctivley. The refinement ratio, r, is the level of refinement between grids where a refinement ratio of 2 means the grid spacing is halved.

$$p = \frac{\ln(\frac{f_3 - f_2}{f_2 - f_1})}{\ln r} \tag{B.1}$$

The relative errors for the coarse mesh, ϵ_{12}, and fine mesh, ϵ_{23} are defined in Equation B.2 and Equation B.3 resepctivley.

$$\epsilon_{12} = \frac{f_2 - f_1}{f_1} \tag{B.2}$$

$$\epsilon_{23} = \frac{f_3 - f_2}{f_3} \tag{B.3}$$

The value of the parameter of interest for a grid with zero spacing, f_0 ,is extrapolated using Equation B.4.

$$f_0 = f_2 + \frac{(f_1 - f_2)r^p}{r^p - 1} \tag{B.4}$$

The grid convergence index, GCI, defined in Equation B.5is dependent on the choice of factor of safety, F_s, in this project a conservative value of 3 has been used. For adequate grid convergence for the asymptotic range, AR, should be a close to possible as one. The asymptotic range is defined in Equation B.6.

$$GCI = F_s \frac{|\epsilon|}{r^p - 1} \tag{B.5}$$

$$AR \cong \frac{GCI_{2-3}}{r^p GCI_{1-2}} \cong 1 \tag{B.6}$$

Note in order to use this method the parameter of interest should change monotonically with grid mesh refinement.

A grid sensitivity study for the SR2 CFD model was calculated for three grids which have 1.6, 3.5 and 5.4 million nodes in the inner rotatonal domain for the coarse, medium and fine grids resepctivley. The rotor operating conditions where a setting angle, β of

45.8°, freestream Mach number, M_o of 0.2 and advance ratio, J, of 1.1. The results of the Richardson extrapolation for this case is shown in Table B.1 where an asymptotic range of one was achieved for the thrust coefficient, C_T.

	Coarse (f_1)	Med (f_2)	Fine (f_3)	p	Zero (f_0)	ϵ_{12}	ϵ_{23}	GCI_{12}	GCI_{23}	AR
C_T	0.6075	0.6080	0.6082	1.74	0.6082	-0.0009	-0.0003	-0.0011	-0.0003	1.0009

TABLE B.1: Richardson Extrapolation results for SR2 grid sensitivity study

A grid sensitivity study was also performed the two blade analogue CFD model. The rotor operating conditions where a setting angle, β of 22.8 °, freestream Mach number, M_o of 0.144 and rpm of 6875.5. The results of the Richardson extrapolation are shown in Table B.2 for the torque moment where grids with inner rotational domains with 1.7, 3.5 and 7.5 million nodes where used. An asymptotic range of one was also achieved.

	Coarse (f_1)	Med (f_2)	Fine (f_3)	p	Zero (f_0)	ϵ_{12}	ϵ_{23}	GCI_{12}	GCI_{23}	AR
Torque (Nm)	1.4343	1.4472	1.4549	0.66611	1.46797	-0.0085	-0.0053	-0.0435	-0.0272	1.0085

TABLE B.2: Richardson Extrapolation results for open rotor analogueue grid sensitivity study

B.3 Coordinate transformation into vortex cross plane

Section B.3 includes details of the coordinate systems and defining equations used to view the vortex in a plane normal to its path - known as the vortex cross plane in this thesis The method is also explained in[62]. The first step is to take a slice in a plane downstream of the propeller pitch change axis normal to the engine change axis which is also in the same plane as the PIV laser sheets. The location of a plane normal to the engine axis at an axial distance, Y_core, downstream of the propeller pitch change axis is shown in Figure B.4.

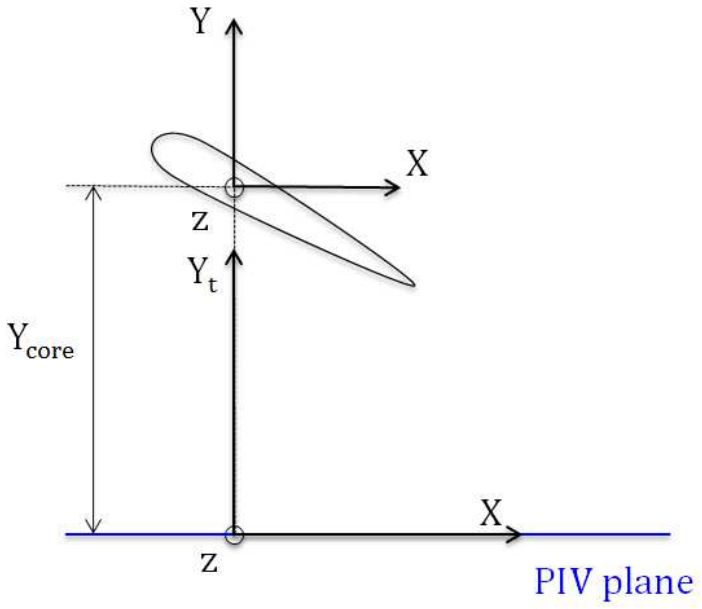

FIGURE B.4: Axial slice downstream of propeller pitch change axis

The vortex cross plane is taken normal about the coordinates $(X_{core}, Y_{core}, Z_{core})$ in Tecplot using its 'arbitrary slice' option. Where:

$$X_t = X - X_{core} \tag{B.7}$$

$$Y_t = Y + Y_{core} \tag{B.8}$$

$$Z_t = Z - Z_{core} \tag{B.9}$$

The phase angle, θ, is shown in Figure B.5 and is defined as the arc tangent of X_{core} and Z_{core}. The velocity component nomenclature corresponds to their respective axis in Figure B.5.

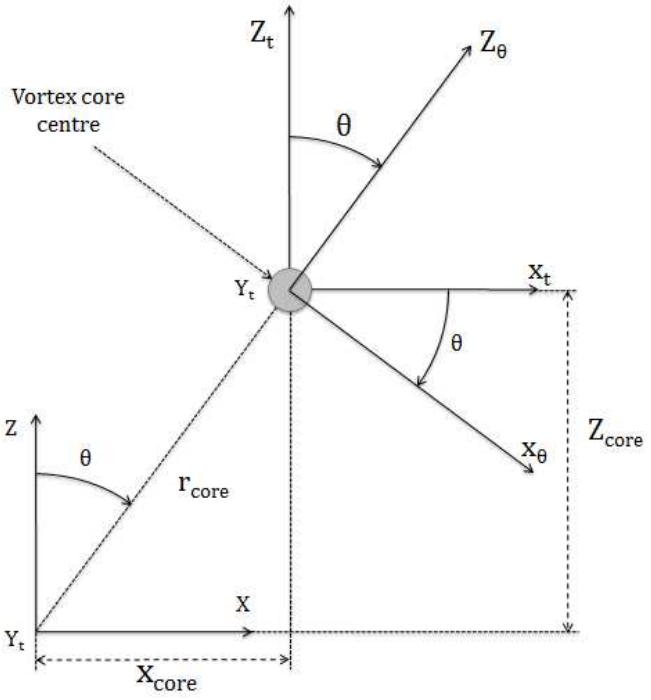

FIGURE B.5: X-Z Plane and definition of phase angle θ

$$\theta = \tan^{-1}\left(\frac{X_{core}}{Z_{core}}\right) \tag{B.10}$$

$$r_{core} = |X_{core} + Z_{core}| \tag{B.11}$$

$$X_\theta = X_t \cos\theta - Z_t \sin\theta \tag{B.12}$$

$$Z_\theta = Z_{plane} = Z_t \cos\theta + X_t \sin\theta \tag{B.13}$$

Another important angle in the transformation is the helix angle, φ, and it is the angle between the tip vortex path and engine axis plane as shown in Figure B.6. All velocity components are in the relative frame of reference.

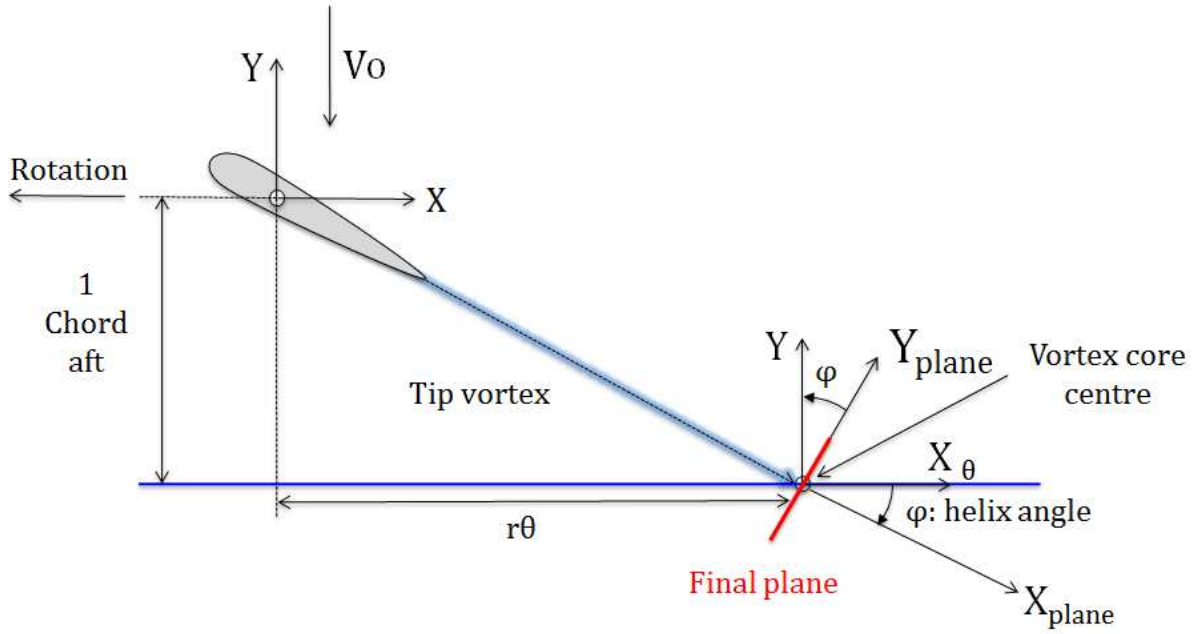

FIGURE B.6: Orientation of vortex cross plane relative to tip vortex path and PIV plane

$$\varphi = \tan^{-1}\left(\frac{Y_{core}}{r_{core}\theta}\right) \tag{B.14}$$

$$X_{plane} = X_\theta \cos\varphi - Y_t \sin\varphi \tag{B.15}$$

$$Y_{plane} = Y_t \cos\varphi + X_\theta \sin\varphi \tag{B.16}$$

$$U_{yt} = U_y - V_i \tag{B.17}$$

$$U_{x\theta} = U_x \cos\theta - U_z \sin\theta \tag{B.18}$$

$$U_{xplane} = U_{x\theta} \cos\varphi - U_{yt} \sin\varphi \tag{B.19}$$

$$U_{yplane} = U_{yt} \cos\varphi + U_{x\theta} \sin\varphi \tag{B.20}$$

The Cartesian components U_{Yplane} and U_{zplane} are transformed into the polar coordinates $V_{\theta plane}$ and V_{rplane} according to the coordinate system shown in Figure B.7 and defined by Equation B.21 and Equation B.22.

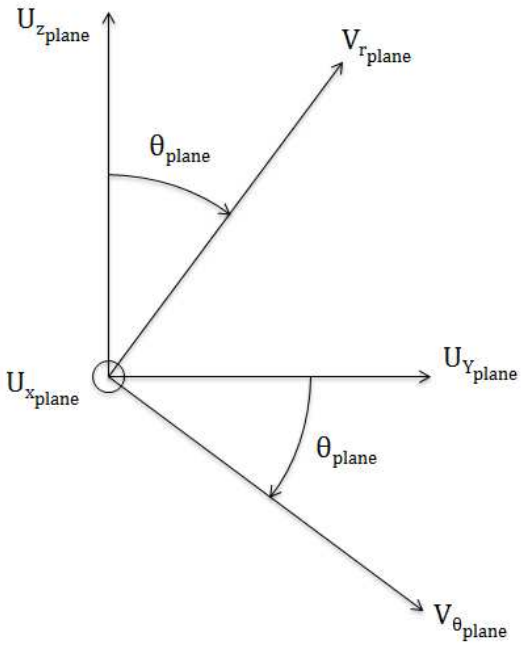

FIGURE B.7: Cartesian to polar coordinate transformation for V_θ and V_r

$$V_{rplane} = U_{zplane} \cos\varphi + U_{yplane} \sin\varphi \tag{B.21}$$

$$V_{\theta plane} = U_{yplane} \cos\varphi - U_{zplane} \sin\varphi \tag{B.22}$$

Appendix C

Open Rotor Analogue PIV

Appendix C provides a brief overview of the Particle Image Velocimetry (PIV) that was used to analyse the tip vortex of the two blade analogue propeller blade.

With reference to Figure C.1 three planes normal to the engine axis were used at one, two and three chords downstream of the propeller pitch axis. Two cameras were used as illustrated in Figure C.2, the use of two cameras allows for stereoscopic measurement of three Cartesian velocity components. The measurements in the PIV plane were projected onto the vortex cross plane using the method detailed in Section B.3 of Appendix B and a columnar vortex assumption. The propeller rotation was generated using an electrical motor with a limited power output, which is one of the reasons for using a two bladed system. The measurements were conducted in the Cranfield University 8x6 low-speed wind tunnel with Laskin seeder and rakes.

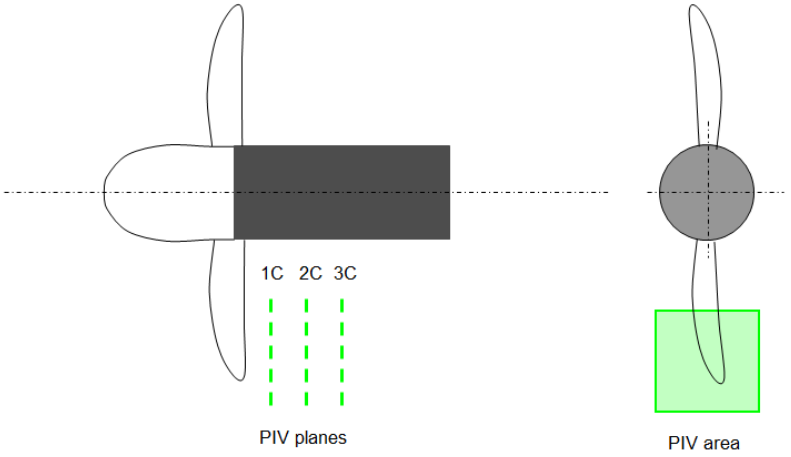

FIGURE C.1: PIV configuration for open rotor analogue [Ref:Dr MacManus]

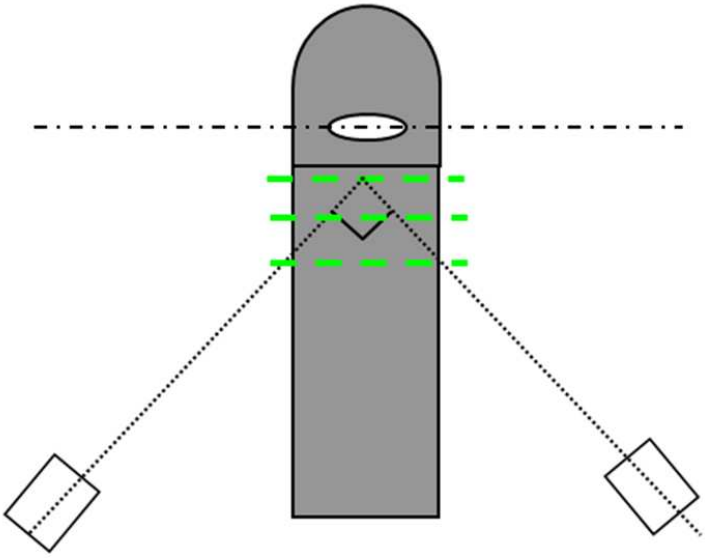

FIGURE C.2: Location of cameras relative to PIV planes and propeller blade [Ref:Dr MacManus]

Appendix D

Additional Aeroacoustic Results

Appendix includes additional directivity responses for six interaction tones for each of the cases in the synthesis matrix.

D.1 Additional Directivity Responses

D.1.1 Case One and Two: Type of Vortex model uses

Case One: Baseline CRPFAN vortex model

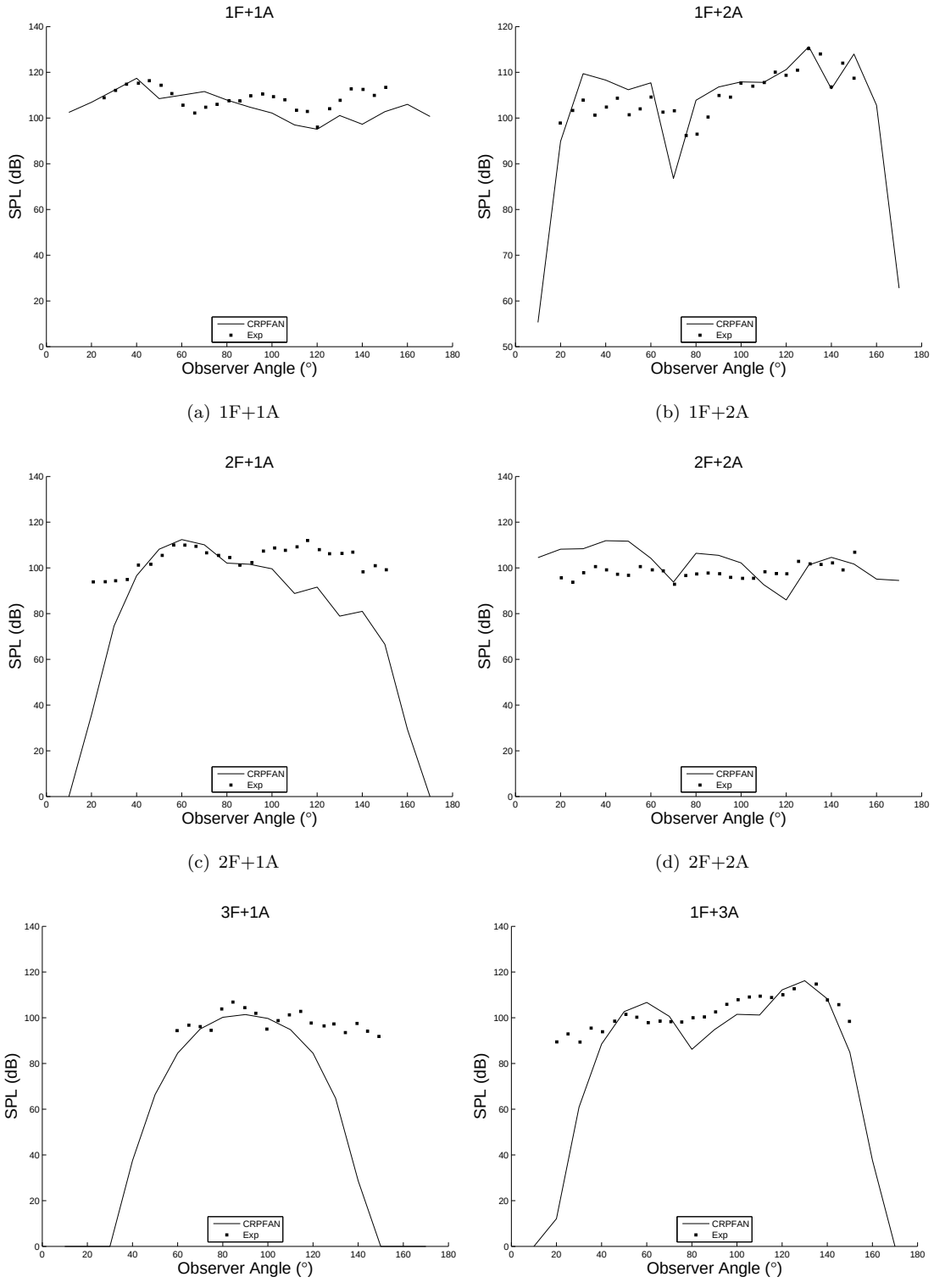

(a) 1F+1A

(b) 1F+2A

(c) 2F+1A

(d) 2F+2A

(e) 3F+1A

(f) 1F+3a

FIGURE D.1: Case 1 : Baseline CRPFAN model

Case Two: Vatistas Vortex model

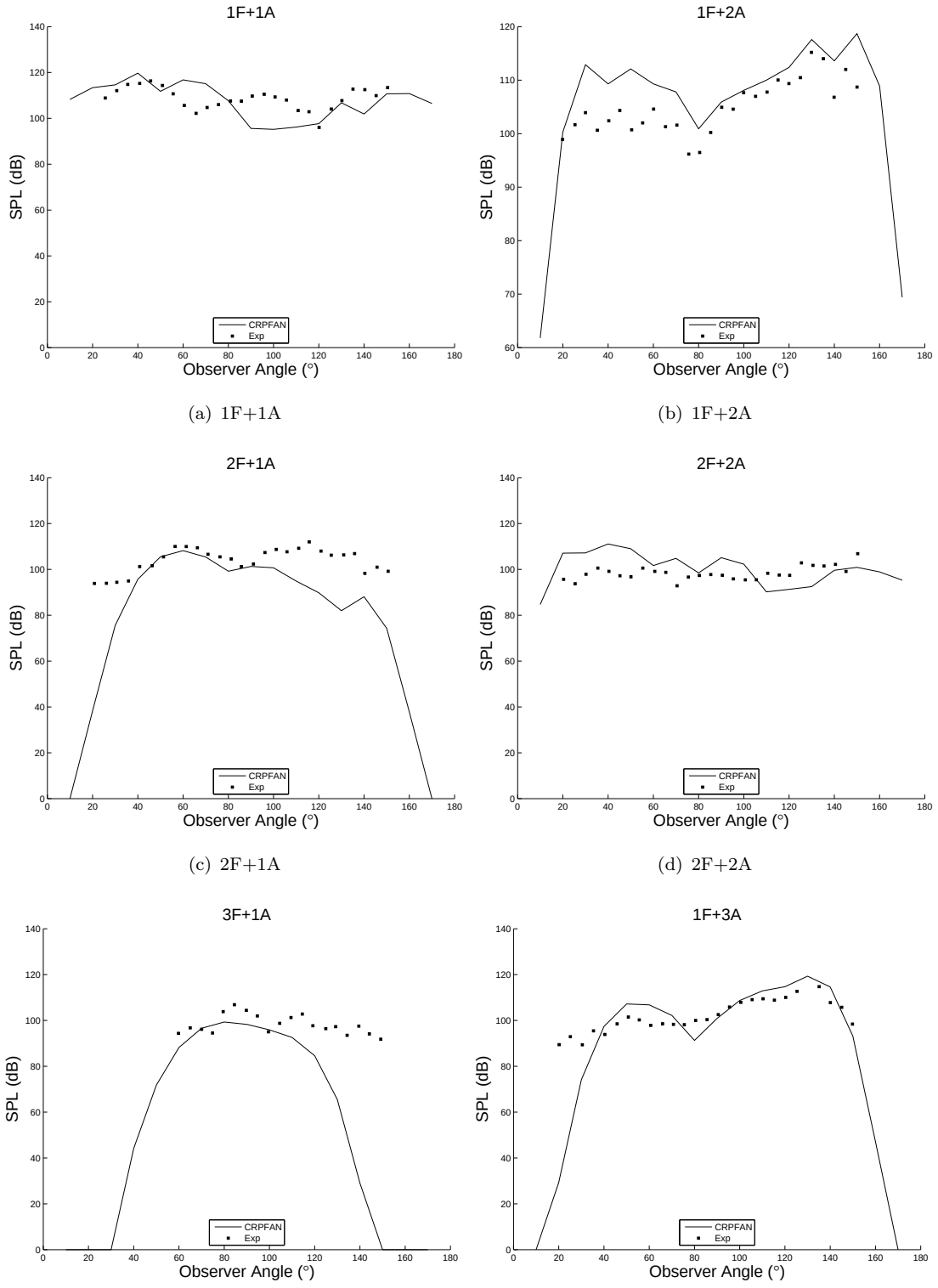

(a) 1F+1A

(b) 1F+2A

(c) 2F+1A

(d) 2F+2A

(e) 3F+1A

(f) 1F+3a

FIGURE D.2: Case 2: Use of Vatistas vortex model

D.1.2 Case Three: Streamline descritisation effects

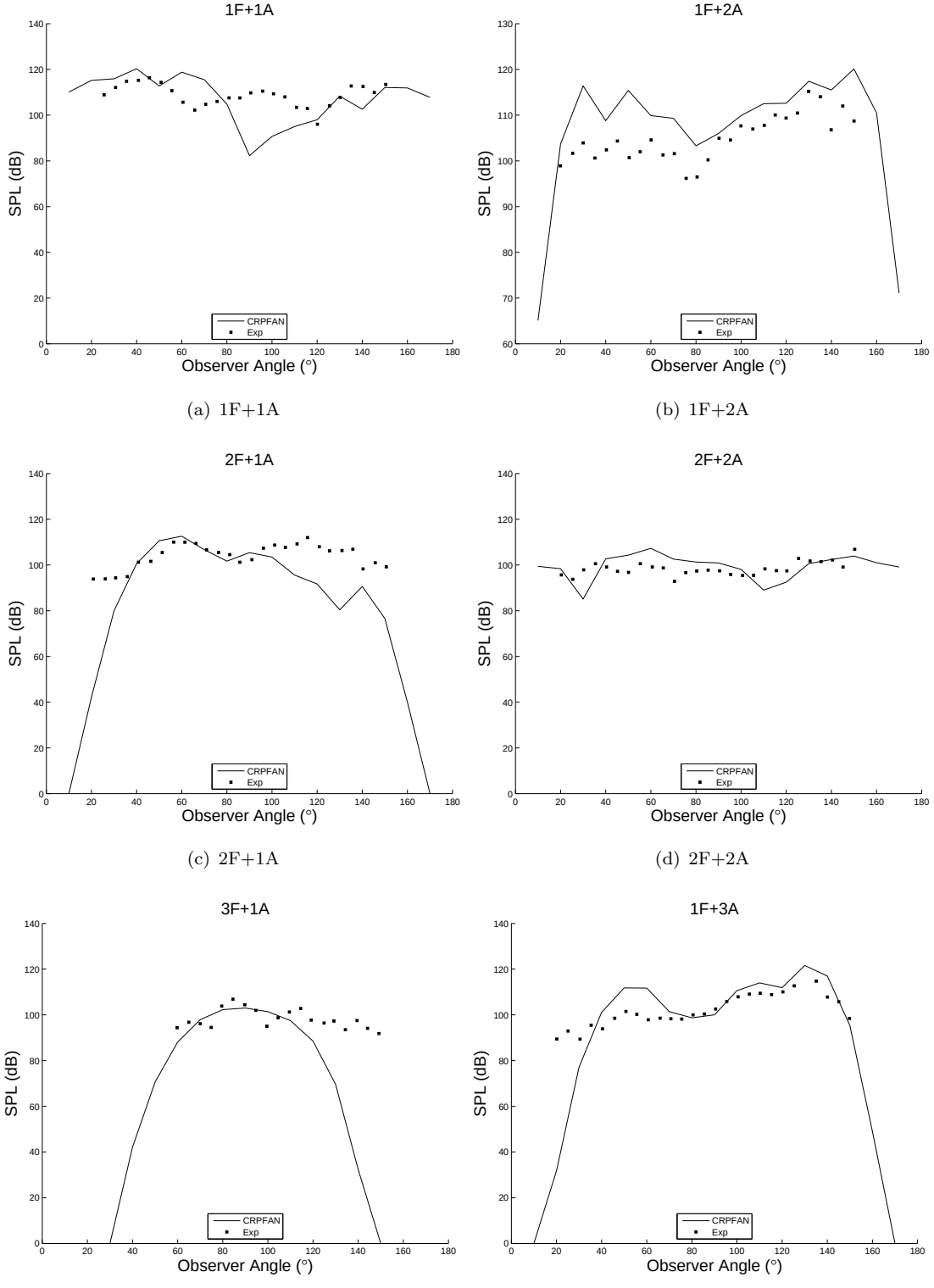

(a) 1F+1A

(b) 1F+2A

(c) 2F+1A

(d) 2F+2A

(e) 3F+1A

(f) 1F+3a

FIGURE D.3: Case 3: Effect of streamline descritisation

D.1.3 Case Four: Vortex Spatial Orientation

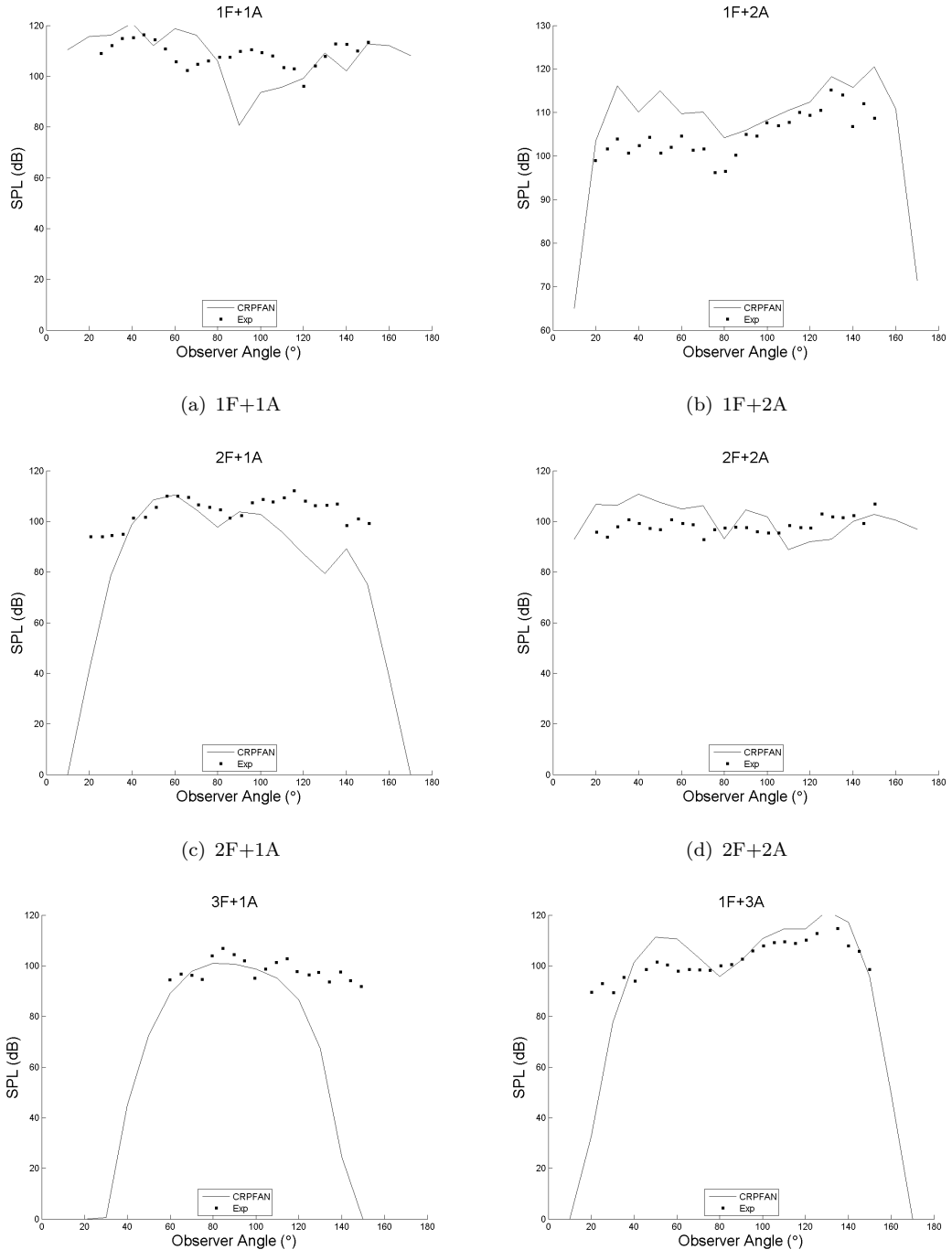

(a) 1F+1A

(b) 1F+2A

(c) 2F+1A

(d) 2F+2A

(e) 3F+1A

(f) 1F+3a

FIGURE D.4: Case 4: Effect of vortex spatial orientation

D.1.4 Case Five: Vortex axial velocity modelling

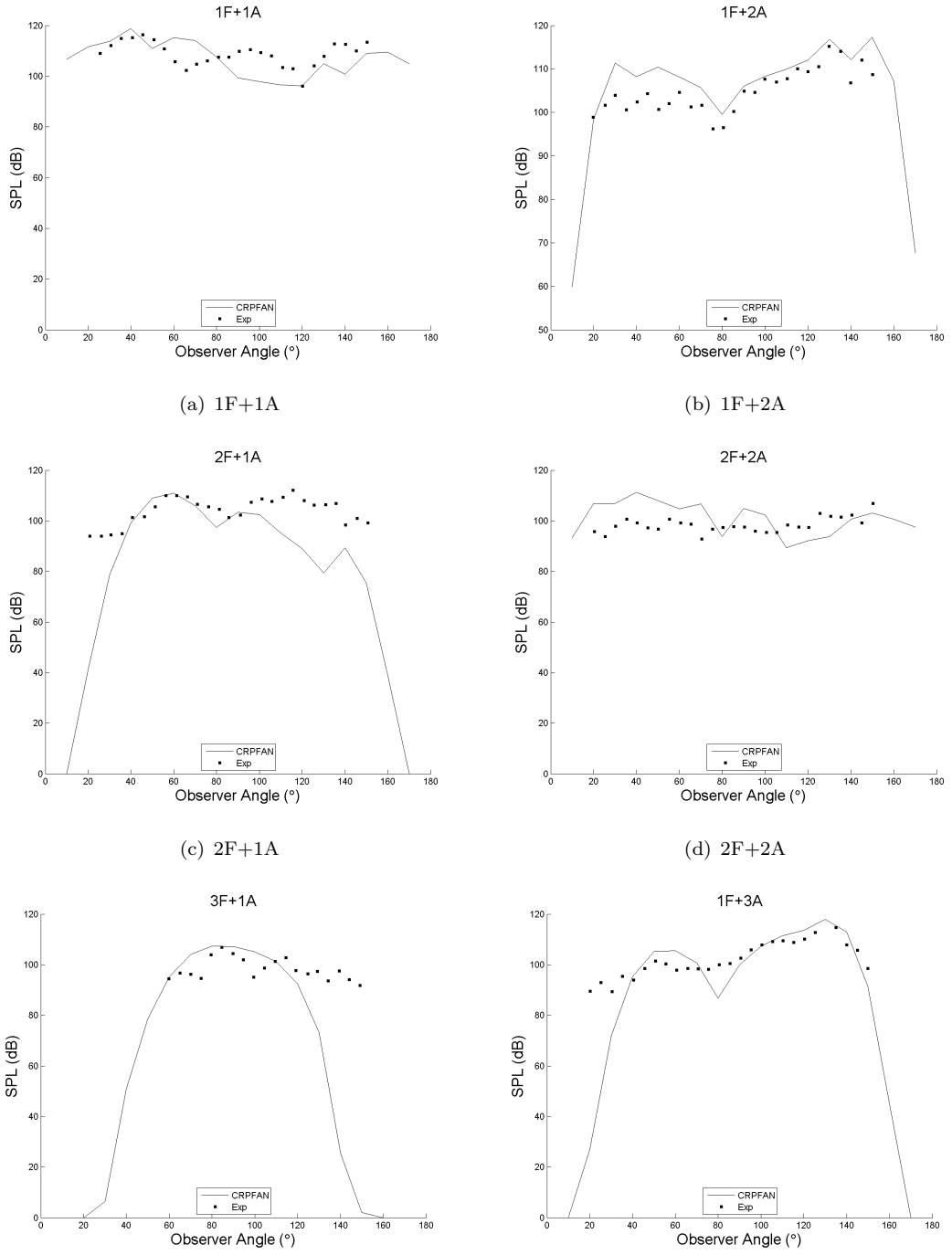

(a) 1F+1A

(b) 1F+2A

(c) 2F+1A

(d) 2F+2A

(e) 3F+1A

(f) 1F+3a

FIGURE D.5: Case 5: Effect of including vortex axial velocity component

D.1.5 Case Six: Trajectory Modelling

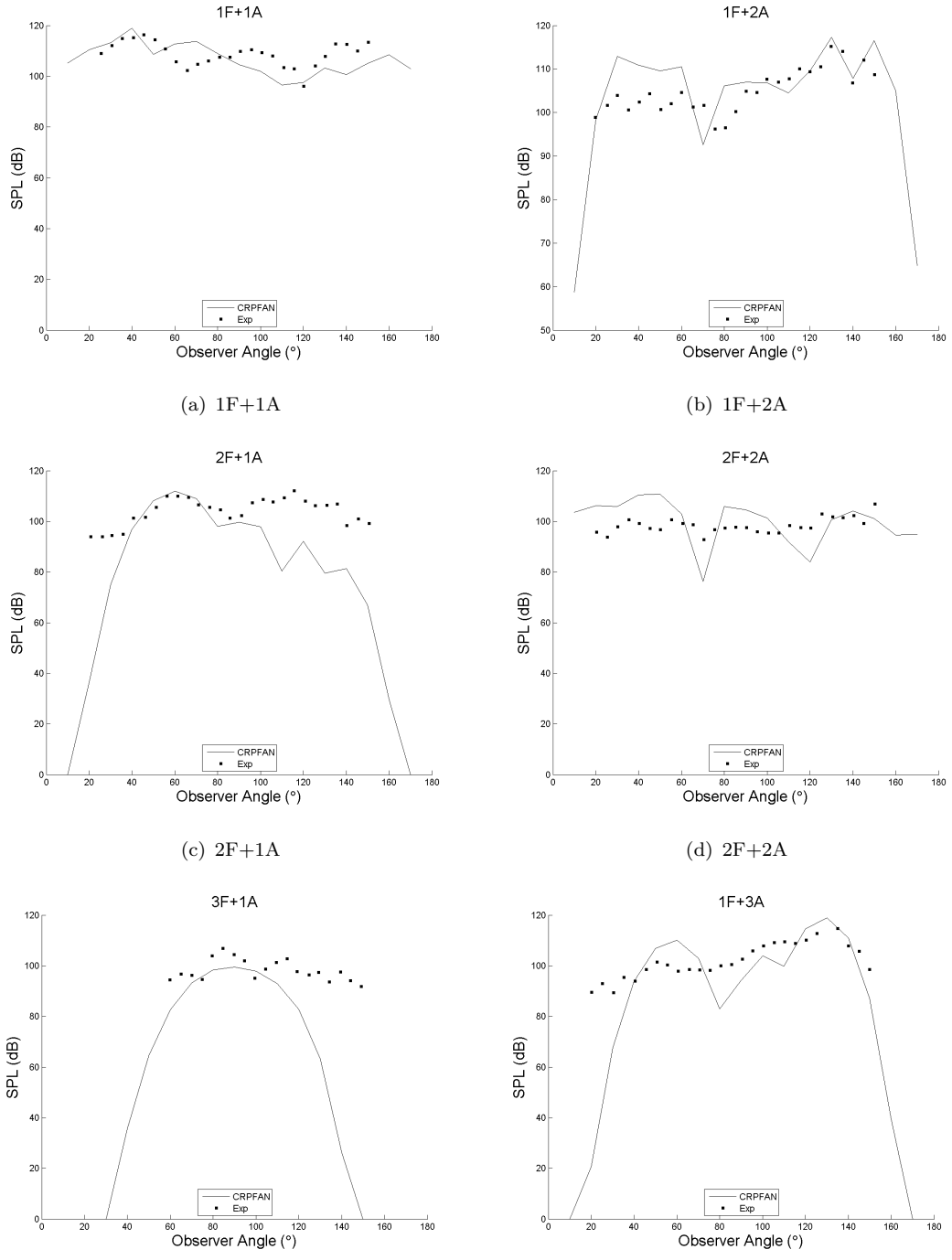

(a) 1F+1A

(b) 1F+2A

(c) 2F+1A

(d) 2F+2A

(e) 3F+1A

(f) 1F+3a

FIGURE D.6: Case 6: Effect of revised trajectory model

D.1.6 Case: 7 Revised tip vortex correlations

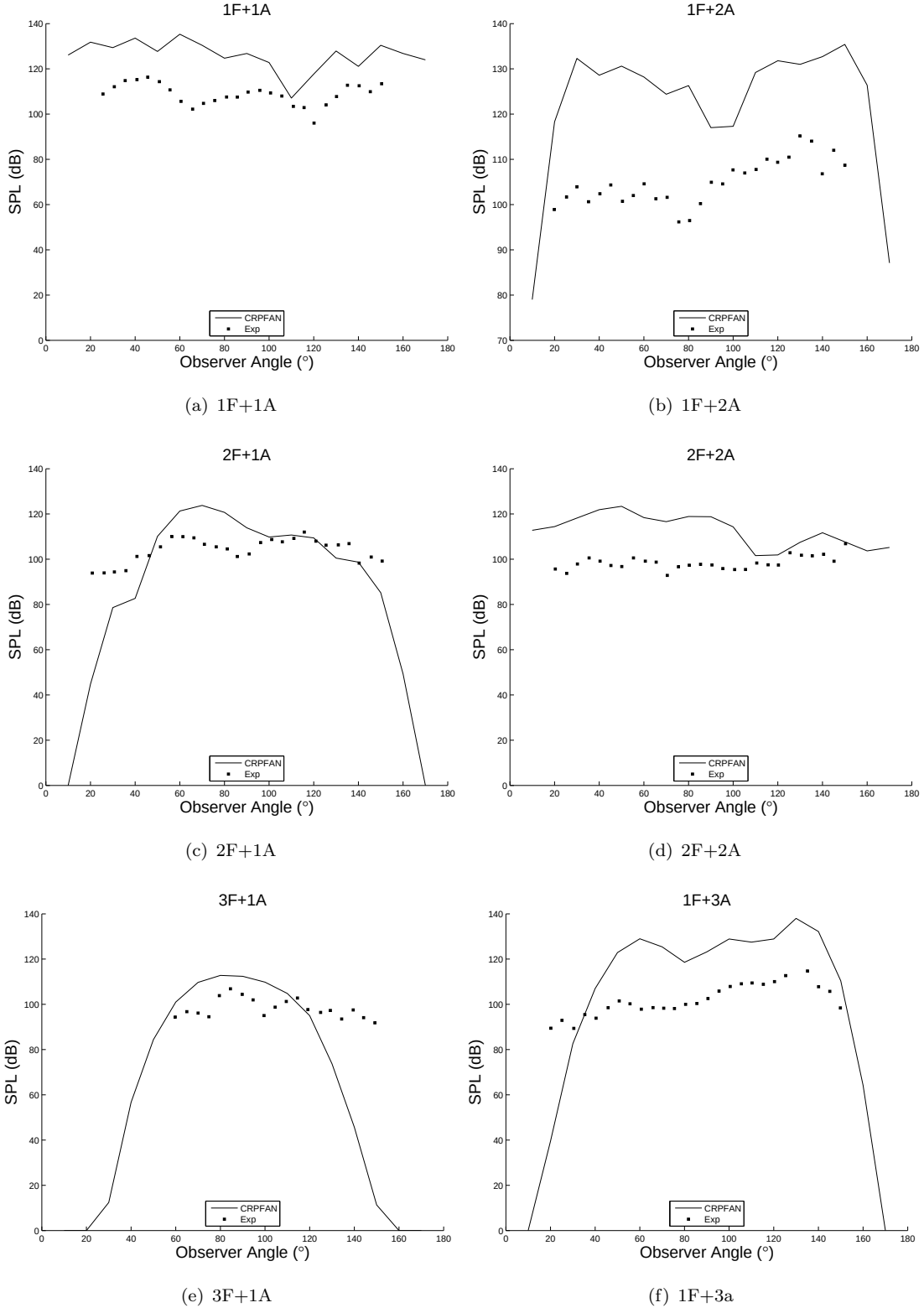

(a) 1F+1A

(b) 1F+2A

(c) 2F+1A

(d) 2F+2A

(e) 3F+1A

(f) 1F+3a

FIGURE D.7: Case 7: Effect of using revised tip vortex correlations

D.1.7 Case 8 additional directivity diagram

Case 8a

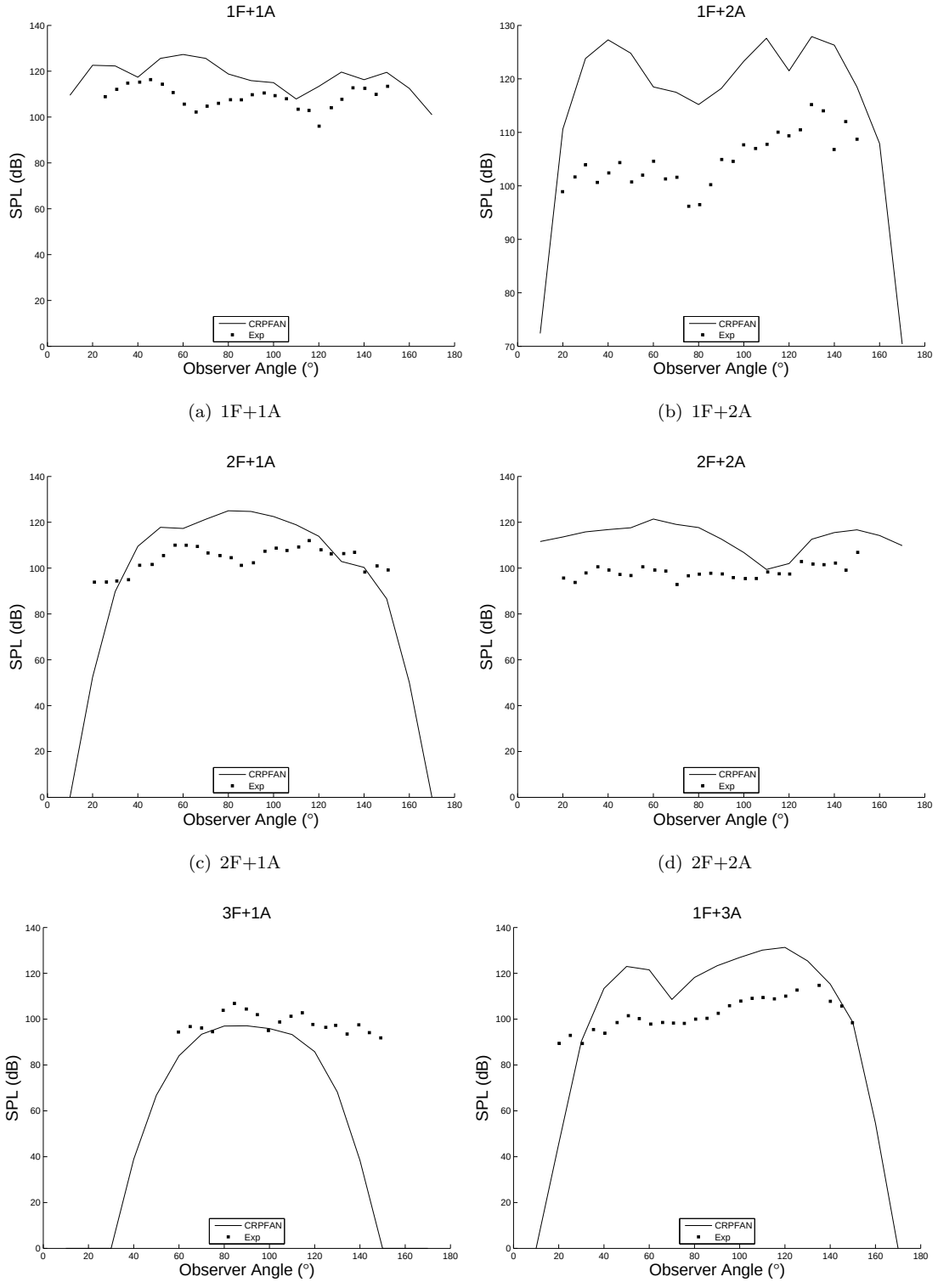

(a) 1F+1A

(b) 1F+2A

(c) 2F+1A

(d) 2F+2A

(e) 3F+1A

(f) 1F+3a

FIGURE D.8: Case 8a additional directivity responses

Case 8c

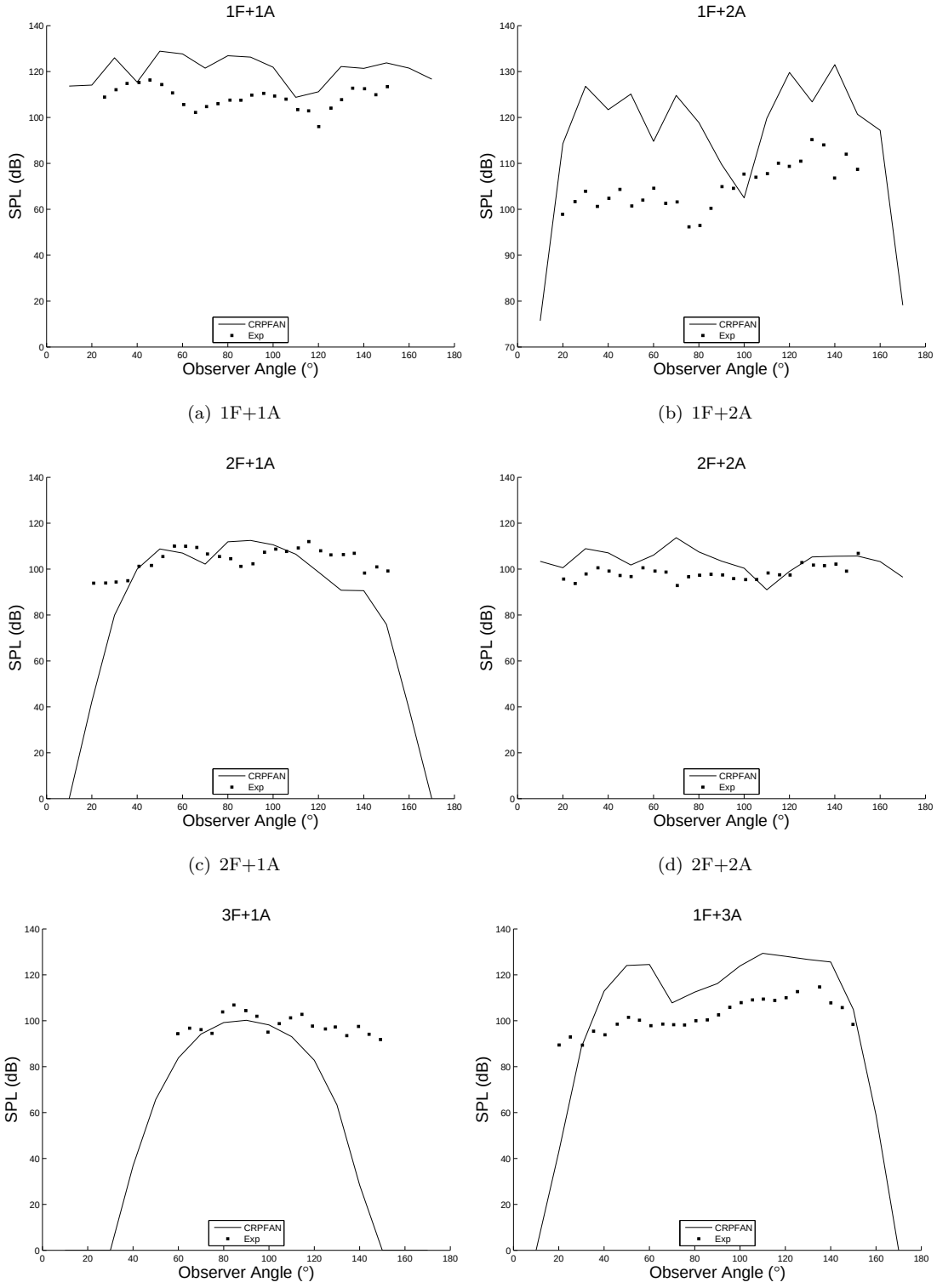

(a) 1F+1A

(b) 1F+2A

(c) 2F+1A

(d) 2F+2A

(e) 3F+1A

(f) 1F+3a

FIGURE D.9: Case 8c additional directivity responses

Appendix E

Theodorsen Method strip theory code

Within the installation module of CRPFAN is a Theodorsen code which is not used in the default isolated operation of CRPFAN. It uses the general CRPFAN input files for the propeller geometry and operating conditions. The general process is summarised in Figure E.2. With reference to the velocity triangles in Figure E.1 the first stage of the calculation process is to make an estimate for the angles of flow relative to blade from tangential direction for the front and aft rotor, ϕ_F and ϕ_R. Then for each radial section the local angle of attack onto the blades are calculated followed by the slipstream contraction factors. The sectional angle of attack values are used to interpolate from a lift and drag curve sectional values for C_L and C_D. The lift and drag coefficients are used to calculate C_X and C_Y and after adjustment using a Prandtl tip loss factor the axial and tangential interference factors are calculated for each blade row which are fed back to calculate the relative flow angles and the whole process is repeated until convergence of the relative flow angles is achieved.

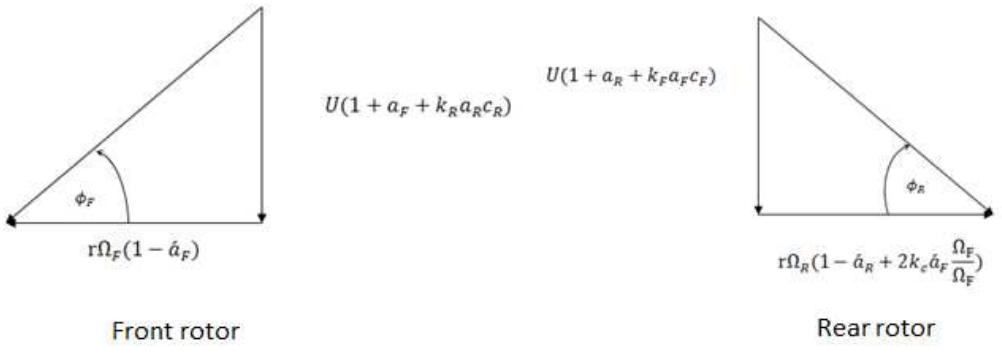

FIGURE E.1: Velocity triangles for Theodorson method code[5]

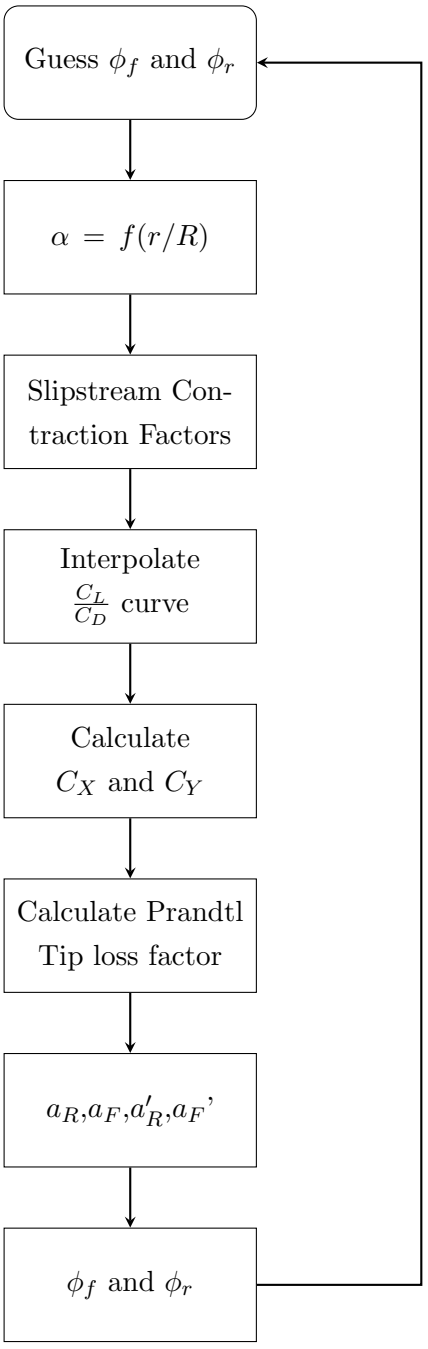

FIGURE E.2: Theodorsen code flow chart

$$c = 1 \pm \frac{x}{\sqrt{x^2 + r^2}} \tag{E.1}$$

$$C_y = C_L cos\phi - C_D sin\phi \tag{E.2}$$

$$C_x = C_L sin\phi + C_D cos\phi \tag{E.3}$$

$$\frac{a'F}{(1 - a'F)} = \frac{C_{xF}\sigma_F}{4cos\phi_F sin\phi_F k_F} \tag{E.4}$$

$$\frac{a'R}{1-a'R+2k_F a'_F \Omega_F} = \frac{C_{xR}\sigma_R}{4cos\phi_R sin\phi_R k_R} \tag{E.5}$$

$$a_F = \frac{(1-a'F)}{k_F}(\frac{r}{R})(\frac{C_{yF}}{4\lambda_F})(\frac{\sigma_F}{sin\phi_F cos\phi_F}) \tag{E.6}$$

$$a_R = \frac{(1+2k_F(\Omega_F/\Omega_R)-a'_R)}{k_R}(\frac{r}{R})(\frac{C_{yR}}{4\lambda_R})(\frac{\sigma_R}{sin\phi_R cos\phi_R}) \tag{E.7}$$

$$\lambda_F = tan(\phi_F)(\frac{r}{R})\frac{(1-a'F)}{(1+a_F+k_R a_R C_R)} \tag{E.8}$$

$$\lambda_R = tan(\phi_R)(\frac{r}{R})\frac{(1-a'_R+2k_F a'_F \Omega_F/\Omega_R)}{(1+a_R+k_F a_F C_F)} \tag{E.9}$$

Where:

a - Axial interference factor
a' - Tangential interference factor
c - Slipstream contraction factor
k - Prandtl tip loss factor
r - Propeller sectiona, radius
U' - Forward flight velocity
Ω - Angular velocity of propeller
ϕ - Angle of flow relative to blade from tangential

References

[1]Sébastien, D., "Toward acare 2020: innovative engine architectures to achieve the environmental goals?" *26th International Congress of the Aeronautical Sciences*, 2008.

[2]"Clean Sky Website," `http://www.cleansky.eu/content/page/sage-1-%E2%80%93-open-rotor`, Accessed: 2015.

[3]Stuermer, A. and Yin, J., "Low-Speed Aerodynamics and Aeroacoustics of CROR Propulsion Systems," 2009.

[4]Blandeau, V., *Aerodynamic broadband noise from contra-rtating open rotors*, Ph.D. thesis, Southhampton University, 2011.

[5]Whitfield, C., Mani, R., and Gliebe, P., "High speed turboprop aeroacoustic study (counterrotation). Volume 1: Model development," *Final Report General Electric Co., Cincinnati, OH. Advanced Technology Operations.*, Vol. 1, 1990.

[6]Mason, W., "The farfield structure of aircraft wake turbulence." 1972.

[7]Peters, A. and Spakovszky, Z., "Rotor interaction noise in counter-rotating propfan propulsion systems," *Journal of Turbomachinery*, Vol. 134, 2012, pp. 011002.

[8]Zachariadis, A., Hall, C. A., and Parry, A. B., "Contra-rotating open rotor operation for improved aerodynamics and noise at takeoff," *ASME Paper GT*, Vol. 45205, 2011.

[9]Kingan, M. J. and Self, R. H., "Counter-rotation propeller tip vortex interaction noise," *AIAA Paper*, Vol. 3135, 2009.

[10]Majjigi, R., Uenishi, K., and Gliebe, P. R., "An investigation of counterrotating tip vortex interaction," *Unknown*, Vol. 1, 1989.

[11]Fukumoto, Y. and Okulov, V., "The velocity field induced by a helical vortex tube," *Physics of Fluids (1994-present)*, Vol. 17, No. 10, 2005, pp. 107101.

[12]plc (United Kingdom);, R.-R., *The jet engine*, 1986.

[13]Groeneweg, J. F. and Bober, L. J., "NASA advanced propeller research," 1988.

[14]Magliozzi, B., Hanson, D., and Amiet, K., "Aeroacoustics of Flight Vehicles: Theory and Practice," *edited by HH Hubbard, NASA TR*, 1991, pp. 90–3052.

[15]J Trchalik, Y. M., "Possible Configurations and Aircraft Installations of an Open Rotor Engine," *IMechE Symposium Towards Sustainable Aviation Propulsion*, 2008.

[16]Russell, D. A., Titlow, J. P., and Bemmen, Y.-J., "Acoustic monopoles, dipoles, and quadrupoles: An experiment revisited," *American Journal of Physics*, Vol. 67, No. 8, 1999, pp. 660–664.

[17]Gutin, L., "On the sound field of a rotating propeller," 1948.

[18]Parry, A. B., *Theoretical prediction of counter-rotating propeller noise*, Ph.D. thesis, University of Leeds, 1988.

[19]Parzych, D. J., "A modal evaluation of noise generated by the front rotor of a counter-rotating propfan," *AIAA, Space Programs and Technologies Conference*, Vol. 1, 1990.

[20]Dittmar, J. H., "The effect of front-to-rear propeller spacing on the interaction noise of a model counterrotation propeller at cruise conditions," *Unknown*, Vol. 1, 1987.

[21]Hanson, D. B., "Noise of counter-rotation propellers," *Journal of Aircraft*, Vol. 22, No. 7, 1985, pp. 609–617.

[22]Woodward, R. P., "Noise of a model high speed counterrotation propeller at simulated takeoff/approach conditions (F7/A7)," 1987.

[23]Haller, G., "An objective definition of a vortex," *Journal of Fluid Mechanics*, Vol. 525, 2005, pp. 1–26.

[24]Anderson John, D., "Fundamentals of aerodynamics," 2005.

[25]Green, S. I., "Introduction to vorticity," *Fluid Vortices*, Springer, 1995, pp. 1–34.

[26]Shapiro, A. H., Churchill, J., and Britannica, E., *Vorticity*, Encyclopaedia Britannica Educational Corporation, 1988.

[27]Saffman, P. G., *Vortex dynamics*, Cambridge university press, 1992.

[28]Bhagwat, M. and Leishman, J., "Generalized viscous vortex model for application to free-vortex wake and aeroacoustic calculations," *Annual Forum Proceedings-American Helictoper Society*, Vol. 58, American Helicopter Society, 2002, pp. 2042–2057.

[29]Leishman, J. G., *Principles of Helicopter Aerodynamics*, Cambridge university press, 2006.

[30]Lamb, H., *Hydrodynamics*, Cambridge University Press, 1993.

[31]Mason, W. and Marchman Ill, J., "Far-field structure of aircraft wake turbulence," *Journal of Aircraft*, Vol. 10, No. 2, 1973, pp. 86–92.

[32]Young, L. A., "Vortex core size in the rotor near-wake," *NASA Technical Memorandum*, Vol. 212275, 2003.

[33]Grow, T. L., "Effect of a wing on its tip vortex." *Journal of Aircraft*, Vol. 6, No. 1, 1969, pp. 37–41.

[34]Hanson, D. and Patrick, W., "Investigation of the near wake of a propfan," *Journal of Aircraft*, Vol. 27, No. 6, 1990, pp. 536–542.

[35]Tillman, T. and Simonich, J., "Hot wire measurements downstream of a propfan," *Journal of Propulsion and Power*, Vol. 7, No. 5, 1991, pp. 776–783.

[36]Podboy, G. G. and Krupar, M. J., "Laser velocimeter measurements of the flowfield generated by an advanced counterrotating propeller," 1989.

[37]Simonich, J., McCormick, D., and Lavrich, P., "Role of leading-edge vortex flows in prop-fan interaction noise," *Journal of aircraft*, Vol. 30, No. 2, 1993, pp. 255–261.

[38]Lavrich, P. L., McCormick, D. C., and Parzych, D. J., "Vortex structure of wakes behind an advanced propeller at takeoff load conditions," *AIAA, Space Programs and Technologies Conference*, Vol. 1, 1990.

[39]TSAI, T., DEJONG, F., and LEVY, R., "Computation of the tip vortex flowfield for advanced aircraft propellers," 1988.

[40]Vaczy, C. and McCormick, D., "A study of the leading edge vortex and tip vortex on prop-fan blades," *Journal of turbomachinery*, Vol. 109, No. 3, 1987, pp. 325–331.

[41]Janardan, B. A. and Gliebe, P., "Acoustic Characteristics of Counterroating Unducted Fans From Model Scale Tests," *J. Aircraft*, Vol. 27, 1990, pp. 268–275.

[42]Zachariadis, A. and Hall, C., "Application of a Navier-Stokes Solver to the Study of Open Rotor Aerodynamics," *Proceedings of ASME Turbo Expo*, 2009.

[43]Schnell, R., Yin, J., Voss, C., and Nicke, E., "Assessment and Optimization of the Aerodynamic and Acoustic Characteristics of a Counter Rotating Open Rotor," ASME, 2010.

[44]Olausson, M., Avellán, R., Sörman, N., Rudebeck, F., and Eriksson, L., "Aeroacoustics and Performance Modeling of a Counter-Rotating Propfan," ASME, 2010.

[45]Laban, M., Kok, J., and Prananta, B., "Numerical tools for contra-rotating open-rotor performance, noise and vibration assessment," 2010.

[46]Stuermer, A., "Unsteady cfd simulations of contra-rotating propeller propulsion systems," *AIAA paper*, Vol. 5218, 2008.

[47]Spalart, P., Travin, A., Shur, M., and Strelets, M., "Initial Noise Predictions for Open Rotors Using First Principles," *16th AIAA/CEAS Aeroacoustics Conference, Stockholm, Sweden*, 2010.

[48]Brailko, I., Mileshin, V., Nyukhtikov, M., and Pankov, S., "Computational and Experimental Investigation of Unsteady and Acoustic Characteristics of Counter-Rotating Fans," ASME, 2004.

[49]Mileshin, V., Nyukhtikov, M., Orekhov, I., Pankov, S., and Shchipin, S., "Open Counter–Rotation Fan Blades Optimization Based On 3d Inverse Problem Navier-Stokes Solution Method With The Aim Of Tonal Noise Reduction," *Proceedings of GT2008 ASME Turbo Expo*, 2008, pp. 9–13.

[50]Stefko, G. and Jeracki, R., "Wind tunnel results of advanced high speed propellers in the takeoff, climb, and landing operating regimes," *AIAA, SAE, ASME, and ASEE, Joint Propulsion Conference, 21 st, Monterey, CA*, 1985, p. 1985.

[51]Duraisamy, K., *Studies in tip vortex formation, evolution and control*, Ph.D. thesis, 2005.

[52]Roache, P., "Quantification of uncertainty in computational fluid dynamics," *Annual Review of Fluid Mechanics*, Vol. 29, No. 1, 1997, pp. 123–160.

[53]Ansys, C., "Ansys CFX-Solver Theory Guide," *Release*, Vol. 11, 2006, pp. 2006.

[54]Versteeg, H. K. and Malalasekera, W., *An introduction to computational fluid dynamics: the finite volume method*, Pearson Education, 2007.

[55]Birch, D., Lee, T., Mokhtarian, F., and Kafyeke, F., "Structure and induced drag of a tip vortex," *Journal of Aircraft*, Vol. 41, No. 5, 2004, pp. 1138–1145.

[56]Lee, T. and Pereira, J., "Nature of wakelike and jetlike axial tip vortex flows," *Journal of Aircraft*, Vol. 47, No. 6, 2010, pp. 1946–1954.

[57]Zhou, Y., Zhang, H. J., and Whitelaw, J. H., "Wing-tip vortex measurement with particle image velocimetry," *AIAA Paper-2433*, 2004.

[58]McAlister, K. W. and Takahashi, R., "NACA 0015 wing pressure and trailing vortex measurements," Tech. rep., DTIC Document, 1991.

[59]Avakian, S., *Preliminary aerodynamic performance study of a coaxial helicopter pusher propeller*, Master's thesis, Cranfield University, 2013.

[60]Houghton, E. L. and Carpenter, P. W., *Aerodynamics for engineering students*, Butterworth-Heinemann, 2003.

[61]Wald, Q. R., "The aerodynamics of propellers," *Progress in Aerospace Sciences*, Vol. 42, No. 2, 2006, pp. 85–128.

[62]Ouboussad, S., *Open rotor tip vortex aerodynamics*, Master's thesis, Cranfield university, 2009.